Exploration of Novel Chemotypes that Ameliorate Cellular Senescence

A thesis submitted to fulfil
requirements for the degree of

Doctor of Philosophy

by

Nathan J. Castellino

September 2024

School of Chemistry
Faculty of Science

“So you’re pretty much making the philosopher’s stone!”

– Dane Francis Leslie Tregeagle

Contents

Declaration

This thesis is a summary of research performed by the author in the School of Chemistry, University of Sydney, under the supervision of Professor Michael Kassiou between July 2020 and September 2024. This thesis contains no material which has been accepted for the award of any degree at any university. No other individual's work has been used without recognition and every effort has been made to acknowledge previously published material. This thesis contains less than 80,000 words.

Nathan J. Castellino

As the supervisor for the candidate upon which this thesis is based, I can confirm that the authorship attribution statements above are correct.

Professor Michael Kassiou

Acknowledgements

I would like to thank Prof. Michael Kassiou for his supervision of the research contained in this thesis. He has had more faith in me than I have had in myself, provided an endless source of wisdom in medicinal chemistry and always pointed me in the right direction when I felt lost. I am grateful for the opportunity to work in his group, and his guidance over these past four years.

I must also acknowledge the support of the Kassiou and Danon groups throughout my time here. I am especially thankful to Dr. Andrew Montgomery, Dr. Jakob Lane and Dr. Wendy Tran. They have provided an inordinate amount of mentorship, encouragement and support, particularly in all the proof-reading they have done in my expedited writing process. Acknowledgement must be made to Dane Tregeagle and Nick Lynch, who also assisted in proof-reading, have been the source of much synthetic knowledge in the lab and have been great friends outside the lab. I must also thank Bill Chan and Kris Dhar, who not only offered invaluable advice in my gym journey, but always engaged with my increasingly unhinged and politically charged ranting and provided a helpful sounding board for the insane ideas I had. While I will not regret leaving research behind, I will sorely miss the camaraderie of the Birch lab.

There are too many people at EFCA to name who have supported me, but I will do my best: Matthew Lai, Jessica Yu, Benjamin Kah, Vanora Hou, Cyril Ho, Angel Cheung, Ernie Au-Yeung, Phillip Cheung, Matthew Chow, Stephanie Wong, Daniel Au, Matthew Thien, Julia Kam and Naomi Zhen have taken time to listen to, care for and encourage me when I wanted to drop out. I am indebted to them for the love, kindness and generosity they have shown me these last few years. From the bottom of my heart, thank you.

I am also thankful to my colleagues at Matrix Education who I have had the pleasure of teaching alongside and enjoying fancy dinners with throughout my candidature. Special thanks must go to Bianca Setionago, Jason Lin and Allan Shi for their friendship throughout this time.

Dr. Ramesh Shankara deserves his own paragraph here for powering my research with the moral support of buying me cocktails, his insights on the military-industrial complex and for being an all-round genuine mate. Here's to many more foreign policy discussions and a long career in the political machine.

I would like to thank Dr. Ian Luck, Dr. Nicholas Proschogo and Dr. Cody Szczepina for their assistance in the analytical facilities. Carlo Piscicelli and Dennis Cheng have done a

phenomenal job of maintaining the research infrastructure of the Chemistry Building, and I am grateful for their hard work and assistance. I thank Dr. Jonathan Du for his help in my molecular docking studies. I also acknowledge the contributions of Dr. Alexandra Maximova, who performed the biological evaluation in this work.

Grateful acknowledgement is made to the Australian Government and the University of Sydney for the provision of a Research Training Program Scholarship and a Faculty of Science Completion Scholarship respectively.

Finally, I wish to thank my parents. They have been my biggest supporters throughout the entire journey, and have instilled in me the value of education, perseverance and hard work. I could not have achieved anything without their endless love, words of wisdom and the safe home they have provided my entire life. Thank you for everything.

Abstract

Dementia is an umbrella term which refers to a variety of debilitating neurodegenerative diseases with fatal prognoses. The aetiologies of various neurodegenerative disease states and the mechanisms by which they progress are unclear, thus current treatment options are limited and few disease-modifying therapies exist. Most dementias affect elderly people. With the global population and human lifespans continuing to increase, it is expected that more people will be diagnosed with some form of neurodegenerative disease. This will place an ever-greater burden on carers, healthcare systems and economies. Therefore, the need for better therapeutics to combat dementia is more pressing than ever.

One hypothesis for the onset of neurodegenerative disease is the accumulation of senescent cells (SCs). Cellular senescence refers to a growth arrest in cells, and normally serves as a protection mechanism against cancer. However, it may also occur due to telomere shortening, which is a consequence of the ageing process and repeated DNA replication. Cellular senescence is particularly damaging as SCs secrete a cocktail of inflammatory factors, known as the senescence-associated secretory phenotype (SASP). This has unsurprisingly been implicated in many disease states correlated with inflammation. In the brain microenvironment, the SASP damages neurons and glial cells, leading to impairment which is symptomatic of neurodegeneration. Senescent cell anti-apoptotic pathways (SCAPs) are overexpressed in such cells and are critical to maintaining the viability of SCs and propagating their detrimental effects. Molecules capable of clearing SCs, termed ‘senolytics’, exploit their unique features to induce apoptosis. These drugs and drug candidates are an emerging area of research within medicinal chemistry, and some senolytics have already been shown in ameliorate some diseases associated with inflammation. The focus of this work has therefore been to explore novel chemotypes which can ameliorate senescence.

The B-cell lymphoma-2 (BCL-2) family of proteins is one such group in which certain members have been implicated in prevention of apoptosis. Indeed, animal models have demonstrated that the inhibition of this pathway reduces the burden of senescent cells while also maintaining the function of healthy cells. Such a pathway therefore provides an attractive target for which this work has focused on. Indeed, several inhibitors of these proteins are reported in literature, and thus have become useful starting points for the investigations detailed in this work.

A fundamental concept within medicinal chemistry is the design of new structures with biological activity. Numerous approaches to this task are reported in the literature to explore chemical space, understand the interaction of structures with a biological target and refine their structures to increase potency and specificity. A major focus of this work has been the application of various techniques in medicinal chemistry to assess different molecules which have shown senolytic potential, and subsequently explore derivatives thereof. One such method discussed is the iterative reconstruction of a known inhibitor of the BCL-2 family, where the lead molecule is sequentially built up from a smaller structure. Another is the application of scaffold hopping to known BCL-2 family inhibitors, generating previously unknown derivatives with similar electrostatics. Finally, structure-activity relationships around a known MCL-1 inhibitor were probed to explore novel chemical space. The biological evaluation of these compounds, while still ongoing, may provide valuable information to advance the current understanding of senolytics and treatments for neurodegenerative disease.

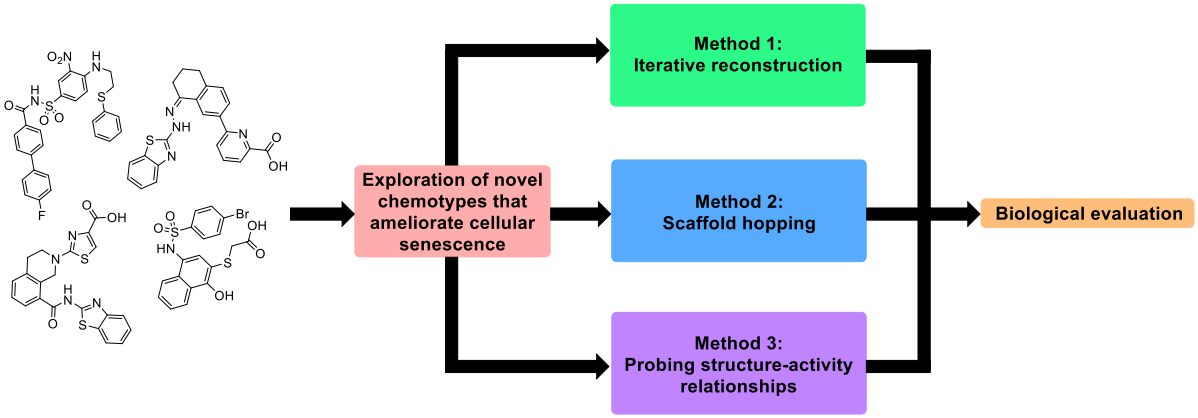

List of Abbreviations

Å	Ångstrom(s)
δ	Chemical shift
μM	Micromolar
°C	Degrees Celcius
$^1O_2$	Singlet oxygen
$^3O_2$	Triplet oxygen
AcCl	Acetyl chloride
ACh	Acetylcholine
AChE	Acetylcholinesterase
AChEI	Acetylcholinesterase inhibitor
AD	Alzheimer's disease
ALS	Amyotrophic lateral sclerosis
ANOVA	Analysis of variance
aq.	Aqueous
AT	Angiotensin
ATM	Ataxia-telangiectasia mutated
ATP	Adenosine triphosphate
b.p.	Boiling point
B_2pin_2	Bis(pinacolato)diboron
BCL-2	B-cell lymphoma-2
BET	Bromodomain and extraterminal domain
BH	BCL-2 homology
BIF	Bioisostere factor
Boc	*tert*-Butyloxycarbonyl
br	Broad
C log *P*	Calculated partition coefficient
calcd	Calculated
CAR	Chimeric antigen receptor
cat.	Catalytic
CB_2R	Cannabinoid 2 receptor
CDI	*N*,*N*′-carbonyldiimidazole
CDK	Cyclin-dependent kinase

CG	Cardiac glycoside
CJD	Creutzfeldt-Jakob disease
cm^{-1}	Wavenumber(s)
CNS	Central nervous system
CRM	Complex reaction mixture
CRYAB	α-crystallin β chain
d	Doublet
Da	Dalton(s)
DIPEA	Diisopropylethylamine
DMAP	4-(Dimethylamino)pyridine
DME	1,2-dimethoxyethane
DMF	*N*,*N*'-dimethylformamide
DMP	Dess-Martin Periodinane
DMSO	Dimethylsulfoxide
DNA	Deoxyribonucleic acid
DPPA	Diphenylphosphoryl azide
DR	Dependence receptor
ECM	Extracellular matrix
EDC·HCl	*N*-Ethyl-*N*'-(3-dimethylaminopropyl)carbodiimide hydrochloride
equiv.	Equivalents
EOD	Early-onset dementia
ESI	Electrospray ionisation
Et	Ethyl
Et_2O	Diethyl ether
Et_3N	Triethylamine
ETC	Electron transport chain
$EtNH_2$	Ethylamine
EtOAc	Ethyl acetate
EtOH	Ethanol
FDA	U.S. Food and Drug Administration
FP	Fluorescence polarisation
FTD	Frontotemporal dementia
FT-IR	Fourier transform-infrared spectroscopy
g	Gram(s)

GlyR	Glycine receptor
h	Hour(s)
HATU	Hexafluorophosphate azabenzotriazole tetramethyl uronium
HDAC	Histone deacetylase
HDF	Human dermal fibroblast
hept	Heptet
HIV	Human immunodeficiency virus
HPLC	High-performance liquid chromatography
HRMS	High-resolution mass spectrometry
HSP	Heat shock protein
HSQC	Heteronuclear single quantum correlation
HTS	High-throughput screening
HUVEC	Human umbilical vein endothelial cell
Hz	Hertz
IC_{50}	Half-maximal inhibitory concentration
IL	Interleukin
i-PrOH	Propan-2-ol
J	Coupling constant
JAK	Janus kinase
K_i	Inhibition constant
KOAc	Potassium acetate
LBD	Lewy body dementia
LOD	Late-onset dementia
log *P*	Partition coefficient
LRMS	Low-resolution mass spectrometry
M	Molar
m	Multiplet
m/z	Mass-to-charge ratio
mAb	Monoclonal antibody
MALDI	Matrix-assisted laser desorption ionisation
MCI	Mild cognitive impairment
MCL-1	Myeloid cell leukaemia sequence 1
MDM2	Mouse double minute 2
Me	Methyl

MeCN	Acetonitrile
$MeNH_2$	Methylamine
MeOH	Methanol
min	Minute(s)
mL	Millilitre(s)
mmol	Millimole(s)
MMP-3	Matrix metalloprotein 3
mol	Mole(s)
MOM	Mitochondrial outer membrane
MOMP	Mitochondrial outer membrane permeabilisation
MRI	Magnetic resonance imaging
MS	Mass spectrometry
MW	Molecular weight
n-BuLi	*n*-Butyllithium
n-BuOH	Butan-1-ol
NFT	Neurofibrillary tangle
$Ni(acac)_2$	Nickel(II) acetylacetonate
NIS	*N*-iodosuccinimide
nM	Nanomolar
nm	Nanometre(s)
NMDA	*N*-methyl-D-aspartate
NMDARA	*N*-methyl-D-aspartate receptor antagonist
NMO	*N*-methylmorpholine *N*-oxide
NMR	Nuclear magnetic resonance
OXR1	Oxidation resistance 1
p	Pentet
Ph	Phenyl
PAI-1	Plasminogen activator inhibitor 1
PAIN	Pan-assay interference compounds
PCy_3	Tricyclohexylphosphine
PD	Parkinson's disease
$Pd(dba)_2$	Tris(dibenzylideneacetone)dipalladium(0)
$Pd(dppf)Cl_2$	[1,1′-Bis(diphenylphosphino)ferrocene]dichloropalladium(II)
$Pd(OAc)_2$	Palladium(II) acetate

$Pd(PPh_3)_2Cl_2$	Bis(triphenylphosphine)palladium chloride
$Pd(PPh_3)_4$	Tetrakis(triphenylphosphine)palladium(0)
Pd/C	Palladium on carbon
PDB	Protein data bank
PET	Positron emission tomography
PhMe	Toluene
PI3K	Phosphoinositide-3-kinase
PKB	Protein kinase B
PPA	Primary progressive aphasia
PPARα	Peroxisome proliferator-activated receptor α
PPI	Protein-protein interaction
ppm	Parts per million
PROTAC	Proteolysis-targeting chimera
PT	Proton transfer
q	Quartet
QSAR	Quantitative structure-activity relationships
Rb	Retinoblastoma protein
R_f	Retention factor
RNA	Ribonucleic acid
ROS	Reactive oxidative species
RT	Room temperature
R_T	Retention time
s	Singlet
S log *P*	Wildman-Crippen partition coefficient
SA-β-Gal	Senescence-associated β-galactosidase
SAR	Structure-activity relationships
SASP	Senescence-associated secretory phenotype
sat.	Saturated
SC	Senescent cell
SCAP	Senescent cell anti-apoptotic pathway
SD	Standard deviation
S_EAr	Electrophilic aromatic substitution
SET	Single electron transfer
SMS	Senescence-messaging secretome

S_N2	Bimolecular nucleophilic substitution
S_NAr	Nucleophilic aromatic substitution
SPhos	Dicyclohexyl(2′,6′-dimethoxy[1,1′-biphenyl]-2-yl)phosphane
SPR	Surface plasmon resonance
t	Triplet
T2DM	Type 2 diabetes mellitus
TBAB	Tetrabutylammonium bromide
TCA	Tricarboxylic acid cycle
TFA	Trifluoroacetic acid
THF	Tetrahydrofuran
TLC	Thin-layer chromatography
TMSA	Trimethylsilylacetylene
TNF-α	Tumour necrosis factor α
TPAP	Tetrapropylammonium perruthenate
TPSA	Topological polar surface area
TR-FRET	Time-resolved fluorescence resonance energy transfer
u-PAR	Urokinase-type plasminogen activator receptor
UPS	Ubiquitin-proteosome system
UV	Ultraviolet
VD	Vascular dementia
VEGF	Vascular endothelial growth factor
VHL	Von Hippel-Lindau
VS	Virtual screening
WEHI	Walter and Eliza Hall Institute
WHO	World Health Organization
Xantphos	(9,9-Dimethyl-9*H*-xanthene-4,5-diyl)bis(diphenylphosphane)
XPhos	Dicyclohexyl[2′,4′,6′-tris(propan-2-yl)[1,1′-biphenyl]-2-yl]phosphane

This Page Intentionally Left Blank

This Page Intentionally Left Blank

Chapter 1

Introduction

Chapter 1 – Introduction

1.1. Global Statistics on Dementia

The World Health Organization (WHO) estimates that 55 million people live with some form of dementia as of 2019.[1] Dementia is particularly prevalent among the elderly: while only 1% of people aged 60 have some form of dementia, this rate rises to 35% by age 90.[1, 2] The WHO estimates that as of 2020, 1 billion people were over the age of 60, an age group that is expected to climb to 2.1 billion people in 2050.[3] Concurrently, the global cost of dementia is expected to rise from US$1.3 trillion in 2019 to US$2.8 trillion by only 2030.[4] Given this statistic, the influx of people into this age group is anticipated to cause an explosion in the number of dementia cases worldwide. In Australia, dementia is the second leading burden of disease, behind coronary heart disease.[5] The sheer volume of patients requiring long-term, expensive forms of care is expected to place immense strain on healthcare systems worldwide, potentially becoming one of the greatest medical challenges the world will ever have to face. This is shown in **Figure 1**, highlighting that low- and middle-income countries are especially vulnerable to these stresses as their patients will account for most dementia cases worldwide.[4] Thus, it is essential that further research in disease-modifying treatments is undertaken now, to ensure these people can live healthy lives, for as long as possible.

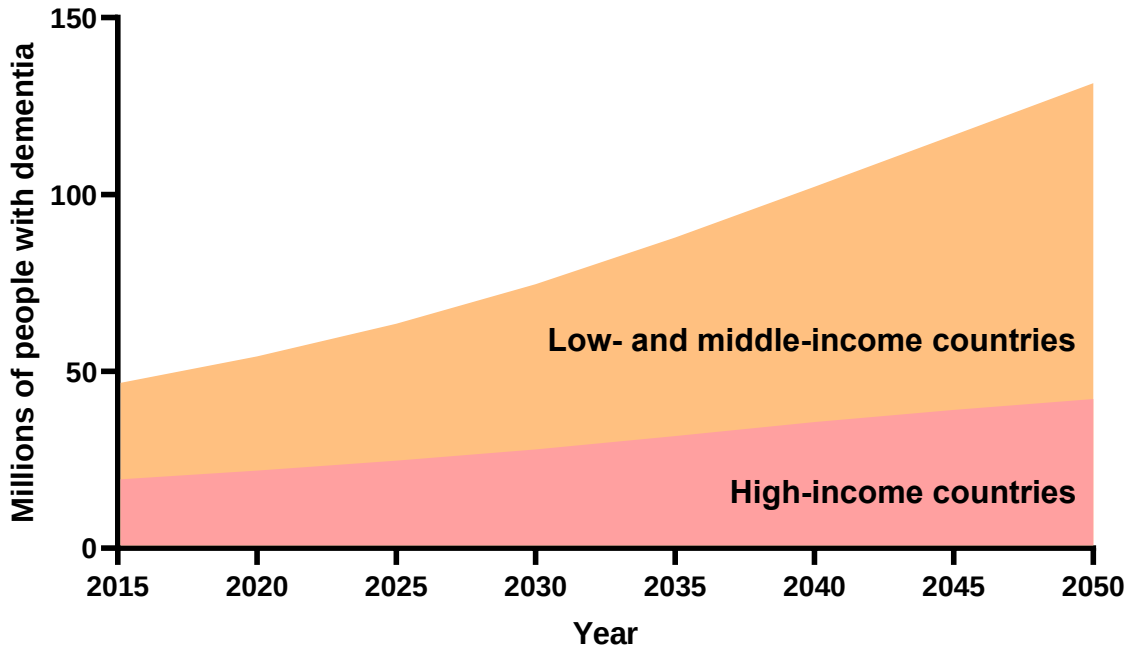

Figure 1: Projected number of people with dementia (millions) in low- and middle-income countries compared to high-income countries. Adapted from *World Alzheimer Report 2015*.[4]

1.1.1. Defining Dementia and Neurodegeneration

The term *dementia* is an umbrella term which refers to a variety of clinical syndromes affecting brain function within three specific areas: cognitive impairment, behavioural symptoms and impairment of activities of daily living.[2] Clinically, dementia describes chronic, progressive neurodegeneration, that is, atrophy of brain tissue, which manifests as the symptoms described above. It is thought that the concept of dementias is as old as human civilisation itself, with the earliest records of these symptoms being identified by ancient Egyptians in 3,000 B.C.,[6] although clinical formalisms of individual pathologies were not clarified until the 20th century. Despite its prevalence being heavily correlated with age, dementia is not a natural consequence of ageing.[7] Although dementia is most prevalent among elderly patients, a small subset of patients was found to have developed symptoms before the age of 65.[8] Known as early-onset dementia (EOD), these account for between 2–10% of all dementia cases. EOD poses significant issues in diagnosis, as symptoms such as cognitive decline, apraxia and disorientation are often mistaken as signs of contagious diseases such as human immunodeficiency virus (HIV) and syphilis.[8] This worsens the mental toll of symptoms for sufferers, as it can take a much greater duration to correctly diagnose EOD: on average, it takes 1.6 years longer to diagnose EOD than for late-onset dementia (LOD).[9]

1.1.2. Types of Dementia

Several types of dementia are clinically recognised, including, but not limited to Alzheimer's disease (AD); Parkinson's disease (PD); vascular dementia (VD); amyotrophic lateral sclerosis (ALS); Lewy body dementia (LBD); frontotemporal dementia (FTD); primary progressive aphasia (PPA); and Creutzfeldt-Jakob disease (CJD). Dementia may also be roughly classed according to severity, reflecting a patient's level of impairment. The results of a British study of the prevalence of the various forms of dementia and disease severity is shown in **Figure 2**, demonstrating that AD is by far the most common pathology, and most people have mild-stage impairment.[10]

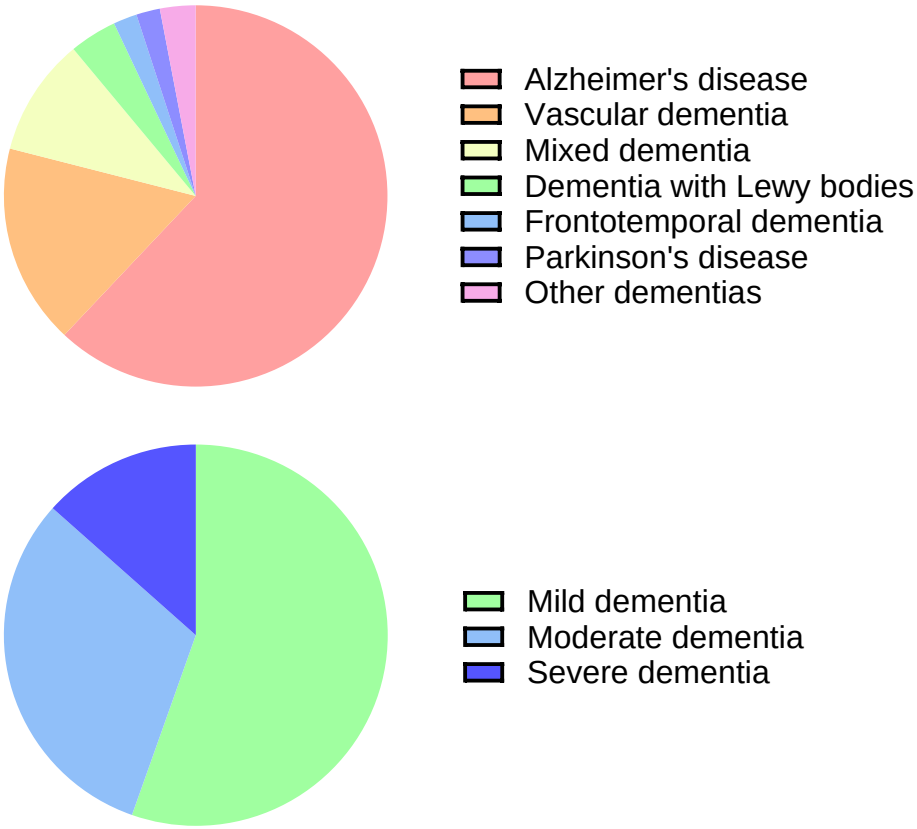

Figure 2: Prevalence and severity of various types of dementia. Adapted from Dementia UK: Update.[10]

Each type of dementia is characterised by a particular pathology and symptoms. For example, impairment of speech or language is a hallmark of PPA,[11] while fluctuating states of confusion and loss of attention span may indicate LBD.[12] Comprehensive reviews are available discussing suspected causes and current research into each neurodegenerative disease in detail.[13-19]

1.1.3. Symptoms of Dementia

The physiological manifestations of the various forms of dementia differ from patient to patient and are dependent of the type of dementia as well as progression of disease. Common symptoms are well-known by the general public due to its prevalence in society. At the onset of disease, patients experience forgetfulness, difficulty solving problems and making decisions and taking longer to perform challenging mental activities. This is often recognised as mild cognitive impairment (MCI). Other early symptoms include misplacing items, changes in mood leading to aggressive behaviour and becoming disorientated on otherwise familiar routes.[20] Early-stage dementias can often be managed with the use of medication and/or appropriate support from caregivers, but symptoms cannot be completely eliminated. However,

as disease progresses, more disturbing symptoms begin to manifest with a significant loss of quality of life. These include changes to sleeping patterns, forgetting events in one's life, hallucinations, abnormal violent behaviour and social withdrawal. Patients with severe dementia reach a state where they can no longer recognise close family members, are unable to express themselves and are often fully dependent on caregivers to eat, dress themselves or bathe.[21-23] Not only is dementia truly debilitating for sufferers, but places tremendous emotional and financial stress on caregivers and family members. Overall, the prognosis for all dementias is fatal, as neurodegeneration causes brain atrophy so severe that the patient's body no longer functions.

1.1.4. Diagnoses for Dementia

When diagnosing dementia, questions posed to the patient and/or caregiver aim to identify the 'first' or most prominent symptom, upon which examination allows deduction of the specific pathology responsible.[2] This is initiated by cognitive and neuropsychological tests, wherein a medical profession evaluates the patient's mental abilities. This involves examination of memory, attention, speech, reflexes, balance, problem-solving and fine motor skills.[24] However, a diagnosis of dementia is often confirmed using brain scans, in particular computed tomography (CT),[25] positron emission tomography (PET)[26] and magnetic resonance imaging (MRI).[27] Reviews cited in **Chapter 1.1.1.** provide detail on the kind of brain atrophy which distinguishes each type of dementia. As stated previously, all dementias are characterised by their neurodegenerative effects. In most cases however, the cause of such neurodegeneration is unknown. Various risk factors have been postulated, including, ethnicity, sex, smoking, alcohol and drug use, education and environmental factors.[28] In rare cases, the onset of dementia occurs due to genetic factors; a key example of this is familial Alzheimer's disease.[29] Nonetheless, it is believed that for most neurodegenerative diseases, the onset is sporadic.

1.2. Current Treatments for Dementia

All dementias have fatal prognoses. The median life expectancy of sufferers following a dementia diagnosis can vary between three to ten years depending on various factors, such as age and gender.[30, 31] The US Food and Drug Administration (FDA) has approved several small-molecule treatments and more recently, monoclonal antibody (MAB) treatments for AD, the most common form of dementia.[32] As the mechanisms by which neurodegeneration is initiated and progressed are poorly understood, small-molecules do not provide any curative or disease-

modifying benefit, *i.e.* they do not halt or reverse neurodegeneration. While the development of bio-therapeutics in the form of MABs has offered some disease-modifying results, their use has been met with controversy due to their limited effects. Indeed, small-molecule treatments only temporarily reduce symptoms of dementia and will become redundant with repeated use. Historically, non-pharmaceutical strategies have primarily been relied upon for the management of symptoms. The progression of dementia may be slowed with pharmacological interventions.

1.2.1. Non-pharmaceutical Management Strategies

Non-pharmaceutical strategies for the management of dementias are aimed at improving quality of life and wellbeing for patients. Research has demonstrated that cognitive stimulation, such as playing board games or arts and craft, and physical exercise, such as moderate-to-high intensity aerobics, can preserve mental functioning and delay decline compared to a negative control group.[33-35] It should be noted that at best, symptoms of disease progression can only be delayed with these activities, and eventually patients are either no longer able to engage in them, or they become unsafe, particularly in regards to exercise.

1.2.2. Small-molecule Drug Treatments

Current small-molecule drug treatments are only available for AD, and none of these possess disease-modifying abilities. Therefore, they are only used to minimise symptoms and slow a patient's cognitive decline. These medications fall into two categories: acetylcholinesterase inhibitors (AChEIs) *donepezil* **1** (Aricept®), *rivastigmine* **2** (Exelon®) and *galantamine* **3** (Razadyne®), and the *N*-methyl D-aspartate receptor antagonist (NMDARA) *memantine* **4** (Namenda®). Table **1** summarises the key information surrounding these drugs. Two other small-molecule treatments for AD are of note: *tacrine* **5** (Cognex®) was approved by the FDA in 1993, but its use was discontinued in 2013 due to hepatotoxicity issues.[36] Namzaric® is a combination treatment of *donepezil* **1** and *memantine* **4**, which was approved by the FDA in 2014 and is prescribed for the management of moderate to severe AD.

Table 1: Summary of small-molecule drug treatments currently available for management of AD.

Name	Structure	Year of FDA Approval	Drug Class	Stage of Dementia
Donepezil (Aricept®)	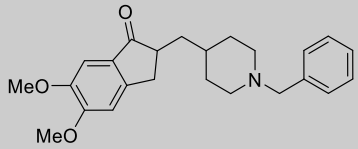 **1**	1996	AChEI	All stages Mild to severe
Rivastigmine (Exelon®)	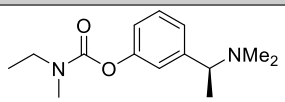 **2**	2000 (Oral capsules) 2007 (Transdermal patch)	AChEI	
Galantamine (Razadyne®)	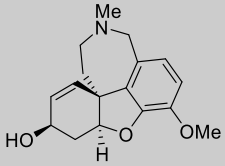 **3**	2001	AChEI	
Memantine (Namenda®)	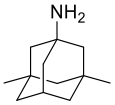 **4**	2003	NMDARA	
Tacrine (Cognex®)	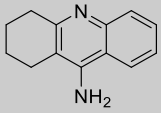 **5**	1993 (Discontinued 2013)	AChEI	Moderate to severe
Namzaric®	Combination of **1** and **4**	2014	AChEI and NMDARA	

1.2.2.1. Acetylcholinesterase Inhibitors

AChEIs are frequently prescribed for mild to moderate AD. Acetylcholinesterase (AChE) is a serine protease which is responsible for modulating neural functions, such as learning, attention, memory, wakefulness and sleep.[37] Signal transmission at synapses occurs when the neurotransmitter acetylcholine (ACh) is released by pre-synaptic neurons, then diffused across the junction, where it reversibly activates the cholinergic receptors (nicotinic and muscarinic receptors), passing on the signal.[38] ACh is then hydrolysed by AChE into acetate and choline (Ch) to prevent neurotransmission from continuing indefinitely. Ch is then recycled into the pre-synaptic neuron *via* the Ch pump to be acetylated once more to ACh. (**Figure 3**).[39] It is

therefore not unexpected that improper functioning of AChE has been implicated in neurodegenerative disorders.[40, 41] AChEIs are understood to delay ACh degradation, which may prevent faulty neurotransmission for some time, improving memory, comprehension and communication.[42, 43] These drugs are a standard treatment for AD, however individuals may respond differently to each medication, meaning that trial and error is often the only reliable method of optimising treatment for early-stage AD.

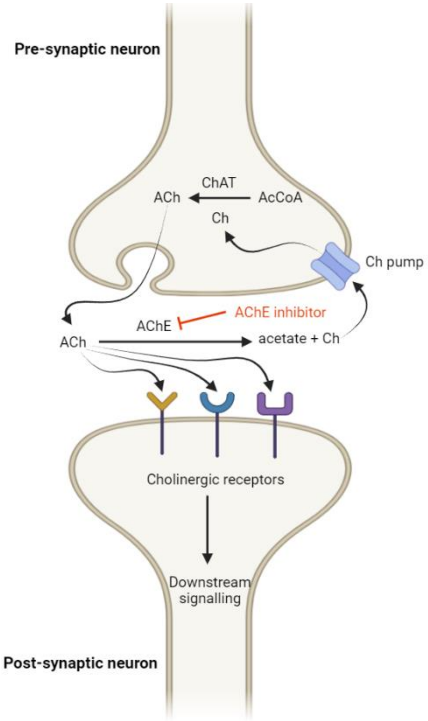

Figure 3: Schematic of a synapse. AChE is released by the pre-synaptic neuron, activating the cholinergic receptors. AChE is rapidly degraded into acetate and Ch, so that signalling does not continue indefinitely. AChEIs slow this degradation to increase the duration of signalling. Created with BioRender.com.

1.2.2.2. N-methyl-D-aspartate Receptor Antagonist

N-methyl-D-aspartate (NMDA) receptors are cation-selective ligand-gated ion channels involved in the mediation of synaptic transmission.[44] The binding of both glycine and glutamate to their respective orthosteric sites triggers conformational changes to the receptor, permitting the flow of Ca^{2+} and Na^{+} down their electrochemical gradients (**Figure 4**).[45, 46] Moderate to severe cases of AD may be treated using *memantine*. *Memantine* is understood to protect neurons from overexcitation by competing with glutamate for receptor binding. In doing this, Ca^{2+} ion uptake into neurons is decreased, which has demonstrated improved cognition after six months of use.[47]

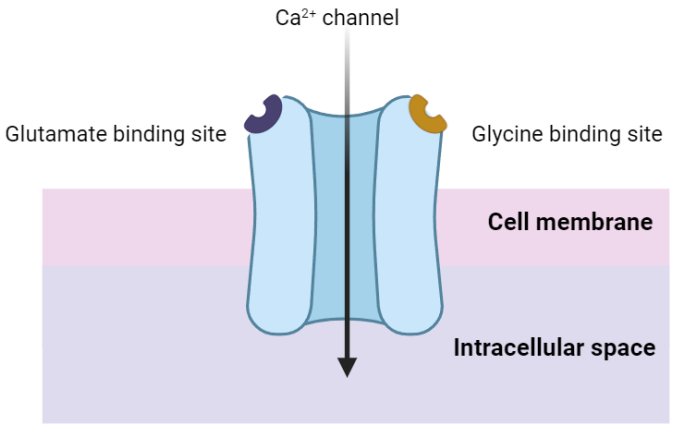

Figure 4: Schematic of an NMDA receptor. *Memantine* binds to the glutamate binding site, preventing Ca^{2+} uptake into neurons and hence preventing overexcitation. Created with BioRender.com.

1.2.3. Concurrent Treatments and Side Effects

It is also not uncommon for dementia cases to coincide with mental illnesses, such as depression and schizophrenia.[48] Hence, other classes of drugs such as antidepressants, antipsychotics and anxiolytics are often prescribed in addition to dementia-specific pharmaceuticals to ease such symptoms, particularly in severe cases.[49-51] Despite this, the continued use of these medications is questionable, as no clinical evidence has suggested a clear improvement or benefit in quality of life.[52-54]

These medications are also not without side effects, including nausea, vomiting and diarrhoea for AChEIs and dizziness, headaches and confusion for *memantine*. Adverse reactions to medications may be severely debilitating or even dangerous to the elderly patients they are designed for, further reducing potential quality of life, especially if they lead to disorientation or physical injuries. Moreover, while behavioural issues in AD patients may be treated with standard antidepressants and antipsychotics, such medications are associated with a host of common side effects as well. Critically, none of the aforementioned treatments are disease-modifying, *i.e.* they do not halt or reverse neurodegeneration. Indeed, they only temporarily reduce symptoms of dementia, and will become redundant with repeated use.

1.2.4. Monoclonal Antibody Therapeutics

A significant paradigm shift in dementia treatments began in 2021, when *aducanumab* (Aduhelm®) was approved for clinical use by the FDA as a treatment for AD, with an estimated treatment cost of US$56,000 per year.[55] *Aducanumab* is a monoclonal antibody (mAb) developed by Biogen which showed evidence of clearing amyloid-β (Aβ) plaques in clinical trials.[56] In the immune system, endogenously produced antibodies bind to antigens, eliciting a

response that recruits immune cells to mark and target the antigen for destruction.[57] Laboratory-produced antibodies – hence the name 'monoclonal' – can be tailored to target specific cells in a potent treatment against a variety of diseases.[57] The treatment approach of *aducanamab* is grounded in the 'amyloid hypothesis', purporting that a build-up of Aβ triggers a cascade of changes leading to neuronal dysfunction, neuroinflammation and the aggregation and spread of hyperphosphorylated neurofibrillary tangles (NFTs) of tau protein.[13, 58, 59] The approval of this treatment, the first of its kind and the first AD treatment in more than 20 years, was groundbreaking as it claimed to represent the first disease-modifying treatment available.[56] However, the approval was also highly controversial, as Glymour and co-workers had previously demonstrated that the clearance of Aβ was not disease-modifying and therefore contradicted the mechanism of action of mAb treatments.[60] Furthermore, phase III clinical trials of the drug were met with heavy criticism due to conflicting results, although Biogen later announced that a subgroup of patients had improved cognitive function.[61, 62] An FDA panel of experts expressed significant concerns with Biogen's statistical methodology, which has compounded scepticism regarding the effectiveness of the treatment. In 2024, Biogen therefore discontinued *aducanumab* to focus on the mAb *lecanemab* (Leqembi®), which demonstrated promising results in clinical trials and was approved by the FDA as an amyloid-clearing treatment for AD.[63] Meanwhile, the successful clinical trial results of Eli Lilly's mAb *donanemab* (Kisunla®) prompted is own FDA approval in 2024. *Lecanemab* is now offered as a fortnightly injection, while *donanemab* is administered similarly on a monthly basis. While these treatments are in very early stages and it remains to be seen whether this treatment will prove effective, they are highly promising in halting or reversing disease progression in AD.

In summary, current treatment options for neurodegenerative diseases are limited, hence the diagnosis of any dementia is terminal. Often, the best care for patients is to minimise suffering, especially in more severe stages. Therefore, a pressing medical need remains for a better understanding of neurodegenerative pathologies and their onset so that more effective treatments may be designed. New treatment pathways must be explored to combat these diseases, and one phenomenon implicated in neurodegeneration is inflammation caused by cellular senescence.

1.3. Cellular Senescence

A multicellular organism is highly complex, containing many cell types which each have distinct functions and features. Co-ordination of the entire organism is based on the principle

that the survival of the entire organism is more important that of a single cell.[64, 65] The malfunctioning of a single cell threatens the survival of the organism, thus two mechanisms have evolved to manage incidences of aberrant cells. The first is controlled cell death, where the cell recognises its own dysfunction and undergoes the process known as apoptosis. The second is recognition of damage by specialised cells, which then act to destroy it. Often, a combination of these methods is used to remove damaged cells. One of these methods is cellular senescence, which is defined as a cell cycle arrest that occurs in the G_1 or G_2 phase of the cell cycle (**Figure 5**) as a response to endogenous and exogenous stress.[66, 67] During both G_1 and G_2 phases, the cell synthesises new organelles, grows larger and prepares itself for mitosis. Examples of stresses that lead to senescence include excessive oncogene signaling, loss of tumour suppression,[68] aberrant DNA replication and DNA damage accumulation.[69, 70]

The term senescence is derived from the Latin *senex*, meaning 'growing old'. Indeed, an increased burden of senescent cells (SCs) is heavily correlated with ageing. SCs recognise their own dysfunction to undergo this growth arrest, then secrete signals to neighboring cells so that they can be removed by the immune system.[71] The discovery of SCs was reported in 1961 by Hayflick and Moorehead when human embryonic fibroblasts were observed to be unable to replicate but did not undergo apoptosis.[72] Such cells had undergone mitosis between 40–60 times, reaching a stage known as the Hayflick limit, in which proliferation had ceased. It was shown that telomere shortening was responsible for this instance of senescence.[73] Senescence is observed at various stages during the human life cycle. *In utero*, embryonic SCs contribute to tissue development; in adulthood, they prevent propagation of damaged cells; play a rolein tissue repair; and suppress formation of tumours.[73]

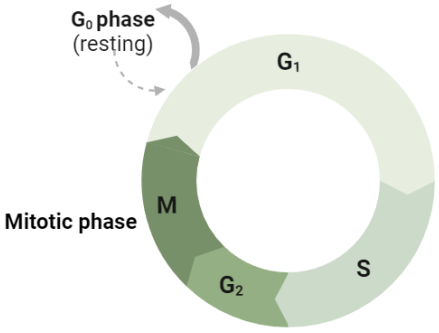

Figure 5: Schematic diagram of the cell cycle. Cellular senescence is only induced during the G_1 and G_2 phases. Created with BioRender.com.

1.3.1. Identification of Senescent Cells

Senescence must be distinguished from the processes of quiescence and terminal differentiation: quiescence is a reversible growth arrest that occurs in the G_0 phase of the cell cycle where proliferation may resume in the presence of appropriate conditions;[74] while terminal differentiation is a permanent growth arrest which results in the acquisition of specific cellular functions.[73] Despite this, unambiguous identification of SCs when compared to other cells is difficult, as there exist no biomarkers which are produced solely by those in the senescent state.[75] However, Campisi and co-workers have purported general criteria to distinguish SCs: (1) a growth arrest in response to deleterious stimuli (although the growth arrest is generally considered to be irreversible, SCs have been observed to re-enter the cell cycle under specific circumstances, particularly in cancerous cells);[76-79]) (2) enlargement of cells up to twice the size of other cells,[80] in addition to other changes in morphology, such as vacuolation and flattening;[81] (3) secretion of senescence-associated β-galactosidase (SA-β-Gal), indicative of increased lysosomal quantity and mass;[82] (4) expression of $p16^{INK4a}$, a tumour suppression protein which is not normally secreted during quiescence or terminal differentiation,[68, 83-86] and; (5) secretion of growth factors, proteases, cytokines and other factors which have both autocrine (acting on the cell's own surface receptors) and paracrine (acting on adjacent cells) functions.[87-89] This is referred to as the senescence-associated secretory phenotype (SASP). These criteria should only be understood in a general sense, in that not all SCs possess these features, and not all cells that do possess any single one of these features must be considered senescent.[75]

1.3.2. Induction of Senescence

Senescence occurs as a response to endogenous or exogenous stresses, as shown in **Figure 6**. These include oncogenic signalling and telomere shortening as endogenous stresses, and DNA damage caused by genotoxins, cytotoxins or radiation as exogenous stresses.[90] Cell cycle arrest is primarily mediated *via* activation of p53 or the cyclin-dependent kinase (CDK) inhibitors p16, p21 and p38.[90] These pathways are highly complex, involving many upstream regulators and downstream effectors, with a large level of crosstalk between them.[91-95] This results in the inhibition of CDK2, CDK4 and CDK6, which collaborate to maintain a dephosphorylated form of the Rb protein.[96] In its dephosphorylated form, Rb blocks progression of the cell cycle, thus inducing the senescent state.[97]

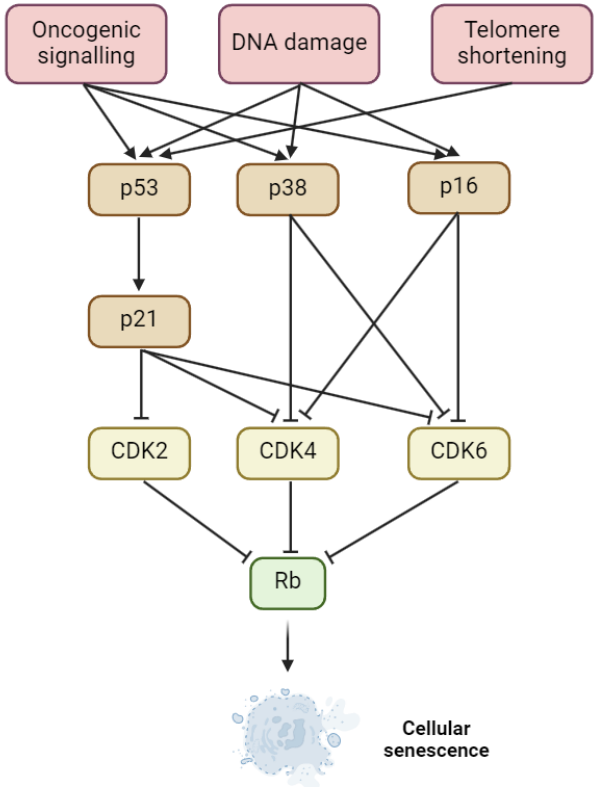

Figure 6: Simplified diagram of cellular pathways leading to the induction of senescence. Created with BioRender.com.

1.3.3. Features of Senescent Cells

Genetically, most of the differences between pre-senescent (non-senescent) and SCs lie in cell cycle-related genes, metabolism-related genes or genes encoding secretions known as the SASP or senescence-messaging secretome (SMS).[98] In stark contrast to pre-senescent cells, SCs secrete this distinct cocktail of soluble and insoluble inflammatory factors.[88, 98-102] The components of the SASP can be identified as belonging to three broad categories: soluble signaling factors, such as interleukins, chemokines and growth factors; proteases; and insoluble proteins or extracellular matrix (ECM) components.[98] The release of proteases is of particular concern, as they have a number of paracrine effects: (a) they cause shedding of membrane-bound receptors; (b) they hydrolyse signaling molecules; and (c) they degrade the ECM.[98] Through this, the SASP is highly potent in modifying tissue microenvironments, and has been heavily implicated in disease states. While the secretion of the SASP has evolutionary purposes, it is far more well-known for its deleterious effects on the cell's surroundings. A list of factors which have been significantly altered between pre-senescent and SCs is provided in **Table A** in **Appendix A**.[98] Investigation of the SASP is still ongoing through efforts such as the SASP Atlas, to produce a comprehensive understanding of the secretome.[103]

1.3.3.1. Macromolecular Damage

In addition to the SASP, SCs have been observed to carry macromolecular damage. It has previously been mentioned that DNA damage is a principal inducer of senescence. This most frequently happens due to oxidative stress, exposure to mutagenic agents or irradiation with ultraviolet (UV) light. Senescence also occurs naturally when cells reach the aforementioned Hayflick limit, signified by the inexorable loss of telomeric DNA.[104-106] Moreover, stress caused by reactive oxidative species (ROS) not only damages nucleic acids, but has been demonstrated to oxidise methionine and cysteine residues, thus affecting both the folding and function of proteins.[107] In the presence of metals, carbonylation of proline, threonine, lysine and arginine residues can also occur, with widespread effect; hydrophobic residues become exposed, or carbonyl groups may react with amines to form Schiff bases, leading to unfolding and aggregation.[108] This damage is generally irreversible, although aberrant proteins may be cleared by the ubiquitin-proteosome system (UPS) or through autophagy.[109] Nonetheless, the presence of such proteins, and the resulting proteotoxicity, are hallmarks of senescence.[110] Finally, the senescent state is also correlated with lipid damage. Lipids are essential molecules as structural components, energy storage and signal transducers.[111] It has been observed that the pathology of several age-related diseases display altered lipid metabolism, as well as an increase in lipid peroxidation products.[112] Mitochondrial damage in SCs also causes a build-up of lipid deposits and insoluble aggregates known as lipofuscin.[113-115]

1.3.3.2. Deregulation of Metabolism

Unsurprisingly, a pattern of deregulated metabolism is also observed in SCs. Damage to various mitochondrial structures or function, such as the electron transport chain (ETC), complex I assembly, fission and biogenesis, mitochondrial sirtuins, or disruption of the tricarboxylic acid (TCA) cycle is known to induce senescence.[113, 116-121] This leads to an altered morphology and function, including increased mass, decreased membrane potential, decreased reproductive rate, increased proton leak and an increase in TCA cycle metabolites.[117, 122] Additionally, SCs contain more mitochondria, but due to the impairment, they are less productive in generating ATP.[123, 124] It has been mentioned previously that lysosomal quantities and mass are also increased in SCs.[125] Lysosomes are responsible for degradation and recycling of cellular components and extracellular material,[126] thus the secretion of the SASP is highly dependent on lysosome function.[127] As such, the hydrolases present in these organelles is also elevated to maintain simultaneous activation of catabolic and anabolic processes.[73, 128]

1.3.4. Beneficial Effects and Evolutionary Purposes of Senescence

It is believed that the most critical role of senescence in mammals is to serve as a safeguard against cancer, preventing the replication of those cells which have undergone insult capable of damaging DNA.[129] Indeed, cellular senescence is believed to have evolved as an anti-cancer mechanism alongside apoptosis as the proinflammatory and chemotactic factors found in the SASP stimulate recognition and clearance by the immune system.[130] Senescence may also provide an evolutionary advantage over apoptosis: since cell death irrevocably removes cells, this is an undesirable consequence when a certain population is required to maintain homeostatic physiological functioning.[129] However, the senescent state has the advantage of keeping these cells functional but unable to proliferate. While the effect of senescence in preventing cancer is beneficial, it also has far more damaging consequences for ageing and disease, as will be discussed below.[131-134] These concepts appear to be paradoxical, but the dual nature of SCs is nonetheless consistent with the antagonistic pleiotropy hypothesis of ageing: that genes offering positive effects early in life are evolutionarily favourable, even if they contribute negative effects later in the life span of an organism.[134, 135]

Since Hayflick's original discovery, senescence has been better understood to have a variety of purposes from embryonic development to adulthood. Cells with senescent features have been observed within the developing embryo, with roles to play in organogenesis.[136, 137] It is important to note, however, that while these embryonic "senescent" cells are hyporeplicative and secrete SA-β-Gal, their DNA is undamaged, they do not express p16 and do not secrete the SASP. Furthermore, it has been hypothesised that the SASP also originated as a healing mechanism when wounding occurs.[138] Indeed, the function of proinflammatory factors may have been communication with neighboring cells, indicating a compromised state and initiating the process of tissue repair and regeneration by stimulating progenitor cells.[139-144] Furthermore, data indicates that in adult animals, p16 is quickly activated after injury.[145, 146] In mouse models, activation was first noticed 2–3 days after injury, peaked 4–7 days and subsided over 2–3 weeks.[145, 147] A large number of SASP cytokines were also observed at the wound site.[145, 148] These findings, along with the finding that clearance of p16 delays recovery, suggest that the senescent state is critical for optimising the healing process.[145] These beneficial roles of cellular senescence are shown in **Figure 7**.

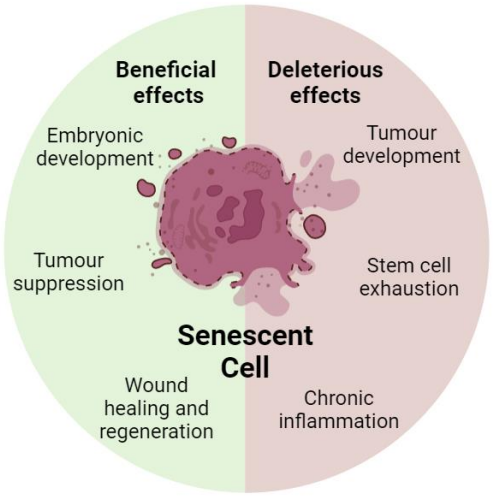

Figure 7: Senescent cells have both beneficial and deleterious effects on tissues.

1.3.5. Senescence in Disease

Despite evolving as a beneficial measure to control aberrant cells, the senescence response is correlated with detrimental processes, especially ageing. Indeed, Hayflick and Moorehead's seminal publication on senescence demonstrated that senescence contributes to the ageing process itself.[72] Indeed, the immune system normally clears SCs over a period of days to weeks,[149, 150] but once this burden exceeds a certain threshold, the immune system is unable to maintain such clearance. This is particularly problematic due to the aforementioned SASP,[151] which has been linked to the development of an inflammation-related disease, termed 'inflammageing'.[152] Several disease states have been associated with senescence (**Figure 8**).

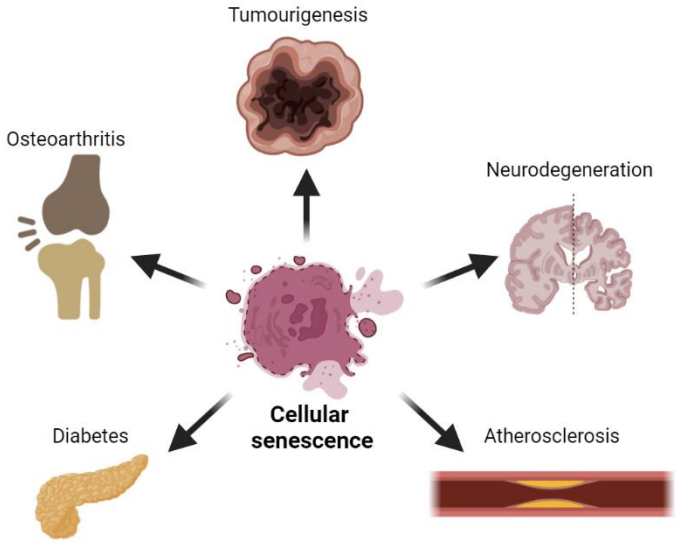

Figure 8: Senescence has been implicated in the aetiology of many diseases, which may be related or unrelated to inflammation. Created with BioRender.com.

Senescence therefore has a deleterious effect when cells are not effectively cleared by the immune system and therefore accumulate in tissues, an increased burden which has been shown in humans, primates and mice.[153-156] It has been proposed that immune system clearance begins to fail as the aforementioned SASP-expressing cells induce the paracrine and endocrine spread of senescence in a chain reaction which far exceeds the immune system's capacity.[149, 157] Interestingly, it was also highlighted that delaying the accumulation of SCs in mouse models led to an increased lifespan, suggesting that clearance of SCs could be a powerful therapeutic opportunity to ameliorate age-related disease.[158, 159]

Senescence has been linked with several diseases associated with inflammation. Increased expression of p16 and secretions of IL-6, IL-1 and MMP-3 within joints have implicated senescence in the aetiology of osteoarthritis.[160-162] Senescence has also been observed in idiopathic pulmonary fibrosis patients through the expression of markers p21, p16 and SA-β-Gal.[163, 164] Furthermore, the increased release of p21, p16 and SA-β-Gal in vascular endothelial cells demonstrates a senescent phenotype, which has been linked to the buildup of atherosclerotic plaques and cardiovascular disease.[165-167] While the aetiology and pathology of these diseases manifests in different ways, it is important to notice that they each share common markers that implicate the deleterious effects of cellular senescence.

Additionally, senescence has been observed in conditions not typically associated with inflammation. In Type 2 diabetes mellitus (T2DM), excessive demand is placed on insulin-producing β-cells and induces their proliferation, but this increased replication leads to senescence by attrition of telomeric DNA.[168] In addition, SCs and the SASP have been observed to exacerbate insulin resistance in adipose tissue.[169] These two factors indicate that senescence in both pancreatic β-cells and adipose tissue drive progression of T2DM.[170] Finally, despite evolving as a mechanism to arrest the cell cycle and prevent aberrant cells from becoming cancerous, the SASP and its chronic inflammatory microenvironment has been heavily implicated in tumorigenesis.[171-174] Inflammation caused by the SASP is known to drive cell migration, growth, invasion, angiogenesis and metastasis.[175-182] Moreover, the SASP may also contribute to tumour progression *via* negative modulation of the immune system. Such factors have been shown to block tumour immune surveillance.[179, 183] Hence these actions, while paradoxical to the evolutionary purpose of senescence, nonetheless exhibit the role of senescence in cancer.[184]

1.3.6. Senescence in Neurodegeneration

Cells within the central nervous system (CNS) are divided into two broad categories: neurons and glial cells. Neurons are electrically excitable cells with their primary function being to transmit signals to other neurons *via* synapses using action potentials, working collaboratively to form neural circuits and larger brain networks. Glial cells, including astrocytes, microglia and oligodendrocytes, among others, are non-neuronal cells that exist to support and maintain the function of neurons. The ratio of neurons to glial cells is believed to be approximately 1:1, with the human brain containing between 40–130 billion of each category of cell.[185]

In the brain, the amount of senescent cells present increases with ageing, and has been heavily linked to neurodegenerative diseases.[156, 186] Indeed, senescence has been observed in the central nervous system (CNS), including in neurons,[187, 188] astrocytes,[189-192] microglia,[193-195] oligodendrocytes,[196] endothelial cells,[197] and neural stem cells.[198-200] Unsurprisingly, SCs have therefore been implicated in the aetiology of many types of dementia, including AD, PD, FTD, ALS and multiple sclerosis.[199, 201-207]

1.3.6.1. Neurons

Neurons, shown in **Figure 9**, are responsible for the transmission of electrical signals throughout the brain. A typical multipolar neuron (the most common type) consists of a soma, or cell body, to which are connected dendrites and an axon. Dendrites receive electrical signals from other neurons, and these signals are conducted through the axon towards axon terminals, enabling further transmission to more neurons. Neuronal cells are post-mitotic and non-cycling, meaning that they do not replicate *via* mitosis and last a lifetime. As discussed previously, senescence is not solely identified by a growth arrest, therefore other markers are used to establish the senescent state in neurons.[208] Indeed, the increased expression of SA-β-Gal,[209, 210] in addition to SASP factors point to induction of senescence.[211] SASP factors are known to induce senescence in nearby cells within the brain in a paracrine manner,[212] hence leading to brain atrophy observed in neurodegeneration.[213]

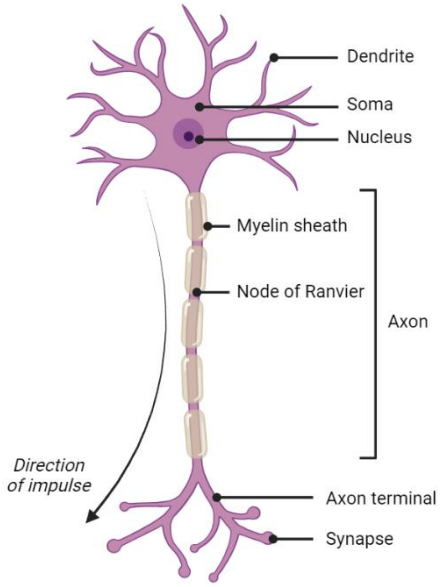

Figure 9: Schematic diagram of a multipolar neuron, the most common type of neuron, showing the soma, dendrites, axon surrounded by myelin sheaths and axon terminals.

1.3.6.2. Astrocytes

Astrocytes, shown in **Figure 10** (*a*), are star-shaped cells which play a critical role in maintaining homeostasis within the brain environment and control blood-brain barrier permeability through their end feet (**Figure 10** (*b*)). Importantly, they are responsible for transferring mitochondria to neurons and thus fuel their metabolism (**Figure 10** (*c*)),[214] while also clearing debris,[215] in addition to their regulation of neurotransmitters such as glutamate, ATP and serine.[216] The senescent state has been observed in astrocytes through increased secretion of SASP cytokines IL-6, IL-8 and IL-1β, as well as ROS.[217] Unsurprisingly, the impairment of astrocytes through senescence causes inhibition of their functions, and are therefore heavily implicated in neurodegenerative pathologies.[217]

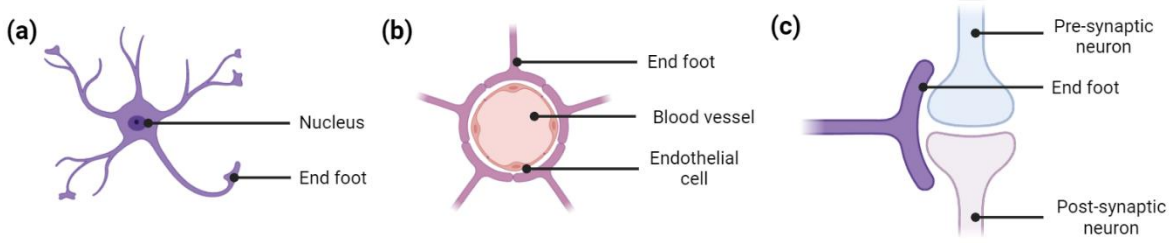

Figure 10: Schematic diagrams of an astrocyte, showing (*a*) their general shape; (*b*) how end feet are involved in maintaining the blood-brain barrer; and (*c*) how end feet are involved in maintaining synapses.

1.3.6.3. Microglia

Microglia, shown in **Figure 11**, serve as macrophage-like cells which carefully regulate the macroenvironment of the brain. Importantly, they are responsible for the elimination of dead cells, microorganisms and protein aggregates that may impair the function of the CNS.[218] Under normal circumstances, the activation of microglia *via* injury or inflammatory stimuli may cause microglia to take on an ameboid morphology, which is associated with phagocytosis and inflammatory secretion.[219] However, senescent microglia exhibit a lengthened sustained inflammatory response[220]and these cells demonstrate a reduced capacity for phagocytosis, and decreased mobility throughout the brain.[208, 221] These have been observed through their increased release of SASP factors IL-1β, TNF-α and IL-6.[222] Consequently, the induction of senescence in microglia has been associated with neuroinflammation, and thus linked to neurodegeneration.[223]

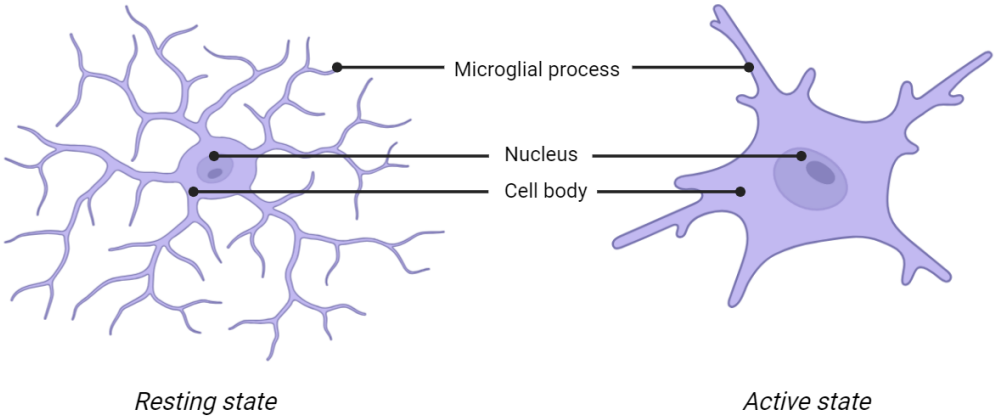

Figure 11: Schematic diagram of a microglial cell, showing morphological difference between resting and activated state.

1.3.6.4. Oligodendrocytes

Oligodendrocytes, shown in **Figure 12**, play a critical role in the central nervous system by providing support and insulation for axons through the process of myelination whereby myelin sheaths are formed around the axon. Myelin sheaths are vital for the nominal conduction of electrical signals along axons: without myelination, axons cannot be afforded nutritional and homeostatic support, and conduction is slower or may be halted altogether. Senescence in oligodendrocytes has been shown to lead to impair myelination, which significantly affects neural conductivity and leads to a loss of neuronal function.[213] This loss of neuronal function is known to occur naturally through ageing,[224] but is heightened further in neurodegeneration.[225]

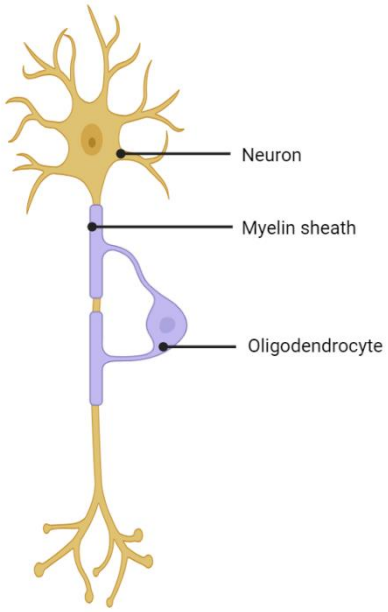

Figure 12: Schematic diagram of a neuron (yellow) and oligodendrocyte (purple), showing myelination of the neuron's axon.

A significant body of evidence suggests that cellular senescence is a hallmark within many diseases associated with ageing, particularly in the CNS. However, senescence is a relatively unexplored field in the design of new therapeutics for such diseases and therefore presents highly promising opportunities in confronting global health challenges.

1.4. Strategies for Targeting Senescence

The clearance of SCs by the immune system is already well-known,[136, 226] however the burden of senescence accumulates with ageing in such a manner that dysfunction becomes readily apparent.[227] As such, there is significant interest in strategies for the selective clearance of senescent cells, as they promise critical insights into 'senotherapeutics' that aim to address the medical challenges of ageing. This has proven difficult due to the inherent similarities between pre-senescent and senescent cells, although a number of approaches have been proposed, as will be discussed in this section.[228] Below is provided a broad overview of these strategies, with significant attention given to senescent-cell anti-apoptotic pathways (SCAPs), which forms the basis for this work.

1.4.1. Immune System-mediated Clearance

The SASP sheds several receptors and ligands, as discussed in **Chapter 1.3.3.** Among the normal functions of these secretions is signaling to the immune system for removal. This feature has been exploited to clear senescent cells using chimeric antigen receptor (CAR) T-

cells, which target urokinase-type plasminogen activator receptor (u-PAR).[229] The receptor plays an important role in degradation of the ECM,[230] and is upregulated as a component of the SASP. Such treatment has shown remarkable ability to clear SCs both *in vitro* and *in vivo*, producing beneficial outcomes in murine models.[229] However, this strategy is not without risks. First, administration of CAR T-cells has been associated with inflammation, weight loss and hypothermia, presenting worrying issues for therapeutics targeted at elderly populations.[228] Second, this treatment also requires immune suppression, which again is highly compromising for elderly patients.[228] Immune-mediated clearance is therefore a highly promising treatment that will need optimisation before progressing to clinical use.

1.4.2. Exploiting Overactive Organelles

It has been mentioned previously that lysosomal function of SCs is heavily increased and the secretion of SA-β-Gal is also heightened; both features may be leveraged for SC clearance. Changes in the morphology and quantity of lysosomes mean that autophagy, the cell's process of recycling organelles and other cellular components, can be exploited to induce SC death, or senolysis.[228] The activation of apoptotic pathways can be accomplished through an autophagic push,[231] which has been demonstrated using fibrate drugs,[232] metformin,[233] mammalian target of rapamycin (mTOR) complex 1 inhibitors,[234] bromodomain and extraterminal domain (BET) inhibition[235] and ataxia-telangiectasia mutated (ATM) inhibitors.[236] SA-β-Gal may also be exploited by administration of prodrugs which are cleaved and activated by the enzyme,[237] or galactose-encapsulated cytotoxic drugs, which will be efficiently released into SCs.[238] A drawback of these methods is off-target effects that may be suffered by other cells with high SA-β-Gal activity, such as activated macrophages.[239]

1.4.3. Leveraging Biochemical Changes

SCs also demonstrate minor biochemical characteristics when contrasted to pre-senescent cells, which can be cleverly targeted for senolysis. SCs have slightly depolarised plasma membranes and higher H^+ concentration, features which make them vulnerable to cardiac glycosides (CGs).[240] CGs affect the Na^+/K^+/ATPase pump, disbalancing the electrochemical gradient, which causes further depolarisation and acidification of the cell, leading to apoptosis.[240-242] Additionally, increased lysosomal activity lowers cellular pH, a characteristic that is resisted by upregulation of buffers, such as the NH_3/NH_4^+ buffer mediated

by glutaminase.[243] In this case, inhibition of glutaminase impairs the cell's ability to resist lowered pH, leading to apoptosis.[243]

1.4.4. Senescent Cell Anti-Apoptotic Pathways

The growth arrest observed in SCs occurs as such cells actively resist the process of apoptosis *via* upregulation of senescent cell anti-apoptotic pathways (SCAPs), also known as pro-survival networks. While SCAPs protect SCs against their own SASP, they have nonetheless been referred to as the 'Achilles' heel' of senescent cells.[244] Zhu and co-workers performed the first studies to identify the precise pathways responsible for apoptosis resistance. Preadipocytes, being the most abundant type of SCs,[245] were irradiated to induce senescence before Affymetrix assays were used to assess gene expression. The effects of these pathways' upregulation were then confirmed through RNA interference studies, highlighting the networks of PI3K and PKB; HSP90; the BCL-2 family; PAI-1; and dependence receptors.[244, 246] Below, a broad discussion of individual pathways responsible for preventing apoptosis is provided.

1.4.4.1. The PI3K–PKB Pathway

The phosphoinositide-3-kinase–protein kinase B (PI3K–PKB) pathway plays a critical role in many cellular processes and is known to be aberrantly activated in cancers.[247, 248] PI3K is responsible for the phosphorylation of phosphatidylinositol-4,5-biphosphate (PIP_2) to phosphatidylinositol-3,4,5-triphosphate (PIP_3), which may recruit a multitude of oncogenic signal proteins, including PKB.[247] This triggers a cascade of further phosphorylations known to promote cancer progression, such as MDM2, TSC2, GSK3, FOXO and mTOR.[249-251] Given that apoptosis is inhibited in cancer, it has naturally followed that such a pathway has also been implicated in senescence.[252]

1.4.4.2. Heat Shock Proteins

Heat shock proteins (HSPs) are so named because they are activated as a response to cellular stresses, stabilising misfolded or unfolded proteins or chaperoning them for degradation.[253, 254] Additionally, HSPs have also been observed to play key roles in protein assembly, export, turnover and regulation.[255] In particular, HSP90 has already been identified as a drug target for cancer as many of these stabilised proteins are required for tumour growth.[255] Upregulation of the previously discussed PKB, a client protein of HSP90, causes resistance to apoptosis.[256, 257] This has hence also been proposed as a pro-survival mechanism

in senescence.[258-261] Problematically, inhibition of both PI3K and HSP90 have demonstrated the unwanted effect of a reduction in motor neuron viability in models of amyotrophic lateral sclerosis, which may lead to decreased motor function.[262]

1.4.4.3. The PAI-1 Pathway

In addition to the aforementioned SCAPs, plasminogen activator inhibitor 1 (PAI-1) modulates cell adhesion, migration and proliferation,[263] and therefore plays an important role in regulating apoptosis. PAI-1 has been observed to influence apoptosis by inhibiting plasmin generation,[264] as the activation of plasminogen to form plasmin leads to cell death.[265] Cells interact and attach to one another in a process called cell adhesion, using specialised molecules on the cellular surface. It has been shown that PAI-1 binds to vitronectin on the cell surface, which prevents the process of cell adhesion and causes apoptosis.[266] Caspases are crucial in mediating apoptosis by catalysing the cleavage of critical cellular proteins,[267] and PAI-1 has been shown to directly inhibit capase-3, which generates resistance to apoptosis.[268] Studies demonstrating increased expression in SCs have also suggested it is a key mediator in maintaining the senescent state.[269-272] Despite contradictory effects of PAI-1, increased expression has been observed to lead to apoptosis resistance and cell survival.[273]

1.4.4.4. Dependence Receptors

Until recently, it was widely held that many membrane receptors were inactivated when unbound to their endogenous ligand. This has recently been demonstrated as inaccurate, and two distinct signaling events may occur depending on presence or absence of a ligand.[274] Ligand binding elicits a 'positive' response, including proliferation, differentiation or survival, while the lack of ligand binding signals a 'negative' pro-apoptotic response.[275] Given that cell survival hinges on the presence of the ligand, this has afforded the terminology 'dependence receptor' (DR) to refer to a family of about twenty members who function according to this schematic. Screening for compounds which clear SCs have indeed identified upregulation of ephrin ligands, which bind to multiple tyrosine receptor kinases and are known DRs.[244, 274] This has therefore highlighted another mechanism by which SCs suppress apoptotic signaling.

Clearly, many pathways exist for SCs to resist and prevent apoptosis and therefore remain active in producing a deleterious SASP. Inhibition of these pathways could therefore prove highly potent in selectively eliminating SCs. We now turn to discuss therapeutic methodologies for senescence.

1.4.4.5. The BCL-2 Family

The B-cell lymphoma-2 (BCL-2) family of proteins (**Figure 13**) are grouped into three subfamilies based on the number of BCL-2 homology (BH) domains they contain: (1) anti-apoptotic proteins (BCL-2, BCL-X_L, BCL-W, *et al.*), which possess the four BH domains BH1–4; (2) pro-apoptotic pore-formers (BAX, BAK and BOK), which possess the three BH domains BH1–3; and (3) pro-apoptotic BH3-only proteins (BAD, BID, BIK, *et al.*), which possess only the BH3 domain.[276, 277]

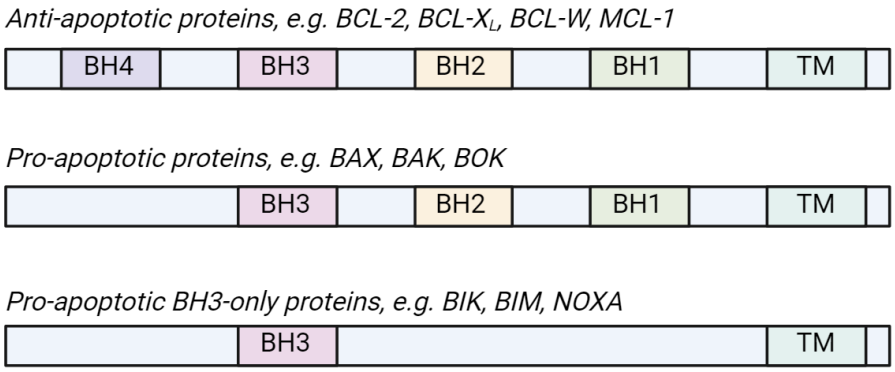

Figure 13: The BCL-2 family of proteins is subdivided into three categories based on the number of BCL-2 homology domains they contain. Created with BioRender.com.

Different models have been proposed to describe the interactions of various proteins within this family.[278] The current understanding is as such: BH3-only proteins sense cellular stresses, initiating their activation. These BH3 proteins then bind to pro-apoptotic pore-formers.[279, 280] This in turn, activates pore-formers, eliciting conformational changes which result in oligomerisation and, as the name implies, the formation of pores within the mitochondrial outer membrane (MOM). This process, known as mitochondrial outer membrane permeabilisation (MOMP), typically results in cell death due to a progressive decline in mitochondrial function (**Figure 14**).[281] Conversely, anti-apoptotic proteins may bind to pore-formers and BH3-only proteins, sequestering either or both and hence inactivating them to prevent apoptosis.[282] Indeed, this pathway is crucial to the natural progression of the cell cycle leading to apoptosis. It is therefore no surprise that resistance to apoptosis in SCs occurs due to increased expression of the anti-apoptotic proteins, primarily at the transcription level.[283, 284] Critically, it has been highlighted that inhibition of the BCL-2 family in models of ALS led to an increase in neuronal function while also preserving motor neuron viability.[262] As such, the BCL-2 family presents a promising pathway to target in therapeutics against senescence-related neurodegeneration.

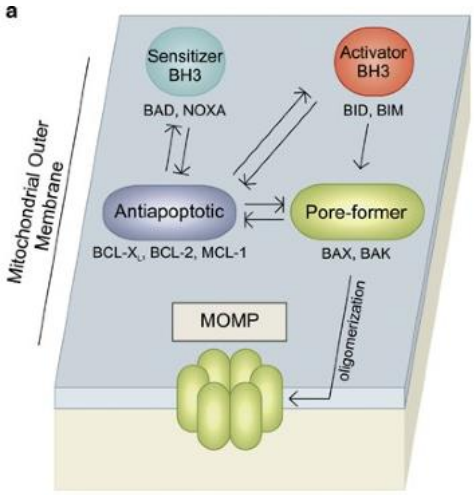

Figure 14: Interactions between pore-former proteins (such as BAX and BAK) and BH3-only proteins (such as BID and BIM) lead to oligomerisation and formation of pores on the MOM, causing cell death by MOMP. Reprinted under a Creative Commons License from *Cell Death Differ.* **25**, 65–80 (2018).[277]

1.5. Current Research in Therapeutics for Senescence

The burden of SCs on an organism has been previously detailed, highlighting that the SASP has significantly damaging effects. Consequently, it has also been demonstrated in mouse models that the clearance of senescent cells has prevented or delayed tissue dysfunction, and extended lifespan.[159] Within the sphere of small-molecule drug research, two classes of therapeutics against SCs exist: (1) senomorphics, which aim to attenuate the SASP; and (2) senolytics, which selectively clear senescent cells by inducing apoptosis.[285] It must be stated that this categorisation may be arbitrary, as a senomorphic compound in a certain cell type may be senolytic in another, and vice-versa.[228]

1.5.1. Senomorphics

Senomorphic compounds aim to attenuate pathways involved in SASP expression, such as Janus kinases (JAKs) and mTOR; and transcription factors such as NF-κB, C/EBP β and STAT3.[286, 287] Blocking the SASP thus suppresses the deleterious effects of SCs that have been previously discussed, without needing to kill cells. Newer treatments have also utilised MABs to bind to and hence impair SASP factors, such as IL-6 and IL-8.[89, 288] Problematically, since SCs are not removed, senomorphics must be administered continuously to achieve silencing or suppression of the SASP. Below, identified senomorphics are discussed, highlighting a diversity of compounds from libraries of natural products and FDA-approved drugs. This information is summarised in **Table B** in **Appendix A**.

1.5.2. Overview of Known Senomorphics

Campisi and co-workers showed that rapamycin **6** suppressed the SASP in human fibroblasts.[289] Concurrently, it was also demonstrated in mouse models that the administration of **6** prolonged their lifespan.[290] It has therefore been suggested that **6** reduces mitochondrial ROS and as such, reduces SASP expression.[291] Similar senomorphic effects have been observed by Spivak and co-workers in their studies of the mTOR inhibitor everolimus **7**.[292]

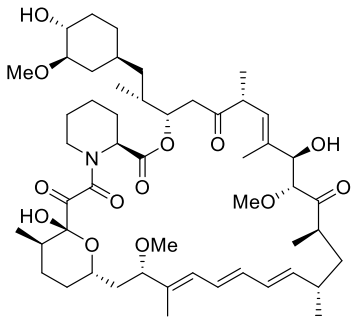

6

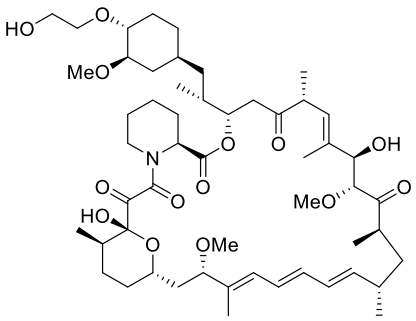

7

Figure 15: Structures of rapamycin **6** and everolimus **7**.

Flavonoids found naturally in plants are known to possess anti-inflammatory and antioxidant capabilities.[293, 294] Unsurprisingly, compounds in this class have been shown to act in a senomorphic manner. Mocali and co-workers found that resveratrol **8** inhibits the NF-κB pathway, a key SASP regulator,[295, 296] and therefore attenuates its release in MRC5 primary fibroblasts.[297, 298] In a similar manner, apigenin **9** reduced SASP expression in murine kidneys,[299] while kaempferol **10** was shown to lessen expression of multiple SASP factors in human dermal fibroblasts (HDFs).[300] Finally, treatment of senescent HDFs with phytochemical epigallocatechin gallate **11** significantly reduced levels of SA-β-Gal and acetylated p53 by maintaining the expression of SIRT1, thus also demonstrating a potent senomorphic effect.[301]

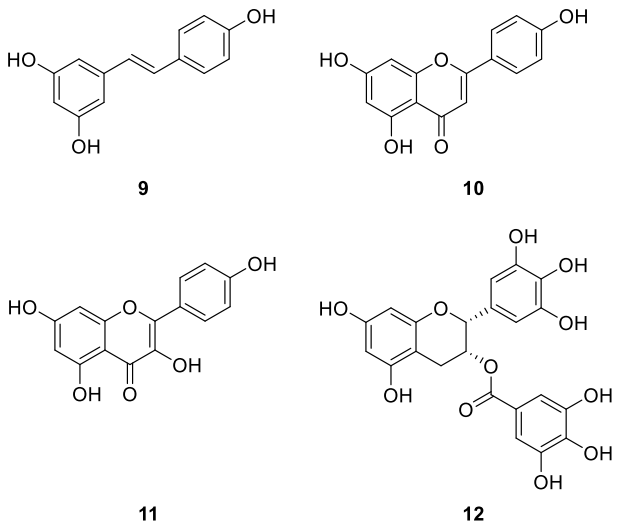

Figure 16: Structures of reservatrol **9**, apigenin **10**, kaempferol **11** and epigallocatechin gallate **12**.

The repurposing of approved drug molecules has also highlighted senomorphic capabilities. Indeed, Ferbeyre and co-workers presented results that treatment of IMR90 fibroblasts with T2DM medication metformin **13** decreased expression of a variety of SASP factors.[302] The JAK1/2 inhibitor ruxolitinib **14**, also an FDA-approved drug, was also found to have suppressed SASP expression in preadipocytes and human umbilical vein endothelial cells (HUVECs).[303] Other currently marketed drugs, such as the Ca^{2+} channel blockers loperamide **15** and niguldipine **16**, have also promoted suppression of the SASP in murine embryonic fibroblasts.[246] Such results have similarly been seen in the ATM kinase inhibitor KU-60019 **17**.[304] However, the exact mechanism by which these molecules exert their senomorphic effect is still under investigation.

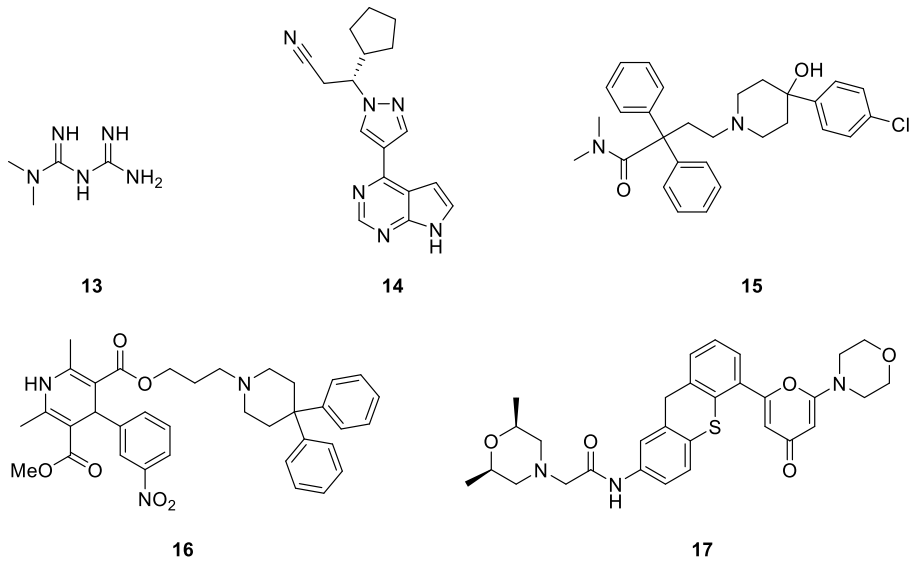

Figure 17: Structures of metformin **13**, ruxolitinib **14**, loperamide **15**, niguldipine **16** and KU-60019 **17**.

1.5.3. Senolytics

Senolytic compounds achieve their aim by selectively targeting mechanisms that promote cellular survival or resistance to apoptosis. Indeed, the discovery of senolytics came about due to the hypothesis that SCs are dependent on anti-apoptotic and pro-survival pathways to avoid self-destruction.[244, 305] Interestingly, it was found that SCAPs implicated in senescence were also responsible for some cancers, such as B-cell lymphoma or chronic lymphocytic leukaemia.[306, 307] In a similar way, disabling these pathways led to apoptosis in SCs, or senolysis, while non-senescent cells remained viable.[308] A broad overview of known senolytics is provided below, with this information summarised in **Table C** of **Appendix A**.

1.5.4. Overview of Known Senolytics

Zhu and co-workers identified the first senolytic compounds in 2015 using bioinformatic screening.[244] Their hits were narrowed down by selecting for certain criteria: (1) several SCAPs were targeted rather than a single protein; (2) they could be orally administered and; (3) they were known natural products with well-known safety profiles or FDA-approved drugs, to increase the possibility of translation from bench to bedside. In doing so, the authors showed that the FDA-approved drug *dasatinib* **18** and the natural product quercetin **19** were promising candidates as senolytics. Screening of the SelleckChem L1200 kinase inhibitor library revealed that *nintedanib* **20** and R406 **21** induced senolysis in HDFs.[309, 310] Further examination of this library also highlighted the aforementioned KU-60019 **17** as a potential senolytic, but the authors were unable to determine whether this compound is merely senomorphic or truly senolytic.[236] Additionally, it was also shown that kinase inhibitors terreic acid **22**, daidzein **23**, PD-98059 **24** and Y-27632 **25** reduced amounts of SCs and attenuated SASP expression, although in this case the authors were also unable to determine if these reduced transition to the senescent state or actually cleared SCs.[311]

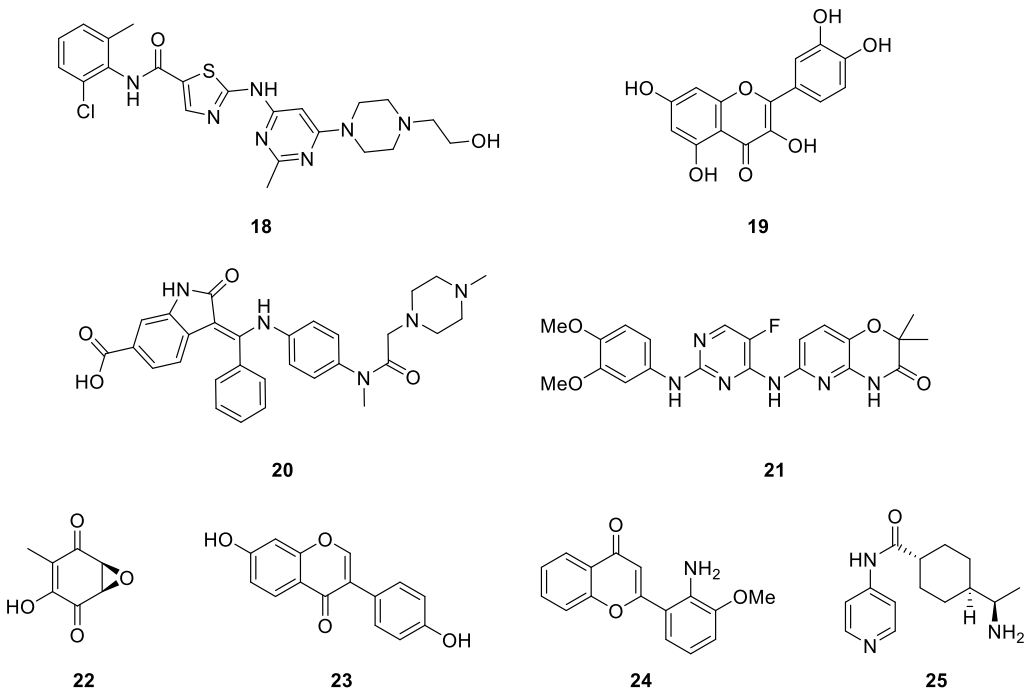

Figure 18: Structures of *dasatinib* **18**, quercetin **19**, *nintedanib* **20**, R406 **21**, terreic acid **22**, daidzein **23**, PD-98059 **24** and Y-27632 **25**.

Plant species produce a variety of bioactive polyphenol compounds, whose consumption has been known to have therapeutic benefits for many chronic conditions.[312] The previously mentioned quercetin **19** and the flavonoid fisetin **26** were highlighted as senolytic against human umbilical vein endothelial cells (HUVECs).[313] In this same screen, curcumin was found to possess weak senolytic activity.[314] This led to the that the curcumin analogue EF24 **27** is senolytic.[315] Further screening of plant extracts identified procyanidin C1 **28**,[316] and gingerenone A **29** as two more senolytic natural products.[317] Moreover, the natural product piperlongumine **30**, from the genus *Piper* was found to be senolytic by binding to oxidation resistance 1 (OXR1).[318] Despite this, the precise mechanism of action is unclear, although analogues of **30** have been synthesised to further investigate their activity.[319]

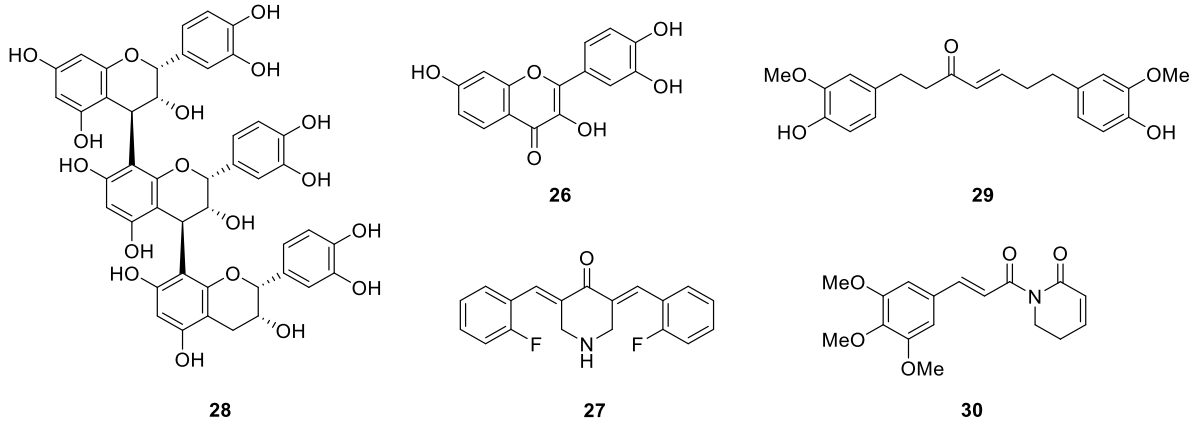

Figure 19: Structures of fisetin **26**, EF24 **27**, procyanidin C1 **28**, gingerenone A **29** and piperlongumine **30**.

Further screens have continued to identify new hit molecules with senolytic effects or potential. An assay of 97 autophagy modulators identified the HSP90 inhibitors *geldanamycin* **31**, *tanespimycin* **32** and *alvespimycin* **33** as senolytics.[246] RNA-sequencing study found the HSP α-crystallin β chain (CRYAB) was a senolytic target. When the known CRYAB inhibitor 25-hydroxycholesterol **34** was evaluated against the HSP, it was also found to be senolytic.[320] Wakita and co-workers conducted the most extensive senolytic screen to date, using the TAKEDA drug discovery library which contains upwards of 47,000 compounds.[235] This revealed the BET family as senolytic targets, and thus concluded that the BET family proteolysis-targeting chimera (PROTAC) ARV825 **35** was a potent senolytic. Separately, it was also shown that the BET inhibitor fragment of the PROTAC, JQ1 **36** also had senolytic properties.[321] The apoptosis activator protein p53 is expressed at reduced levels in SCs.[322] The strategy of stabilizing p53 was therefore shown to be senolytic, demonstrated using inhibitors of the human homolog of mouse double minute 2 (MDM2), RG-7112 **37**[323] and ubiquitin-specific protease 7 (USP7) P5091 **38** and P22077 **39**.[322] Finally, screening of the Prestwick chemical library searched for hits that met two criteria: (1) the drug reduced expression of SA-β-Gal; and (2) it resulted in increased autophagic flux. This led to the discovery that the peroxisome proliferator-activated receptor α (PPARα) agonist *fenofibrate* **40** had senolytic ability.

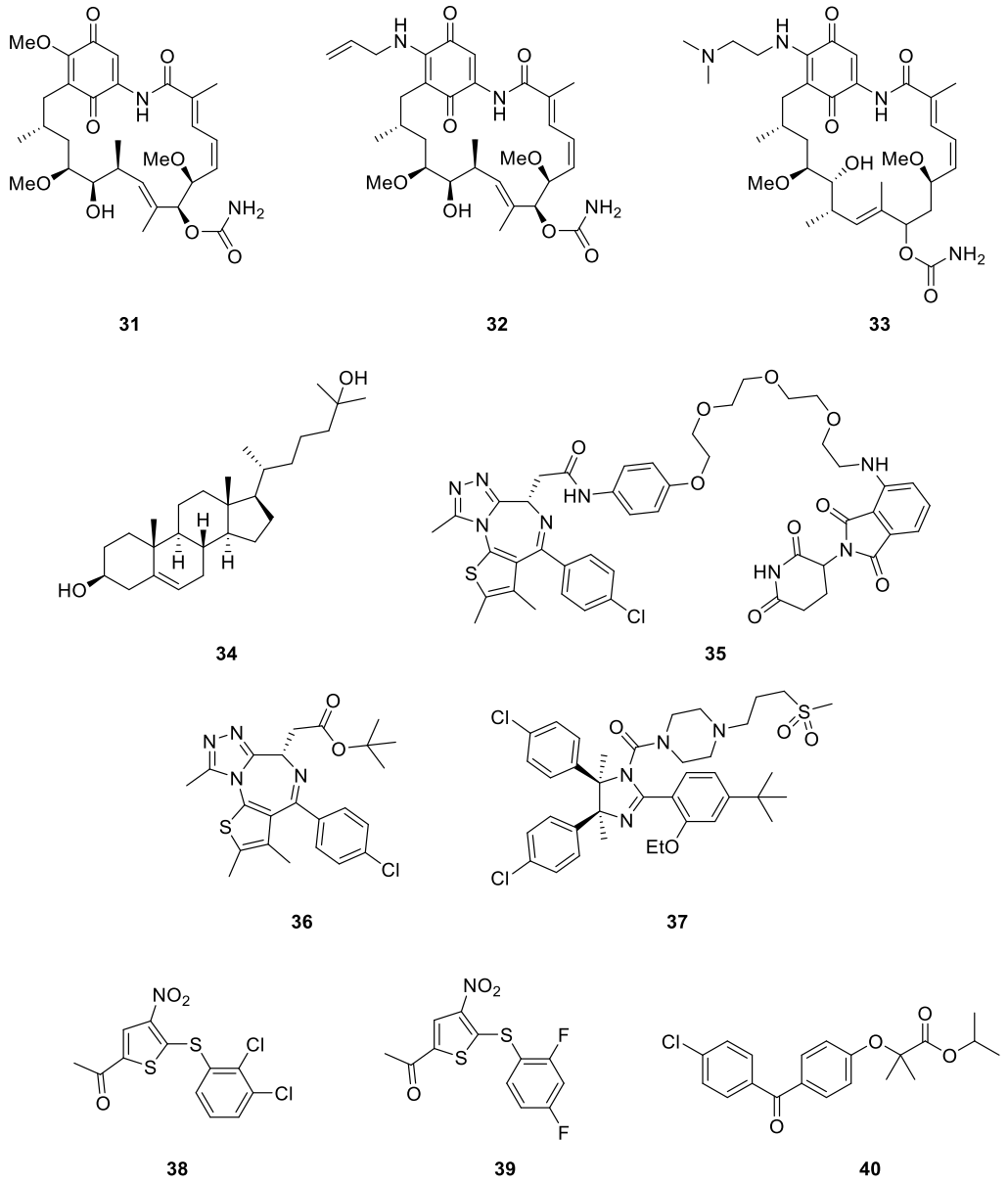

Figure 20: Structures of *geldanamycin* **31**, *tanespimycin* **32**, *alvespimycin* **33**, 25-hydroxycholesterol **34**, ARV825 **35**, JQ1 **36**, RG-7112 **37**, P5091 **38**, P22077 **39** and *fenofibrate* **40**.

Cellular senescence, while evolving as a cancer defence mechanism, shares common cellular characteristics with cancer, such as altered metabolism, resistance to apoptosis and increased autophagy.[324] As such, anti-cancer drugs have been repurposed and found to display senolytic potential. Indeed, senolysis was found to occur following treatment with the synthetic flavonoid GL-V9 **41**,[325] while the histone deacetylase (HDAC) inhibitor *panobinostat* **42** also displayed senolytic effects.[326]

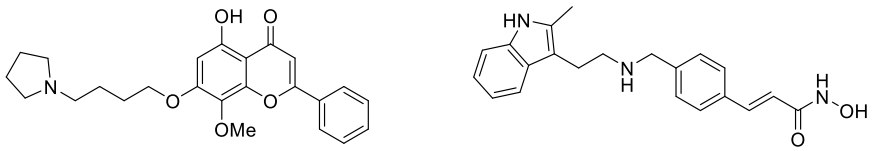

41 **42**

Figure 21: Structures of GL-V9 **41** and *panobinostat* **42**.

Additionally, known antibiotics have been screened, highlighting the senolytic potential of *azithromycin* **43**, *roxithromycin* **44**[327] and *nigericin* **45**.[327] However, the further development of these compounds for clinical use is complicated by risks associated with antimicrobial resistance as such drugs are used more frequently.

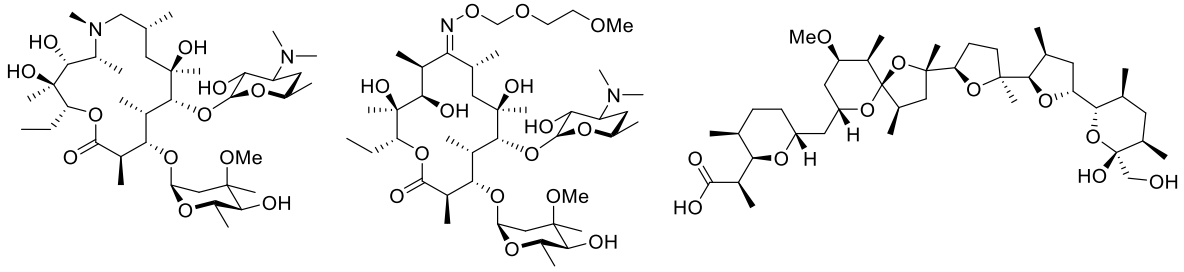

43 **44** **45**

Figure 22: Structures of *azithromycin* **43**, *roxithromycin* **44** and *nigericin* **45**.

The previously discussed BCL-2 family are well-known for their roles in maintaining SC viability. Significant research has been conducted into the anti-apoptotic proteins within this family, due to the positive clinical results seen upon their inhibition in ALS models.[262] To this end, BCL-2 family inhibitors ABT-737 **46** and ABT-263 **47** have been demonstrated to possess senolytic activity in multiple model systems.[328-330] However, a key drawback of these compounds as therapeutics were the major clinical side effects of thrombocytopenia and neutropenia, limiting their progression into further trials. The more recently developed BCL-X_L inhibitors A1331852 **48** and A1155463 **49** have also demonstrated potent senolytic activity, although their safety profile is yet to be evaluated.[313] Targeting other members of the BCL-2 family has also proved effective, as the MCL-1 inhibitors S63845 **50**, AZD5991 **51** and UMI-77 **52** were senolytic in chemotherapy-induced senescent pancreatic tumour cells.[331] Of particular note was that these compounds were even senolytic in cells resistant to treatment with ABT-263 **46**. Indeed, the most promising results of potential senolytic treatments have been reported to act *via* inhibition of the BCL-2 family.

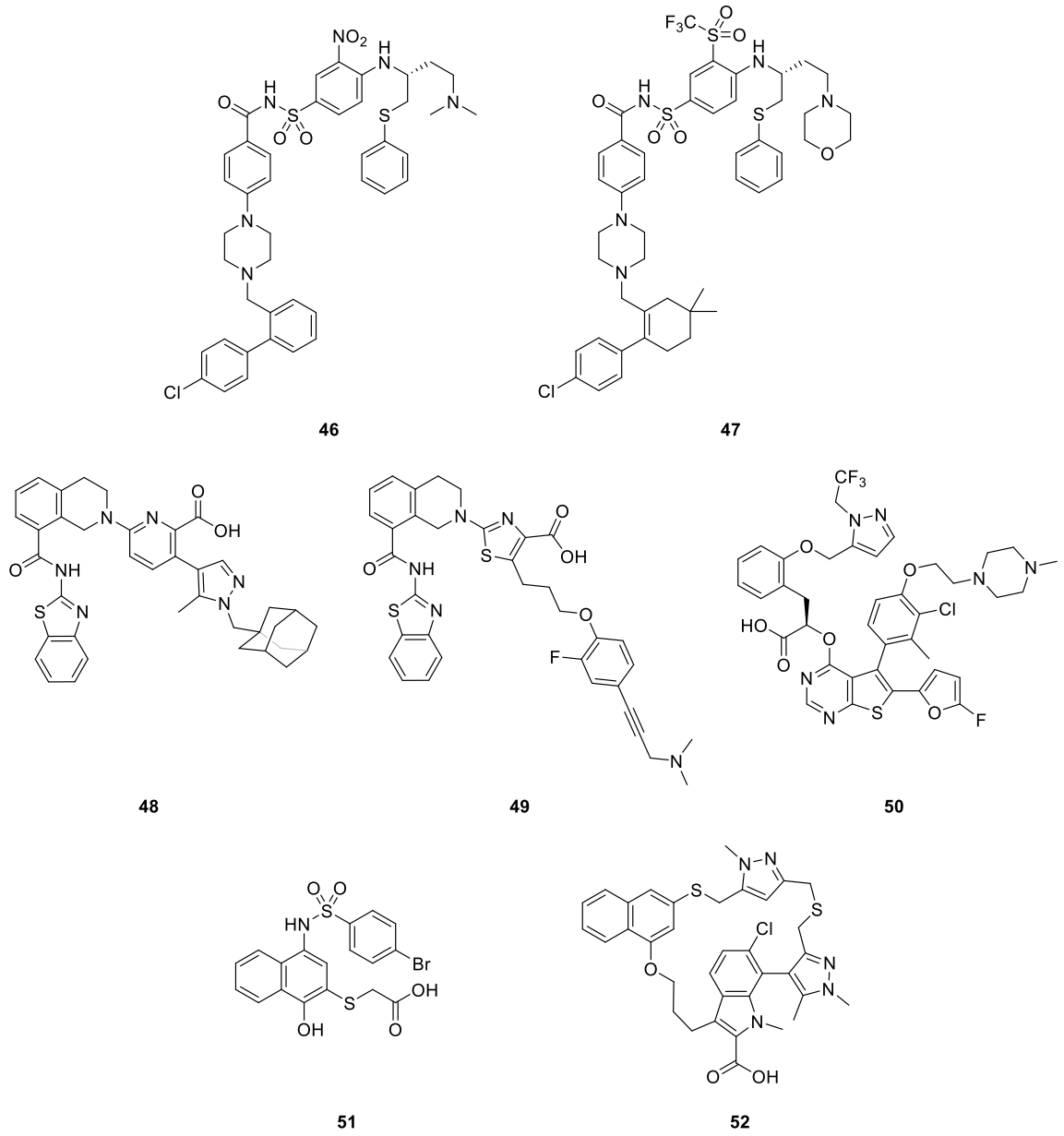

Figure 23: Structures of ABT-737 **46**, ABT-263 **47**, A1331852 **48**, A1155463 **49**, S63845 **50**, UMI-77 **51** and AZD5991 **52**.

While a plethora of studies have demonstrated senomorphic and/or senolytic effects in known natural products, drug candidates and known drug molecules, no such small-molecule treatment has entered the market as a curative treatment for conditions caused by cellular senescence burden. Therefore, there is a significant unmet need for research into novel senolytic chemotypes, and it remains to be seen whether such a molecule may be successfully translated from the bench to bedside.

1.6. Project Aims

The BCL-2 family, containing several anti-apoptotic proteins, offers a viable method of inducing senolysis. This may be accomplished *via* the inhibition of said SCAPs. As such, this project has focused on the use of various techniques within medicinal chemistry to explore novel chemotypes for the amelioration of cellular senescence. It has approached these aims through molecular reconstruction, scaffold hopping and structure-activity relationship (SAR) probing, all of which have been complemented with the application of computational modelling (**Figure 24**). Following the design, synthesis and characterisation of novel chemical libraries, they have been evaluated in a range of *in vitro* studies. The results of these studies are hoped to provide valuable data and inspiration for future expansion of chemical space, pharmacophore exploration and lead optimisation.

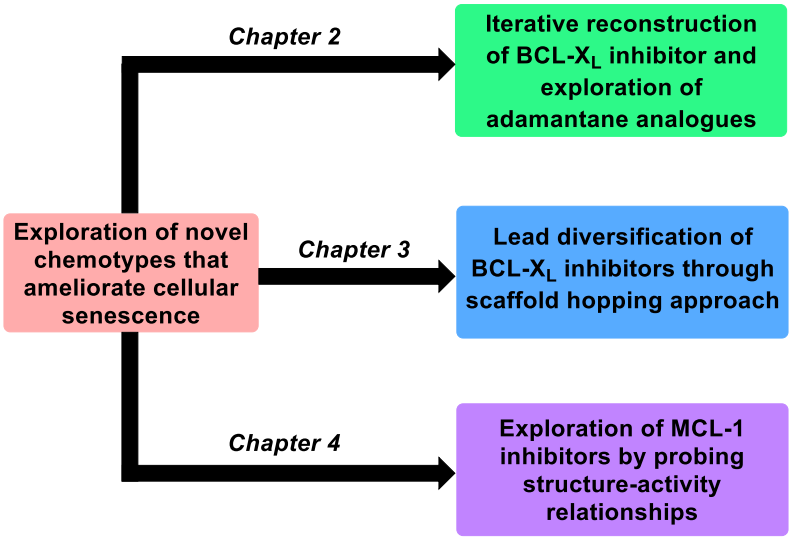

Figure 24: Schematic summary highlighting the overall project aims and a range medicinal chemistry approaches utilised throughout each chapter to explore novel senolytic chemotypes.

1.6.1. Chapter 2 – Iterative Reconstruction of a Known BCL-X$_L$ Inhibitor

As discussed in **Chapter 1.5.2.**, several pharmacophores already exist which target the BCL-2 family. The initial work for this project explored the development of ABT-737 and ABT-263. **Chapter 2** describes small-molecule BCL-X$_L$ inhibitors designed by Abbott Laboratories, and our efforts to determine the minimum pharmacophore required for binding affinity to the protein. This resulted in a library of analogues where each compound contained additional features when compared to previous iterations, culminating in the lead molecule itself. Further explored is the replacement of moieties in this structure with adamantane derivatives, creating an additional library. This chapter also contains an overview of the process of computational

modelling *via* molecular docking studies, and a description of the biological assays used to evaluate compounds synthesised in **Chapter 2** and **Chapter 3**.

1.6.2. Chapter 3 – Scaffold Hopping of Known BCL-X_L Inhibitors

The generation of new pharmacophores is an ever-evolving discipline in medicinal chemistry. One method of doing so is through the application of scaffold hopping. A broad summary of the foundations of scaffold hopping is provided in **Chapter 3**, followed by application of this technique to BCL-X_L inhibitors originally designed by the Walter and Eliza Hall Institute (WEHI). The use of Spark™ software to generate new chemical structures was followed by validation in a molecular docking study. This chapter discusses the synthesis of a library of structurally diverse compounds, exemplifying the use of scaffold hopping as a methodology to rapidly explore overhauls of lead compounds.

1.6.3. Chapter 4 – Probing SAR Around a Known MCL-1 Inhibitor

The inhibition of MCL-1 presents another opportunity for the targeting of a SCAP. In **Chapter 4**, the results of an SAR study conducted in literature were used to design a variety of analogues of a lead compound *in silico*, and a molecular docking study was applied to identify those which were most likely to afford strong binding to the target protein. This presents a study wherein SAR of a molecule and target protein is further probed. Such alterations to molecular structure represent small changes to the overall pharmacophore but highlight the vast unexplored chemical space. Furthermore, biological evaluation of this library is hoped to provide insight into both the binding mode towards MCL-1 and the requirements of senolytic chemotypes.

This Page Intentionally Left Blank

This Page Intentionally Left Blank

Chapter 2

Iterative Reconstruction of a Known BCL-X_L Inhibitor

Chapter 2 – Iterative Reconstruction of a Known BCL-X_L Inhibitor

2.1. Introductory Remarks

Established links exist between the promotion of SCAPs and the pathology associated with the deleterious SASP caused by an increasing burden of SCs. As described in **Chapter 1.5.4.**, a variety of molecules have already been observed to display senolytic abilities, with their mechanism of action also identified. These senolytic targets demonstrate an encouraging capacity to selectively clear SCs, thus there is a clear need to identify and refine chemotypes that may function as potential chemical probes or therapeutic agents. Of these targets, the BCL-2 family of proteins is attractive to study due to its critical role in maintaining the anti-apoptotic state of SCs.[262]

Our investigation began by analysing the known inhibitors of the BCL-2 family that have been previously described in Chapter **1.5.4.** to understand the chemical space that has been explored. Compounds discovered by Abbott Laboratories were of particular interest for multiple reasons: (1) their potency against target proteins; (2) elaboration of chemical motifs and subsequent development of structure-activity relationships; and (3) the progression of these compounds into clinical trials.[332, 333] Elmore and co-workers reported compound **53** in 2007, although its biological activity was not determined. Probing of SAR around **53** led to the discovery of the BCL-2 and BCL-X_L inhibitor ABT-737 (**46**) in 2007,[333] however its poor oral bioavailability prompted the researchers to further improve its physicochemical properties, culminating in the discovery of ABT-263 (**47**), reported the following year (Figure **25**).[332]

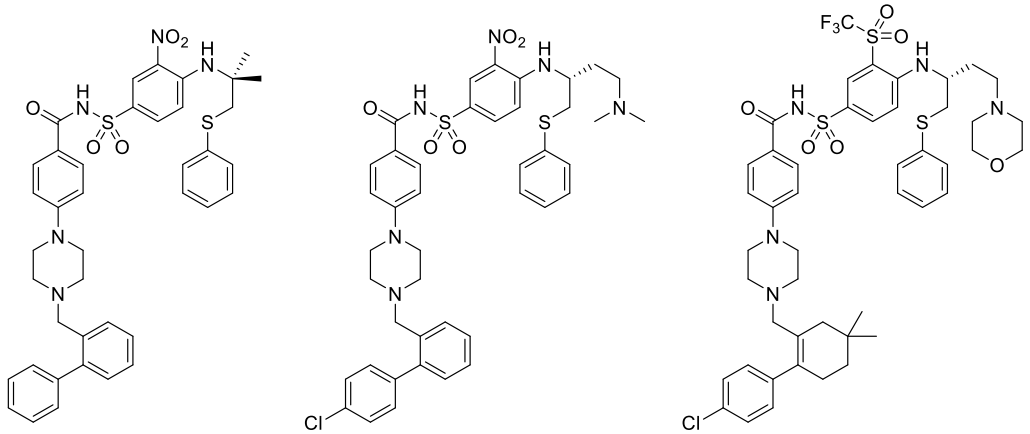

Figure **25**: Compounds **53**, ABT-737 (**46**) and ABT-263 (**47**), developed by Abbott Laboratories.

ABT-737 and ABT-263 were designed as cancer treatments: ABT-737 showed efficacious results in human follicular lymphoma cell lines and murine xenograft models of lymphoma, while ABT-263 induced complete tumour regression in xenograft models of human small cell lung cancer in multiple animals.[332, 333] As has been discussed in Chapter **1.4.4.5.**, apoptosis is prevented when anti-apoptotic members of the BCL-2 family form protein-protein interactions (PPIs) with pro-apoptotic pore-formers or BH3-only proteins, therefore sequestering them from performing their normal function. This SCAP therefore offers a promising method by which SCs could also be targeted: inhibitors of the anti-apoptotic members of the BCL-2 family, such as BCL-2, BCL-X_L, BCL-W and MCL-1 could prevent these PPIs from forming, thus leading to the MOMP and subsequent apoptosis. This chapter therefore discusses work based on these molecules and their application to senescence.

2.2. Abbott's Developmental Work

Tracing the development of ABT-737 and ABT-263 highlighted efforts by Abbott to probe structure-activity relationships of a *de novo* compound.[334] NMR studies of BCL-X_L revealed two binding sites for targeting which were nearby to each other. The active site of the protein is shown in **Figure 26**, with fragments bound to these two sites. An NMR-based screen using a fragment library of 10,000 compounds led to the identification of several fragments, including **54**, as a moderate binder of the first site (shown left), and several weaker binders of the second site.

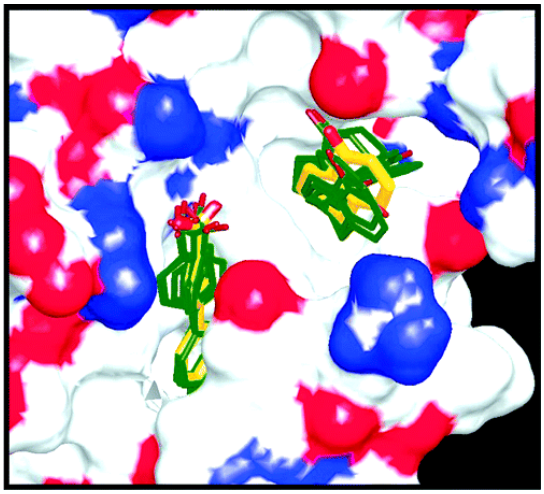

Figure 26: The binding pocket of BCL-X_L, with the superposition of low-energy structures complexed to the two nearby binding sites. The first site (*left*) contains the ligand **54** in yellow. The average-minimized structure of the protein is shown as a solvent-accessible surface, colour coded as follows: oxygen and oxygen-bound protons are red, and nitrogen and nitrogen-bound protons are blue, while all other atoms are grey. Reprinted with permission from *J. Med. Chem.* 2006, 49, 2, 656–663. Copyright 2006 American Chemical Society.

A summary of the authors' workflow in improving the activity of **54** is shown in **Figure 27**. Attempts were made to link these two fragments using groups such as alkyl chains, *trans*-olefins, amides, sulfonamides and alkynes. NMR-based models of the ligand in the binding pocket suggested that none of these linkers gave the molecule the ideal shape required. This prompted the authors to propose linking these fragments with an *N*-acylsulfonamide, as shown in **55**. The *N*-acylsulfonamide has a pK_a in the range of 3–5 and has features of carboxylic acids, amides and sulfonamides,[335, 336] making it suitable for overcoming the issues faced with other linkers. To optimise binding to the second site, **55** was modified to be linked to a library of 120 primary sulfonamides, of which **56** was found to exhibit the greatest affinity for BCL-X_L, with an inhibition constant (K_i) of 0.245 ± 0.013 μM. To probe the binding pocket, substitutions were made *ortho* to the nitro group of **56**, allowing for rapid diversification of the compound library through nucleophilic aromatic substitution reactions.[334] The amines selected for these reactions were chosen on the basis of traditional medicinal chemistry principles such as Hansch analysis and a Topliss scheme,[337, 338] diversity calculations[339-341] and the authors' own molecular modelling.[334] Of 125 compounds synthesised in this round of SAR, it was found that **57** had significantly improved binding affinity at BCL-X_L, with a K_i of 36 ± 2 nM.

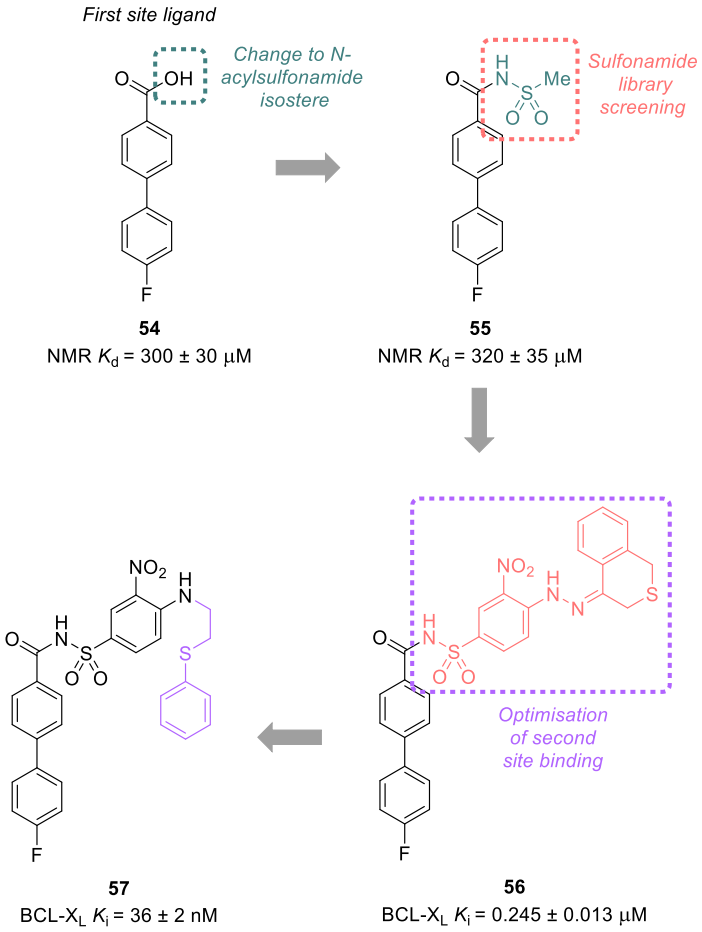

Figure 27: NMR screening identified the first site ligand **54** in the active site of BCL-X_L. Coupling with 120 different primary sulfonamides revealed **56** as the strongest binder. Further elaboration of the amine *ortho* to the nitro group highlighted **57** as a lead with high binding affinity.

Further elaboration of the structural motifs present in **57**, performed *via* probing of the SAR, led to the design of the aforementioned ABT-737 and ABT-263.[332, 333, 342] Our particular interest was **57**, which demonstrated high potency for BCL-X_L but also offered promising *in vivo* results as a cancer treatment.[343] It was with these results in mind that we focused our attention on the structure of **57** and how it could be utilised in the context of senescence, which forms the foundation for the work detailed in this chapter.

2.3. Chapter Aims

ABT-737 and ABT-263 had exceptional binding affinity to BCL-X_L, however their molecular masses exceed 800 Da and they also possess C log *P* values greater than 10. On the other hand, **57** retains nanomolar binding affinity while having a much smaller molecular mass of 551 Da and lower C log *P* of 7.48. With this intriguing chemotype, we set out to determine the minimum pharmacophore required to exhibit biological activity against BCL-2 family

proteins. Indeed, while the fragment **54** does display weak binding to the target, we wished to know whether binding affinity would steadily increase as the reconstruction progressed, or if a certain pharmacophoric alteration would provide the link that significantly altered affinity. This chapter therefore focuses on an 'iterative reconstruction' strategy, wherein compounds were synthesised to iteratively build the molecule from the significantly simplified **58**, towards the lead compound **57**, as shown in **Figure 27**. Additionally, computational docking studies of the proposed library are presented in an attempt to predict which structural changes to the ligand would increase binding affinity.

2.4. Proposed Compound Library and Rationale

The starting point of this study, *N*-acylsulfonamide **58** was chosen as it had also demonstrated low-potency anti-cancer activity, with an IC_{50} of 0.17 ± 0.3 μM against VEGF-HUVECs although the precise mechanism of this activity is unknown.[344] The iterative reconstruction was envisioned to proceed through three stages, as shown in **Figure 28**: (1) expansion and modification of the 2,4-dichlorophenyl ring by building the 4-fluorophenyl ring in the *para* position of the benzoic acid through compounds **58**–**63**; (2) expansion of the 4-chlorobenzenesulfonamide ring by adding nitro and amino groups through compounds **64** and **65**; and (3) completion of the reconstruction by expanding the amine tail through compounds **66**, **67** and **57**.

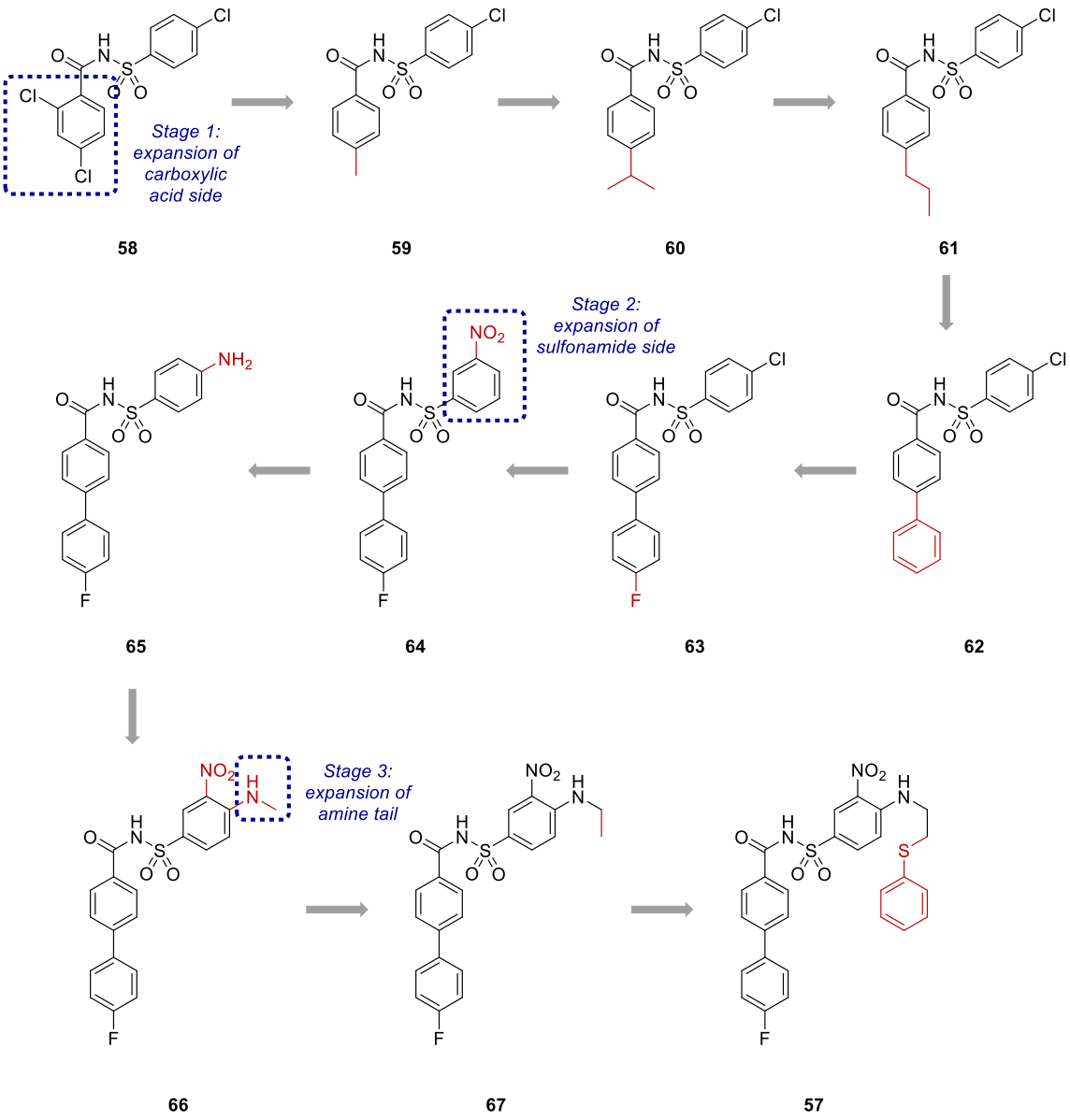

Figure 28: Compounds to be synthesised in iterative reconstruction, which proceeds through three stages of building up the molecule from **58** to **57**.

2.5. Iterative Reconstruction of **57**

2.5.1. Synthesis of N-acylsulfonamides **58–63**

To synthesise acylsulfonamides **62** and **63**, biphenyl carboxylic acids **69** and **70** were required. Both compounds were synthesised from 4-bromobenzoic acid **68** *via* Suzuki coupling using phenylboronic acid and 4-fluorophenylboronic acid respectively (**Scheme 1**), which produced the desired products in good yields.

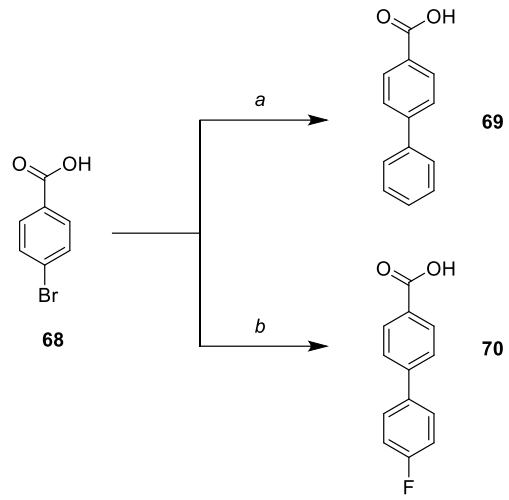

Scheme 1: Synthesis of biphenyl carboxylic acids **69** and **70**. *Reagents and conditions*: (*a*) phenylboronic acid, $Pd(dppf)Cl_2$, K_2CO_3, 1,4-dioxane, H_2O, 80 °C, 16 h, 62% yield; (*b*) 4-fluorophenylboronic acid, $Pd(dppf)Cl_2$, K_2CO_3, 1,4-dioxane, H_2O, 80 °C, 16 h, 77% yield.

With these materials in hand, attention was turned to the synthesis of *N*-acylsulfonamides **58**–**63**. The sulfonamide precursor **72** was prepared *via* amination of 4-chlorobenzenesulfonyl chloride **71** using saturated aqueous NH_3 solution, which yielded 4-chlorobenzenesulfonamide **72** in excellent yield. Subsequent couplings using this primary sulfonamide and required 4-substituted benzoic acids (methyl, *i*-propyl, *n*-propyl, phenyl and 4-fluorophenyl) gave the desired products **58**–**63**. These couplings were perfomed using *N*-ethyl-*N*′-(3-dimethylaminopropyl)carbodiimide hydrochloride (EDC·HCl) and 4-(*N*,*N*-dimethyl)aminopyridine (DMAP) as described by Lobb and co-workers (**Scheme 2**).[344]

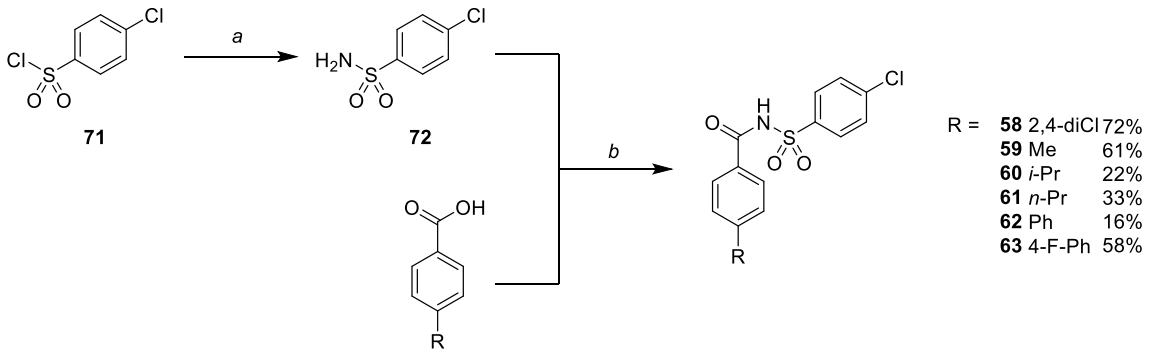

Scheme 2: Synthesis of *N*-acylsulfonamides **58**–**63**. *Reagents and conditions*: (*a*) NH_3 (aq), 50 °C, 2 h, 98% yield; (*b*) EDC·HCl, DMAP, CH_2Cl_2, RT, 16 h.

The purification of these compounds *via* isocratic flash column chromatography proved challenging due to co-elution of the reaction products. These issues were rectified using a very slow gradient elution, which was subsequently applied to all further sulfonamide coupling

reactions. These reactions yielded compounds **58**–**63** in 16-61% yield, hence completing the elaboration of stage 1 of the iterative reconstruction.

2.5.2. Synthesis of N-acylsulfonamide **64**

To synthesise *N*-acylsulfonamide **64**, 3-nitrobenzenesulfonyl chloride **73** was first aminated using saturated aqueous NH_3 solution in Et_2O using the method utilised by Lobb and co-workers, yielding primary sulfonamide **74** in good yield without the need for purification.[344] With this material in hand, *N*-acylsulfonamide **64** was synthesised by coupling with EDC·HCl and DMAP, yielding the desired product (**Scheme 3**).

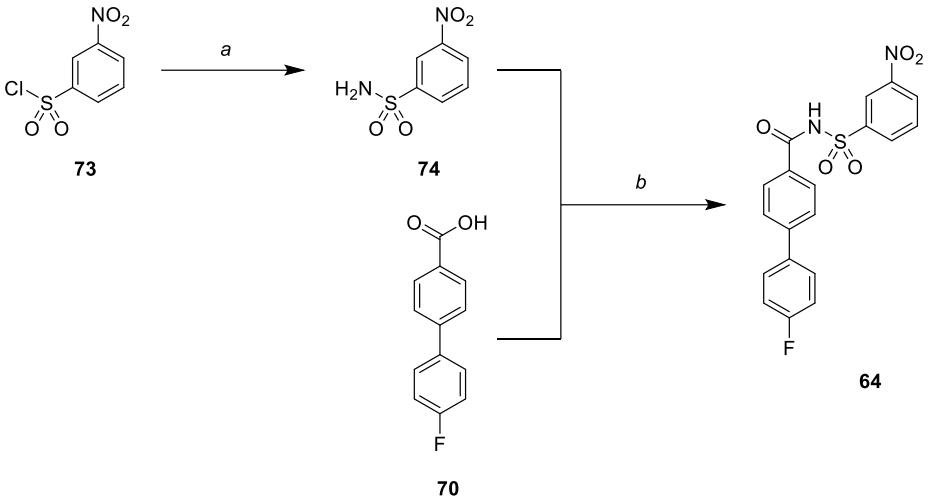

Scheme 3: Synthesis of *N*-acylsulfonamide **64**. *Reagents and conditions*: (*a*) NH_3 (aq), Et_2O, RT, 1 h, 80% yield; (*b*) EDC·HCl, DMAP, CH_2Cl_2, RT, 16 h, 75% yield.

2.5.3. Synthesis of N-acylsulfonamide **65**

In preparing *N*-acylsulfonamide **65**, 4-nitrobenzenesulfonyl chloride **75** was aminated using the previously described procedure with saturated aqueous NH_3 solution in Et_2O, affording the product **76** in good yield. This material was then coupled to the biphenyl carboxylic acid **70** using EDC·HCl and DMAP as shown in **Scheme 4**, which gave the desired *N*-acylsulfonamide in fair yield.

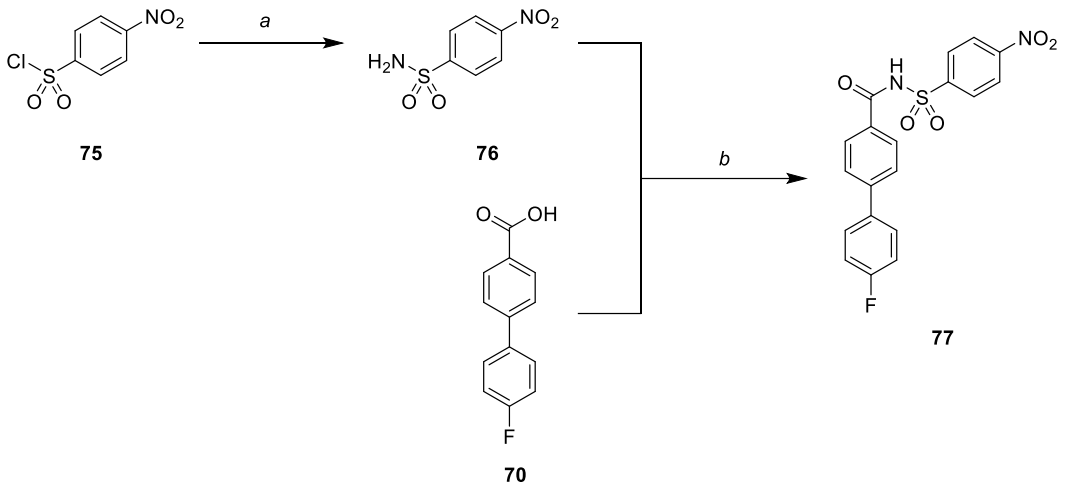

Scheme 4: Synthesis of *N*-acylsulfonamide **77**. *Reagents and conditions*: (*a*) NH_3 (aq), Et_2O, RT, 1 h, 70% yield; (*b*) EDC·HCl, DMAP, CH_2Cl_2, RT, 16 h, 52% yield.

Following this, it was necessary to reduce the nitroarene to the corresponding aniline. Initially, a Pd-catalysed hydrogenation was attempted (**Scheme 5**), which gave the product, but the formation of dehalogenated impurity **78** was also observed in the ^{1}H NMR spectrum due to proto-dehalogenation.[345] Attempts to purify this mixture were unsuccessful, as the R_f values of these two products were extremely close, thus separation could not be achieved.

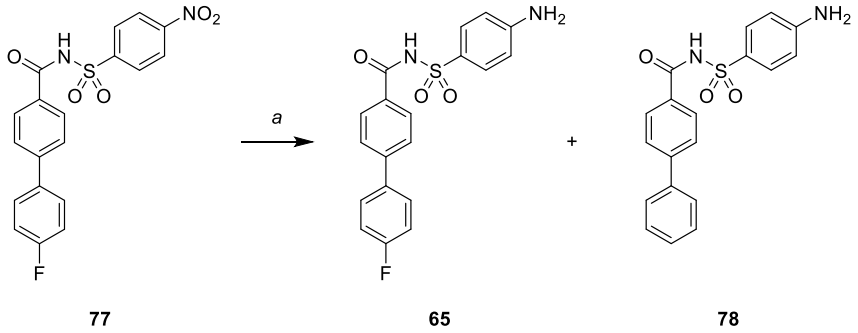

Scheme 5: Attempted synthesis of *N*-acylsulfonamide **65**. *Reagents and conditions*: (*a*) H_2, Pd/C, MeOH, 24 h, RT.

To avoid this issue, we explored the Béchamp reduction, a robust procedure using elemental iron and an acidic medium,[346, 347] to cleanly afford the desired aniline. The reaction mechanism is of particular note, with the zero-valent iron acting as a source of electrons, while the acidic medium – in this case, ammonium chloride – acts as a proton source. As shown in **Scheme 6**, the reaction proceeds *via* a series of proton transfers (PT) and single electron transfers (SET). This process first eliminates H_2O to form the nitroso species, which is then protonated to give a hydroxylamine. A further elimination of H_2O forms a nitrenium species, which upon protonation gives the corresponding aniline.[348]

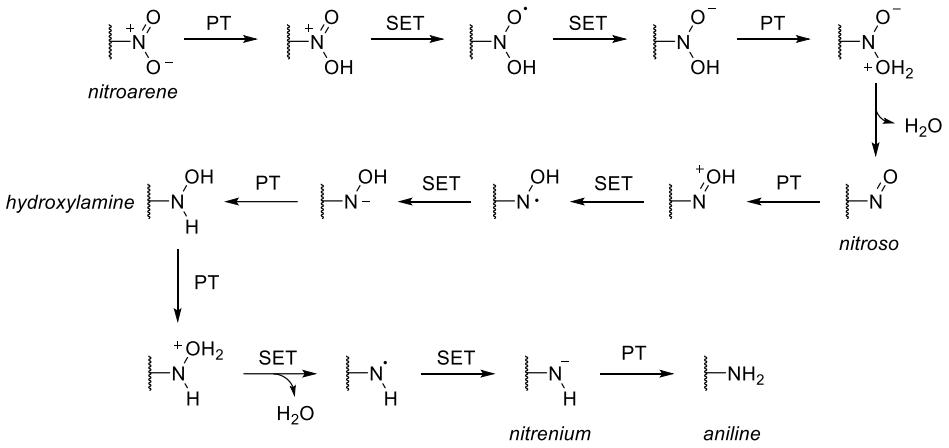

Scheme 6: Mechanism of the Béchamp reduction. PT = proton transfer; SET = single electron transfer.[348]

The Bechamp reduction thus afforded the desired sulfonamide in good yield (**Scheme 7**) without the need for purification, which completed the required compounds for the stage 2 of the iterative reconstruction.

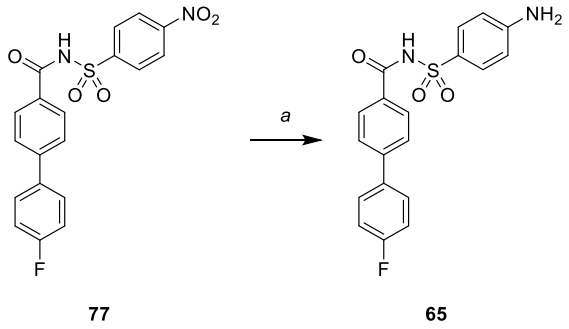

Scheme 7: Synthesis of *N*-acylsulfonamide **65**. *Reagents and conditions*: (*a*) Fe, NH_4Cl (aq), EtOH, 78 °C, 1 h, 77% yield.

2.5.4. Synthesis of N-acylsulfonamides **66**, **67** and **57**

To synthesise *N*-acylsulfonamides **66**, **67** and **57**, 4-chloro-3-nitrobenzenesulfonyl chloride **79** was first aminated using saturated aqueous NH_3 solution in Et_2O, which gave the sulfonamide **80** in good yield. This was then coupled to carboxylic acid **70** using EDC·HCl and DMAP, which gave the *N*-acylsulfonamide **81** in moderate yield following purification by column chromatography (**Scheme 8**).

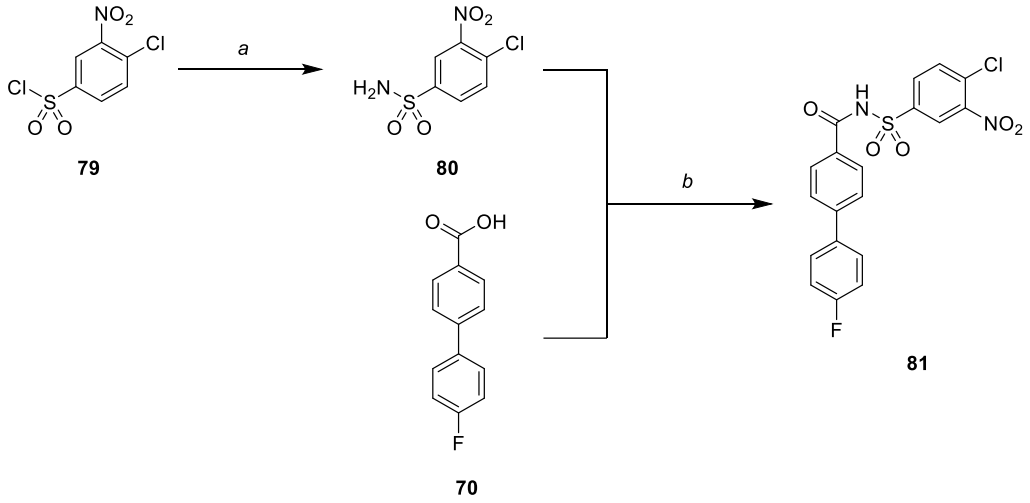

Scheme 8: Synthesis of *N*-acylsulfonamide **81**. *Reagents and conditions*: (*a*) NH_3 (aq), Et_2O, RT, 1 h, 80% yield; (*b*) EDC·HCl, DMAP, CH_2Cl_2, RT, 16 h, 59% yield.

Conversion of the aryl chloride to the secondary amine was attempted through a nucleophilic aromatic substitution (S_NAr), which is conveniently aided by the nitro group (**Scheme 9**). This electron-withdrawing group significantly decreases the electron-density of the phenyl ring, particularly at the positions *ortho* and *para* to it. This facilitates attack by the nucleophilic amine and subsequent formation of the desired aniline. *N*-acylsulfonamide **81** was thus treated with methylamine solution (40% w/w) in *N*,*N*-dimethylformamide (DMF) and heated to 100 °C.

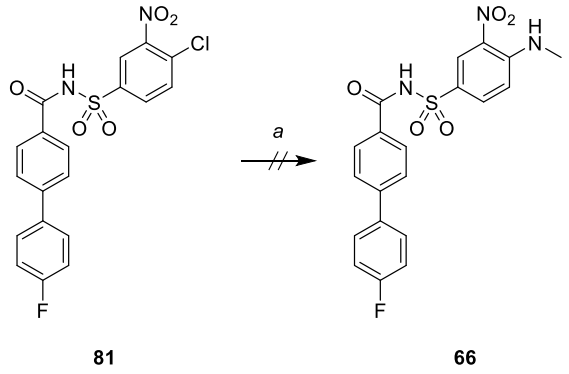

Scheme 9: Attempted synthesis of *N*-acylsulfonamide **66**. *Reagents and conditions*: $MeNH_2$, DMF, 100 °C, 16 h.

Upon completion of the reaction, two products were observed in the ^1H NMR spectrum, shown in **Figure 29** (*a*). The signal at δ 2.99 appears as a doublet due to coupling to the adjacent NH. Of note was the singlet at δ 2.87. We initially proposed this had formed due to another S_NAr occurring at the fluoro-position to form **82** (**Figure 30**) but were able to discount this for two reasons: firstly, the fluorophenyl ring is not especially electron-poor, and therefore the

possibility of a S_NAr reaction is unlikely, particularly so in producing a side product in greater proportion than the desired aniline **66**. Secondly, analysis of this mixture by electrospray ionisation mass spectrometry (ESI-MS) showed the presence of the desired product at *m/z* 428 (calcd for $C_{20}H_{15}FN_3O_5S^-$ *m/z* 428) and an additional signal at *m/z* 442.

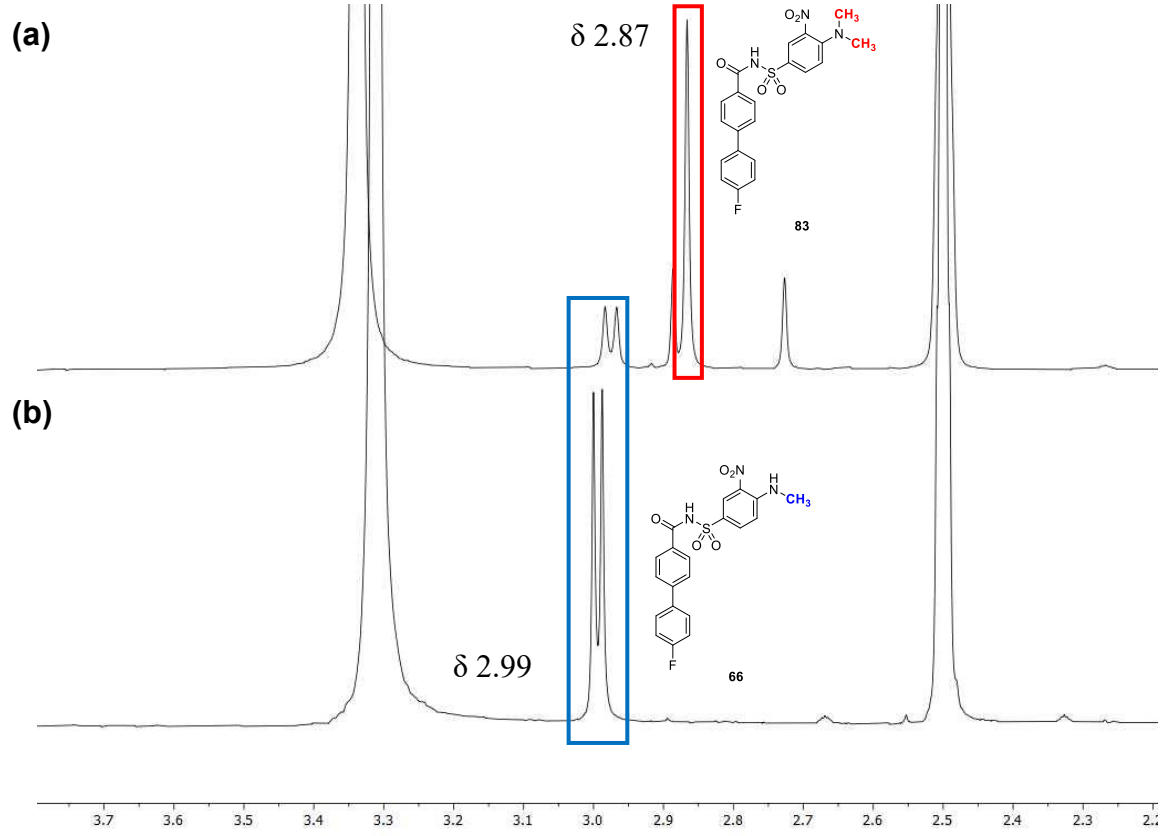

Figure 29: ^{1}H NMR spectra of crude mixture from S_NAr of *N*-acylsulfonamide **81** (*a*) and purified aniline **66** (*b*). The doublet corresponding to the methyl aniline is shown in **blue**, while the singlet corresponding to the dimethyl aniline is shown in **red**.

It is known that DMF slowly decomposes under ambient conditions to yield carbon monoxide and dimethylamine,[349] although the precise mechanism of decomposition is poorly understood. It was therefore hypothesised that this pathway, which is accelerated by heat, produced dimethylamine *in situ* to react in competition with methylamine, affording the impurity **83** which matched the mass detected *via* ESI-MS. Moreover, there is no longer an NH to allow for coupling, causing the singlet observed in the ^{1}H NMR spectrum at δ 2.87.

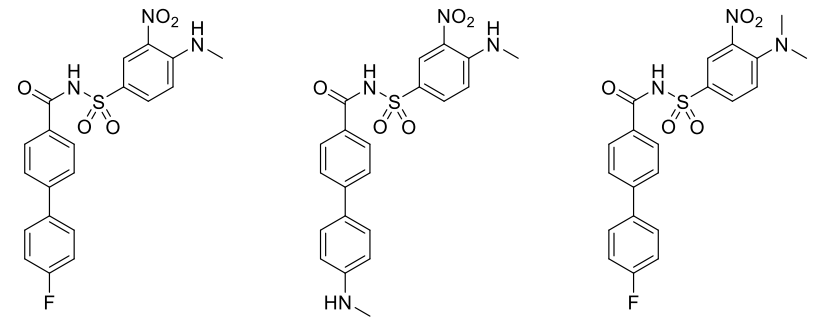

Figure 30: Calculated *m/z* values for desired *N*-acylsulfonamide **66**, proposed impurity **82**, and actual impurity **83**.

As the formation of this impurity became apparent, no solvent system gave separation using thin layer chromatography (TLC). Difficulty in separation was obvious when considering the HPLC chromatogram (**Figure 31**), which showed the two products having very close retention times of 26.25 minutes and 26.75 minutes, that translated to extremely close R_f values. It was thus considered infeasible to separate *via* column chromatography.

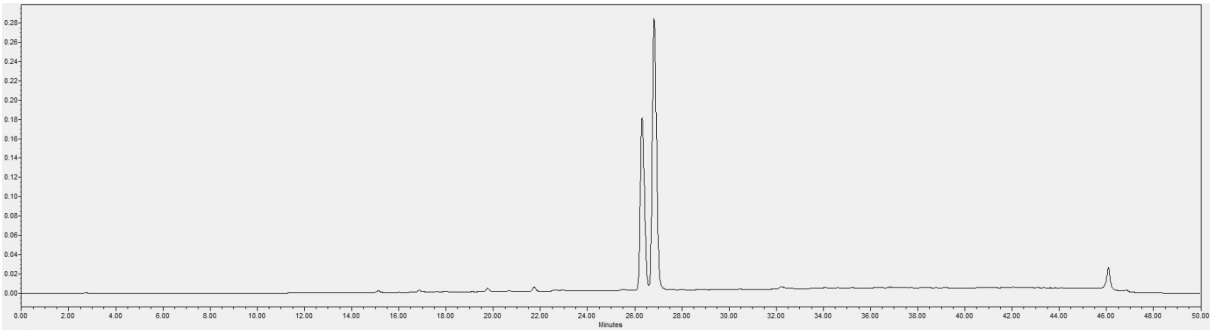

Figure 31: HPLC chromatogram of the mixture of *N*-acylsulfonamides **66** and impurity **83**, highlighting the difficulty of separation.

Instead, the reaction was repeated using DMSO as the solvent, which is known to be relatively stable under these conditions. This gave the desired product in good yield (**Scheme 10**). Knowing that the use of DMF as a solvent would continue to yield the unwanted dimethylaniline **83**, further S_NAr reactions were performed using DMSO. *N*-acylsulfonamide **67** was synthesised in a similar manner using 2 M ethylamine solution in MeOH, which yielded the product in moderate yield (**Scheme 10**).

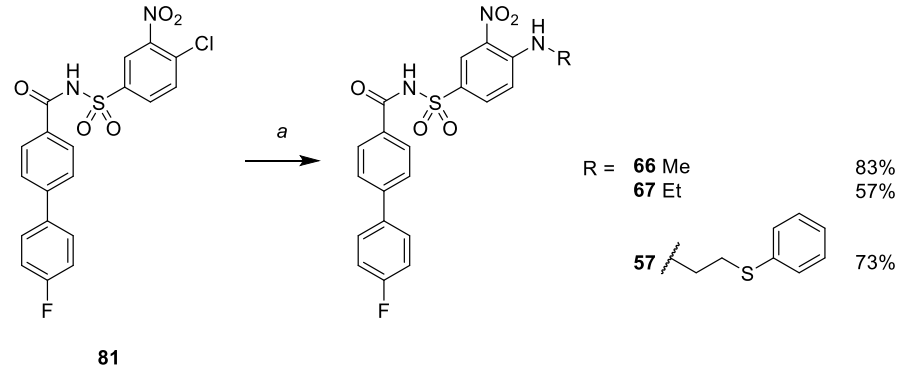

81

Scheme 10: Synthesis of *N*-acylsulfonamides **66**, **67** and **57**. *Reagents and conditions*: R-NH_2, DMSO, 100 °C, 16 h.

Finally, the preparation of *N*-acylsulfonamide **57** required 2-(thiophenol)ethylamine **86**. Several conditions were trialled before this compound could be successfully synthesised (**Scheme 11** and **Table 2**). It was desirable to avoid the use of thiophenol in this synthesis, due its toxicity and overwhelming stench. As such, we opted to use the far safer sodium thiophenolate **85**.

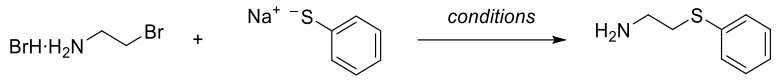

84 85 86

Scheme 11: Synthesis of 2-(phenylthio)ethan-1-amine **86**.

Table 2: Optimisation of the synthesis of 2-(phenylthio)ethan-1-amine **86**.

Entry	Conditions	Result
1	NaOH, H_2O, RT	No reaction
2	NaOH, DMSO, RT	No reaction
3	NaOH, DMSO, 100 °C	Complex reaction mixture
4	K_2CO_3, CH_2Cl_2, RT	40% yield

Initially, we adapted protocols developed by Chen and co-workers,[350] wherein 2-bromoethan-1-amine **84** (as the HBr salt) was deprotonated by NaOH in H_2O, then the thiophenolate **85** was added to participate in an S_N2 reaction (entry 1, **Table 2**). This resulted in no reaction being observed *via* TLC. This is rationalised by considering that aziridine may have been formed instead of the desired product, and its high volatility (*b.p.* 57 °C) meant it rapidly evaporated upon TLC analysis. We thus resolved to change the solvent to DMSO, a polar aprotic solvent (entry 2, **Table 2**). With no consumption of thiophenolate **85** observed at room temperature, the mixture was gradually heated up to 100 °C (entry 3, **Table 2**), but this

instead produced a complex mixture of products, likely due to decomposition of the reactants. Indeed, no trace of the desired product was observed by ESI-MS. Lastly, we attempted to use the weaker K_2CO_3 to deprotonate the amine **84**, adapting conditions developed by Mehta and co-workers (entry 4, **Table 2**).[351] The weaker base may have also prevented substitution from occurring by attack of the OH^- ion. This gave the desired amine **86** as the sole product, which was used immediately in an S_NAr reaction to afford *N*-acylsulfonamide **57** (**Scheme 10**). This reaction proceeded in moderate yields, although some decomposition was observed upon TLC of the reaction mixture, with the R_f values of these impurities relatively close to **57**. Isolation of the product was therefore challenging, requiring an initial purification using silica gel column chromatography, followed by further purification using preparatory TLC. This marks the completion of stage 3, and the proposed iterative reconstruction.

2.6. Biological Data for Iterative Reconstruction

The *in vitro* evaluations performed and presented throughout this chapter were performed by Dr. Alexandra Maximova within the Faculty of Health Sciences at the University of Sydney. Her contributions to this work are greatly appreciated.

While many assays for assessing the amelioration of cellular senescence have been developed,[352] no such method exists for evaluating the senolytic potential of molecules in brain cells. Indeed, there is also no 'gold-standard' method that is widely accepted as a model for studying pharmacological clearance of SCs. It was therefore decided to assess the synthesised compounds in enzymatic assays – in particular, their antagonisation of BCL-2 and BCL-X_L – to evaluate their potential as novel senolytics. Assay details and methods are provided in **Chapter 6.8.** Evaluation of the compounds synthesised was conducted with two different methods for BCL-X_L and BCL-2, the principles of which are briefly described below.

Evaluation of compounds against BCL-X_L was performed using a time-resolved fluorescence resonance energy transfer (TR-FRET) assay kit (BPS Bioscience). A schematic representation is shown in **Figure 32**. A His-tagged BCL-X_L protein binds to a terbium-labelled antibody donor. Concurrently, a known peptide ligand of BCL-X_L, BIM, is labelled with biotin, which binds to a dye-labelled streptavidin acceptor, which acts as the positive control. The proximity of Tb-labelled antibody and dye-labelled streptavidin permits generation of a TR-FRET signal. However, if a small molecule inhibitor ligand competes with the peptide for binding to BCL-X_L, the intensity of the TR-FRET signal is reduced. Hence, results for this

assay are given in **Figure 34** as the intensity of the TR-FRET signal as a proportion of the positive control.

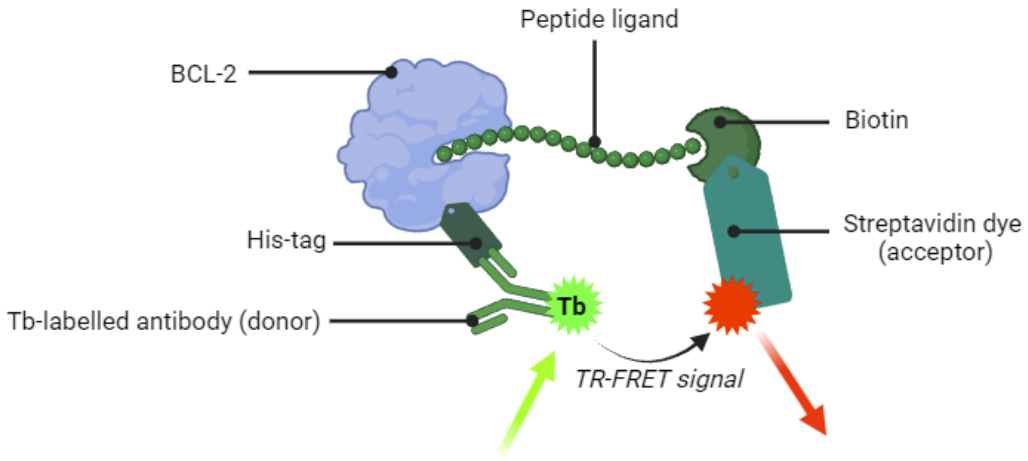

Figure 32: Schematic of the BCL-X_L TR-FRET assay. Proximity between the Tb-tagged antibody donor, attached to the protein of interest, and the streptavidin-tagged dye acceptor permits the energy transfer, thereby producing a FRET signal. Created with Biorender.com.

Evaluation of compounds against BCL-2 was performed using an AlphaScreen® (ALPHA for amplified luminescent proximity homogeneous assay). Fundamentally, this bead-based assay used to study interactions between proximal objects functions similarly to the previously discussed TR-FRET assay. AlphaScreen® assays use two types of hydrogel-coated beads, known as the donor and acceptor. The donor bead contains a photosensitiser which, upon excitation by 680 nm light, causes the excitation of triplet oxygen ($^3O_2$) to singlet oxygen ($^1O_2$). $^1O_2$ may diffuse approximately 200 nm in solution prior to relaxing to its ground state. If in proximity to an acceptor bead, $^1O_2$ can transfer its energy to it. The acceptor bead contains the chemical dyes thioxene, anthracene and rubrene. Therefore, the transfer of energy from $^1O_2$ to the acceptor results in broad emission from 520 to 620 nm. In a similar manner to the TR-FRET assay, donor beads are bound to streptavidin conjugates, which facilitates the labelling of the control inhibitor protein BIM. Likewise, the acceptor is bonded to an antibody, which binds to a His-tag on the protein of interest. In the control, BIM binds to BCL-2, thus allowing energy transfer by $^1O_2$ and subsequent emission. This transfer is disrupted by the presence of an inhibitor ligand. Again, results for this assay are given as the intensity of light emission as proportion of the positive control, in **Figure 34**. A schematic representation of an AlphaScreen® is shown in **Figure 33**.

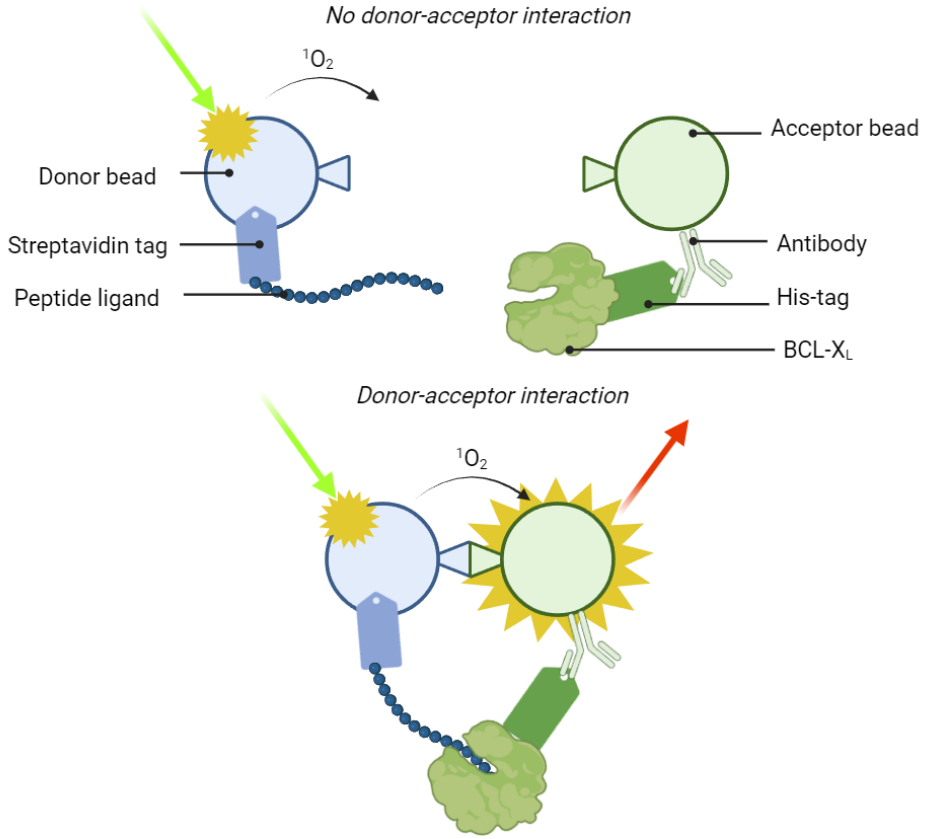

Figure 33: Schematic diagram of the AlphaScreen® assay. *Top*: When the donor and acceptor beads are not in proximity, energy transfer by $^1O_2$ cannot occur, thus no light emission is detected. *Bottom*: Proximity of the donor and acceptor beads facilitates energy transfer by $^1O_2$, thus resulting in broad light emission from 520 to 620 nm. Created with Biorender.com.

Using these methods, the compounds synthesised in **Chapter 2.4.** were evaluated for their binding affinity towards both BCL-X_L and BCL-2. As a benchmark for this assay, the BCL-X_L inhibitor ABT-737 (**46**) was also evaluated as a comparison against the compounds prepared throughout the iterative reconstruction. Unfortunately, no statistically significant reduction in intensity was observed for any of the synthesised compounds in either the TR-FRET or AlphaScreen® assays at a concentration of 10 µM. As such, the binding described in the literature for **57** was not observed.[334] In fact, many of these compounds resulted in an increased TR-FRET intensity, which was an undesirable outcome for this assay. While a slight reduction was seen for **61**, this was not deemed significant as to warrant further investigation into the SAR of this compound. Biological evaluation described in literature employed a fluorescence polarisation assay, which differs slightly to the TR-FRET and AlphaScreen® procedures used in this work. Despite this, we expected that similar results would be observed in the case of **57**, given the binding affinity determined by the authors. Due to the underwhelming nature of these results, we therefore considered structural modifications to explore novel chemical space.

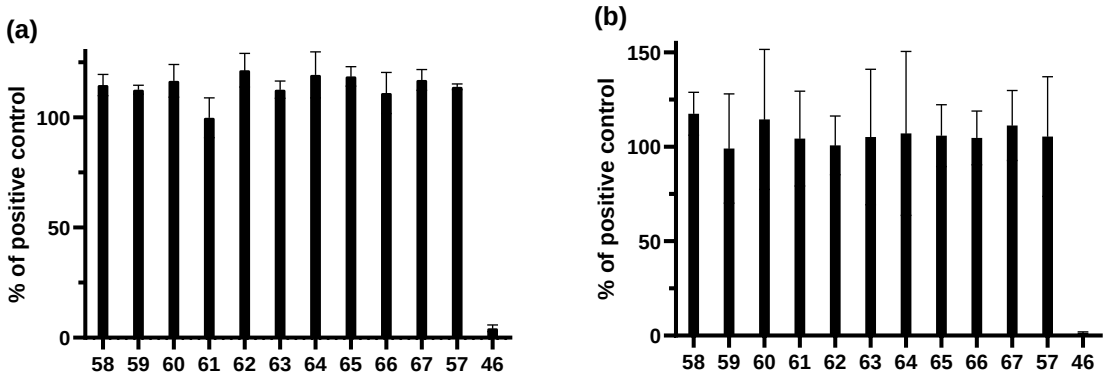

Figure 34: Biological evaluation of compounds **58**–**67**, **57** and **46**. (*a*) TR-FRET intensity of synthesised compounds as a percentage of positive control; (*b*) AlphaScreen® intensity of synthesised compounds as a percentage of positive control. Data represents mean ± SD, n = 3.

2.7. Proposal of Adamantane Analogues

Given the results of the biological evaluation for compounds synthesised in the iterative reconstruction, we also considered whether structure-activity relationships of this molecule could be further probed using unexplored chemical motifs. Indeed, adamantanes have proven particularly powerful in medicinal chemistry: the precursors are commercially available, they have been demonstrated to improve a drug's pharmacokinetic and pharmacodynamic profile and offer improved blood-brain barrier permeability and decreased metabolic clearance, as the rigid hydrocarbon protects proximal functional groups from cleavage.[353] As such, we proposed to study derivatives of **57** where the entire carboxylic acid side would be replaced with adamantanes, linking them to the *N*-acylsulfonamide motif with aliphatic linkers of varying lengths (**Figure 35**). In doing so, the sulfonamide side of the molecule would be iteratively reconstructed in a manner akin to that described in **Chapter 2.3**.

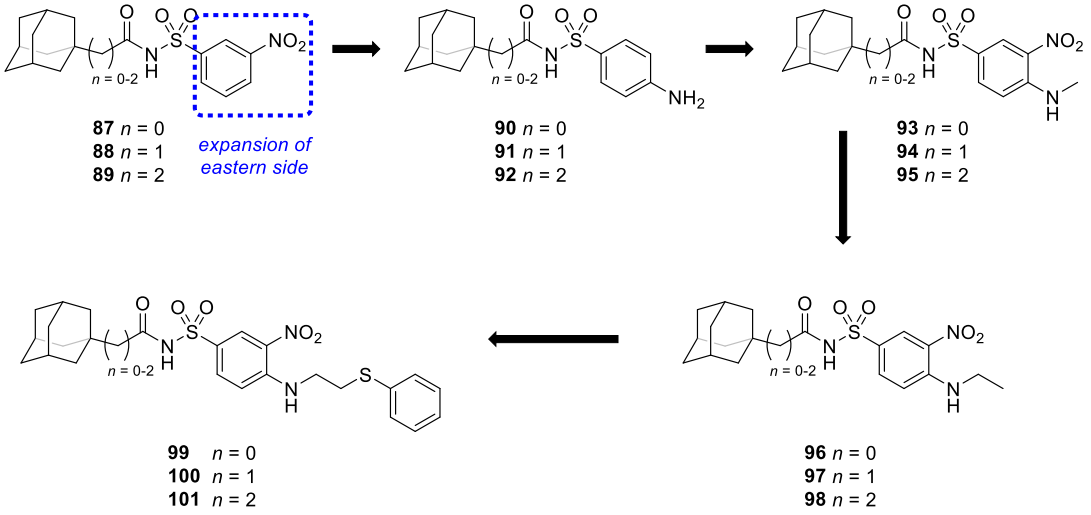

Figure 35: Proposed adamantane analogues for second iterative reconstruction.

2.8. Computational Molecular Docking Studies

We wanted to confirm through molecular docking studies that adamantane would provide a suitable replacement for the 4-fluorobiphenyl moiety before beginning the synthesis of the adamantane analogues of *N*-acylsulfonamides **87**–**101**. Molecular docking is a technique for assessing the binding affinity of ligands into a known receptor protein.[354] Ligands may be screened from large libraries or generated by the user, while the specified binding site in the protein may be a known active site, dimer interface, or some other area of interest.[355]

2.8.1. Overview of Molecular Docking

Prior to docking, it is first important to perform preparation steps for both the ligands and the protein. Molecules imported from databases or drawn on applications such as ChemDraw exist as 2-dimensional representations that often do not accurately reflect their shape, bonding, electronics or even the atoms present, as hydrogens are implicit. However, docking applications require that atoms in both the ligand and protein have a charge and atom type. Thus, ligand preparation carried out by the docking application involves adding hydrogens, bond orders and formal charges to each atom, while also generating ionisation or tautomeric states for the ligand.[356] The aim of ligand preparation is therefore to calculate reasonable states that the ligand is likely to exist in. Protein structures, which may be imported directly from the X-ray crystal structures available in the Protein Data Bank (PDB), similarly lack the characteristics required for docking algorithms to effectively approximate binding affinity. Hence protein preparation samples degrees of freedom that may be ambiguous in crystallographic data, treats residues with missing density and optimises the placement of rotatable hydrogen atoms, among a multitude of other functions.[356] Following this, a receptor grid is generated to identify the site of the protein at which docking is to occur. At this stage, the process of molecular docking may be undertaken, which is broadly summarised in two main steps:

1. Ligand sampling: in this step, the docking application aims to calculate potential direction and conformations, or molecular "poses" of the ligand within the receptor.[357] Three sub-categories of ligand sampling methods exist: shape matching; systematic or direct methods; and stochastic or random methods.[355, 358]
2. Scoring functions: once ligand poses have been generated, the docking application then ranks these according to their predicted binding affinity, giving a 'docking score'. Four main methods have been developed for ranking: force field-based scoring functions; empirical scoring functions; knowledge-based scoring functions; and consensus scoring.

Indeed, computational methods are a critical step in modern drug discovery programs: in hit identification, high-throughput docking can be used to determine which molecules should be prioritised for further investigation, while in lead optimisation, small changes to the molecular structure of a drug candidate can be rapidly tested without the need for chemical synthesis.[359-361] Furthermore, structure-based virtual screening methods may be used to complement other screening techniques, which has greatly contributed to the acceleration of modern drug discovery.[362] Molecular docking studies were performed using Schrödinger's Maestro[363] suite. Ligands were prepared using LigPrep[364] and proteins were prepared using Protein Preparation Wizard,[365] both embedded within Maestro. The program Glide[366] within Maestro then samples ligand poses and ranks the resultant structures to give a 'Glide score'. The Glide score acts as a surrogate for the free energy of binding, thus more negative scores indicate higher binding affinity.[367]

Despite the power of computational docking methods in drug discovery, such techniques are not without limitations, which must be considered when making decisions for a medicinal chemistry program. Most substantially, input models of both ligands and the protein must be of sufficiently high detail to output accurate calculations of the free energy of binding. Even so, the highest resolutions possible with crystallographic data cannot perfectly predict the interactions of a protein's active site and a ligand.[358] Protein flexibility can also affect the accuracy of a docking algorithm, as proteins are not rigid structures and therefore contains thousands of bonds, each rotating and/or vibrating in 3-dimensional space.[368] However, simulating all these movements is extremely computationally expensive, so concessions must be made to limit flexibility and simplify the model.[368] Finally, there is no consensus on the 'best' scoring algorithm currently available, as a plethora of different methodologies have been developed, each with its unique advantages and disadvantages. Considering all these factors, sole reliance on docking applications is not guaranteed to reveal compounds that are most pharmacologically active, with the potential for both false positives and false negatives.[369]

2.8.2. Molecular Docking of Adamantane Analogues

Elmore and co-workers' development of the previously discussed compound **57** utilised a molecular docking study to examine interactions with BCL-X_L.[334] In our study, we used the same NMR-derived protein structure (PDB: 2O2N) to closely simulate the conditions used by the authors. The position of the known inhibitor was used to generate the receptor grid, then each of the proposed adamantane-based ligands was docked into the active site of BCL-X_L.

The results of our docking study are shown in **Table 3**. While the fully constructed compounds **99**–**101** gave the lowest Glide scores and thus the highest predicted binding affinity, a range of higher predicted free energies of binding were predicted for the remainder of the compounds. This is unsurprising, given the biological evaluation discussed in **Chapter 2.5.** which demonstrated that iterative reconstruction of the amine tail resulted in compounds with no binding affinity. Nonetheless, a clear increase in predicted binding affinity could be seen in going from ethyl anilines **96**–**98** to the fully reconstructed derivates **99**–**101**. When simulated in the binding pocket of BCL-X_L, the fully constructed analogues display key interactions (**Figure 36**), which helped us to rationalise this conclusion. Indeed, the nitro groups show π-cation interactions with Phe105, while the carbonyl group forms a hydrogen bond with Ser106.

Table 3: Glide score values for adamantane analogues **87**–**101**.

Compound	**Glide Score**	**Compound**	**Glide Score**	**Compound**	**Glide Score**
n = 0 analogues		*n* = 1 analogues		*n* = 2 analogues	
87	−3.12	**88**	−2.55	**89**	−2.60
90	−3.24	**91**	−2.14	**92**	−2.76
93	−3.74	**94**	−4.62	**95**	−3.41
96	−3.27	**97**	−4.07	**98**	−4.02
99	−7.98	**100**	−7.67	**101**	−7.49

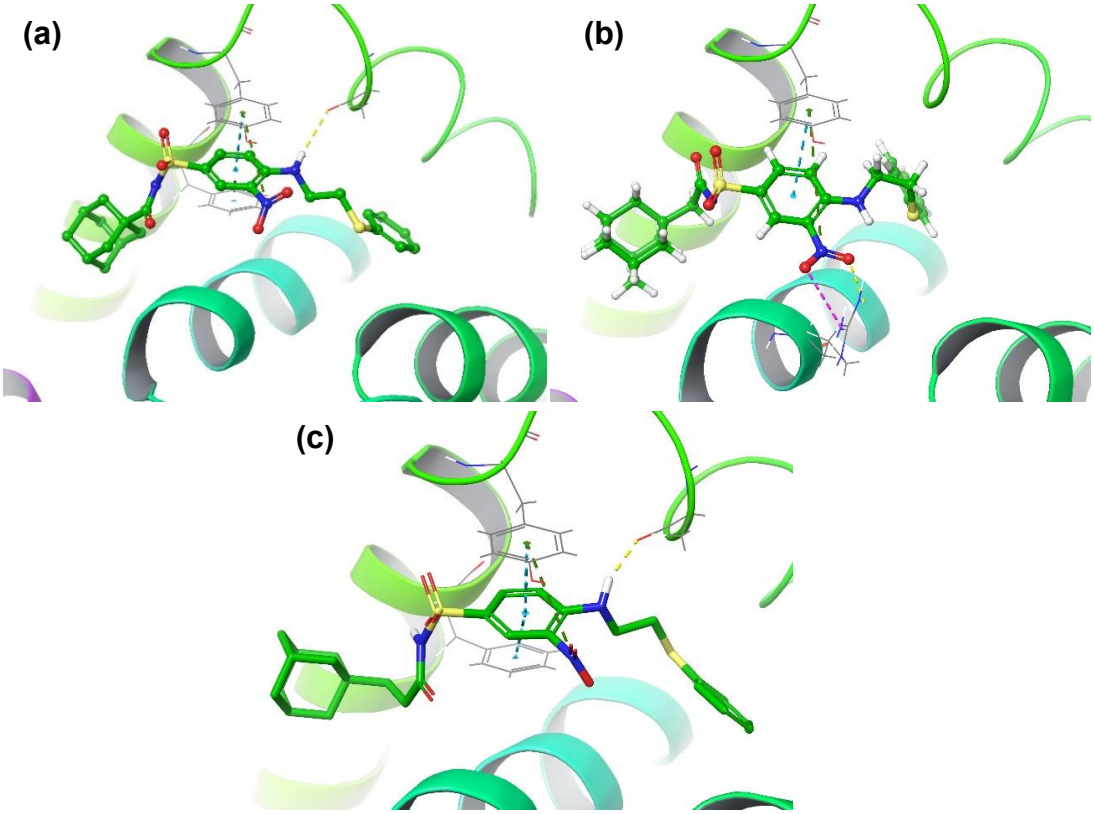

Figure 36: NMR-derived structure (PDB: 2O2N) of **99** (*a*), **100** (*b*) and **101** (*c*) bound to BCL-X_L. Green dotted lines indicate π-cation interactions, light blue dotted lines indicate π-π stacking interactions, while yellow dotted lines indicate H-bonding.

Given the results of our docking study, especially the scores of **99**–**101**, we were encouraged by the predicted binding affinities and hence began the synthesis of the proposed adamantane derivatives.

2.9. Synthesis of Adamantane Analogues of **57**

2.9.1. Synthesis of Adamantane Propanoic Acid **106**

The syntheses of acylsulfonamides **89**, **92**, **95**, **98** and **101** required adamantane propanoic acid. This necessitated functional group manipulation of the carboxylic acid and subsequent Wittig reaction to perform a two-carbon homologation. Adamantane carboxylic acid **102** was first reduced to the corresponding alcohol **103** *via* treatment with $LiAlH_4$ in THF at reflux (**Scheme 12**), giving clean conversion in excellent yield.

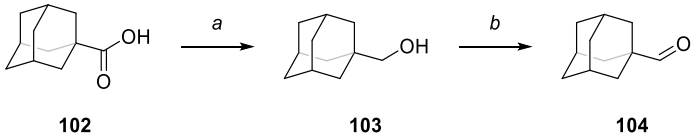

Scheme 12: Synthesis of adamantane-1-carbaldehyde **104**. *Reagents and conditions*: (*a*) $LiAlH_4$, THF, 0 °C – reflux, 3 h, 95% yield; (*b*) TPAP, NMO, MeCN, 1.5 h, 9% yield.

Oxidation was first attempted using tetrapropylammonium perruthenate (TPAP) and *N*-methylmorpholine *N*-oxide (NMO), known as the Ley-Griffith oxidation.[370] In this system, the catalytic TPAP oxidises the alcohol while the metal centre itself is reduced. Stoichiometric NMO then re-oxidises the metal for it to continue the reaction (**Scheme 13**), forming *N*-methylmorpholine. However, it was found that upon workup, a large proportion of the aldehyde **104** decomposed when concentrated with spent *N*-methylmorpholine. The basic nitrogen was likely to have attacked the carbonyl group in a side reaction which resulted in the loss of aldehyde **104**. As a result of the poor yield obtained, an alternative oxidation method was sought for this step.

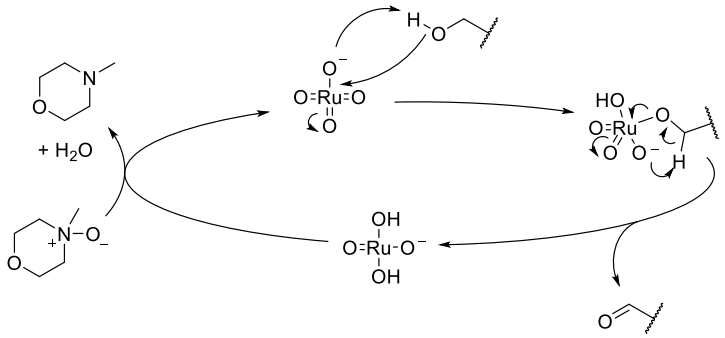

Scheme 13: Mechanism of the Ley-Griffith oxidation.

Dess-Martin periodinane (DMP) is a mild oxidising reagent containing hypervalent iodine, which facilitates the oxidation, as shown in **Figure 14**.[371] Treatment of alcohol **103** with DMP gave the desired product in significantly improved yield of 72% following straightforward purification by column chromatography to remove the spent oxidant.

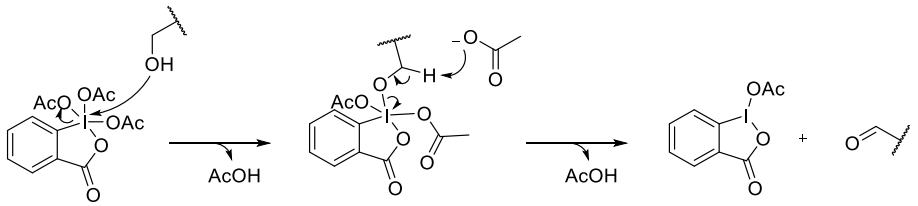

Scheme 14: Mechanism of the Dess-Martin oxidation.

With the aldehyde **104** in hand, the 2-carbon homologation could now be performed. This was achieved using benzyl(triphenylphosphoranylidene)acetate in a Wittig reaction, which proceeds by an initial [2+2] cycloaddition of the ylide the carbonyl compound, as shown in **Scheme 15**.[372] In this specific reaction, the ylide is adjacent to an electron-withdrawing ester and is therefore stabilised. A subsequent ring opening, driven by the formation of the byproduct triphenylphosphine oxide, results in the formation of a predominantly (*E*)-alkene.

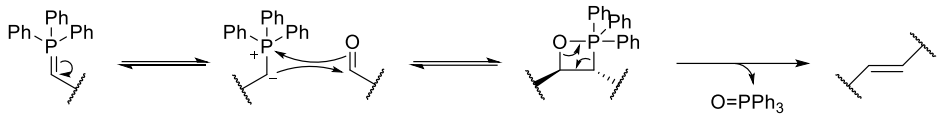

Scheme 15: Mechanism of the Wittig reaction.

Ascertaining reaction completion proved difficult, as aldehyde **104** does not stain well on TLC plates, even with the typical stain for aldehydes, dinitrophenylhydrazine. Consequently, analysis of the product by NMR following work-up of the reaction revealed that a small amount of aldehyde **104** was still unreacted. Moreover, the NMR spectrum of the crude product revealed that the Wittig reaction had exclusively produced the (*E*)-alkene, as evidenced by the two doublets in the alkene region at δ 6.86 and 5.70. Analysis of the NOESY spectrum did not indicate a correlation between these two signals, confirming that the (*E*)-isomer was the sole product. Purification of the mixture was therefore attempted, which gratifyingly removed triphenylphosphine oxide from the mixture. However, co-elution of aldehyde **104** and ester **105** was observed, so further purification was not attempted at this stage. Therefore, the material was telescoped to the next step.

Since the ester **105** contained both an alkene and benzyl group, a Pd-catalysed hydrogenation was highly convenient, facilitating a global deprotection in removing both groups. This hydrogenation proceeded cleanly to furnish the desired acid **106** (**Scheme 16**). Gratifyingly, the polarity difference between the carboxylic acid **106** and the unreacted aldehyde **104** from the previous step was large enough that column chromatography smoothly purified the desired product. With adamantane propanoic acid **106** in hand, attention was then turned to the synthesis of adamantane derivatives.

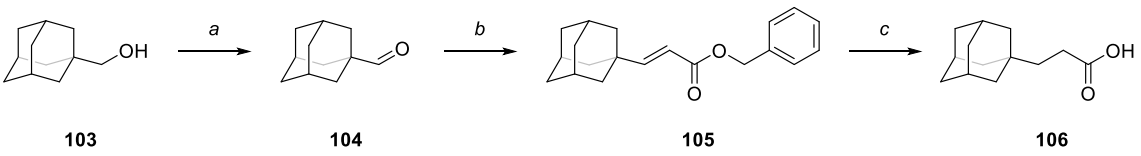

Scheme 16: Synthesis of adamantane propanoic acid **106**. *Reagents and conditions*: (*a*) DMP, CH_2Cl_2, RT, 1 h, 72% yield; (*b*) benzyl(triphosphoranylidene) acetate, PhMe, 110 °C, 16 h; (*c*) H_2, Pd/C, MeOH, RT, 16 h, 38% yield (over 2 steps).

2.9.2. Synthesis of N-acylsulfonamides **87**–**101**

With adamantane propanoic acid in hand, and the other adamantane carboxylic acids obtained from commercial sources, we could now turn our attention to the synthesis of the compounds required for the second iterative reconstruction. Synthesis of *N*-acylsulfonamides

87–**89** was completed using EDC·HCl and DMAP coupling conditions as previously described, affording the desired compounds in moderate to good yields (**Scheme 17**).

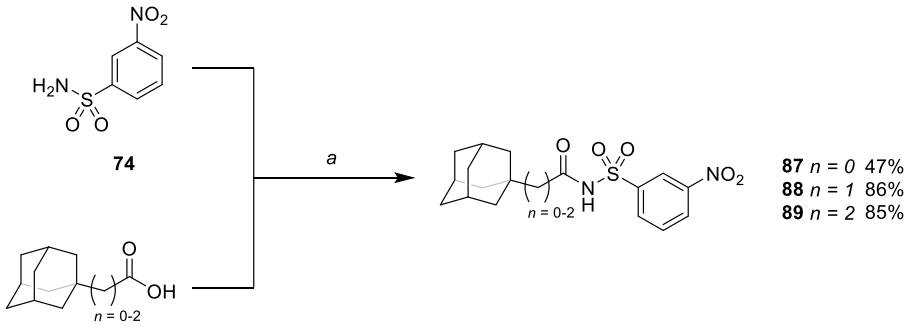

Scheme 17: Synthesis of *N*-acylsulfonamides **87**–**89**. *Reagents and conditions*: (*a*) EDC·HCl, DMAP, CH_2Cl_2, RT, 16 h.

Next, *N*-acylsulfonamides **90**–**92** were prepared by coupling of adamantane carboxylic acids to 4-nitrobenzenesulfonamide **76** using EDC·HCl and DMAP, which proceeded in moderate to excellent yields. This was followed by previously discussed Béchamp reductions (**Scheme 18**), which cleanly afforded the desired products in good yields.

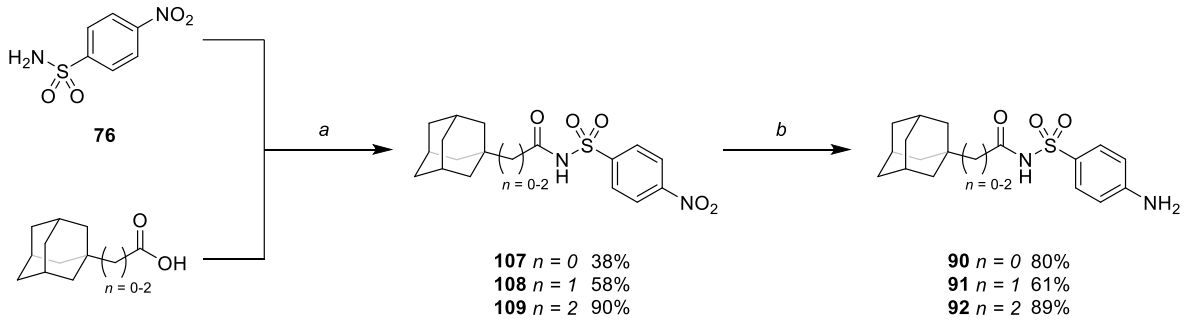

Scheme 18: Synthesis of *N*-acylsulfonamides **90**–**92**. *Reagents and conditions*: (*a*) EDC·HCl, DMAP, CH_2Cl_2, RT, 16 h; (*b*) Fe, NH_4Cl (aq), EtOH, 78 °C, 1 h.

The final stages of the iterative reconstruction of adamantane analogues were completed by first coupling the adamantane carboxylic acids to 4-chloro-3-nitrobenzenesulfonamide **80** with EDC·HCl and DMAP, yielding all sulfonamides in good yield. Nucleophilic aromatic substitutions could then be performed to give the required compounds, as shown in **Scheme 19**. These proceeded in fair to good yields, however purification of some of these was challenging, particularly following substitutions with 2-(phenylthio)ethan-1-amine **86**. Nonetheless, an initial purification by silica gel column chromatography, followed by preparatory TLC successfully isolated the desired compounds.

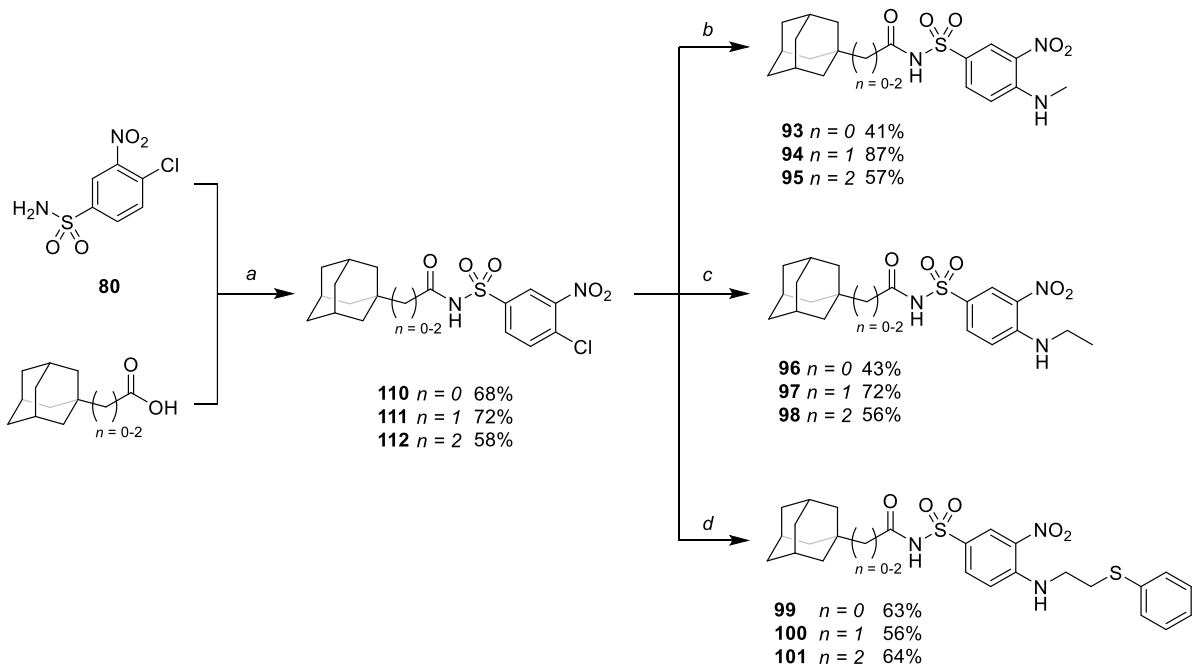

Scheme 19: Synthesis of *N*-acylsulfonamides **93**–**101**. *Reagents and conditions*: (*a*) EDC·HCl, DMAP, CH_2Cl_2, RT, 16 h; (*b*) $MeNH_2$, DMSO, 100 °C, 16 h; (*c*) $EtNH_2$, DMSO, 100 °C, 16 h (*d*) **86**, DMSO, 100 °C, 16 h.

2.10. Biological Evaluation of Adamantane Analogues of **57**

The compounds synthesised in **Chapter 2.9.2.** were evaluated using a TR-FRET assay for BCL-X_L and AlphaScreen® assay for BCL-2, as described in **Chapter 2.6**. Again, these compounds were all tested at a concentration of 10 μM. These results are shown in **Figure 37**, with the previously evaluated ABT-737 (**46**) included as a benchmark.

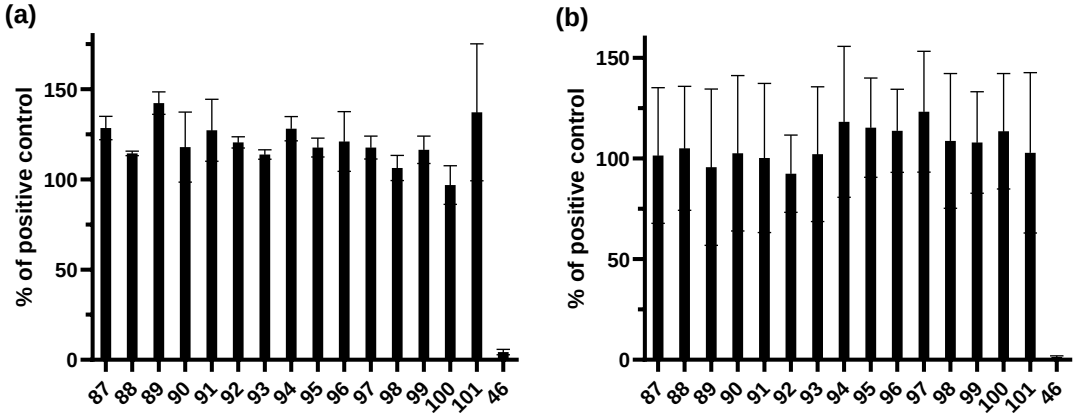

Figure 37: Biological evaluation of compounds **87**–**101**. (*a*) TR-FRET intensity of synthesised compounds as a percentage of positive control; (*b*) AlphaScreen® intensity of synthesised compounds as a percentage of positive control. Data represents mean ± SD, n ≥ 3.

Disappointingly, none of these compounds showed any significant binding against BCL-X_L or BCL-2, despite the results of our docking studies, which indicated that compounds **99**–

101 would possess the highest predicted binding affinity. While the standard deviation is quite large for compound **101** in the TR-FRET assay, and for all compounds analysed in the AlphaScreen®, this was not considered significant enough to warrant further investigation into SAR. Not only do these results highlight the difficulty in accurately predicting binding using computational models, but unfortunately it also demonstrates that our iterative reconstruction approach has not yielded any new senolytic drug candidates.

2.11. Summary and Concluding Remarks

This chapter has focused on the identification of highly potent inhibitors of BCL-X_L and efforts in synthesis, characterisation, and *in vitro* assessment of derivatives of such molecules. Indeed, the iterative reconstruction approach demonstrated how a much smaller, biologically inactive fragment could be built up to a larger molecule that has shown promising results in literature.[334] Unfortunately, none of these compounds displayed any binding affinity to the target protein. Subsequently, docking studies suggested that replacing the 4-fluorobiphenyl moiety of these compounds could prove more potent in binding. Thus, we embarked on preparing and characterising these analogues for their biological evaluation in the same way. However, these also showed none of the desired biological activity.

The iterative reconstruction approach for identifying new biologically active scaffolds failed, in this case, to provide useful leads for further optimisation. Nonetheless, the lead compound **57** was completely deconstructed and a thorough exploration of this compound was accomplished. As this study was unable to generate new insights into inhibitors of SCAPs, we were encouraged to consider other techniques in medicinal chemistry to discover new senolytic chemotypes. Consequently, **Chapter 3** and **Chapter 4** begin to apply some of the lessons learned in this chapter in demonstrating other methods of hit identification.

This Page Intentionally Left Blank

This Page Intentionally Left Blank

Chapter 3

Scaffold Hopping of Known BCL-X_L Inhibitors

Chapter 3 – Scaffold Hopping of Known BCL-X_L Inhibitors

3.1. Introductory Remarks

Given the disappointing biological results of the compounds synthesised in **Chapter 2**, we instead considered other methods to explore new senolytic chemotypes. Indeed, many methods exist for the identification of new pharmacophores and chemical motifs that offer biological activity against a specific target. Examples of these are the previously discussed iterative reconstruction approach, high-throughput screening (HTS), rational design using SAR information and scaffold hopping. Of these, scaffold hopping presents an interesting approach to drug discovery, which refers to a variety of bioisosteric replacement strategies.[373] These often use computational aids to search for new core structures, a topic of significant interest in medicinal chemistry.[374] A more detailed overview of scaffold hopping and its benefits is provided in **Chapter 3.4.**

3.2. Choosing Lead Compounds

As we were unable to observe the reported binding affinity between **57** and BCL-X_L, we instead searched for a new lead molecule with high potency against the BCL-2 family. This led us to developmental work performed by Lessene and co-workers at the Walter and Eliza Hall Institute (WEHI), who performed HTS of 100,000 compounds[374] against BCL-W, a member of the BCL-2 family. Importantly, this screen also identified and disregarded structures that were known to be pan-assay interference compounds (PAINs). Subsequently, the hits of this screen were further validated based on their ability to disrupt protein-protein interactions (PPIs) between BCL-X_L or MCL-1 and BIM, a BH3-only protein. This PPI is known to have an anti-apoptotic effect, as discussed in **Chapter 1.4.4.5.** The authors' investigations led to the identification of **113** as a lead molecule.[375] Minor modifications to the structure were performed by synthesising analogues of **113**, including deletion of the methyl group on the terminal phenyl ring and the installation of a methyl group on the hydrazone carbon. These changes validated the screening results and began to probe SAR, revealing **114**–**116** as a more potent inhibitors of BCL-X_L (**Figure 38**).

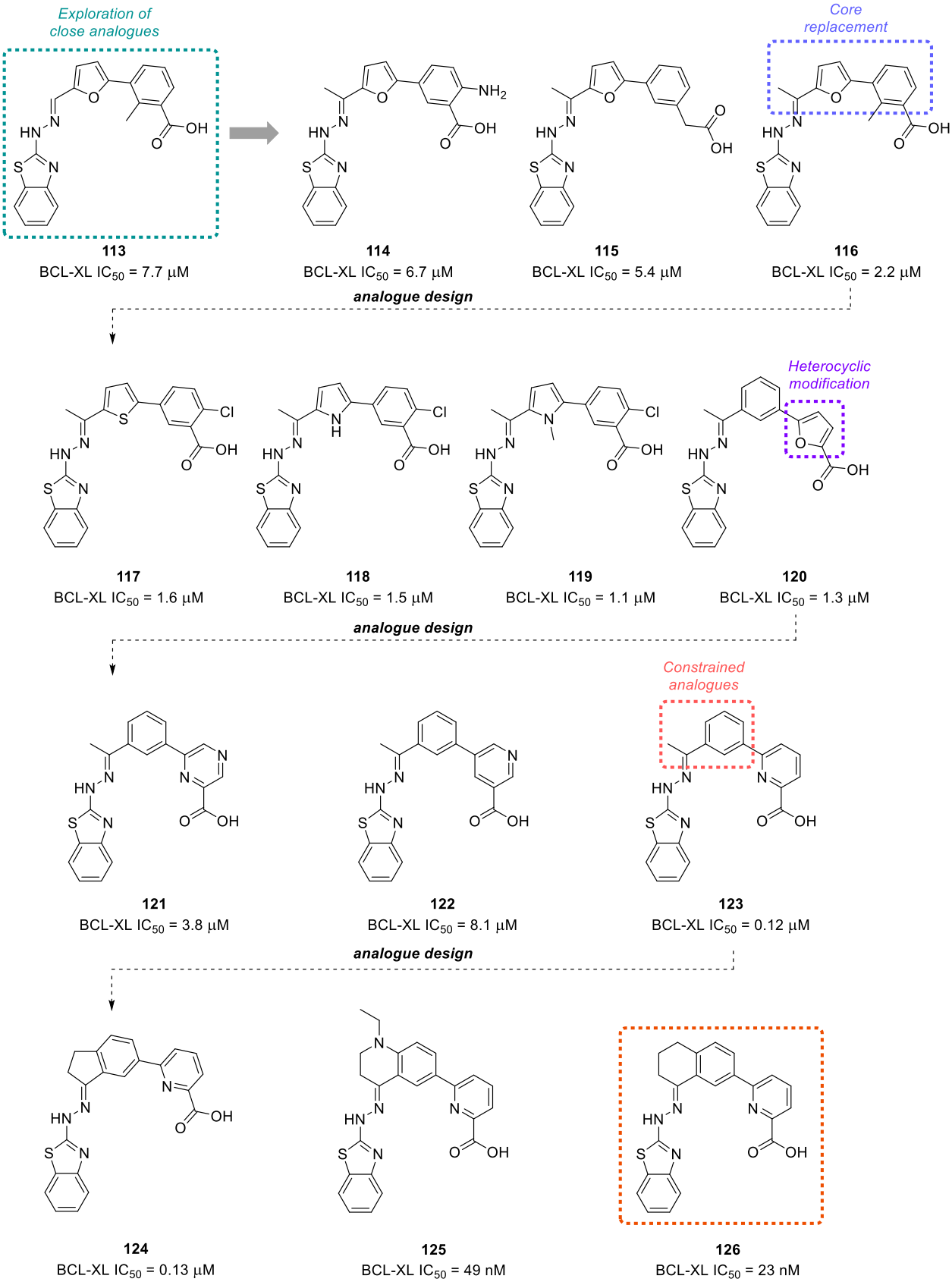

Figure 38: Developmental work performed by WEHI in the design of BCL-X_L inhibitors **113**–**126**.[376]

To continue improving potency at the target, the authors subsequently focused efforts on optimisation of the core of the molecule, highlighted in **blue** in **Figure 38**. This work demonstrated that the furan core, which is a known metabolic liability,[377] could be replaced by other ring structures such as in **117**–**120** with high tolerance. It was also shown that heterocyclic replacement of the terminal ring (highlighted in **purple**) also improved potency, but crucially, the position of the heteroatom dramatically affects potency. In this case, a picolinic acid derivative **123** gave nanomolar potency while the nicotinic acid derivative **122** returned potency to micromolar levels. Finally, constraining the molecule (highlighted in **red**) with a bicyclic core also resulted in high potency while simultaneously locking the conformation of the molecule, as demonstrated in **124**–**126**. Together, these SAR studies resulted in a molecule with a greatly improved IC_{50} of 23 nM. Strong interactions could be seen between **126** and BCL-X_L in a crystal structure (obtained *via* X-ray diffraction) determined by the authors (**Figure 39**). Indeed, hydrogen bonding was observed between the benzothiazole nitrogen and Asp107; the hydrazone nitrogen and Ser106; and the carboxylic acid and Arg139 and Asn136.

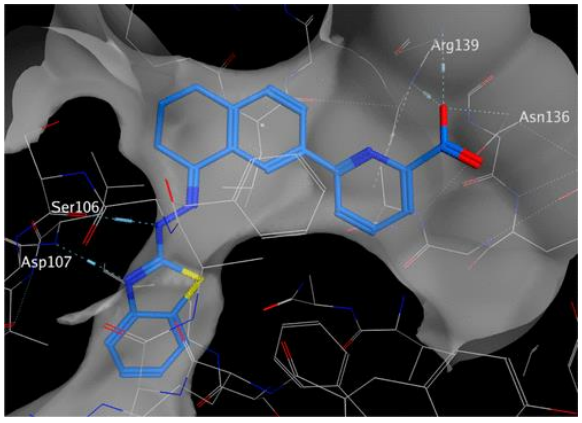

Figure 39: X-ray crystal structure of **126** bound to BCL-X_L at a resolution of 2.3 Å. Hydrogen bonds to Asp107, Ser106, Arg139 and Asn136 are indicated with dashed lines. Reprinted with permission from *ACS Med. Chem. Lett.* 2014, 5, 6, 662–667.[378] Copyright 2014 American Chemical Society.

The authors' work presented the continued exploration of this chemotype for the improvement of drug-like properties. This was done as the *in vivo* hydrolysis of the hydrazone in **126** could potentially release toxic 2-hydrazinylbenzothiazole upon exposure to water.[378] The replacement of the 1,2,3,4-tetrahydronaphthalene core with a 1,2,3,4-tetrahydroisoquinoline, and the hydrazone linker with an amide, culminated with the inhibitor **127** (**Figure 40**), which had a slightly lower potency (IC_{50} = 91 nM) but was still of great interest in our search for lead molecules due to its similar features to the aforementioned **126**. Informed by these data, both **126** and **127** were selected as lead compounds for investigation in this chapter.

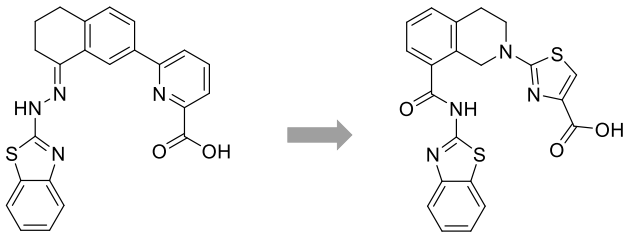

126
BCL-XL IC_{50} = 23 nM

127
BCL-XL IC_{50} = 91 nM

Figure 40: A structure-guided rescaffolding of **126** gave the BCL-X_L inhibitor **127**, both of which were selected as lead molecules for exploration in this chapter.[378]

3.3. Chapter Aims

This chapter focuses on the scaffold hopping of the known BCL-X_L inhibitors **126** and **127**. We first provide a broad overview to scaffold hopping and the processes used in this work to explore bioisosteric replacements of structural features in **126** and **127**. The diversification of **126** and **127**, using Cresset's Spark™ software, provided several novel target molecules, which were subsequently synthesised to explore their biological activity.

3.4. Overview of Scaffold Hopping

Scaffold hopping, also known as lead hopping, is relatively young as a concept, but has been applied in various forms since the infancy of drug discovery programs.[379] It has been found to be a particularly powerful tool in modern drug discovery: while many biologically active compounds have been identified through HTS or virtual screening (VS), such strategies have begun to lose efficiency and economic viability, as these compounds are already optimised for different targets.[380] This is especially true when considering that many therapeutic targets are not new, and therefore exploration of novel chemotypes is based on known ligands. As such, scaffold hopping attempts to jumpstart drug discovery programs by replacing functional groups or chemical motifs with other structures that possess similar electrostatic and physical properties. Such a methodology has been used to remarkable effect in drug discovery programs, resulting in significant savings over the cost of a drug discovery program.[373, 381, 382] Once new bioactive chemotypes have been identified, further scaffold hopping may be undertaken to generate molecules that bear little resemblance to the original candidate. The technique is employed for various purposes: increasing potency; eliminating toxicity; acquiring novel chemical space to navigate intellectual property restrictions; and many more.[383] Consequentially, the new molecule may possess different molecular shape or size; electrostatic

properties; polarity; pK_a; dipole moment; or polarizability, which may be beneficial or detrimental to the needs of a medicinal chemistry program.[383]

It should be noted however, that no precise definition for 'scaffold hopping' is universally agreed on. Indeed, the term has been used ambiguously throughout the vast array of literature that has applied such a method. While the purpose of scaffold hopping is to focus on the replacement of larger structural motifs within a molecule, it is indeed still a topic of debate as to how large these fragments should be, and the difference between 'scaffold hopping' and bioisosteric replacement. Although the concept of novel chemical motifs is common, the question remains: how different from their parent molecule must the derivative be to be considered a 'scaffold hop'? To address this query, Sun and co-workers have identified four major classifications of scaffold hopping, based on the structural changes elicited in the newly designed molecules.[380] These are summarised in **Table 4**.

Table 4: Summary of scaffold hopping classification

Classification	General description
Primary (1°)	Heterocyclic replacement
Secondary (2°)	Ring opening or closure
Tertiary (3°)	Pseudopeptide or peptidomimetic replacement
Quaternary (4°)	Topology- or shape-based scaffold hopping

3.4.2. 1° Scaffold Hopping: Heterocyclic Replacement

1° scaffold hopping therefore aims to vary ring structures to improve bioactivity or some other physicochemical property. This is aptly demonstrated in the replacement of the phenyl ring in cannabinoid 2 receptor (CB_2R) inhibitor **128** with a spirocyclopropane piperidine in **129** (**Figure 41**).[384] Not only did this maintain potency at CB_2R, but also improved drug-likeness by lowering log *P* from 2.81 to 1.48.[385, 386]

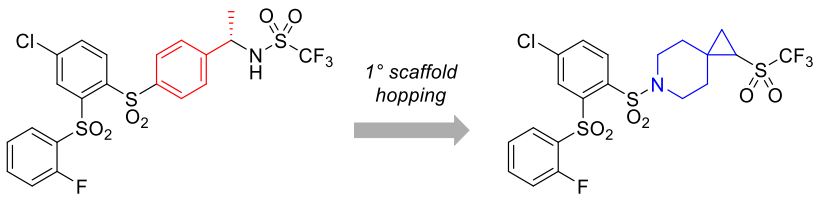

128 **129**

Figure 41: 1° scaffold hopping employed by Merck to improve lipophilicity of CB_2 receptor **128**.[384]

3.4.1. 2° Scaffold Hopping: Ring Opening or Closure

The flexibility of a molecule has a significant effect on the entropic component of binding free energy, in addition to membrane permeability and absorption.[387] 2° scaffold hopping aims to open or close ring structures in a lead molecule, changing the number of freely rotatable bonds. An example of ring closure is shown in **Figure 42** (*a*), wherein researchers from GlaxoSmithKline formed a 5-membered ring in the indole analogue **131**. The molecule was thereby locked into a bioactive conformation, which maintained sub-nanomolar activity in functional assays.[388] A ring-opening strategy is demonstrated in Furet and co-workers' study of the tyrosine kinase inhibitor **132** (**Figure 42** (*b*)), where the urea derivative **133** was synthesised by opening the pyrimidone ring and modifying the position of the pyrimidine nitrogen.[389] This continued to exhibit sub-micromolar inhibition against the target, while also decreasing the compound's log *P*.[385]

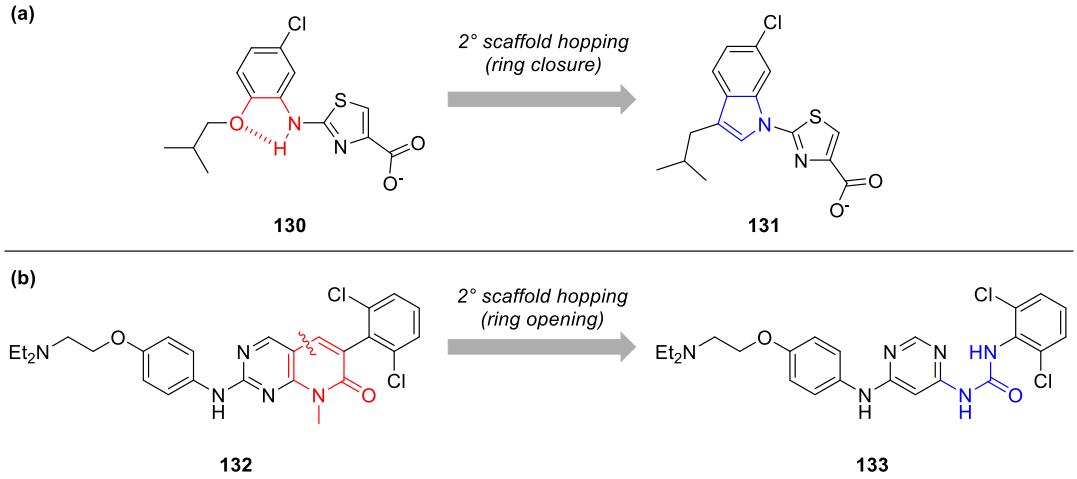

Figure 42: (*a*) a ring closure strategy was employed on **130** to form the indole analogue **131**;[388] (*b*) a ring opening strategy on the pyrimidone of **132** was used to generate the urea derivative **133**.[389]

3.4.3. 3° Scaffold Hopping: Pseudopeptide or Peptidomimetic Replacement

The development of peptides as drug molecules is severely limited due to their metabolic instability and poor bioavailability.[390] 3° scaffold hopping aims to reduces peptidic characteristics that lead to proteolysis while maintaining the 3-dimensional shapes required in PPIs, such as α-helices and β-sheets. To this end, Rosenström and co-workers modified the octapeptide hormone angiotensin II (**134**, amino acid sequence DRVYIHPF) to introduce a benzodiazepine motif in **135**, replacing the tyrosine and isoleucine residues (**Figure 43**). This maintained high binding affinities at the angiotensin 1 and 2 receptors (AT_1 and AT_2 respectively) while also increased metabolic stability.[391]

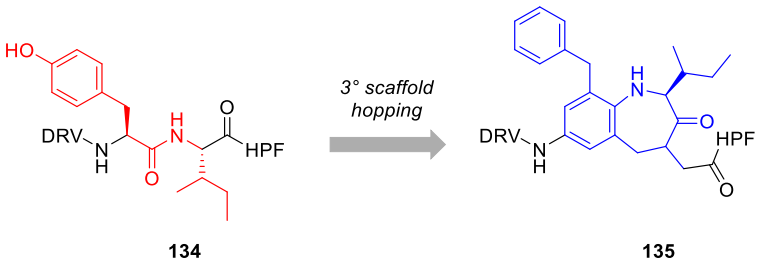

Figure 43: 3° scaffold hopping was utilised on angiotensin II **134** by replacing tyrosine and isoleucine residues with a benzodiazepine motif in **135**.[391]

3.4.4. 4° Scaffold Hopping: Topology- or Shape-based Scaffold Hopping

4° scaffold hopping introduces large changes to lead molecules based on their topology and shape. Such methods are rare in the literature, as they represent an ambitious attempt to explore chemotypes that are significantly different to the original candidate, but nonetheless retain a similar level of biological activity. A successful example of this is shown in **Figure 44**, wherein Amgen researchers performed scaffold hopping on the glycine receptor (GlyR) positive modulator **136**. The tricyclic motif proved potent against GlyR,[392] however further diversification was challenging due to the complexity of the ring system, particularly due to its optical activity. 4° scaffold hopping revealed the simplified analogue **137**, containing an azetidine ring, retained potency while also displaying a desirable physicochemical profile.[393]

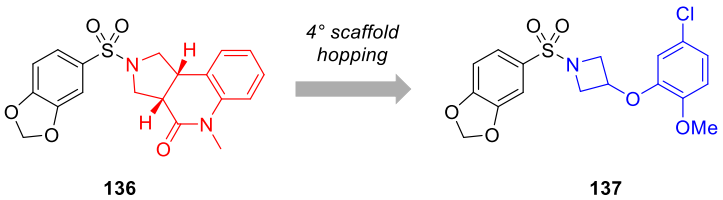

Figure 44: 4° scaffold hopping of GlyR positive modulator **136** dramatically modified its structure to give **137**.[393]

Each classification of scaffold hopping has associated advantages and disadvantages but is nonetheless a powerful tool available to the medicinal chemist for structure diversification. Fundamentally, a biological target is not simply affected by an empirical structure, but activity is instead caused by intermolecular interactions that occur between a ligand and the target. Thus, structural modification to a known ligand is to be encouraged in the hope of generating different and novel bioactive chemotypes. The work presented in this chapter applies 4° scaffold hopping to the aforementioned lead compounds **126** and **127** in an attempt to realise new senolytic chemotypes.

3.5. In Silico Scaffold Hopping Experiments and Docking Validation

Scaffold hopping was performed on the BCL-X_L inhibitors **126** and **127** using Cresset's Spark software,[394, 395] which has been successfully used previously to identify biologically active ligands for a variety of targets.[396-399] This software allows the user to select a segment of the molecule, which is then compared to a database of fragments. By minimising electrostatic interactions to single field points,[395] Spark identifies fragments which interact with these single field points and ranks them by their 'bioisostere factor' (BIF). This is indicative of how much better or worse the replacement is than with capping the attachment point to hydrogen. This is then compared with the original molecule used in the scaffold hop to generate a BIF percentage (BIF%). Full experimental details of the procedures used for scaffold hopping are provided in **Chapter 6.6. Figure 45** displays the segments of each of the lead molecules which were input into the Spark software.

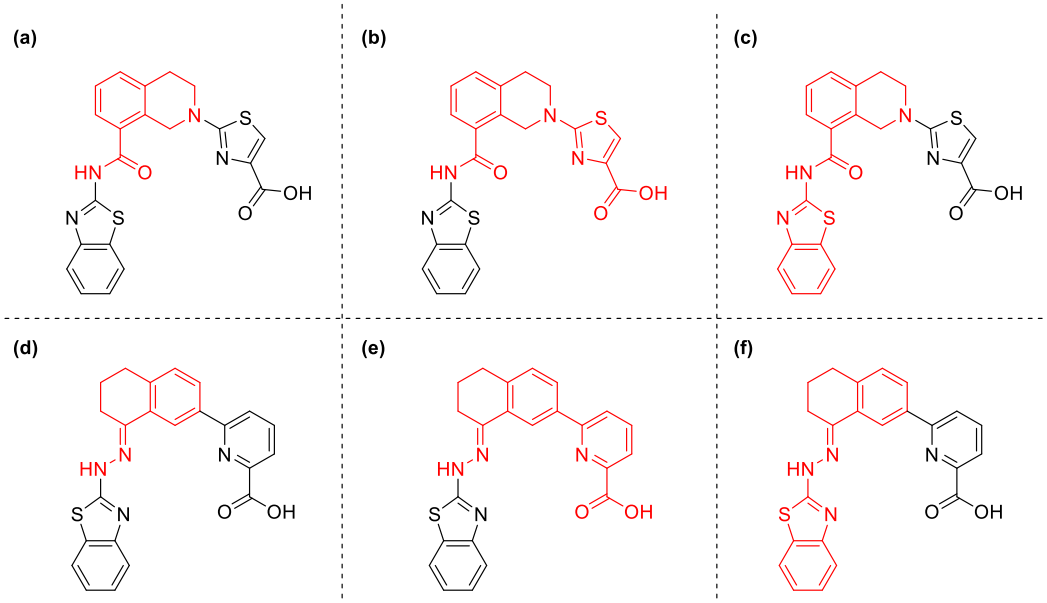

Figure 45: Segments of the lead molecules **126** and **127** (highlighted in **red**) were input into the Spark software to generate bioisosteric replacements. Scaffold hops (*c*), (*e*) and (*f*) did not generate any analogues with BIF% above 80%.

3.5.1. Scaffold Hops Generated by Spark

With the derivatives calculated by Spark, we then excluded any analogues with a BIF% less than 80%, as these would suggest less than 80% similarity to the original leads based on shape and electrostatic fields.[395] The remaining compounds were then carefully examined and selected based on synthetic accessibility. We were interested in a broad selection of compounds with varying molecular weight (MW), Wildman-Crippen partition coefficients (S log *P*),[400] and

topological polar surface area (TPSA). The molecules selected for synthesis are shown in **Table 5**, alongside the lead compounds.

Table 5: Structures, calculated scores and calculated physicochemical properties of lead compounds **126** and **127**, and compounds selected from scaffold hopping. Scores and calculations performed by Spark.[394]

Compound	BIF%[a]	Score[b]	Field Score[c]	Shape Score[d]	MW (g mol^{-1})	S log *P*[e]	TPSA
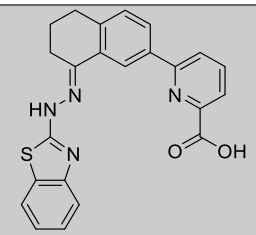 **126**	-	-	-	-	415	5.2	87
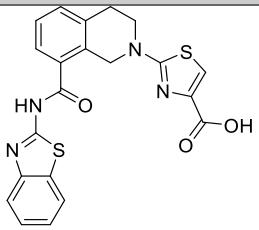 **127**	-	-	-	-	437	4.3	95
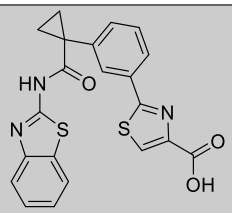 **139**	51	0.866	0.844	0.887	421	4.8	92
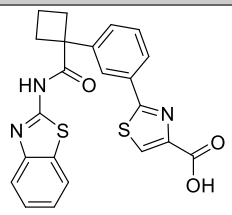 **140**	55	0.876	0.841	0.912	436	5.2	92
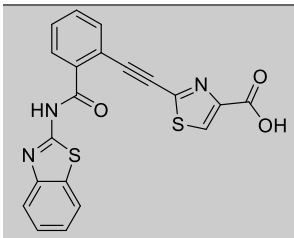 **141**	61	0.892	0.878	0.906	405	4.1	92

Compound	BIF%[a]	Score[b]	Field Score[c]	Shape Score[d]	MW (g mol^{-1})	S log *P*[e]	TPSA
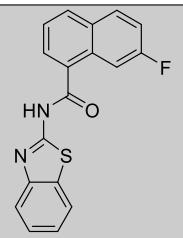 **142**	59	0.840	0.836	0.845	322	5.1	42
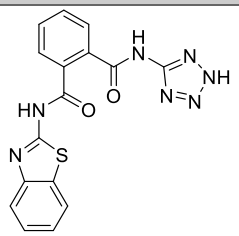 **143**	54	0.818	0.766	0.871	364	2.3	121
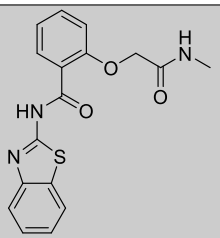 **144**	52	0.812	0.814	0.810	341	3.1	80
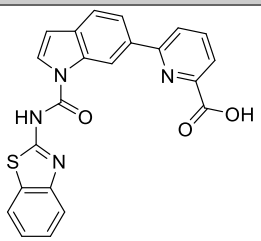 **145**	64	0.918	0.879	0.957	414	4.7	97

[a]Bioisostere factor (BIF) represents how much better or worse a replacement fragment is compared to capping the attachment point with hydrogen. This is expressed as a percentage compared to the BIF of the original lead molecule to give BIF%. [b]Average of field score and shape score. [c]Similarity of the replacement and the original lead molecule based only on field data. [d]Similarity of the replacement and the original lead molecule based only on three-dimensional shape. [e]Wildman-Crippen log *P*.

3-dimensional field point representations of the lead compounds and those generated by Spark are shown in **Figure 46**. These help to illustrate the similarities in shape and electrostatic character. The electrostatic field points shown display consistency across the lead compounds and the analogues generated. Indeed, negative charges (represented by blue spheres) are produced between the benzothiazole and the terminal ring, regardless of the heterocycle present. Moreover, the linking aromatic core elicits both positively charged regions

(represented by red spheres) and hydrophobic interactions (represented by orange spheres), irrespective of the presence of aliphatic, phenyl or bicyclic groups. This offers not only an excellent representation of the success of our scaffold hop, but further highlights the fundamental concept in bioisosteric replacement: that biological activity is not a product of specific atoms or functional groups, but rather the electrostatic interactions between the shape of a molecule and the binding pocket of a target.

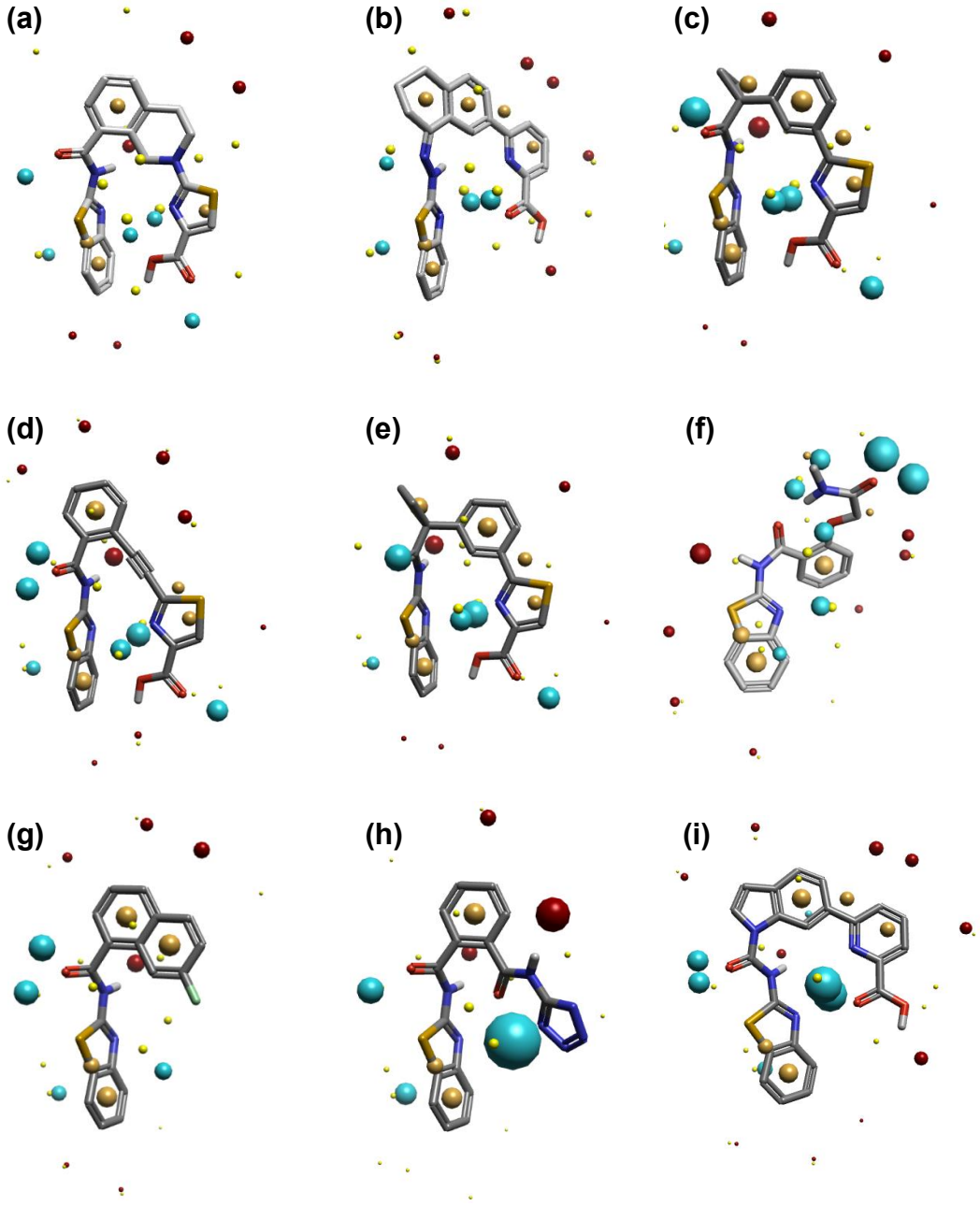

Figure 46: Three-dimensional field point representations of lead compounds **126** and **127** ((*a*) and (*b*), respectively) and compounds generated through scaffold hopping **139–145** ((*c*) to (*k*), respectively). Coloured spheres are representative of electrostatic field points: red = positively charged; blue = negatively charged; yellow = van der Waals interactions; orange = hydrophobic interactions. Generated by Spark software.

3.5.2. Validation by Molecular Docking

We further wished to validate the similarity scores obtained from scaffold hopping by conducting an independent docking study on the lead compounds and those obtained through the Spark software. In a similar manner to the procedure described in **Chapter 2.8.2.**, lead molecules **126**, **127**, and **139**–**145** were docked to the same structure used by the authors in their rescaffolding efforts (PDB: 3ZLN).[378] The Glide scores for this study are shown in **Table 6**.

Table 6: Glide scores for docking study of lead compounds **126**, **127**, and **139**–**145**.

Compound	Glide score (kcal/mol)
126	−9.68
127	−11.24
139	−10.30
140	−11.80
141	−10.31
142	−8.92
143	−7.66
144	−10.14
145	−11.66

Interestingly, the less potent BCL-X_L inhibitor **127** (BCL-X_L IC_{50} = 91 nM) displayed a more negative Glide score than **126** (BCL-X_L IC_{50} = 23 nM), again highlighting potential issues associated with over-reliance on computational data. Analysis of the binding poses demonstrated that in each compound, the benzothiazole nitrogen formed a H-bond with Leu108. Additionally, all compounds containing carboxylic acids formed a network of H-bonds with Asn136 and Arg139. In those without the carboxylic acid, **144** formed a H-bond between the methyl amide carbonyl and Arg139; and the tetrazole of **143** formed a H-bond with Arg139. Moreover, all compounds except **143**, **144** and **142** formed π-π stacking between aromatic rings and Phe105. All these results highlight that the compounds generated *via* use of Spark took on similar binding poses to the lead compounds within the target protein. This suggested that our 4° scaffold hopping had hypothesised compounds which may be excellent binders of BCL-X_L, notably **139**–**141**, **143** and **145**. Although worse binding was predicted for **142** and **143**, we were also interested in these compounds, as less potent observed biological activity would

serve to validate both our scaffold hopping work and docking study, and to provide important information for potential future lead optimisation.

3.6. Synthesis of Lead Compounds and Compound Library

3.6.1. Synthesis of Lead Compounds **126** *and* **127**

To compare the compounds generated through 4° scaffold hopping, it was necessary to prepare the lead compounds known in literature. Hydrazone **126** was synthesised according to literature procedures (**Scheme 20**).[376] The pinacol boronate functionality was installed onto 7-bromo-3,4-dihydronaphthalen-1(2H)-one **146** *via* a Suzuki-Miyaura borylation, affording the pinacol boronate product **147** in poor, but sufficient, yield. The pinacol boronate **147** was then utilised as a coupling partner for a Suzuki coupling with 6-bromopicolinic acid. This reaction used tetrabutylammonium bromide (TBAB), K_2CO_3 and bis(triphenylphosphine)palladium(II) dichloride as a catalyst system and produced ketone **148** in good yield. Through careful adjustment of the pH during work-up, purification by flash column chromatography was avoided in this step. Concurrently, an S_NAr reaction between 2-chlorobenzothiazole **149** and aqueous hydrazine solution readily gave hydrazine **150** in excellent yield. Finally, heating ketone **148** and hydrazine **150** in ethanol afforded the desired hydrazone **126** in poor 30% yield, completing the synthesis. Characterisation data matched that of Sleebs and coworkers, confirming that the specific hydrazone isomer had been formed.[376]

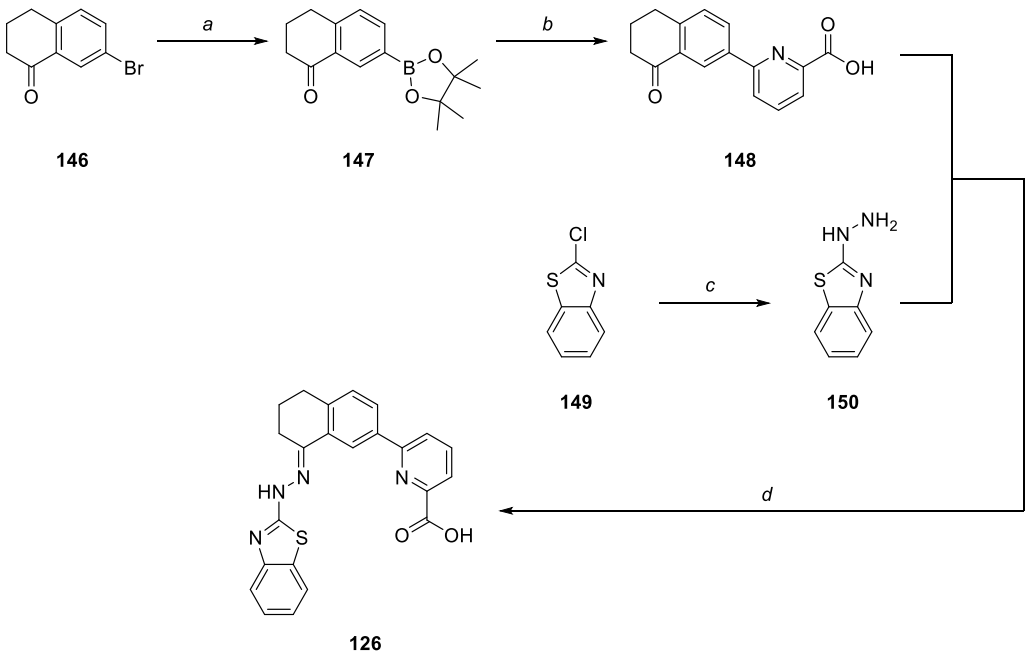

Scheme 20: Synthesis of lead compound **126**. *Reagents and conditions*: (*a*) B_2pin_2, KOAc, $Pd(dppf)Cl_2$, MeOH, 60 °C, 16 h, 25% yield; (*b*) 6-bromopicolinic acid, TBAB, K_2CO_3, $Pd(PPh_3)_2Cl_2$, H_2O, 1,4-dioxane, 100 °C, 1 h, 62% yield; (*c*) 60% aq. N_2H_4, 80 °C, 2 h, 94% yield; (*d*) EtOH, 80 °C, 1 h, 30% yield.

Lead compound **127** was also synthesised according to a modified literature procedure, as shown in **Scheme 21**.[378] Fischer esterification of 2-bromothiazole-5-carboxylic acid **151** gave the corresponding methyl ester **152** in excellent yield.[401] Concurrently, an amide coupling mediated by hexafluorophosphate azabenzotriazole tetramethyluronium (HATU) was conducted between the Boc-protected 1,2,3,4-tetrahydroisoquinoline-8-carboxylic acid **153** and 2-aminobenzothiazole **154**. This produced the desired amide **155** in good yield. Subsequent deprotection of the Boc group yielded the free amine **156** as a hydrochloride salt in quantitative yield. An S_NAr reaction between ester **152** and amine **156** successfully joined these two components together in good yield to give **157**. Finally, hydrolysis of the ester gave the desired lead compound **127** in quantitative yield.

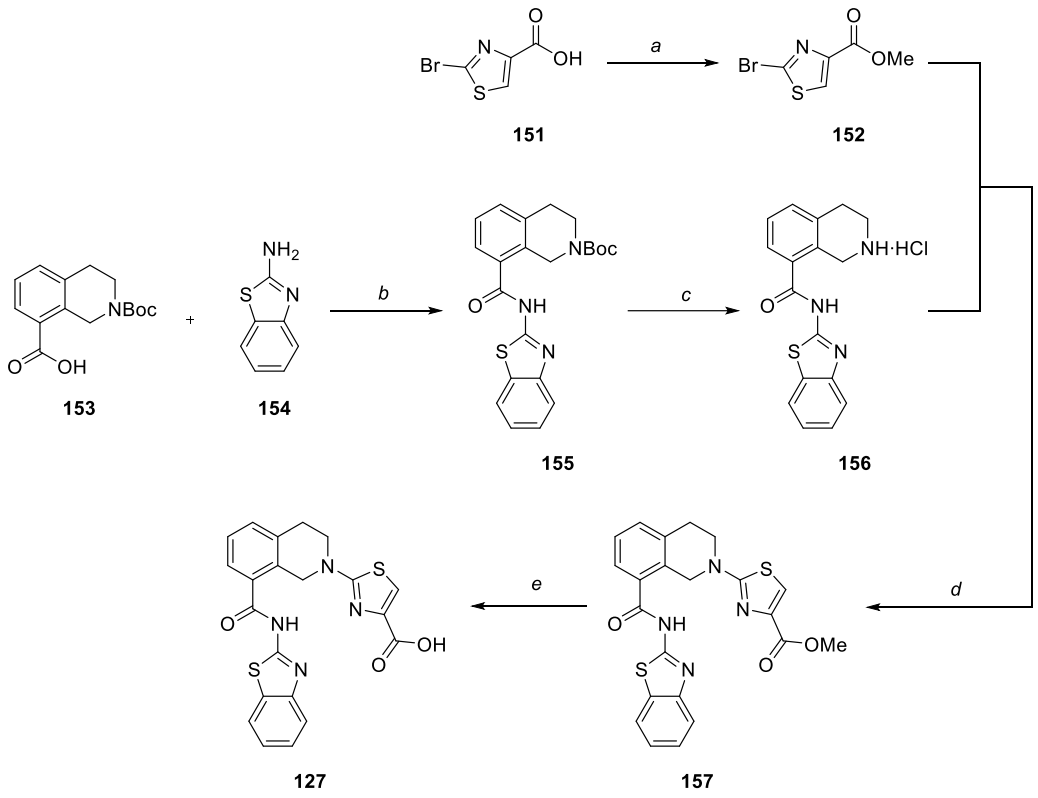

Scheme 21: Synthesis of lead compound **127**. *Reagents and conditions*: (*a*) H_2SO_4, MeOH, 65 °C, 1 h, 89% yield; (*b*) HATU, DIPEA, CH_2Cl_2, RT, 1 h, 71% yield; (*c*) HCl in 1,4-dioxane, CH_2Cl_2, 0 °C to RT, 16 h, 99% yield; (*d*) Cs_2CO_3, DMA, 50 °C, 16 h, 63% yield; (*e*) LiOH, THF, H_2O, RT, 30 min, 99% yield.

3.6.2. Synthesis of Cyclopropane Derivative **139**

A retrosynthetic analysis (**Scheme 22**) envisioned that the cyclopropane derivative **139** could be prepared by a Suzuki coupling of the pinacol boronate **160** and aryl bromide **158**. In turn, the pinacol boronate could be prepared from a borylation of previously synthesised ester **152**, while the aryl bromide could be prepared from commercially available 2-

aminobenzothiazole **154** and acid **159**. The successful borylation of **152** would prove particularly useful, as **160** could also be used for the preparation of cyclobutane derivative **140**.

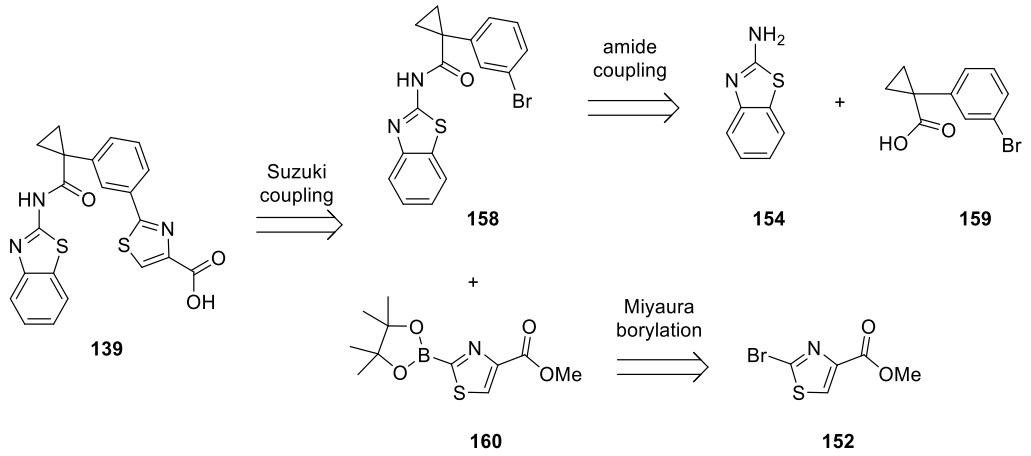

Scheme 22: Retrosynthetic analysis of cyclopropane derivative **139** *via* Suzuki coupling of **158** and **160**. Compound **158** could be prepared from amide coupling of **154** and **159**, while **160** could be obtained *via* Miyaura borylation.

Initial efforts to prepare pinacol boronate **160** focused on a Miyaura borylation (**Scheme 23**). This was first attempted using B_2pin_2, KOAc and Pd(dppf)Cl_2 as a catalyst system, conditions intially developed by Miyaura and co-workers (entry 1, **Table 7**).[402] This failed to yield the product, instead producing a complex mixture which included some proto-dehalogenated material as observed by ESI-MS. Noting the success of other solvents for this transformation, the reaction was also attempted using MeOH, THF and 1,4-dioxane (entries 2–4, **Table 7**), using a pressure tube for MeOH and THF so these could be heated to 80 °C.[403-405] However, these resulted in a similar complex mixture as above, or no reaction at all. Given the failures of these Pd-catalysed borylations, we proposed a Barbier-type reaction by first conducting a halogen-lithium exchange with *n*-butyllithium (*n*-BuLi), followed by quenching a boron reagent. We first attempted this with B_2pin_2 as the quenching reagent (entry 5, **Table 7**), but this also led to a complex reaction mixture, with no trace of the desired product. A final trial was conducted using triisopropyl borate as the quenching reagent (entry 6, **Table 7**), but this also provided a complex reaction mixture. Issues with these reaction indicated that thiazole **152** would prove to be a poor coupling partner in Pd-catalysed coupling reactions, possibly due to co-ordination between the soft heteroatomic sulfur and the soft Pd^{2+} centre of the catalyst. Consequently, we explored alternative methods to form the biaryl bond of **139**.

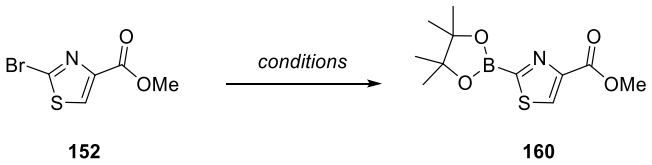

152 160

Scheme 23: Attempted synthesis of pinacol boronate **160**. For conditions, see **Table 7**.

Table 7: Attempted synthesis of pinacol boronate **160**.

Entry	Reagents	Solvent	Temperature & Time	Result
1	B_2pin_2, KOAc, Pd(dppf)	DMSO	80 °C, 16 h	CRM[a]
2	B_2pin_2, KOAc, Pd(dppf)	MeOH	80 °C, 16 h	No reaction
3	B_2pin_2, KOAc, Pd(dppf)	THF	80 °C, 16 h	No reaction
4	B_2pin_2, KOAc, Pd(dppf)	1,4-dioxane	80 °C, 16 h	CRM[a]
5	*n*-BuLi, then B_2pin_2	THF	−78 °C, 1 h	CRM[a]
6	*n*-BuLi, then B(*i*-PrO)$_3$	THF	−78 °C, 1 h	CRM[a]

[a]Complex reaction mixture

We therefore modified our retrosynthetic analysis to swap the coupling partners for the final Suzuki coupling, such that the pinacol boronate **162** could be obtained from aryl bromide **158** (**Scheme 24**).

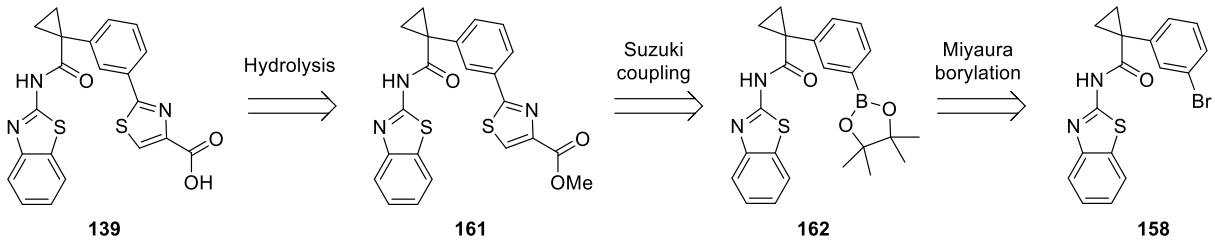

139 161 162 158

Scheme 24: Revised retrosynthesis of cyclopropane derivative **139**.

Our synthetic route began with HATU-mediated amide coupling of 2-aminobenzothiazole **154** and 1-(3-bromophenyl)cyclopropane-1-carboxylic acid **159**, which furnished the desired amide **158** in good yield. A Miyaura borylation was then undertaken to prepare the required pinacol boronate. Optimisation of this procedure identified that the use of DMF as the solvent and heating this reaction at 100 °C for 16 h resulted in complete conversion of the starting material into the desired product **162** with acceptable yield. The following Suzuki coupling of **162** and ester **152** was challenging, further highlighting the poor coupling ability of the thiazole. A mixture of products was formed, including some of ester **152** that was proto-dehalogenated, as was previously observed in unsuccessful borylations. Nonetheless, this

afforded **161** in poor but sufficient yield to continue. Finally, an ester hydrolysis produced **139** in quantitative yield to complete the synthesis (**Scheme 25**).

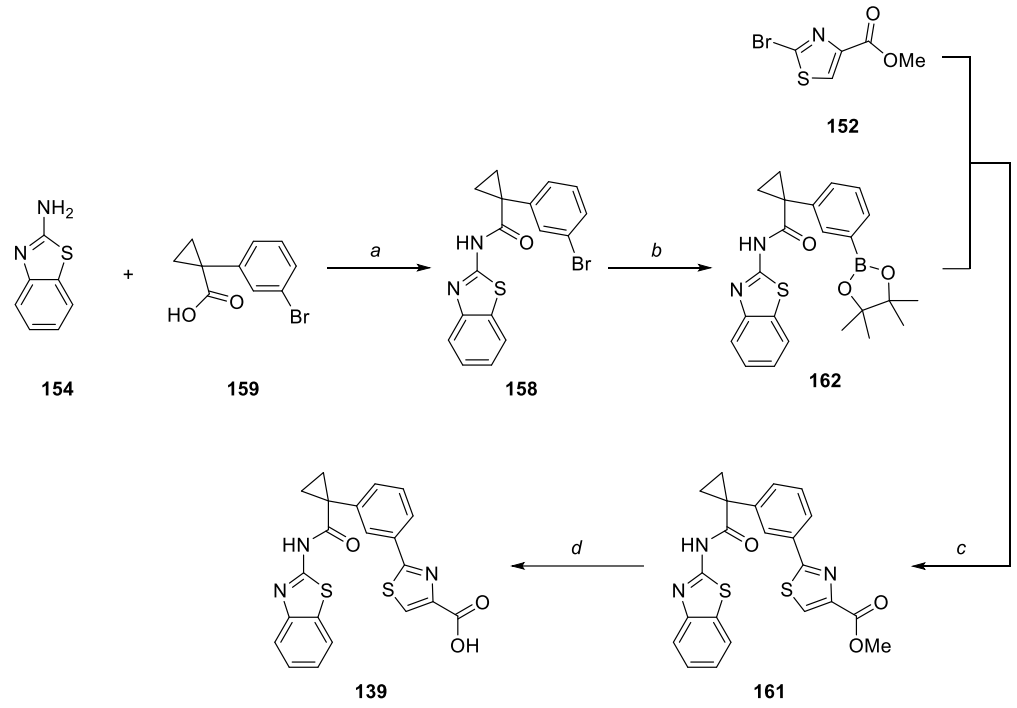

Scheme 25: Synthesis of cyclopropane derivative **139**. *Reagents and conditions*: (*a*) HATU, DIPEA, CH_2Cl_2, RT, 1 h, 83% yield; (*b*) B_2pin_2, KOAc, $Pd(dppf)Cl_2$, DMF, 100 °C, 16 h, 75% yield; (*c*) Na_2CO_3, $Pd(PPh_3)_4$, H_2O, 1,4-dioxane, 80 °C, 16 h, 12% yield; (*d*) LiOH, THF, H_2O, RT, 30 min, 99% yield.

3.6.3. Synthesis of Cyclobutane Derivative **140**

In a similar manner to **139**, retrosynthetic analysis of cyclobutene derivative **140** revealed that it could be made *via* a Suzuki coupling of the pinacol boronate **163** and ester **152**. The pinacol boronate, in turn, could be synthesised from the aryl bromide **164**, which we anticipated could be prepared from 2-aminobenzothiazole **154** and acid **165** (**Scheme 26**).

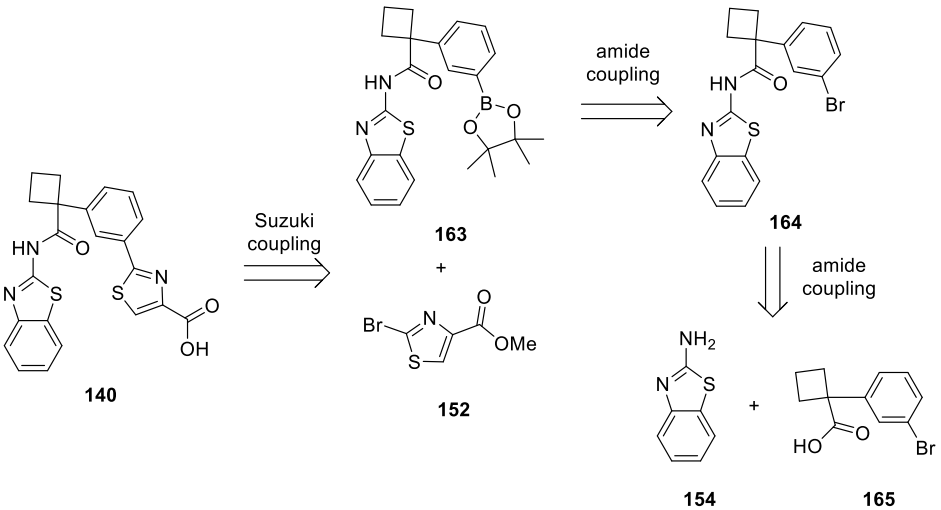

Scheme 26: Retrosynthesis of cyclobutane derivative **140**.

As acid **165** was not commercially available, it was synthesised from 2-(3-bromophenyl)acetonitrile **166**. This was first treated with 2 equivalents of NaH, before 1,3-dibromopropane was added to install the cyclobutane ring *via* two consecutive S_N2 reactions, which yielded nitrile **167** in fair yields. Nitrile **167** was subsequently hydrolysed cleanly to afford the desired acid **165**. An amide coupling between acid **165** and 2-aminobenzothiazole **154** gave amide **164** in good yield. Miyaura borylation of amide **164** furnished pinacol boronate **163** in fair yield, which was ready for the attempted Suzuki coupling (**Scheme 27**).

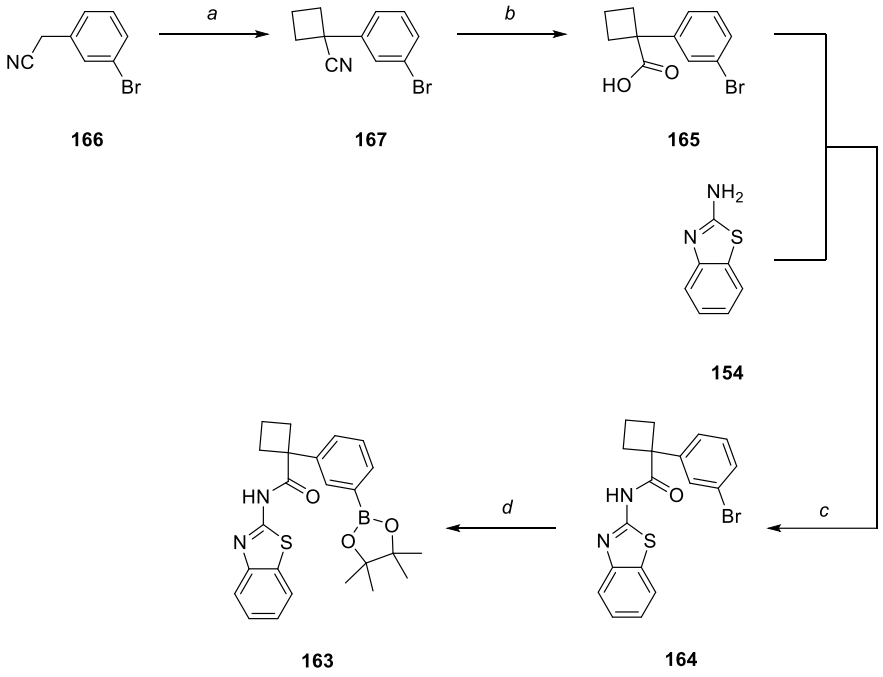

Scheme 27: Synthesis of pinacol boronate **163**. *Reagents and conditions*: (*a*) NaH, DMF, 30 min, RT, then 1,3-dibromopropane, 0 °C to RT, 16 h, 46% yield; (*b*) KOH, EtOH, H_2O, reflux, 16 h, 79% yield; (*c*) HATU, DIPEA, CH_2Cl_2, RT, 1 h, 80% yield; (*d*) B_2pin_2, KOAc, Pd(dppf)Cl_2, DMF, 100 °C, 16 h, 62% yield.

Given the low-yielding Suzuki coupling to synthesise ester **161**, it was unsurprising that the analogous preparation of ester **166** from pinacol boronate **163** and ester **152** was especially difficult (**Scheme 28**). The Suzuki conditions used to synthesise **161** were initially attempted (entry 1, **Table 8**) but this failed to yield the product and instead gave a complex reaction mixture, with some protodeborylation observed. We therefore trialled variations of catalyst systems (entries 2, 4 and 6, **Table 8**), solvents (entries 7–9, **Table 8**), and the addition of TBAB as a phase transfer catalyst (entries 3, 5 and 7, **Table 8**). While most of these attempts continued to produce complex mixtures, a trace amount of the desired product **166** was observed *via* ESI-MS (*m/z* = 472, $[M+Na]^+$) in entry 6, **Table 8**. However, attempted optimisation of this procedure did not afford greater than trace yields.

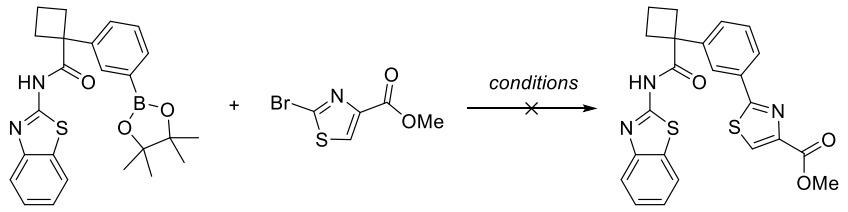

163 152 166

Scheme 28: Attempted Suzuki coupling of pinacol boronate **163** and ester **152**. For conditions, see **Table 8**.

Table 8: Attempted optimisation of reaction conditions for the synthesis of **166**.

Entry	Reagents	Solvent	Result
1	Na_2CO_3, $Pd(PPh_3)_4$	1,4-dioxane/H_2O	CRM[a]
2	Na_2CO_3, $Pd(PPh_3)_2Cl_2$	1,4-dioxane/H_2O	CRM
3	TBAB, Na_2CO_3, $Pd(PPh_3)_2Cl_2$	1,4-dioxane/H_2O	CRM
4	Na_2CO_3, $Pd(OAc)_2$, SPhos	1,4-dioxane/H_2O	CRM
5	TBAB, Na_2CO_3, $Pd(OAc)_2$, SPhos	1,4-dioxane/H_2O	CRM
6	Na_2CO_3, $Pd(OAc)_2$, XPhos	1,4-dioxane/H_2O	CRM, trace **166**
7	TBAB, Na_2CO_3, $Pd(OAc)_2$, XPhos	1,4-dioxane/H_2O	CRM
8	Na_2CO_3, $Pd(OAc)_2$, XPhos	*n*-BuOH[b]	CRM, trace **166**
9	Na_2CO_3, $Pd(OAc)_2$, XPhos	DME[c]	CRM, trace **166**

[a]Complex reaction mixture; [b]*n*-butanol; [c]1,2-dimethoxyethane.

Consequently, we explored other methods of forming the required biaryl bond. A revised retrosynthesis (**Scheme 29**) focused on the construction of the thiazole ring in **168** *via* condensation of thioamide **169** with ethyl glyoxalate. The thioamide, in turn could be prepared from the corresponding nitrile **170**, formed from the already synthesised aryl bromide **164**.

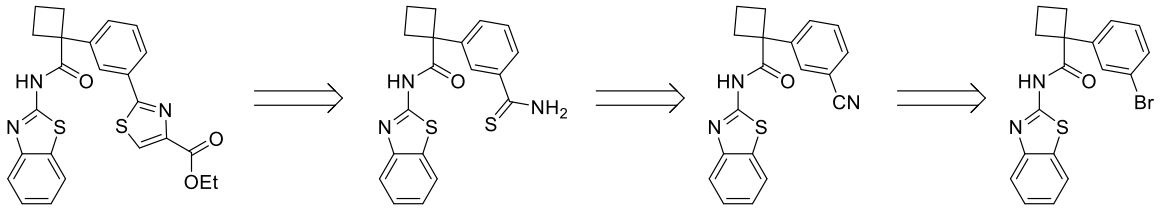

168 169 170 164

Scheme 29: Revised retrosynthesis of cyclobutane derivative precursor **167**, showing the construction of the thioamide ring.

In synthesising the nitrile **170**, we initially wished to avoid using cyanide salts due to serious toxicity concerns. Thus we first attempted a Ni-catalysed cyanation, as shown in

Scheme 30.[406] The mechanism of this reaction (**Scheme 31**) is intriguing: formamide first co-ordinates to the Ni-bpy complex **I**, forming the complex **II**. A series of proton transfers, aided by acac causes complex **VI** to release HCN gas *in situ*. Once generated, a second catalytic cycle which also employs Ni-bpy complex **I** undergoes oxidative addition, ligand exchange and reductive elimination to install the nitrile group. On small scales, this reaction afforded the desired nitrile in good yields of 75%. However, the reaction vessel requires a small headspace, as the high pressure of HCN gas generated forces its dissolution and subsequent reaction. It was found that upscaling of this reaction using a larger vessel was not conducive to efficient dissolution of HCN, furnishing extremely poor conversion of the starting material. As such, an alternative cyanation method was required.

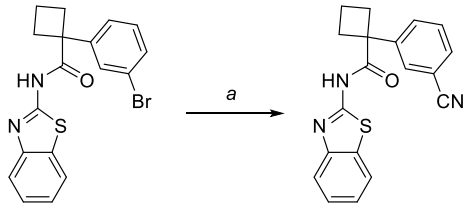

164 **170**

Scheme 30: Synthesis of nitrile **170**. *Reagents and conditions*: $Ni(acac)_2$, $AlCl_3$, 2,2′-bipyridine, ZnO, formamaide, DME, 145 °C, 24 h, 75% yield.

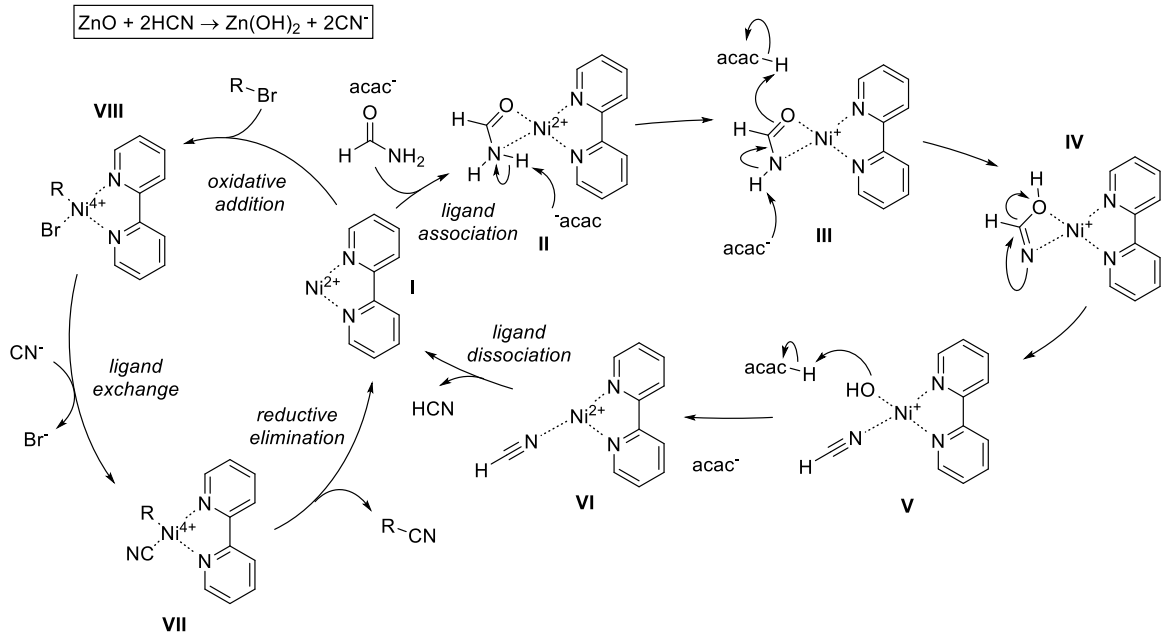

Scheme 31: Mechanism of Ni-catalysed cyanation.

This led us to conduct a Pd-catalysed cyanation, which used $Zn(CN)_2$ (**Scheme 33**). The catalytic cycle of this reaction is shown in **Scheme 32**. Since cyanide is already available in ionic form in this reaction, the mechanism operates *via* oxidative addition to the catalyst **I** to

give complex **II**. A ligand exchange with cyanide gives complex **III**, which finally undergoes reductive elimination to yield the desired nitrile. To safely handle the cyanide salt and any cyanide products during this reaction, the additional precautions were taken by bleaching all tools and vessels used during the procedure. This methodology cleanly furnished the nitrile in excellent yield.

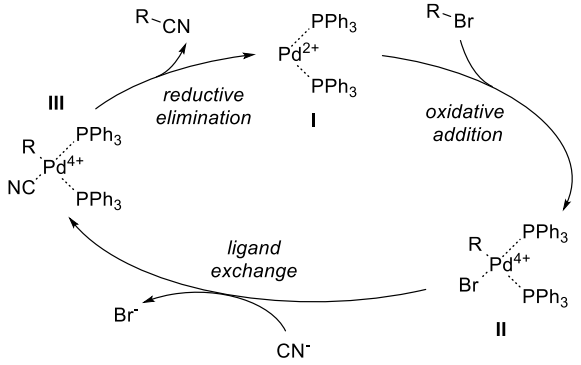

Scheme 32: Mechanism of Pd-catalysed cyanation.

Following this, the nitrile was hydrolysed to the corresponding thioamide **169**.[407] During this reaction, conversion of the starting material stalled, and the addition of more Na_2S did not effect further progression. This produced thioamide **169** in fair yield. A condensation reaction with ethyl bromopyruvate subsequently gave the ethyl ester **168** protected thioamide in good yield,[408] which was then hydrolysed to afford the desired cyclobutane derivative **140** quantitatively.

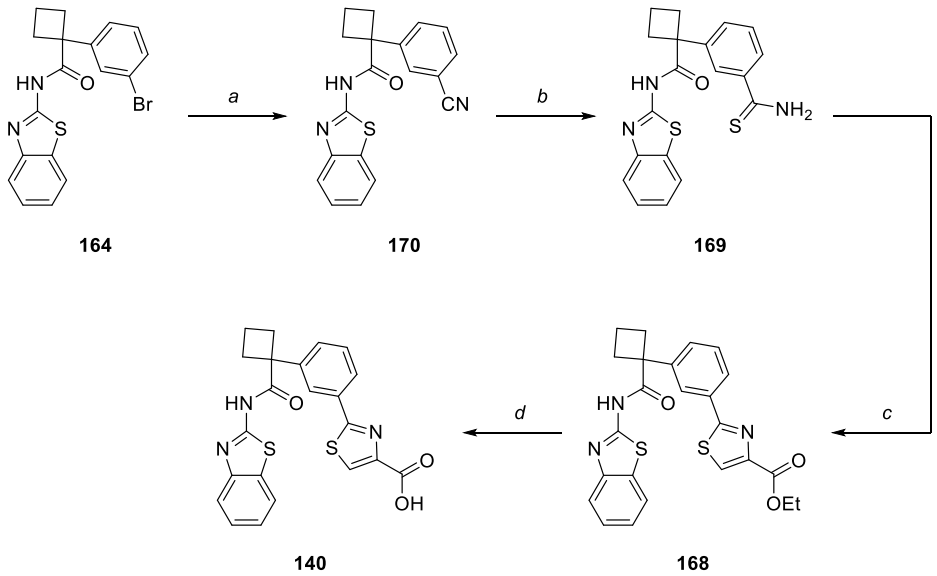

Scheme 33: Synthesis of cyclobutane derivative **140**. *Reagents and conditions*: (*a*) $Zn(CN)_2$, $Pd(PPh_3)_4$, DMF, 100 °C, 2 h, 91% yield; (*b*) $Na_2S{\cdot}9H_2O$, DMF, 130 °C, 2 h, 49% yield; (*c*) ethyl glyoxalate, EtOH, 78 °C, 1 h, 83% yield; (*d*) LiOH, THF, H_2O, RT, 30 min, 99% yield.

3.6.4. Synthesis of Alkyne Derivative **141**

The synthesis of alkyne derivative **141** began with the HATU-mediated amide coupling of 2-aminobenzothiazole **154** and 2-iodobenzoic acid **171**, which afforded amide **172** in moderate yield. A Sonogashira coupling between amide **172** and trimethylsilylacetylene (TMSA) gave the TMS-protected alkyne **173**, albeit in poor 9% yield (**Scheme 34**).

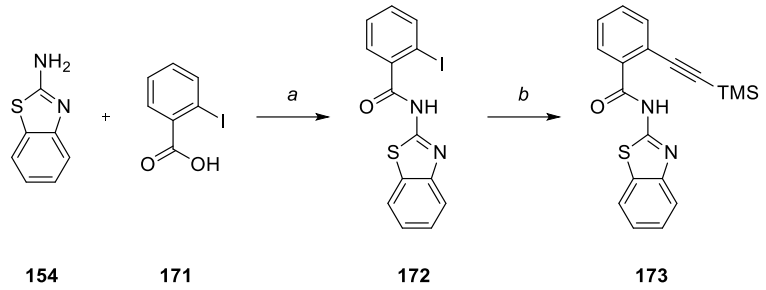

154 **171** **172** **173**

Scheme 34: Synthesis of alkyne **173**. *Reagents and conditions*: (*a*) HATU, DIPEA, CH_2Cl_2, RT, 1 h, 40% yield; (*b*) TMSA, Et_3N, CuI, $Pd(PPh_3)_2Cl_2$, DMF, 30 °C, 1 h, 16% yield.

As a result, we elected to instead install the alkyne on the other coupling partner, ester **152**. This proceeded cleanly in good yields, after which the TMS group was deprotected *via* treatment with tetrabutylammonium fluoride (TBAF). With the free alkyne **175** and aryl iodide **172** in hand, another Sonogashira coupling was used to form the alkyne **176**. Finally, an ester hydrolysis yielded **141** in quantitative yield (**Scheme 35**).

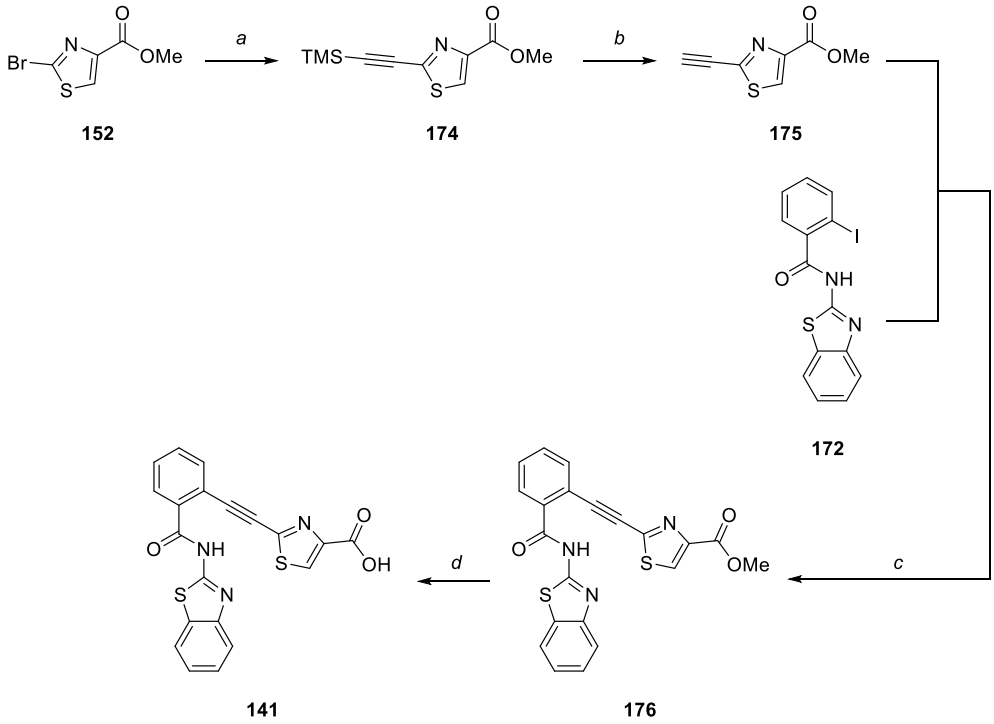

152 **174** **175** **172** **176** **141**

Scheme 35: Synthesis of alkyne derivative **141**. *Reagents and conditions*: (*a*) TMSA, Et_3N, CuI, $Pd(PPh_3)_4$, DMF, 40 °C, 1 h, 68% yield; (*b*) TBAF, THF, RT, 1 h, 92% yield; (*c*) Et_3N, CuI, $Pd(PPh_3)_4$, DMF, 40 °C, 1 h, 24% yield; (*d*) LiOH, THF, H_2O, RT, 30 min, 99% yield.

3.6.5. Synthesis of Naphthalene Derivative **142**

To synthesise naphthalene derivative **142**, 2-fluoronaphthalene **177** was first treated with acetyl chloride (AcCl) and aluminium chloride ($AlCl_3$) in a Friedel-Crafts acylation, which proceeded in moderate yield (**Scheme 36**).[409] This reaction is regioselective for the 7-position of the bicyclic naphthalene core, and NMR data from literature were used to confirm that the correct isomer **178** had been synthesised.[409]

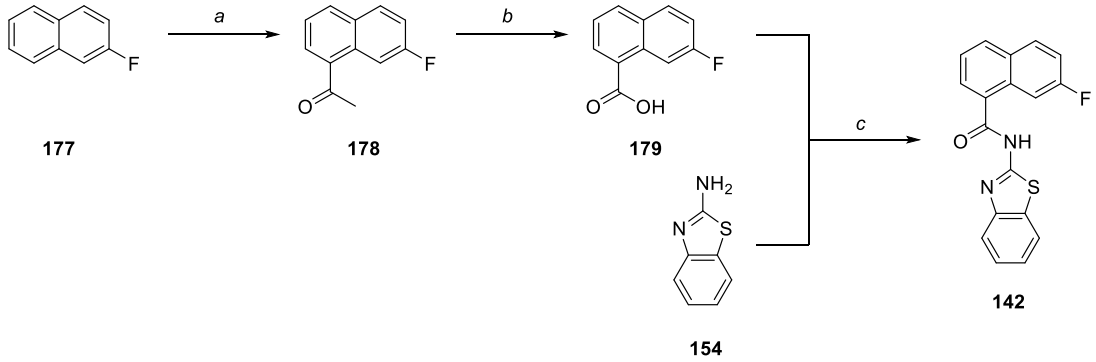

Scheme 36: Synthesis of naphthalene derivative **142**. *Reagents and conditions*: (*a*) AcCl, $AlCl_3$, CH_2Cl_2, −78 ºC to RT, 4 h, 63% yield; (*b*) NaOCl, MeOH, RT, 72 h, 35% yield; (*c*) HATU, DIPEA, CH_2Cl_2, RT, 30 min, 65% yield.

Following this, ketone **178** was treated with aqueous bleach solution in MeOH, which gave acid **179** in poor yield.[409] This reaction proceeded extremely slowly, and much starting material was recovered after 72 hours. It was thus possible to recycle this material to produce more of the desired acid. Finally, an amide coupling between acid **179** and 2-aminobenzothiazole **154** cleanly furnished the desired naphthalene derivative **142** in fair yield.

3.6.6. Attempted Synthesis of Tetrazole Derivative **143**

The synthesis of tetrazole derivative **143** began with the HATU-mediated amide coupling between monomethyl phthalate **180** and 2-aminobenzothiazole **154**, which proceeded in good yield. Following this, the methyl ester **181** was hydrolysed to give acid **182**. The isolation of this material was challenging due to its low solubility in various extraction solvents, including EtOAc, CH_2Cl_2 and $CHCl_3$/*i*-PrOH mixture. Many additional extractions were therefore required to yield the product. Concurrently, 5-aminotetrazole **184** was synthesised by first treating aminoguanidine bicarbonate **183** with $NaNO_2$ at 0 °C. This solution was then basified to pH 9 before being heated to 85 °C. Finally, acidification and cooling of the solution resulting in precipitation of the desired tetrazole **184**. We then attempted HATU-mediated amide coupling between acid **182** and tetrazole **184**, but this did not yield the desired product (**Scheme 37**).

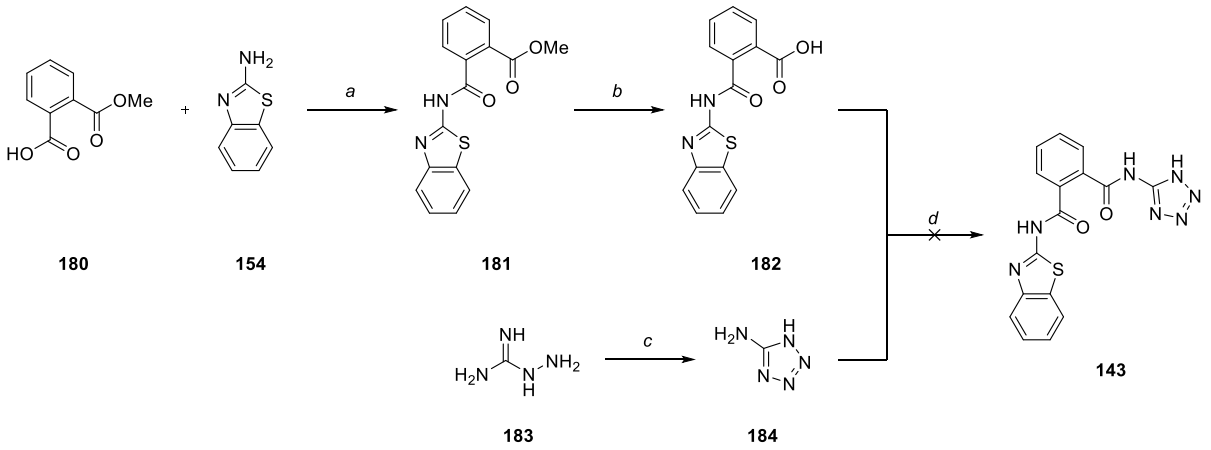

Scheme 37: Attempted synthesis of tetrazole derivative **143**. *Reagents and conditions*: (*a*) HATU, DIPEA, CH_2Cl_2, RT, 1 h, 76% yield; (*b*) LiOH, THF, H_2O, RT, 30 min, 96% yield; (*c*) HCl, $NaNO_2$, 0 ºC, 30 min, then Na_2CO_3, 85 ºC, 3 h, then HCl, −20 ºC, 16 h, 40% yield, (*d*) HATU, DIPEA, CH_2Cl_2, RT, 1 h.

Analysis of the mixture produced from this reaction indicated that phthalimide **185** had instead formed, as shown in **Scheme 38**. We hypothesised that upon treatment of acid **182** with HATU, an intramolecular cyclisation had occurred between the amide nitrogen and the activated carbonyl group. This was confirmed through analysis by NMR: the ^{1}H NMR spectrum showed a total integration of 8H and corresponded to expected shifts of both the benzothiazole and phthalimide moieties. Similarly, the ^{13}C NMR spectrum showed a total of 11 signals. This proposal was further justified by ESI-MS, which gave a signal at *m/z* 303, corresponding to the Na^+ adduct of **185**.

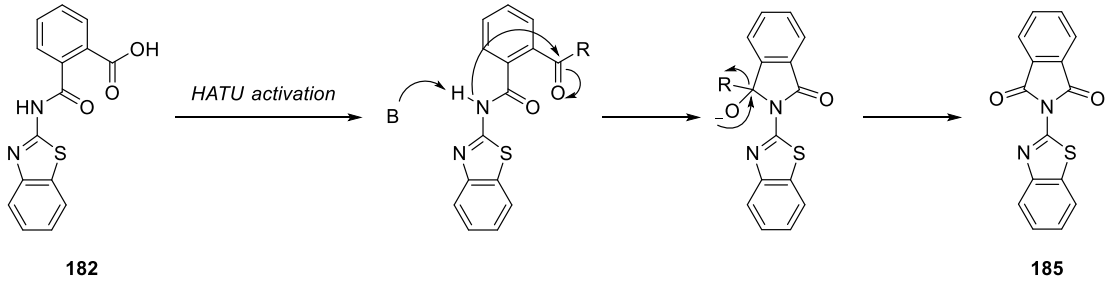

Scheme 38: Formation of phthalimide **185** occurred due to an intramolecular cyclisation of acid **182** upon activation with HATU.

As the HATU-mediated amide coupling requires the presence of a base, we proposed that the use of an acid chloride as an activated acid intermediate would circumvent cyclisation, as shown in **Scheme 39**. To this end, acid **182** was treated with oxalyl chloride ($(COCl)_2$). The acid chloride **186** was subsequently treated with tetrazole **184**, but this also failed to yield the desired amide **143**, instead affording phthalimide **185** once again.

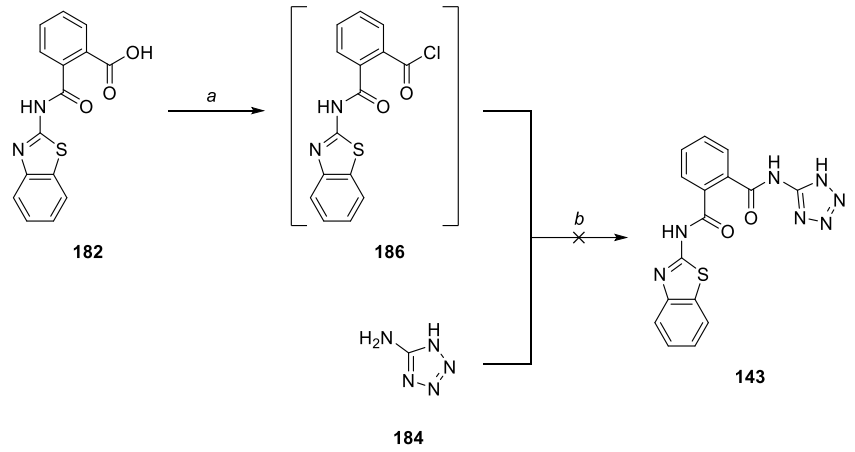

Scheme 39: Attempted synthesis of tetrazole derivative **143** *via* acid chloride intermediate. *Reagents and conditions*: (*a*) $(COCl)_2$, cat. DMF, CH_2Cl_2, 0 °C to RT, 1 h; (*b*) HATU, DIPEA, CH_2Cl_2, RT, 1 h.

Given these results, we therefore attempted to rearrange the order in which the two amide couplings were conducted. This was trialled using HATU-mediated amide coupling, but instead this produced a complex reaction mixture, with no trace of the product observed (**Scheme 40**). However, it was found that HATU had reacted with acid **180** and did not react further, forming the ester **188**. Regrettably, further efforts to synthesise this compound were thus abandoned.

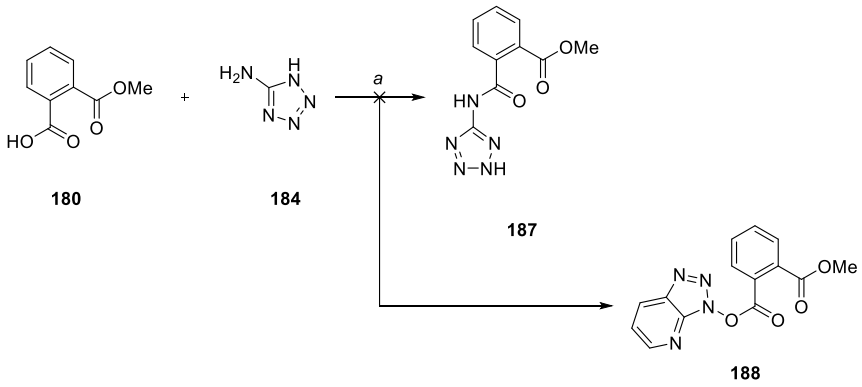

Scheme 40: Attempted synthesis of amide **187**. *Reagents and conditions*: (*a*) HATU, DIPEA, CH_2Cl_2, RT, 1 h.

Future attempts to synthesise tetrazole derivative **143** could involve a construction of the tetrazole moiety *in situ*, as shown in **Scheme 41**. A HATU-mediated amide coupling between monomethyl phthalate **180** and cyanamide would provide amide **189**, which would subsequently be hydrolysed and coupled with 2-aminobenzothiazole **154** using aforementioned amide coupling methods. The tetrazole may be installed by treatment with sodium azide (NaN_3) using procedures developed by Demko and Sharpless to afford the desired tetrazole derivative **143**.[410]

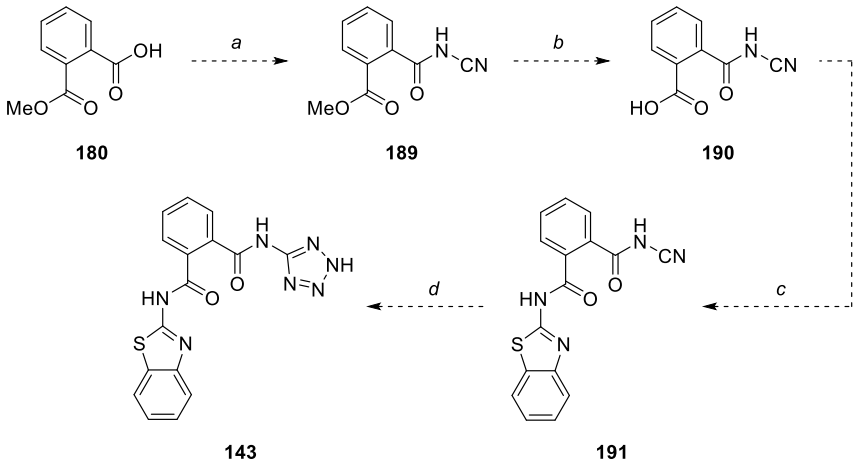

Scheme 41: Proposed synthesis of tetrazole derivative **143**. *Proposed reagents and conditions*: (*a*) cyanamide, HATU, DIPEA, RT, 1 h; (*b*) LiOH, THF, H_2O, RT, 30 min; (*c*) 2-aminobenzothiazole, HATU, DIPEA, RT, 1 h; (*d*) NaN_3, $ZnBr_2$, H_2O, 100 °C, 24 h.

3.6.7. Synthesis of Amide Derivative **144**

In synthesising amide derivative **144**, we initially attempted to perform a HATU-mediated amide coupling of salicylic acid **192** and 2-aminobenzothiazole **154** (**Scheme 42** (*a*)). However, poor yields of the desired amide **193** were obtained. This is likely due to interference of the phenol in the amide coupling, which may also cause coupling between salicylic acid molecules. Furthermore, it proved challenging to purify the reaction mixture. To remedy this, we also attempted a similar amide coupling with acetylsalicylic acid **194**, to protect the phenol and prevent the intermolecular coupling (**Scheme 42** (*b*)). This too, however, resulted in poor yield and the acid coupling to HATU directly and not reacting further. As these two compounds also had very similar R_f values, purification of these did not isolate the desired amide **195**.

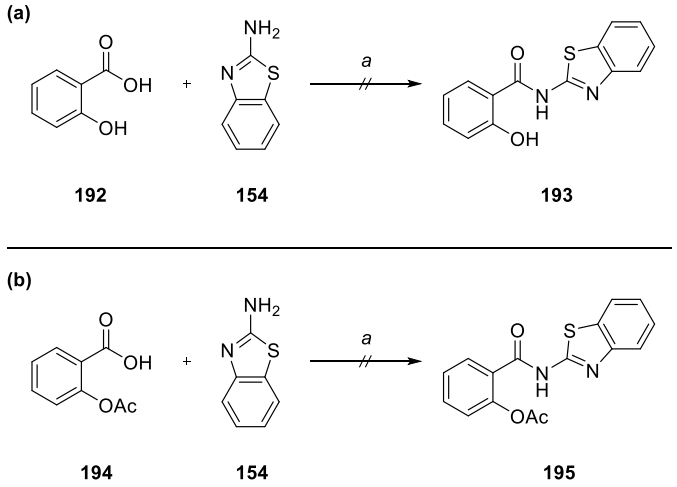

Scheme 42: Attempted synthesis of amides **193** and **195**. *Reagents and conditions*: (*a*) HATU, DIPEA, CH_2Cl_2, RT, 1 h.

Consequently, the order of the synthetic pathway was modified. Benzyl salicylate **196** was first treated with ethyl bromoacetate **197** in an S_N2 reaction to cleanly yield the diester **198** in good yield. A Pd-catalysed hydrogenation then deprotected the benzyl group in good yield, which allowed for the HATU-mediated amide coupling of acid **199** and 2-aminobenzothiazole **154**. The ester **200** was then hydrolysed in quantitative yield to give the acid **201**, after which another HATU-mediated amide coupling to methylamine furnished amide derivative **144** (**Scheme 43**).

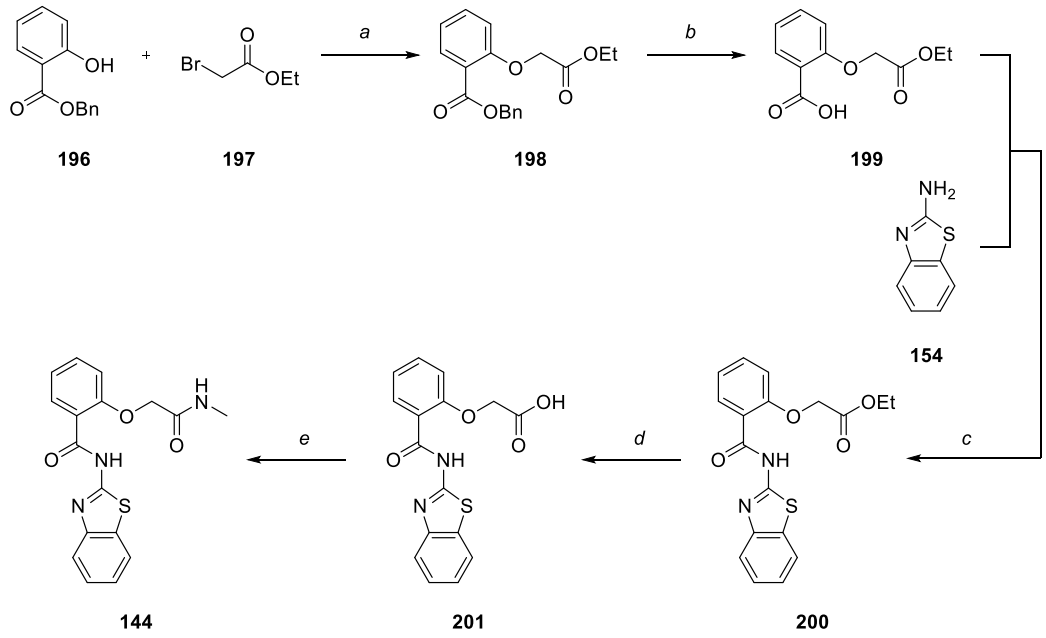

Scheme 43: Synthesis of amide derivative **144**. *Reagents and conditions*: (*a*) ethyl bromoacetate, K_2CO_3, acetone, 56 ºC, 16 h, 81% yield; (*b*) H_2, Pd/C, MeOH, RT, 16 h, 55% yield; (*c*) HATU, DIPEA, CH_2Cl_2, RT, 1 h, 48% yield; (*d*) LiOH, THF, H_2O, RT, 30 min, 99% yield; (*e*) $MeNH_2$, HATU, DIPEA, CH_2Cl_2, RT, 1 h, 61% yield.

3.6.8. Attempted Synthesis of Urea Derivative **145**

In our retrosynthesis of urea derivative **145**, we envisioned three fragments to the molecule that could be pieced together sequentially. Compound **145** could therefore be prepared from a Suzuki coupling of pyridine **202** and pinacol boronate **203**. In turn, the pinacol boronate could be prepared from aryl bromide **204**, which would be synthesised *via* the formation of a urea linkage between 2-aminobenzothiazole **154** and 6-bromoindole **205** (**Scheme 44**).

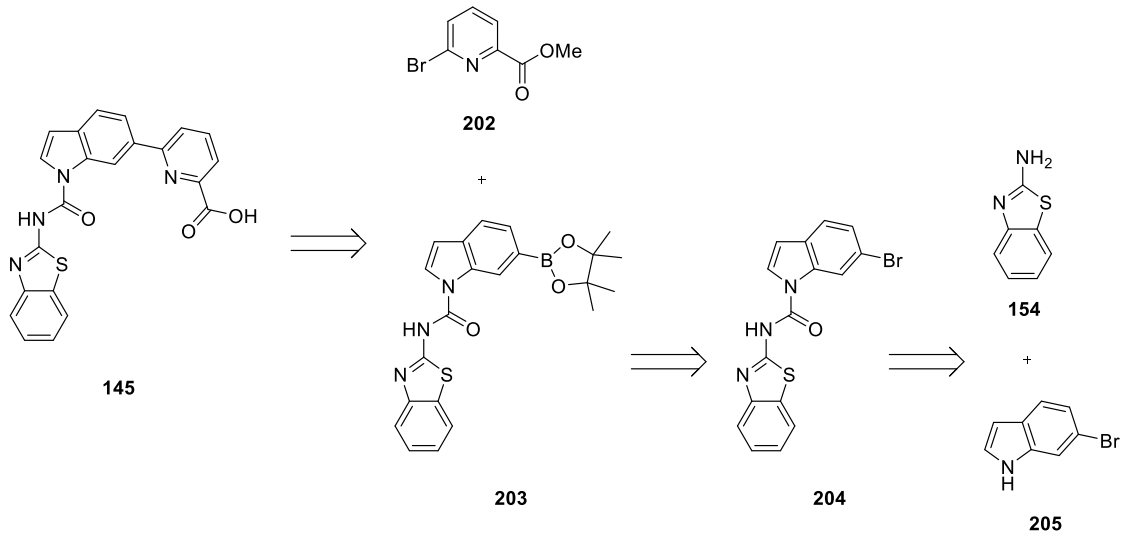

Scheme 44: Retrosynthesis of urea derivative **145**.

Therefore, urea **204** was prepared by treatment of 6-bromoindole **205** with *N*,*N*′-carbonyldiimidazole (CDI) with catalytic DMAP, to obtain the asymmetric urea intermediate **206** (**Scheme 45**). To this was added 2-aminobenzothiazole **154**, which gave the desired urea **204** in moderate yield. We then attempted to form pinacol boronate **203** in preparation for a Suzuki coupling to pyridine **202**, using previously described borylation conditions, but this resulted in no conversion of the starting material. With different catalytic systems giving the same results (**Table 9**), it was hypothesised that co-ordination of the Pd catalyst to the benzothiazole sulfur and carbonyl oxygen formed a complex which prevented successful coupling from occurring.

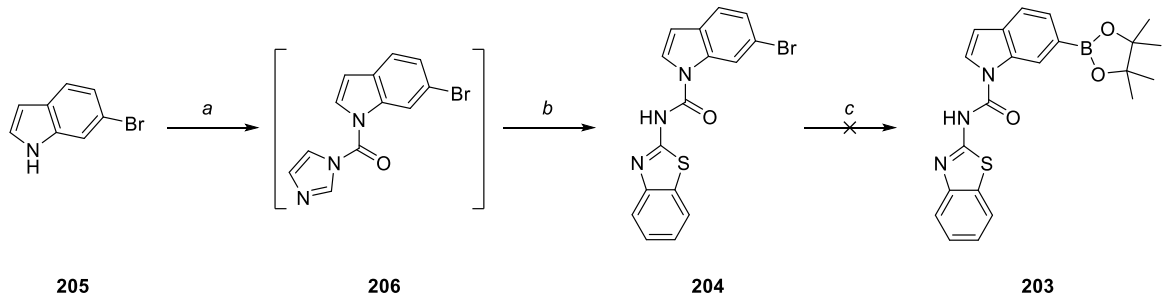

Scheme 45: Attempted synthesis of pinacol boronate **203**. *Reagents and conditions*: (*a*) CDI, DMAP, MeCN, 82 °C, 16 h; (*b*) 2-aminobenzothiazole, 82 °C, 6 h, 50% yield; (*c*) B_2pin_2, KOAc. For catalyst systems attempted, see **Table 9**.

Table 9: Attempted synthesis of pinacol boronate **203**.

Entry	Catalyst system	Result
1	$Pd(dppf)Cl_2$, DMF	NR[a]
2	$Pd(dba)_2$, PCy_3	NR[a]
3	$Pd(OAc)_2$	NR[a]

[a]No reaction.

As such, it was decided to reverse the order of the synthetic pathway. The revised retrosynthesis in **Scheme 46** shows how the molecule may first be disconnected by the urea linkage. Thus, indole **208** would be prepared *via* Suzuki reaction of indole **209** and pyridine **202**.

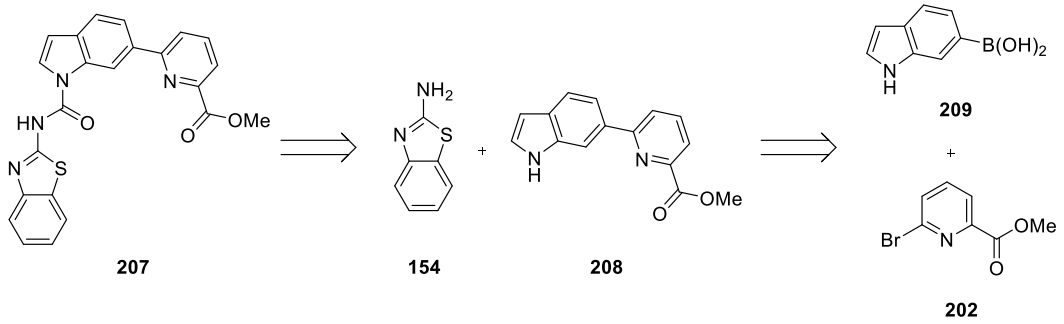

Scheme 46: Revised retrosynthesis of urea derivative precursor **207**.

The carboxylic acid of pyridine **210** was initially protected, to prevent side reactions from occurring later during the urea formation (**Scheme 47**). This esterification proceeded cleanly in excellent yields. A Suzuki reaction between indole **209** and pyridine **202** then gave the desired indole **208** in good yields, although purification of the reaction mixture was challenging due to the production of protodeboronated and homo-coupled material. In a similar manner to urea **204**, we then attempted to prepare urea **207** by treating indole **208** with CDI, followed by the addition of 2-aminobenzothiazole **154**. However, this reaction failed to produce the desired urea **207** (entry 1, **Table 10**). It was hypothesised that deprotonation of the indole proton was necessary to facilitate the formation of the imidazole urea intermediate. This reaction was therefore attempted by initial treatment with NaH (entry 2, **Table 10**) and *n*-BuLi (entry 3, **Table 10**). These conditions unfortunately resulted in the formation of a complex reaction mixture. Indeed, the reactivity of the 3-position of the indole were likely to elicit complex pathways leading to the formation of side products. Due to constraints of time, further efforts toward the synthesis of urea derivative **145** were abandoned.

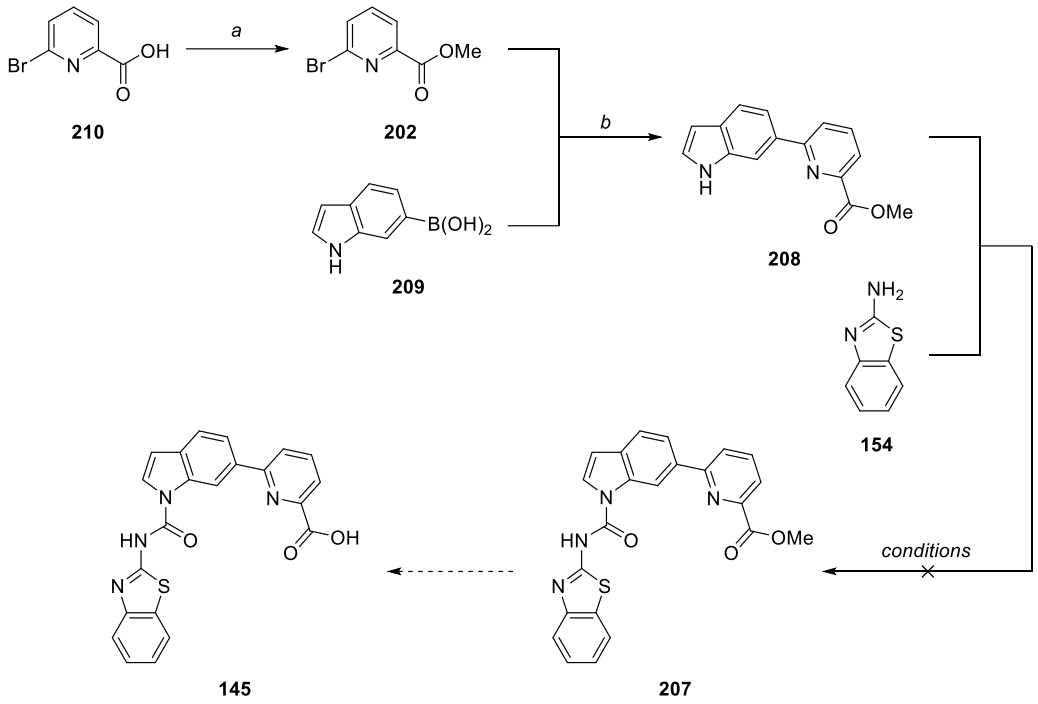

Scheme 47: Attempted synthesis of urea derivative **145**. *Reagents and conditions*: (*a*) H_2SO_4, MeOH, 65 °C, 1 h, 95% yield; (*b*) Na_2CO_3, $Pd(PPh_3)_4$, H_2O, 1,4-dioxane, 80 °C, 16 h, 57% yield. For conditions, see **Table 10**.

Table 10: Attempted synthesis of urea derivative **145**.

Entry	Conditions	Result
1	CDI, cat. DMAP, MeCN, 82 °C, 1 h, then 2-aminobenzothiazole	No reaction
2	NaH, THF, 0 °C, 1 h, then CDI, 1 h, then 2-aminobenzothiazole	CRM[a]
3	*n*-BuLi, THF, −78 °C, 1 h, then CDI, 1 h, then 2-aminobenzothiazole	CRM

[a]Complex reaction mixture.

Two future synthetic routes are proposed for the preparation of urea derivative **145**. **Scheme 48** (*a*) shows how indole **208** may be treated with triphosgene to form carbamyl chloride intermediate **210**. The addition of 2-aminobenzothiazole **154** would then yield ester **207**. Alternatively in **Scheme 48** (*b*), the reaction of 2-aminobenzothiazole **154** with triphosgene would afford carbamyl chloride **211**, which could be heated to form isocyanate **212** *via* Curtius rearrangement. Subsequent treatment of isocyanate **212** with deprotonated indole **213** would then provide ester **207**.

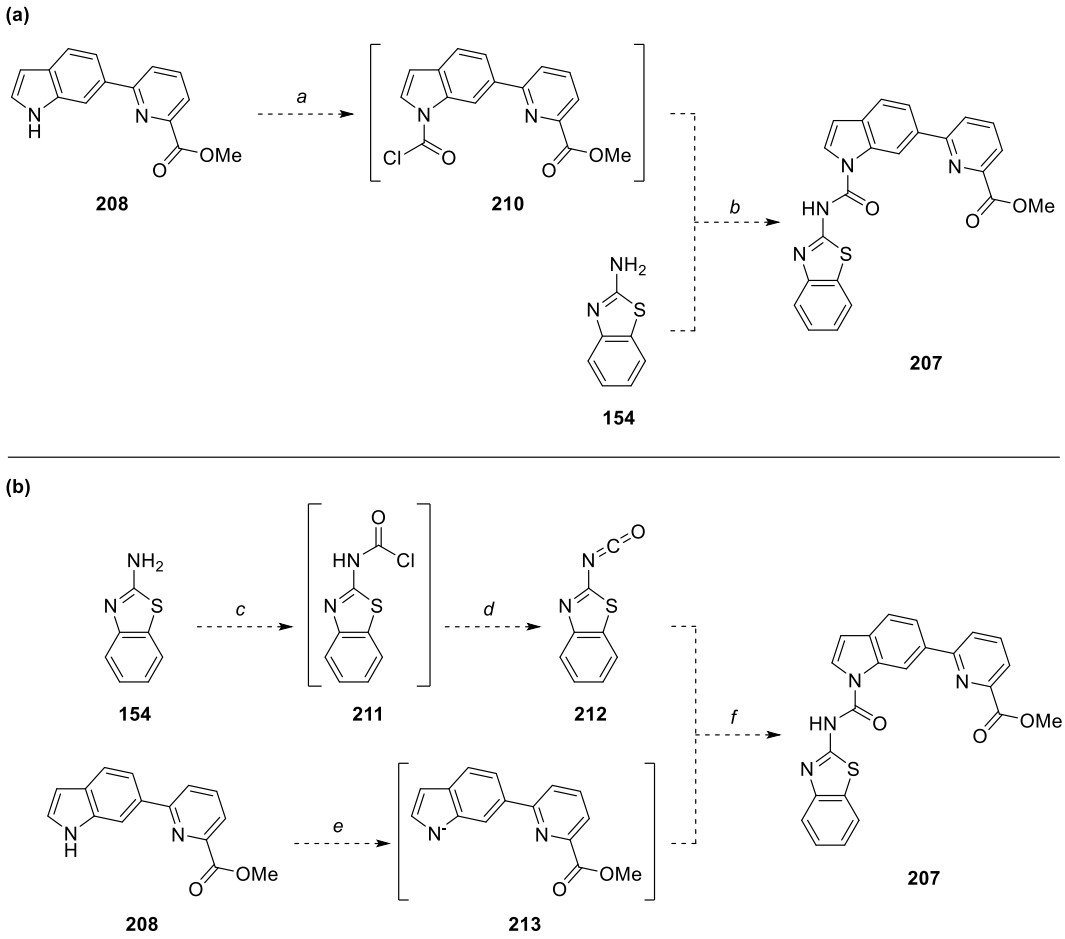

Scheme 48: Proposed synthetic routes towards urea derivative **207**. *Proposed reagents and conditions*: (*a*) triphosgene, cat. DMAP, CH_2Cl_2, 0 °C to RT, 1 h; (*b*) Et_3N, CH_2Cl_2, 0 °C to RT, 3 h; (*c*) triphosgene, CH_2Cl_2, 0 °C to RT, 1 h; (*d*) PhMe, 110 °C, 1 h; (*e*) NaH, THF, 0 °C to RT, 30 min; (*f*) CH_2Cl_2, 0 °C to RT 1 h.

3.6. Biological Evaluation

The compounds synthesised in this chapter, **126**, **127**, **139**–**142** and **144** were delivered for biological evaluation by August 2024. Assays are currently in progress and such data for this library will be reported in due course.

3.7. Summary and Concluding Remarks

This chapter has explored the scaffold hopping of known compounds that act as potent inhibitors of BCL-X_L. Scaffold hopping has been discussed as a technique in medicinal chemistry for generating novel chemotypes. This highlighted a variety of different methods to approach the bioisosteric replacement of molecular fragments. Indeed, the Spark software was utilised to perform 4° scaffold hopping, which replaced large segments of the lead molecules **126** and **127** with differing chemical structures. Electrostatic field point diagrams demonstrated that the interactions between ligands and target proteins are not a result of specific atoms, but

the overall electronic characteristics of a molecule. This was further validated through the Glide scores of the newly generated structures, calculated *via* molecular docking studies. This chapter has also provided a detailed treatise of the synthetic challenges associated with the synthesis of these molecules, particularly in circumstances where initial retrosynthetic efforts were revised as unsatisfactory reaction outcomes were produced.

Biological evaluation of compounds synthesised in **Chapter 3** is still ongoing and these results are keenly anticipated to understand whether members of this library may possess senolytic capabilities. The exploration of novel chemotypes from existing compounds in the literature has proved a fascinating endeavour, and the continuation of such themes are further described in **Chapter 4**.

This Page Intentionally Left Blank

Chapter 4

Probing SAR Around a Known MCL-1 Inhibitor

Chapter 4 – Probing SAR Around a Known MCL-1 Inhibitor

4.1. Introductory Remarks

The exploration of new chemical space by probing SAR underpins much of medicinal chemistry, and indeed is key to many aspects of drug discovery from primary screening to lead optimisation.[411] Given that it was not possible to draw conclusions regarding the biological activity of compounds synthesised in **Chapter 3**, we felt it necessary to now pivot to a new target within the BCL-2 family. Moreover, we also wished to employ another method within medicinal chemistry to venture into these new chemotypes and enhance the knowledge in organic synthesis and SAR.

In this chapter is discussed MCL-1, a member of the BCL-2 family and a key mediator in pathways that prevent apoptosis in SCs. Also introduced is the known inhibitor UMI-77 **51**, which offers excellent scope and opportunities for diversification through the probing of SAR. This chapter details efforts to understand known SAR data, which is followed by the rational design of previously unknown analogues. Computational studies are utilised to select the best of these compounds, providing a library for synthesis. An investigation of these synthetic approaches is discussed, leading to new structures that aim to further the breadth of knowledge of novel senolytic chemotypes.

4.2. MCL-1: Another Anti-apoptotic Target for Senolytics

The BCL-2 family, previously described in **Chapter 1.4.4.5.**, contains the pro-apoptotic proteins BCL-2, BCL-X_L, BCL-W, BFL-1/A1 and MCL-1.[277] Given our focus on BCL-2 and BCL-X_L throughout this work, we also saw it prudent to turn our attention to other members this family. While MCL-1 has been identified as a frequently amplified gene in cancers,[412] Alimonti and co-workers have also highlighted its upregulation in senescent tumour cells.[331] These cells displayed low levels of anti-apoptotic BCL-2, and thus treatment with the BCL-2 inhibitor *navitoclax* demonstrated some reduction in metastases in mice models. The authors wanted to explore the impact of MCL-1 inhibition on senescent tumour cells, and found that the MCL-1 inhibitor S63845 (**50**) caused the complete elimination of such a tumour.[331] Additionally, MCL-1 has also been implicated in enhancing cellular survival[413, 414] and was identified as a target for therapeutic intervention in AD.[415] These results were intriguing and prompted us to examine the development of novel MCL-1 inhibitors.

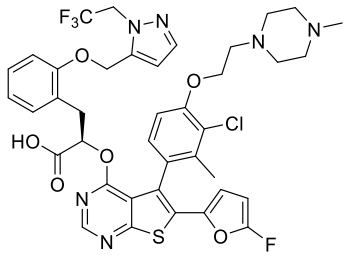

S63845 **50**
MCL-1 K_d = 0.19 nM

Figure 47: Structure of the MCL-1 inhibitor S63845 (**50**).

4.3. Choosing a Lead Compound

Our search for MCL-1 inhibitors in the literature identified a number of small molecules that had demonstrated good potency against the protein.[416-419] This included some which also functioned as dual inhibitors of MCL-1 and other BCL-2 family members.[420-422] Of these, compound **51**, also known as UMI-77 (**Figure 48**), was of particular interest due to its small size (MW = 467 Da) and potential for derivatisation. This compound was identified by Nikolovska-Coleska and co-workers, who had previously performed a HTS of a 53.5K library using a fluorescence polarisation assay.[419] This highlighted **214** as a hit molecule, which was determined to possess a K_i of 1.55 ± 0.18 μM and had previously been shown to act as a proteasome inhibitor.[423]

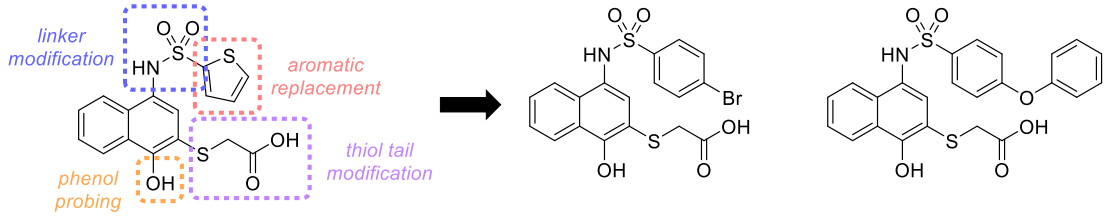

214
K_i (FP) = 1.55 ± 0.18 μM
IC_{50} (SPR) = 7.12 ± 1.02 μM

51 (UMI-77)
K_i (FP) = 0.49 ± 0.06 μM
IC_{50} (SPR) = 2.40 ± 0.17 μM

215
K_i (FP) = 0.18 ± 0.05 μM
IC_{50} (SPR) = 1.45 ± 0.29 μM

Figure 48: Structure of lead molecule **214**, and modifications undertaken by Nikolovska-Coleska and coworkers in the design of UMI-77 **51** and **215**. FP = fluorescence polarisation assay; SPR = surface plasmon resonance assay.

Setting out to improve the binding affinity of **214**, the authors performed structural modifications to the linker group, aromatic ring, thiol tail and the phenol group. Each iteration in probing SAR was aided by both molecular docking studies and $^{1}H–^{15}N$ HSQC NMR studies of the protein and new analogues, which culminated in the generation of **51** (UMI-77) and **215**. The authors' work therefore not only served as the foundation for our own investigation, but the SAR uncovered also aided in the design of our library, which will be discussed below.

The binding mode of the most potent compound in the study, **215**, was investigated by *in silico* induced fit docking studies (PDB: 2NLA, **Figure 49** (*a*)). The naphthalene core and *para*-phenoxyphenyl moiety of **215** fit into two hydrophobic pockets of the active site of MCL-1, mimicking the binding of its endogenous ligand, the BH3-only protein mNOXA. In addition, a network of H-bonding is formed between the carboxylic acid and Arg263 and Asn260. This was further evidenced by our own modelling of **215** in the binding pocket of MCL-1, using the same protein structure (**Figure 49**, (*c*)). The authors further expanded on these findings using $^{1}H–^{15}N$ HSQC NMR studies (**Figure 49**, (*b*)). Indeed, the chemical shifts corresponding to environments in Phe270, Leu267 and Val253 – all residues within the hydrophobic binding pocket) – were observed, as was that of Arg263, which interacts with the carboxylic acid through H-bonding. The authors' comprehensive study of the binding mode of **215** was instrumental in our library design, as it identified key features of MCL-1 inhibitors with high binding affinity.

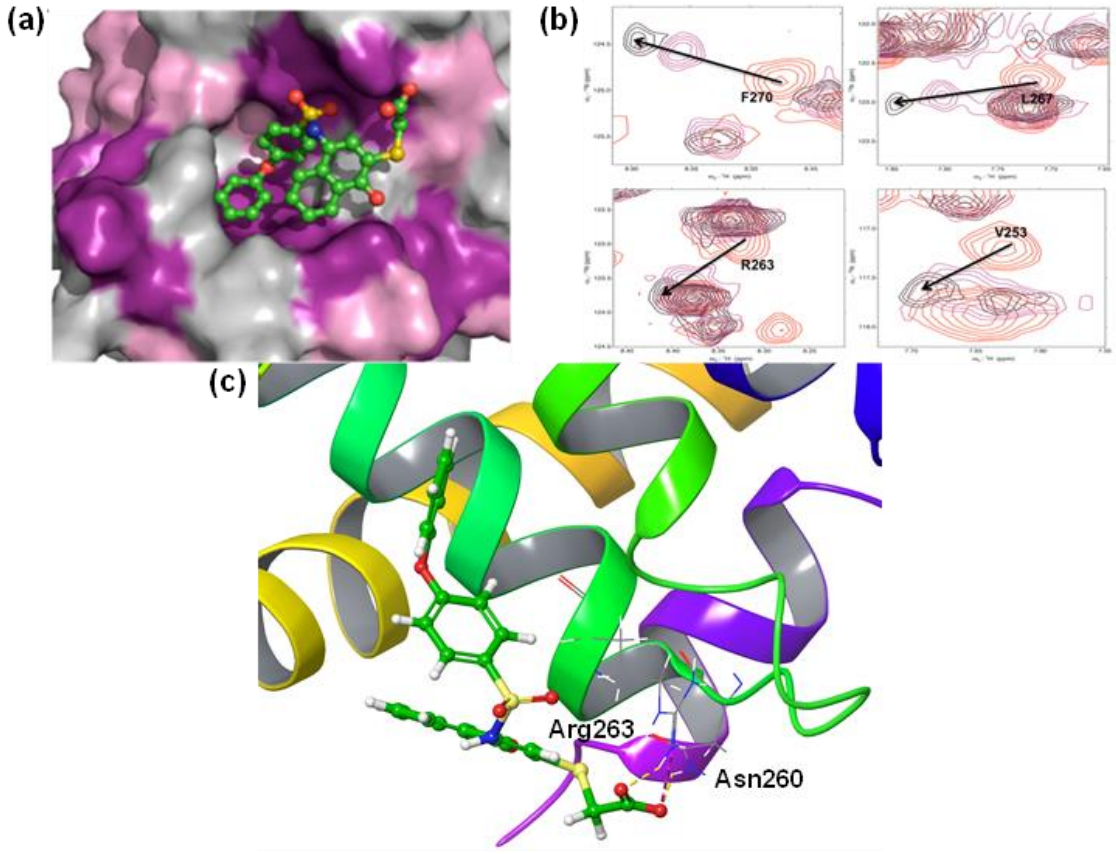

Figure 49: (*a*) Docking study of **215** bound to MCL-1 (PDB: 2NLA) performed Nikolovska-Coleska and coworkers. Side chains of residues are shown in light blue. The protein surface is colour coded according to changes in changes in the chemical shift, where significant shift (> 0.09 ppm) is coloured in purple, while moderate shift (0.03–0.09 ppm) is shown in pink; (*b*) Overlaid $^{1}H–^{15}N$ HSQC NMR spectra of MCL-1 (**red**) and MCL-1 and **215** (**black**), highlighting chemical shift changes in Phe270 (F270), Leu267 (L267), Arg263 (R263), and Val253 (V253); (*c*) Docking study performed in this work showing **215** bound to MCL-1 (PDB: 2NLA), highlighting H-bond interactions between the carboxylic acid and Arg263 and Asn260. Reprinted with permission from *J. Med. Chem.* 2014, 57, 10, 4111–4133. Copyright 2014 American Chemical Society.

4.4. Library Design and Molecular Docking Study

To design a library of compounds for synthesis, we first considered the SAR information determined by Nikolovska-Coleska and coworkers.[419] While no changes were made to the naphthalene core, the four sections shown in **Figure 48** were each probed by the authors. Of note were modifications that resulted in a complete loss of binding affinity to MCL-1. For example, this was seen when the 4-bromophenyl group was replaced by a methyl group in **216**; when the carboxylic acid was replaced by an aliphatic tail in **217**; or when the phenol was replaced with a methoxy group in **218** (**Figure 50**). Such biological data are unsurprising considering the results of the aforementioned molecular docking and ^{1}H-^{15}N HSQC studies. In **216**, a key π-π stacking interaction fails to occur due to the lack of aromatic ring, while in **217** and **218**, the lack of carboxylic acid or phenol prevents critical H-bond interactions from forming.

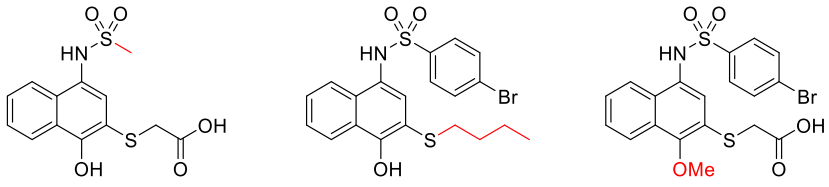

216
K_i (FP) > 74.92 ± 6.33 μM
IC_{50} (SPR) > 100 μM

217
K_i (FP) > 27 μM
IC_{50} (SPR) > 100 μM

218
K_i (FP) > 27 μM
IC_{50} (SPR) > 100 μM

Figure 50: Probing of SAR by Nikolovska-Coleska and coworkers revealed several derivatives where structural modifications resulted in a complete loss of binding affinity. FP = fluorescence polarisation assay; SPR = surface plasmon resonance assay.[419]

We therefore designed a variety of analogues of UMI-77 **51**, with care to ensure that features such as the aromatic ring, carboxylic acid and phenol were not perturbed. Simultaneously moieties were introduced which were previously not prepared by the authors. The full list of these molecules is provided in **Appendix B**. Using these derivatives, we conducted our own molecular docking study, using the same protein model as the authors to validate our design (PDB: 2NLA). In addition to **51** and **215**, our molecular design and docking revealed several compounds which were predicted to bind tightly to MCL-1, shown in **Table 11**.

Table 11: Analogues of **51** with high binding affinity identified in docking study.

Compound	Structure	Glide score
UMI-77 (**51**)	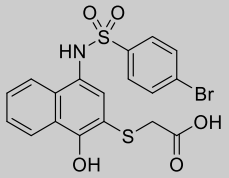	−3.56
215	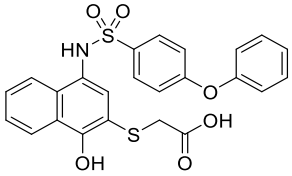	−6.33
219	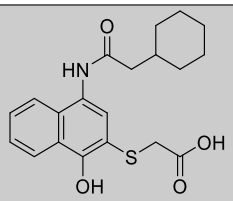	−7.06
220	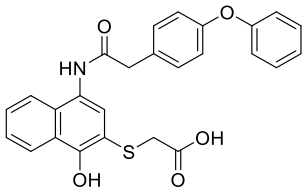	−6.71
221	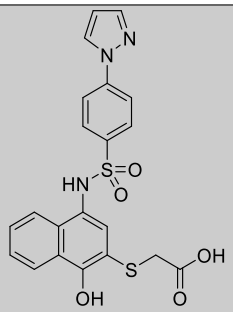	−5.08
222	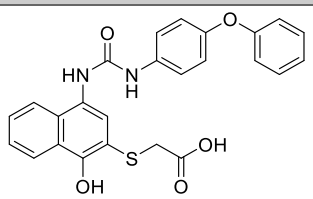	−7.34

Indeed, each of the new analogues maintained similar interactions with MCL-1 as **215**. These are shown in **Figure 51**. In compounds **219** and **220**, π-π stacking was maintained between the naphthalene core and His224, while the carboxylic acid formed H-bonds with Arg263 and Asn260. Meanwhile in compounds **221** and **222**, π-π stacking was seen between the phenyl ring and Phe270, and the carboxylic acid formed the same H-bonding network with

Arg263 and Asn220 previously observed in **215**. With these molecules showing potential as high-affinity binders to MCL-1, we proceeded with their synthesis.

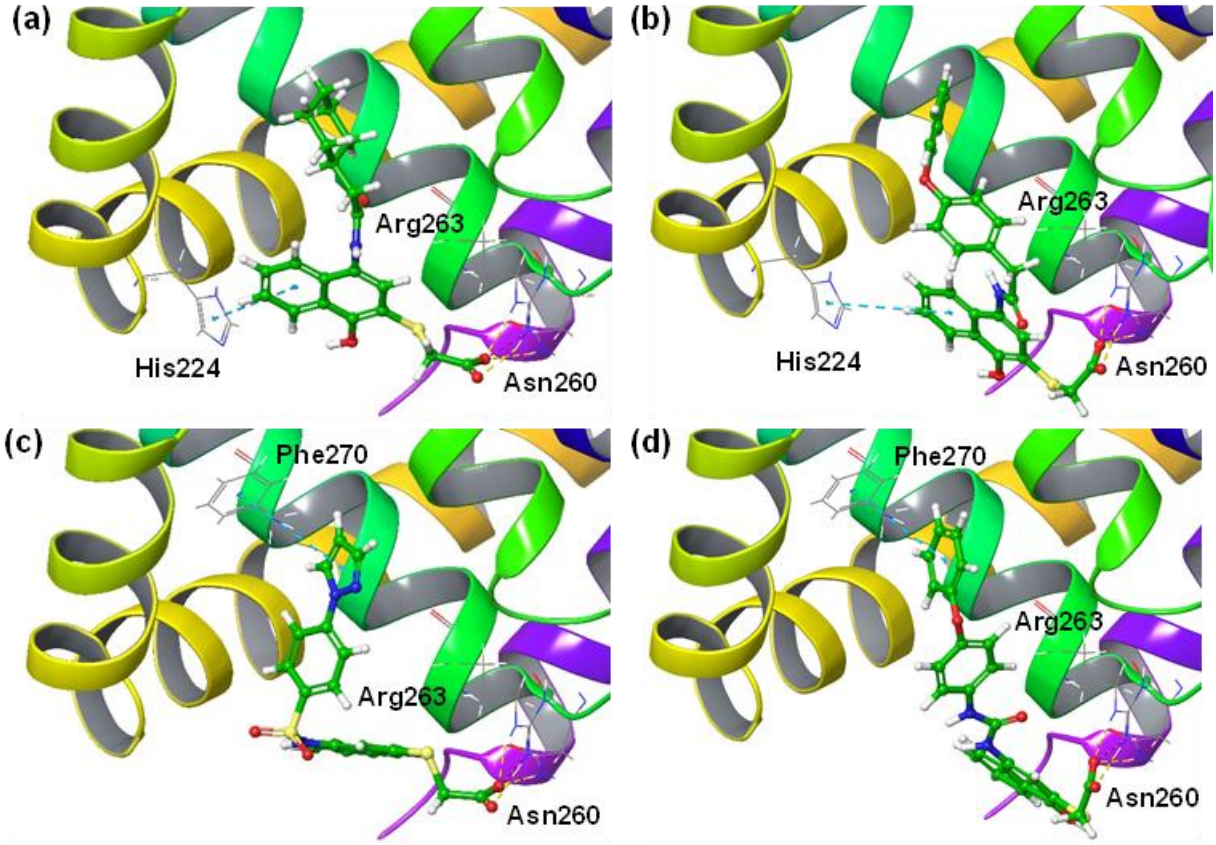

Figure 51: Diagrams showing compounds **219**–**222** docked to MCL-1. (*a*) **219** showing π-π stacking interaction to His224 and H-bonding network between Arg263 and Asn260; (*b*) **220** showing π-π stacking interaction to His224 and H-bonding network between Arg263 and Asn260; (*c*) **221** showing π-π stacking interaction to Phe270 and H-bonding network between Arg263 and Asn260; (*d*) **222** showing π-π stacking interaction to Phe270 and H-bonding network between Arg263 and Asn260.

4.5. Synthesis of Lead Compounds **51** *and* **215**

A retrosynthetic analysis for the synthesis of UMI-77 **51** is shown in **Scheme 49**. Indeed, each of the proposed compounds detailed **Table 11** could be prepared in a similar manner, only differing with the final step of coupling the aromatic group. It was envisioned that **51** could be prepared *via* sulfonamide coupling between amine **223** and 4-bromobenzenesulfonyl chloride **224**. The amine **223** could in turn be produced from the corresponding nitroarene **225**, which would be synthesised from aryl iodide **227** and methyl thioglycolate **226**. Thus, each derivative could conveniently be prepared from the same starting material, the commercially available 1-methoxy-4-nitronaphthalene **228**.

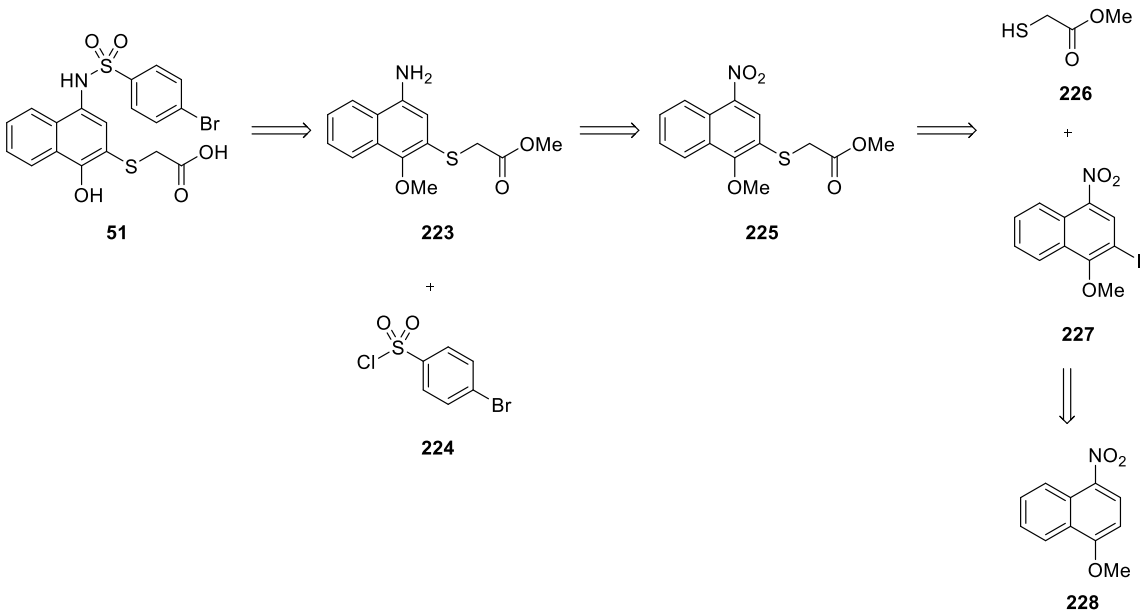

Scheme 49: Potential retrosynthetic analysis of UMI-77 **51**.

4.5.1. Iodination of Naphthalene **228**

The synthesis of UMI-77 **51** began with the selective iodination of 1-methoxy-4-nitronaphthalene **228** according to procedures described in literature.[419] Refluxing naphthalene **228** and *N*-iodosuccinimide (NIS) in trifluoroacetic acid (TFA) resulted in 49% of the starting material being recovered following purification of aryl iodide **227**, which was afforded in 37% yield (**Scheme 50** (*a*) and **Table 12**). The mechanism of this reaction is intriguing: iodine(I) trifluoroacetate **229** is formed *in situ* from the reaction of NIS and TFA (**Scheme 50** (*b*)). Both the protonated NIS species and iodine(I) trifluoroacetate **229** have been calculated to possess excellent potential in electrophilic aromatic substitution (S_EAr) of various arenes, as determined by density functional theory calculations.[424, 425] These intermediates have highly extended bonds to iodine, which therefore increases their polarity and creates exceptionally electron-deficient iodine atoms. **Scheme 50** (*c*) demonstrates how the subsequent S_EAr reaction takes place between naphthalene **228** and iodine(I) trifluoroacetate **229**.

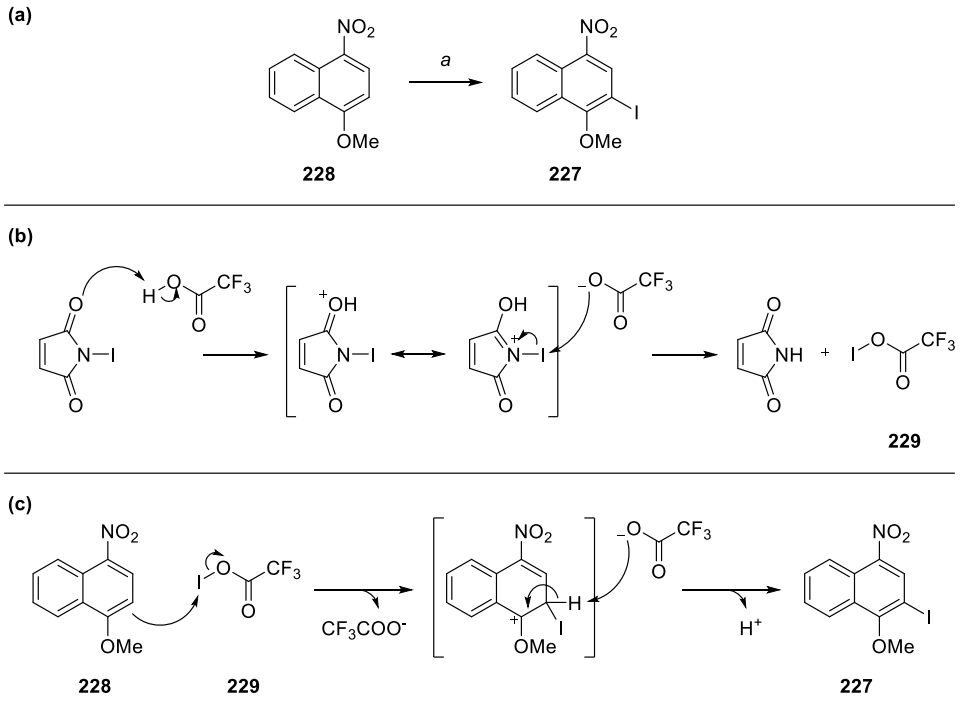

Scheme 50: (*a*) Synthesis of 2-iodo-1-methoxy-4-nitronaphthalene **227**. *Reagents and conditions*: NIS, TFA, 72 °C, 24 h, 37% yield; (*b*) Formation of the iodine(I) trifluoroacetate electrophile **229** as proposed in literature;[424] (*c*) Mechanism of the S_EAr reaction between naphthalene **228** and iodine(I) trifluoroacetate **227**.

In subsequent attempts to optimise this reaction, the addition of an extra 0.50 equivalents of NIS led to the formation unwanted diiodinated isomers (entry 2, **Table 12**), which proved challenging to efficiently separate from the desired monoiodinated product **227**. In a similar manner, we also attempted to perform the reaction in a pressure tube such that the iodination could be conducted at higher temperatures (entry 3, **Table 12**). However, any increase beyond the boiling point of TFA (72 °C) also caused the previously observed diiodination. It was thus concluded that future repetitions of this reaction would increase in scale and recover and recycle unused starting material. Other iodinating reagents have been developed for similar S_EAr reactions, such as I_2-NO_2,[426] *n*-BuLi-F_3CCH_2I[427] and I_2-$AgNO_3$,[428] however the critical drawback of such combinations is their toxicity and associated hazards. Further attempts to improve the yield of this reaction could centre of alternative iodination conditions.

Table 12: Attempted optimisation of iodination of 1-methoxy-4-nitronaphthalene **228**.

Entry	Conditions	Result
1	NIS (1.15 equiv.), TFA, 72 °C, 24 h	37% yield
2	NIS (1.65 equiv.), TFA, 72 °C, 24 h, then NIS (0.5 equiv.), 72 °C, 24 h	Formation of diiodinated products
3	NIS (1.15 equiv.), TFA, 80 °C, 24 h, Pressure tube	Formation of diiodinated products

4.5.2. Thiolation of Aryl Iodide **227**

Following this, the thiolation of aryl iodide **227** was attempted using methyl thioglycolate **226**, Cs_2CO_3, $ZnCl_2$, LiI and $Pd(OAc)_2$ with Xantphos as a catalyst system, according to conditions described in literature (**Scheme 51**).[419, 429-431] Unfortunately, no conversion of the starting material was observed. As such, we therefore explored alternative conditions to prepare the desired thiol **225** in appreciable yield.

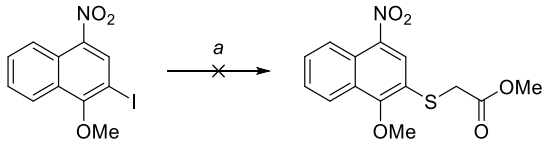

227 **225**

Scheme 51: Attempted thiolation of aryl iodide **227**. *Reagents and conditions*: (*a*) methyl thioglycolate, Cs_2CO_3, LiI, $ZnCl_2$, $Pd(OAc)_2$, Xantphos, THF, 60 °C, 24 h.

Many methods exist in literature for the formation of aryl-sulfur bonds, as the functionality is found in various compounds with biological activity.[432, 433] While the earliest procedures utilised high temperatures and long reaction times,[434] newer, milder methodologies have been developed using Pd-based catalysts,[434-436] among other metals such as Ni and Cu.[437-439] A survey of literature led us to the experimental protocol developed by Mase and co-workers, which used a much simpler catalyst system than the procedure outlined above.[430] Trialling the reported conditions furnished the desired compound in poor yield of 6% and a significant amount of side products formed (**Scheme 52** and entry 1, **Table 13**). It was proposed that some of these side products were dehalogenated in the reaction, and thiolation had occurred on the unsubstituted side of the naphthalene ring. It was not possible to determine which position substitution had occurred in, but this product was detected by ESI-MS. We thus believed optimisation could increase the amount of **225** obtained.

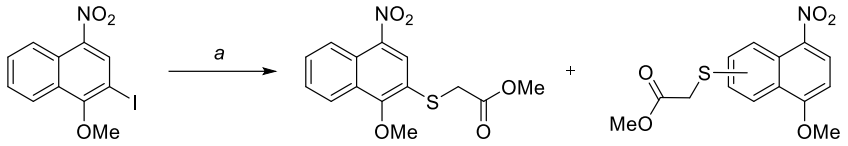

227 225

Scheme 52: Thiolation of iodoarene **227**. *Reagents and conditions*: methyl thioglycolate, DIPEA, $Pd_2(dba)_3$, Xantphos, 1,4-dioxane, 102 °C. For catalyst loading, time and yield, see **Table 13**.

To this end, adjustment of the reaction time revealed that reaction completion occurred within one hour (entries 2 and 3, **Table 13**), as the low yield did not significantly change. As such, we observed that extended heating at reflux was likely the cause of side product formation. Nonetheless, much starting material was also unconverted in this reaction, which we hypothesised was due to poor catalytic turnover. The catalyst loading was therefore increased (entry 4, **Table 13**), which saw a large increase in yield to 34%. Consequently, a further increase in catalyst loading to 10% $Pd_2(dba)_3$ and 15% Xantphos (entry 5, **Table 13**) saw complete consumption of the starting material, with a highly encouraging yield of 85%. Noting the minor side products formed, we then decreased the reaction time again to just 30 minutes (entry 6, **Table 13**), which afforded an excellent yield of 94% with virtually no other contaminants. The optimisation hence cleanly furnished the desired thiol **225**.

Table 13: Optimisation of thiolation of aryl iodide **227**.

Entry	Catalyst loading	Reaction time	Result
1	5% $Pd_2(dba)_3$, 10% Xantphos	6 h	6% yield, significant side products
2	5% $Pd_2(dba)_3$, 10% Xantphos	1 h	6% yield, minor side products
3	5% $Pd_2(dba)_3$, 10% Xantphos	24 h	7% yield, significant side products
4	10% $Pd_2(dba)_3$, 15% Xantphos	1 h	34% yield, minor side products
5	25% $Pd_2(dba)_3$, 30% Xantphos	1 h	85% yield, minor side products
6	25% $Pd_2(dba)_3$, 30% Xantphos	30 min	94% yield

4.5.3. Completing the Synthesis of UMI-77 **51**

With thiol **225** in hand, it was necessary to reduce the nitroarene to the corresponding aniline in preparation for the sulfonamide coupling. Initially, this was attempted with a Béchamp reduction. However, we also became aware of an alternative procedure for nitroarene reduction. This utilises tetrahydroxydiboron ($B_2(OH)_4$) as the reductant and 4,4′-bipyridine as an organocatalyst.[440] We were pleased to find that the latter procedure not only afforded the desired aniline **223** in almost quantitative yield, but also with a much shorter reaction time (**Scheme 53**). A comparison of these two methods is shown in **Table 14**.

Table 14: Comparison of methodologies used for nitroarene reduction of **225**.

Entry	Conditions	Result
1	Fe, NH_4Cl, EtOH, 78 °C, 1 h	87% yield
2	$B_2(OH)_4$, 4,4′-bipyridine, DMF, RT, 10 min	98% yield

Following reduction, aniline **223** was then coupled to 4-bromobenzenesulfonyl chloride **224** using pyridine in CH_2Cl_2, which proceeded in excellent yield to afford sulfonamide **230**. Finally, a global deprotection of both the methyl ester and methoxy group *via* treatment with boron tribromide (BBr_3) gave the desired lead compound **51**, which completed the synthesis.

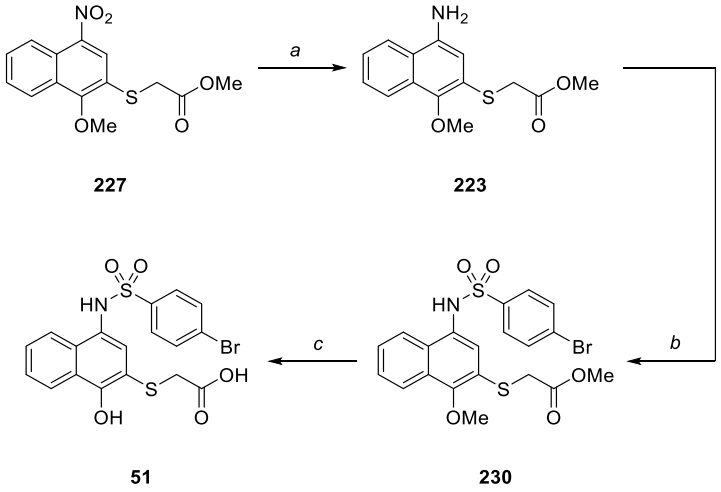

Scheme 53: Synthesis of lead compound **51**. *Reagents and conditions*: (*a*) $B_2(OH)_4$, 4,4′-bipyridine, DMF, RT, 10 min, 98% yield; (*b*) 4-bromobenzenesulfonyl chloride, pyridine, CH_2Cl_2, RT, 3 h, 89% yield; (*c*) BBr_3, CH_2Cl_2, 0 °C to RT, 1 h, 39% yield.

The yield of this final step was poor, and this may be rationalised by considering the mechanism of BBr_3-mediated demethylation, as shown in **Scheme 54**. BBr_3 is initially attacked

by the nucleophilic oxygen of the methoxy group, donating an electron pair into the vacant *p*-orbital of the boron while simultaneously eliminating bromide. Subsequent attack of bromide onto the methyl group allows bromomethane to be eliminated, affording an organoboron species. Finally, aqueous workup decomposes this to the alcohol, also forming boric acid and HBr. Indeed, BBr_3 is highly electrophilic and attack by other nucleophilic sites in the molecule is possible. These reactions therefore produce unwanted side products. Unsurprisingly, similar deprotections performed later in this chapter also suffer from poor yield.

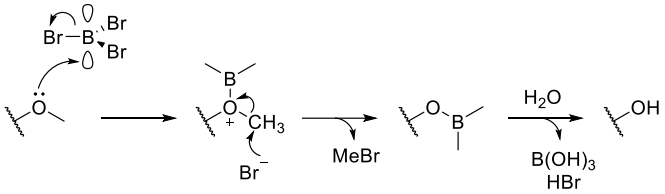

Scheme 54: Mechanism of BBr_3-mediated demethylation.

4.5.4. Synthesis of Lead Compound **215**

The synthesis of lead compound **215** required 4-phenoxybenzenesulfonyl chloride **233**. This was prepared according to literature procedures by first treating diphenyl ether **231** with chlorosulfonic acid (**Scheme 55**).[441] This proceeded cleanly to afford sulfonic acid **232** in quantitative yield. Refluxing **232** with thionyl chloride then furnished sulfonyl chloride **233** in excellent yield of 93%. With this material in hand, it was then coupled to previously prepared aniline **223** in good yield of 76% using the pyridine-mediated sulfonamide coupling procedure described above. Finally, the global deprotection was accomplished *via* treatment with BBr_3, thus affording lead compound **215**.

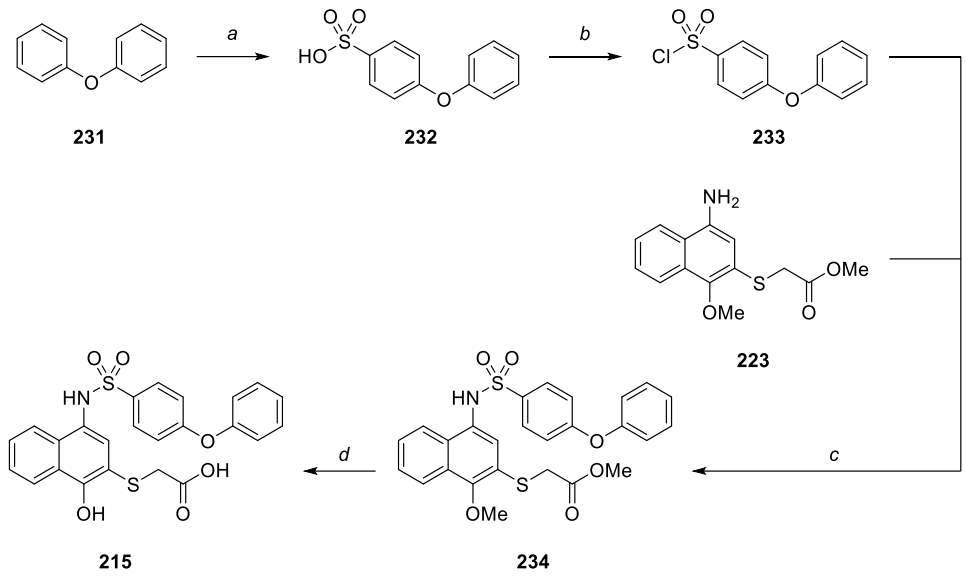

Scheme 55: Synthesis of lead compound **215**. *Reagents and conditions*: (*a*) $ClSO_3H$, CH_2Cl_2, 0 °C to RT, 2 h, 99% yield; (*b*) $SOCl_2$, cat. DMF, 79 °C, 2 h, 93% yield; (*c*) pyridine, CH_2Cl_2, RT, 3 h, 76% yield; (*d*) BBr_3, CH_2Cl_2, 0 °C to RT, 1 h, 41% yield.

4.6. Synthesis of Analogues **219**–**222**

4.6.1. Synthesis of Cyclohexane Derivative **219**

The synthesis of **219** utilised aniline **223** and cyclohexaneacetic acid **235** in a HATU-mediated amide coupling (**Scheme 56**). While this proceeded in appreciable yields, it was observed that an additional product was formed alongside amide **236**. Gratifyingly, this product was readily separated *via* column chromatography, and analysis by ^{1}H NMR revealed that the impurity was azabenzotriazole ester **237**. This is formed when HATU reacts with acid **235** but fails to undergo subsequent attack by the aniline **223**. The presence of this compound was further confirmed by ESI-MS analysis, which displayed a signal at *m/z* 283, corresponding to the Na^+ adduct of **237**.

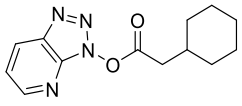

237

Figure 52: Azabenzotriazole ester **237** was formed in large quantities during the amide coupling of aniline **225** and cyclohexaneacetic acid **235**.

Nonetheless, once amide **236** had been isolated in good yield of 74%, we continued with the global deprotection facilitated by BBr_3, which yielded the desired compound **219**.

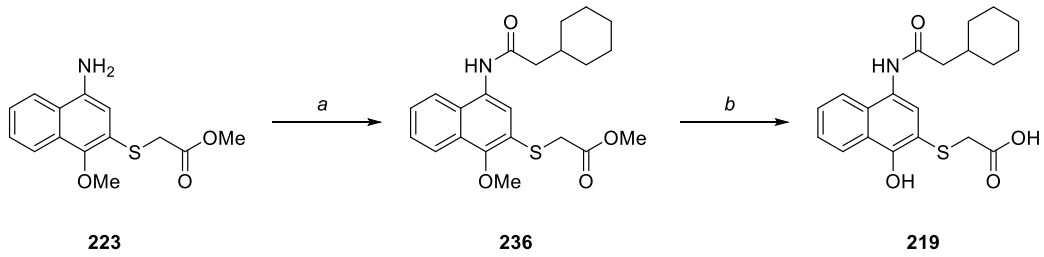

223 236 219

Scheme 56: Synthesis of cyclohexane derivative **219**. *Reagents and conditions*: Cyclohexaneacetic acid, HATU, DIPEA, CH_2Cl_2, 1 h, RT, 74% yield; (*b*) BBr_3, CH_2Cl_2, 0 °C to RT, 1 h, 51% yield.

4.6.2. Synthesis of Amide Derivative **220**

The synthesis of amide derivative **220** required acid **241**, which was synthesised according to literature procedures *via* a Chan-Lam oxidative coupling (**Scheme 57**).[442] Thus methyl 2-(4-hydroxyphenyl)acetate **238** and phenylboronic acid **239** gave ester **240** in poor yield of 45%, which was subsequently hydrolysed to give acid **241** in quantitative yield. A HATU-mediated amide coupling between aniline **223** and acid **241** to afford amide **242**, and purification *via* column chromatography cleanly isolated the product in good yield. Finally, the synthesis was completed using BBr_3 to globally deprotect both the methyl ester and methoxy group, furnishing the desired amide derivative **220** in 77% yield.

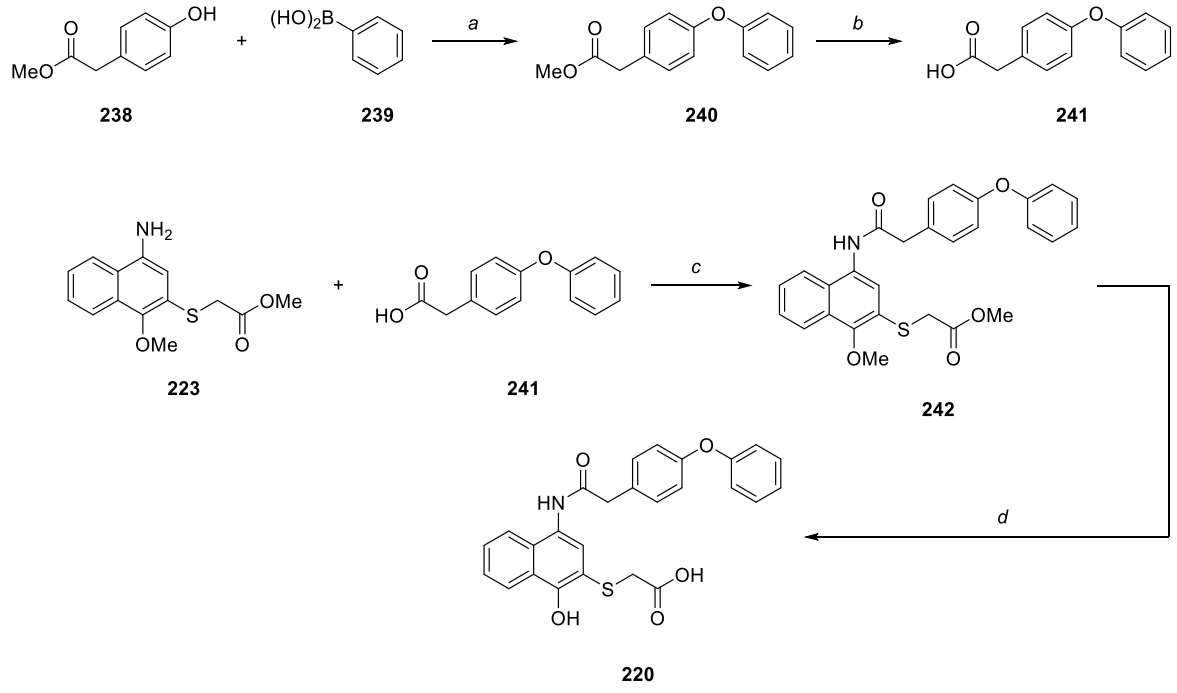

238 239 240 241

223 241 242

220

Scheme 57: Synthesis of amide derivative **220**. *Reagents and conditions*: (*a*) Pyridine, $Cu(OAc)_2$, CH_2Cl_2, RT, 24 h, 45% yield; (*b*) LiOH, THF, H_2O, RT, 30 min, 99%; (*c*) HATU, DIPEA, CH_2Cl_2, RT, 1 h, 77% yield; (*d*) BBr_3, CH_2Cl_2, 0 °C to RT, 1 h, 56% yield.

4.6.3. Synthesis of Pyrazole Derivative **221**

The synthesis of pyrazole derivative **221** began with the pyridine-mediated sulfonamide coupling between amine **223** and the commercially obtained 4-(1*H*-pyrazol-1-yl)benzenesulfonyl chloride **243**, which proceeded cleanly in excellent yield of 86% (**Scheme 58**). The subsequent global deprotection using BBr_3 gave the desired pyrazole derivative **221** in moderate yield of 47%.

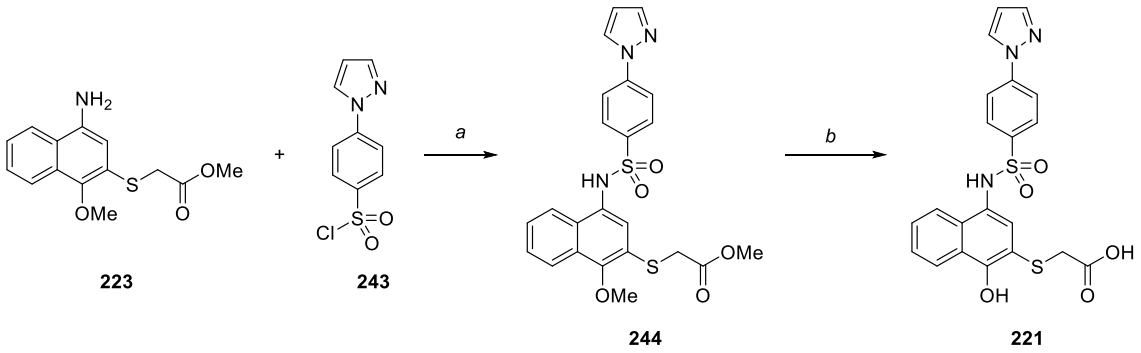

Scheme 58: Synthesis of pyrazole derivative **221**. *Reagents and conditions*: (*a*) Pyridine, CH_2Cl_2, RT, 3 h, 86% yield; (*b*) BBr_3, CH_2Cl_2, 0 °C to RT, 1 h, 47% yield.

4.6.4. Attempted Synthesis of Urea Derivative **222**

The synthesis of urea **222** required aniline **248**, which was prepared according to literature procedures using a S_NAr reaction between 1-fluoro-4-nitrobenzene **245** and phenol **246**, mediated by K_2CO_3 (**Scheme 59**).[443] This afforded the nitroarene **247** in poor yield. Reduction of the nitro group using $B_2(OH)_4$ gave aniline **248** in excellent yield. With this material in hand, aniline **223** was treated with CDI in an attempt to generate the urea intermediate **249**. Unfortunately, this resulted in no conversion of the starting material.

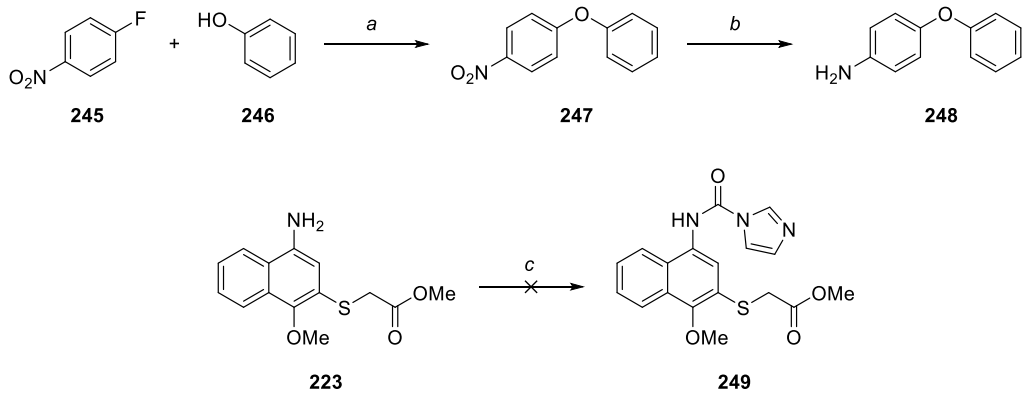

Scheme 59: Synthesis of amine **245** and attempted synthesis of urea intermediate **249**. *Reagents and conditions*: (*a*) K_2CO_3, DMF, RT, 24 h, 36% yield; (*b*) $B_2(OH)_4$, 4,4'-bipyridine, DMF, 0 °C to RT, 10 min, 97% yield; (*c*) CDI, cat. DMAP, MeCN, 82 °C, 3 h.

Consequently, we decided to activate aniline **223** for urea formation using bis(trichloromethyl) carbonate, also known as triphosgene. This allows for the convenient synthesis of carbamyl chlorides, as shown in **Scheme 60**. The nucleophilic amine initially attacks the carbonyl group. As the carbonyl group is regenerated, phosgene is eliminated, which can participate in subsequent reactions in a manner similar to that described. Further attack of chloride generates the carbamyl chloride, which may be treated with an amine to afford a urea.

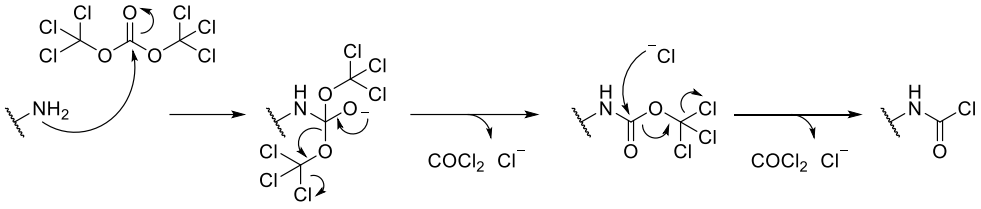

Scheme 60: Mechanism of triphosgene-mediated carbamyl chloride preparation.

Treatment of aniline **223** with triphosgene gave carbamyl chloride intermediate **249** (**Scheme 61**). Subsequently, carbamyl chloride **250** was treated with aniline **248**, which afforded urea **251** in overall yield of 26%. While little material was produced from this reaction, we nonetheless proceeded with the previously attempted BBr_3 global deprotection. Unfortunately, much of this material decomposed during the reaction and it was not possible to isolate a large enough quantity for characterisation and biological evaluation. Regrettably, time constraints prevented further attempts toward the synthesis of urea derivative **222**.

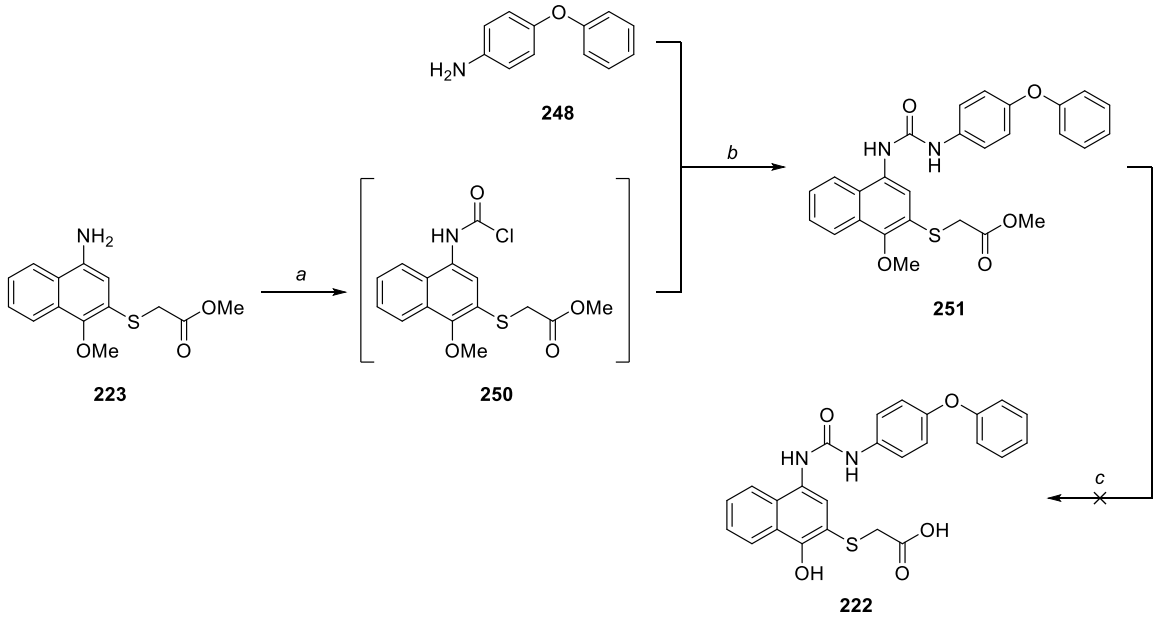

Scheme 61: Attempted synthesis of urea derivative **222**. *Reagents and conditions*: (*a*) triphosgene, Et_3N, CH_2Cl_2, 0 °C to RT, 4 h; (*b*) CH_2Cl_2, RT, 16 h, 11% yield; (*c*) BBr_3, CH_2Cl_2, 0 °C to RT, 1 h.

Further attempts to synthesise urea derivative **222** may centre on different approaches toward the formation of the urea in improved yield. A simple reversal of the coupling partners, shown in **Scheme 62** (*a*) may allow for more attempts at optimisation by using the less costly amine **248** to form carbamyl chloride **252**. Alternatively, by beginning with acid **253** in **Scheme 62** (*b*), this can be treated with diphenylphosphoryl azide (DPPA) to form acyl azide **254**, which may then undergo a Curtius rearrangement to give isocyanate **255**. The reaction of isocyanate **255** with aniline **223** then affords urea derivative precursor **251**.

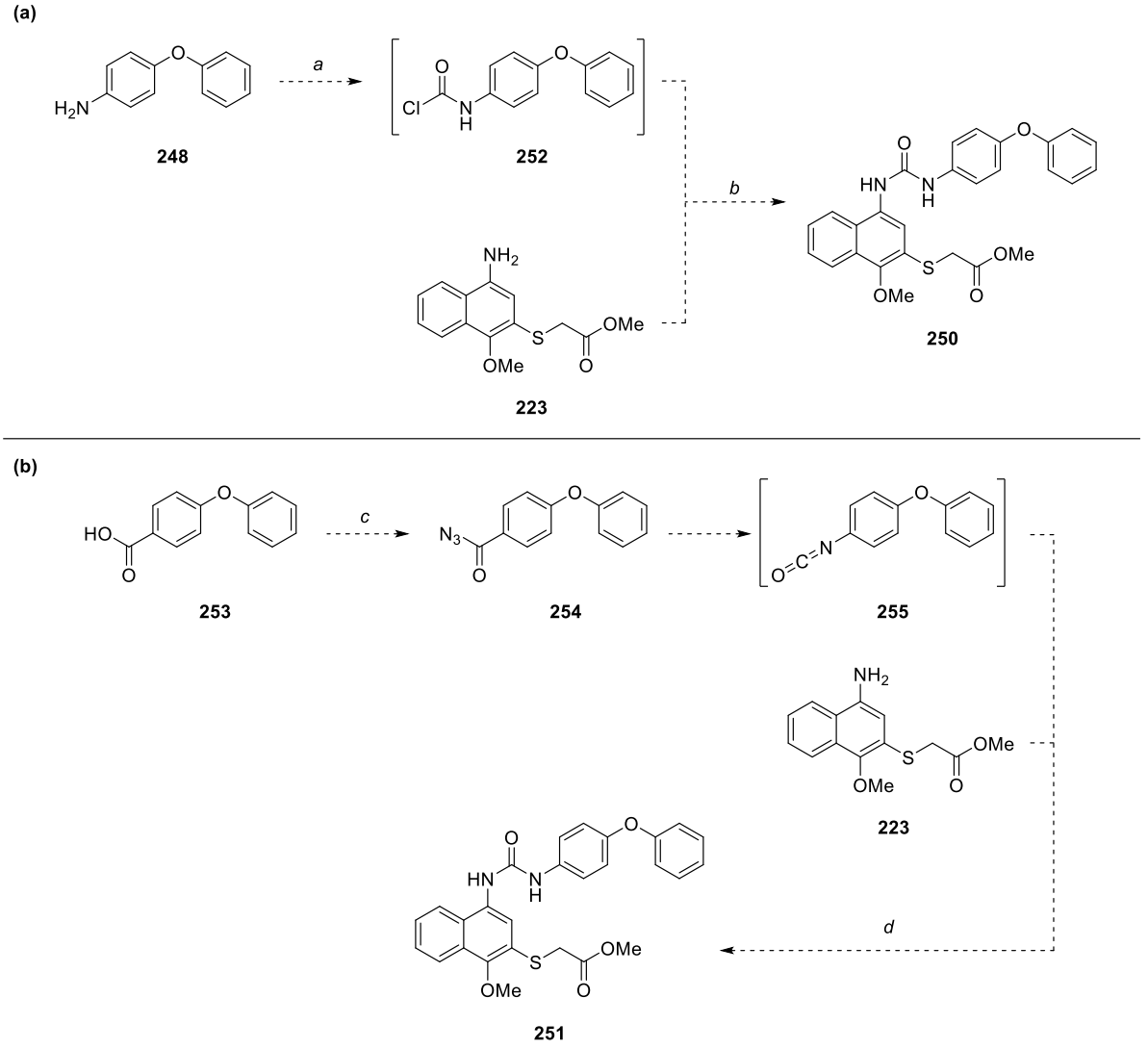

Scheme 62: Proposed synthesis of urea derivative precursor **251**. *Proposed reagents and conditions*: (*a*) triphosgene, Et_3N, CH_2Cl_2, 0 °C to RT, 4 h; (*b*) CH_2Cl_2, RT, 16 h; (*c*) DPPA, Et_3N, PhMe, 110 °C, 6 h; (*d*) CH_2Cl_2, RT, 16 h.

4.7. Biological Evaluation

The compounds synthesised in this chapter, **51**, **215** and **219**–**221**, were delivered for evaluation by August 2024. Assays are currently in progress and such data for this library will be reported in due course.

4.8. Concluding Remarks

In **Chapter 4**, the anti-apoptotic protein MCL-1 has been introduced as a promising target for senolytics. The work performed in this chapter aimed to develop new ligands for MCL-1 to further probe SAR around this biological target. Using known SAR information obtained *via* thorough experimentation of the pharmacophore, we designed novel derivatives of UMI-77 **51**. A docking study then highlighted compounds which were likely to possess strong binding affinity to MCL-1, demonstrating that the protein-ligand interactions were similar to those proposed by Nikolovska-Coleska and coworkers.[419] The synthetic methods detailed in this chapter provide a discussion of the challenges associated with the preparation of these new analogues, particularly optimisation required for the thiolation of naphthalene **227**. Future work could focus on the rapid diversification of this library using amide and sulfonamide coupling methodologies to explore previously unknown chemical space.

As with **Chapter 3**, the biological evaluation of the compounds described in this chapter is still ongoing, and it is hoped that this assay data will provide vital new insights into strong binders of MCL-1. Probing of SAR continues to be a fascinating topic which attracts significant attention from the medicinal chemistry community and will provide key information in the quest to discover novel senolytics.

This Page Intentionally Left Blank

Chapter 5

Summary and Future Work

Chapter 5 – Summary and Future Work

5.1. Summarising Remarks

Neurodegenerative disease presents a major current and future health challenge as global life expectancies increase and the cost of medical care climbs. Current small-molecule treatments have shown no disease-modifying effect and thus far, all dementias have fatal prognoses.[444] This work has presented the increasing burden of cellular senescence, and the sustained release of SASP factors, as a hallmark of neurodegenerative disease. In particular, the BCL-2 family of proteins was identified as a group of key mediators in SCAPs, suggesting potential druggable targets to induce apoptosis in SCs.[262] This work has exemplified various strategies within medicinal chemistry to design and synthesise novel small chemotypes as senolytics. An iterative reconstruction approach, traditional SAR probing, 4° scaffold hopping and computationally aided ligand design have all been utilised for the generation of novel compounds. Biological evaluation of the compounds synthesised is in progress, and the results of these studies will be disclosed in due course. Nonetheless, this work has expanded the breadth of knowledge in senolytic treatments and represents valuable preliminary steps in the amelioration of neurodegeneration.

5.1.1. Summary of Chapter 2

Chapter 2 highlighted work conducted by Abbott Laboratories in the development of BCL-X_L inhibitor **57**.[334] The further development of this compound led to **53**,[342] ABT-737 **46**[333] and ABT-263 **47**,[332] of which the latter two were reported as possessing sub-nanomolar binding affinity to BCL-X_L and BCL-2. We therefore undertook an iterative reconstruction of **57** in an attempt to determine the minimum pharmacophore required for binding to BCL-2. This resulted in the synthesis of ten derivatives, building up the molecule in three stages: (1) expansion of the carboxylic acid side; (2) expansion of the sulfonamide side; and (3) expansion of the amine tail. Together, this gave compounds **58**–**67** in addition to the lead compound **57** (**Figure 53**). Unfortunately, biological evaluation *via* TR-FRET assay (for BCL-X_L) and AlphaScreen® assay (for BCL-2) indicated that no significant binding occurred between either target protein or the compounds prepared.

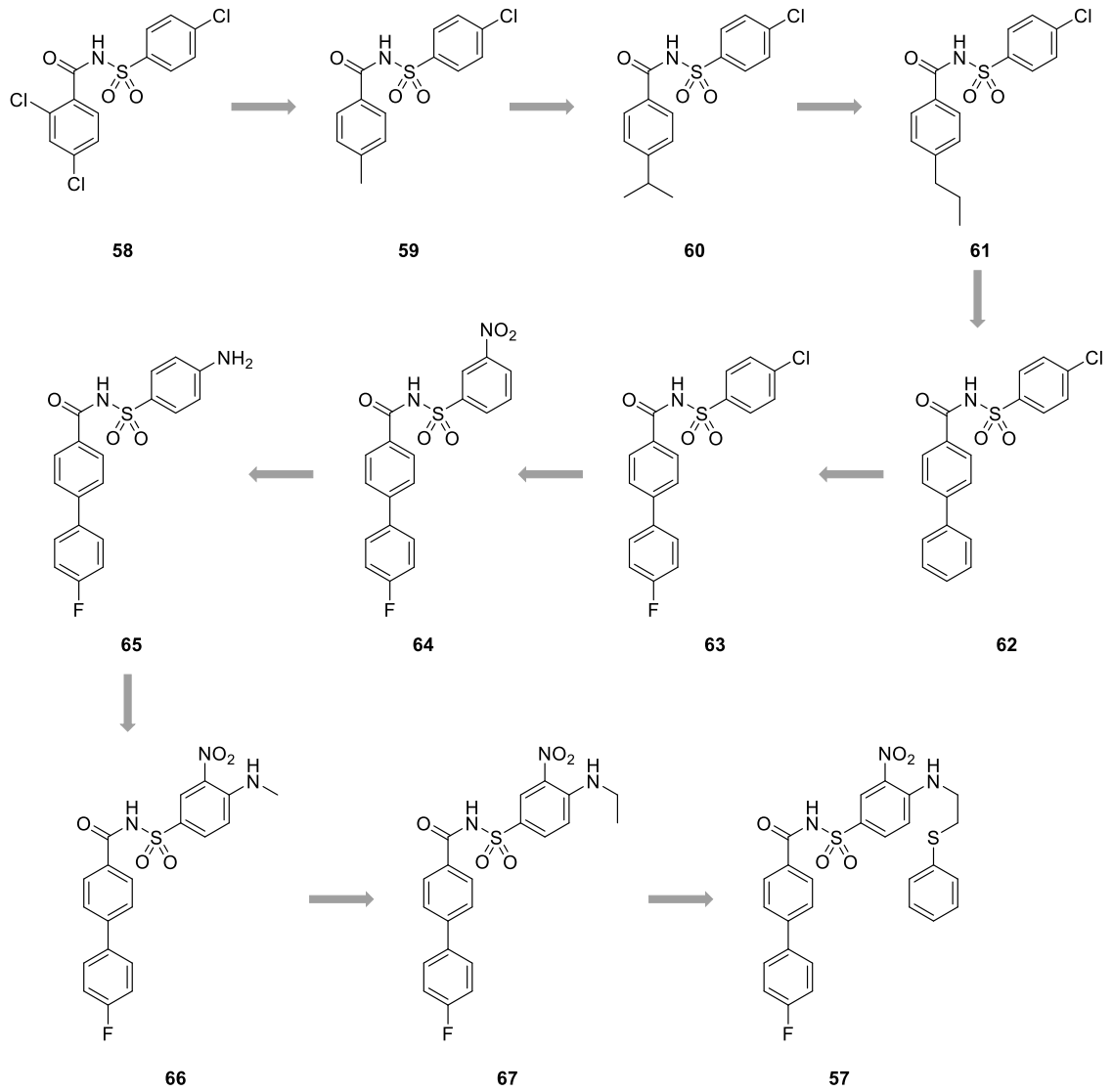

Figure 53: Compounds synthesised as part of the iterative reconstruction described in **Chapter 2**.

Given these results, we therefore designed adamantane analogues of this library to further probe structure-activity relationships with previously unexplored chemical motifs. Binding affinity between these analogues and BCL-X_L was modelled using molecular docking studies, which indicated that analogues **99**–**101** were especially strong binders. The synthesis of this library gave compounds **87**, **90**, **93**, **96** and **99** (*n* = 0 linkers), **88**, **91**, **94**, **97** and **100** (*n* = 1 linkers) and **89**, **92**, **95**, **98** and **101** (*n* = 2 linkers) through the replacement of the carboxylic acid side with various adamantane carboxylic acids (**Figure 54**). However, biological evaluation using the aforementioned assays also revealed that none of these were effective ligands for BCL-X_L. Consequently, this data spurred us to explore alternative senolytic chemotypes.

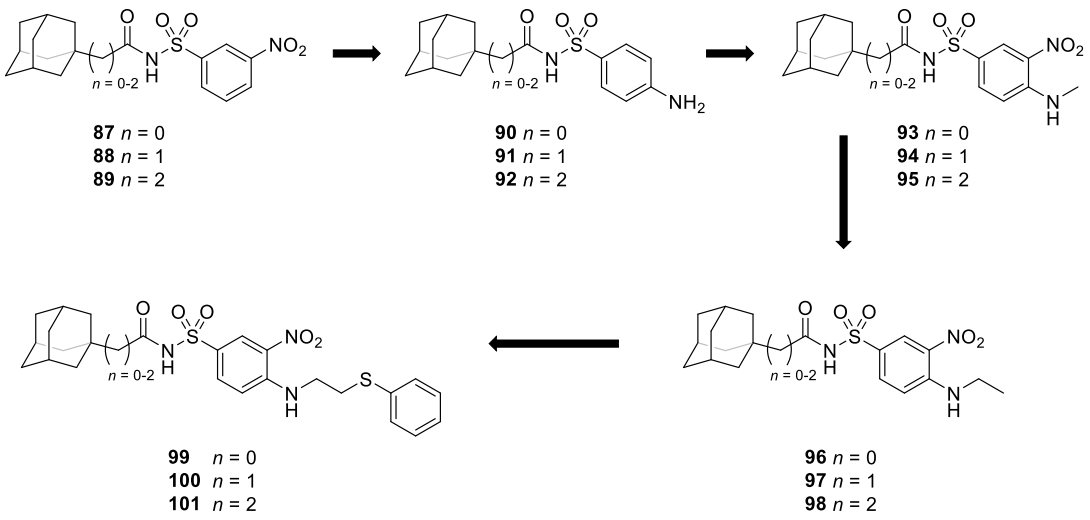

Figure 54: To further probe SAR, adamantane analogues of compounds **87**–**101** were also synthesised in **Chapter 2**.

5.1.2. Summary of Chapter 3

A broad overview of scaffold hopping was presented as the basis for work conducted in **Chapter 3**. The development of compounds **126** and **127** highlighted interesting new lead compounds which were extremely potent against BCL-X_L (**Figure 55**).[375, 378] We subsequently performed scaffold hopping on different segments of these compound using Spark software. In particular, these results were filtered for structures that shared greater than 80% similarity to their respective leads. To further validate our methodology, the binding modes of these compounds were further investigated *via* molecular docking studies. This work showed that many of these compounds were predicted to have similar or greater binding affinity than the leads.

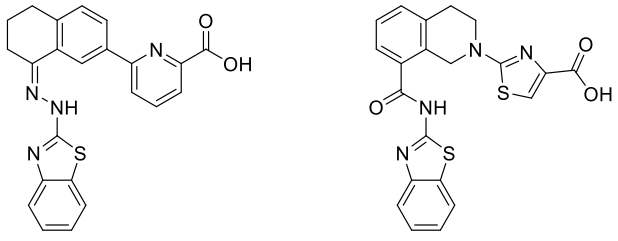

Figure 55: Lead compounds used for scaffold hopping in **Chapter 3**.

This chapter details the synthetic efforts which successfully furnished the lead compounds **126** and **127**; cyclopropane derivative **139**; cyclobutane derivative **140**; alkyne derivative **141**; naphthalene derivative **142**; and amide derivative **144** (**Figure 56**). Indeed, at various points during synthetic pathways it was necessary to modify initial plans adapted from

retrosynthetic analysis. Efforts to prepare tetrazole derivative **143** and urea derivative **145** were also discussed, but unfortunately these syntheses could not be completed due to time constraints. The biological evaluation of the completed compounds is currently in progress.

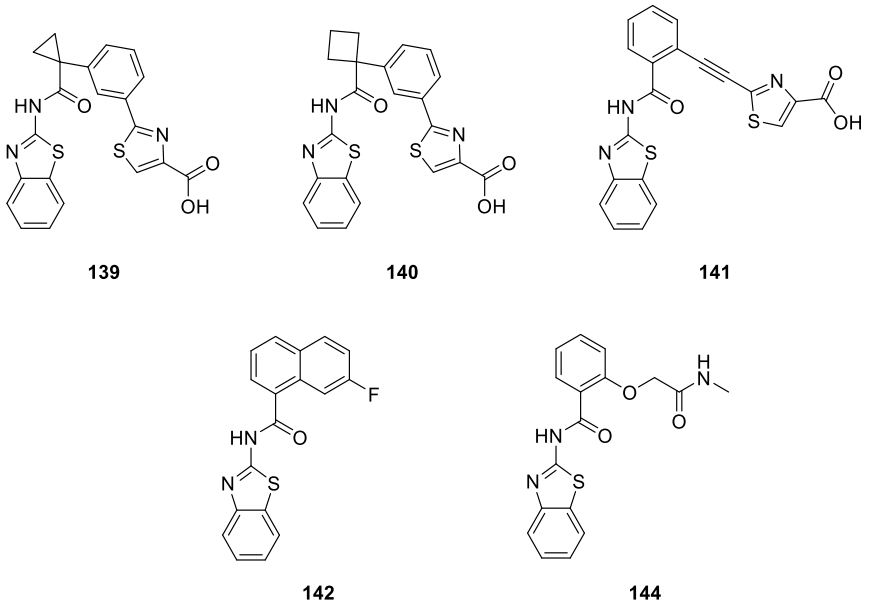

Figure 56: Compounds generated *via* scaffold hopping and subsequently synthesised as discussed in **Chapter 3**.

5.1.3. Summary of Chapter 4

In **Chapter 4**, a new target protein was presented: MCL-1, another member of the BCL-2 family implicated as a SCAP which ensures the survival of SCs. The compounds UMI-77 **51** and **215** developed by Nikolovska-Coleska and co-workers, showed good binding affinity to MCL-1 (**Figure 57**).[419] We thus chose to use these as lead compounds in this chapter. Aided by the results of the authors' SAR studies, we designed a library of similar compounds containing various modifications to explore previously unknown analogues. Molecular docking studies were then performed, identifying derivatives **219**–**222** with promising biological activity.

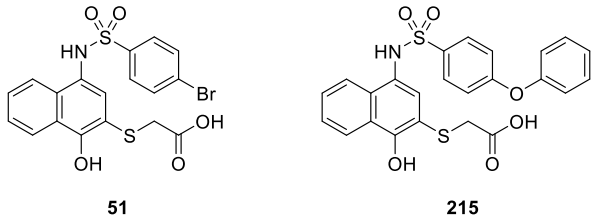

Figure 57: Compounds **51** and **215** were identified as leads for **Chapter 4**.

The synthetic efforts of **Chapter 4** describe pathways which furnished the lead compounds **51** and **215**, as well as derivatives **219**–**221** (**Figure 58**). Also discussed are efforts to prepare the urea derivative **222**, which were unfortunately prevented from reaching fruition

due to constraints of time. In a similar vein to **Chapter 3**, the results of biological evaluation for compounds synthesised in this chapter are still pending.

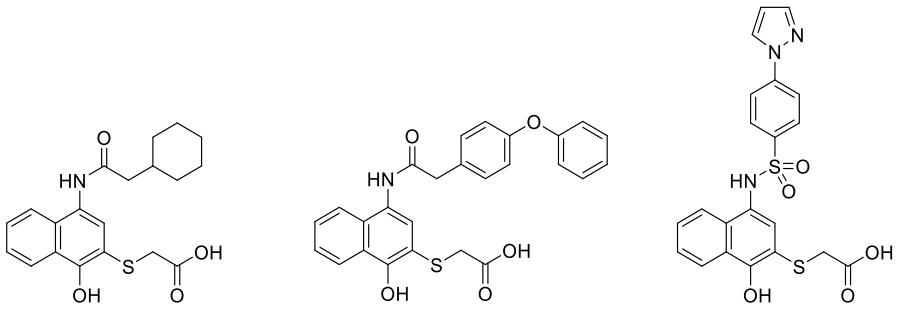

Figure 58: Compounds **219**–**221** were designed using the SAR results from Nikolovska-Coleska and co-workers and subsequently synthesised in **Chapter 4**.

5.2. Future Work

Each of the above chapters offers significant scope for future undertakings in the identification of novel senolytic chemotypes. Indeed, further investigations into the structures prepared throughout **Chapters 2**–**4** have potential to reveal new functionalities with the ability to hinder the activity of SCAPs. Despite the identification of a myriad of senolytic small molecules as discussed in **Chapter 1.5.2.**, the use of these as drug treatments is still in its infancy. The work described in this thesis presents work to further the scope of known senolytics and provided insight into the challenges associated with doing so. Undoubtedly, the results of pending biological evaluation of compounds prepared in this work will influence future directions within the Kassiou group. Nonetheless, the future of such research is bright, and many avenues exist in which to continue this research and explore even more novel chemotypes.

5.2.1. Traditional SAR Methodologies

Of the senolytic compounds discussed in **Chapter 1.5.2.**, few of these have been rigorously explored and probed for SAR. The derivatisation of small molecules is an especially potent strategy to discover novel chemotypes. Molecules such as the USP7 inhibitors P5091 **38** and P22077 **39** are strong candidates for this type of work. Of particular note regarding these compounds is that they are not known as inhibitors of the BCL-2 family, and therefore the targeting of different SCAPs could advance future treatment options and yield new insights into senolytic pathways. A representative example of the kind of derivatisation which may be

attempted on is given in **Figure 59**, wherein the structures of P5091 **38** and P22077 **39** could each be expanded upon *via* a Topliss scheme or a complete Hansch analysis.[338, 445]

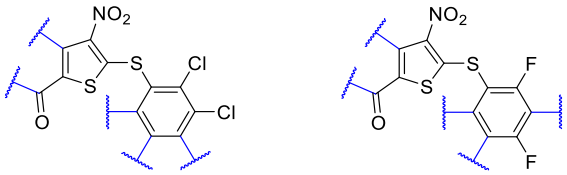

P5091 **38** P22077 **39**

Figure 59: Structures of P5091 **38** and P22077 **39**, showing sites for derivatisation in **blue**.

This would apply a logical workflow to the design of senolytic chemotypes and regardless of biological activity, is sure to lend valuable insights into the mechanism by which these compounds act. Indeed, following the Topliss scheme allows for rapid generation of a large library of compounds, which would greatly expand both chemical space and understanding of SAR around their biological target. Similarly, undertaking a Hansch analysis in the different positions seen in **Figure 59** would lead to rapid molecular diversification and even furnish insights into quantitative SAR (QSAR). Such a methodology may even be exploited for the design of *de novo* ligands for the target proteins. Further derivatisation work could even focus on the late-stage functionalisation of these molecules to both improve potency and drug-like molecular properties.[446-449]

5.2.2. Further Scaffold Hopping

Although only 4° scaffold hopping was undertaken throughout this work, other types of scaffold hopping were discussed in **Chapter 3.4.**, namely heterocyclic replacement; ring opening or closure; and pseudopeptide or peptidomimetic replacement.[380] These strategies introduce smaller structural modifications to molecules than 4° scaffold hopping and therefore have greater likelihood to produce compounds with similar binding modes and affinities to their parent molecules. An example of such rescaffolding is shown in **Figure 60** for piperlongumine **30**.

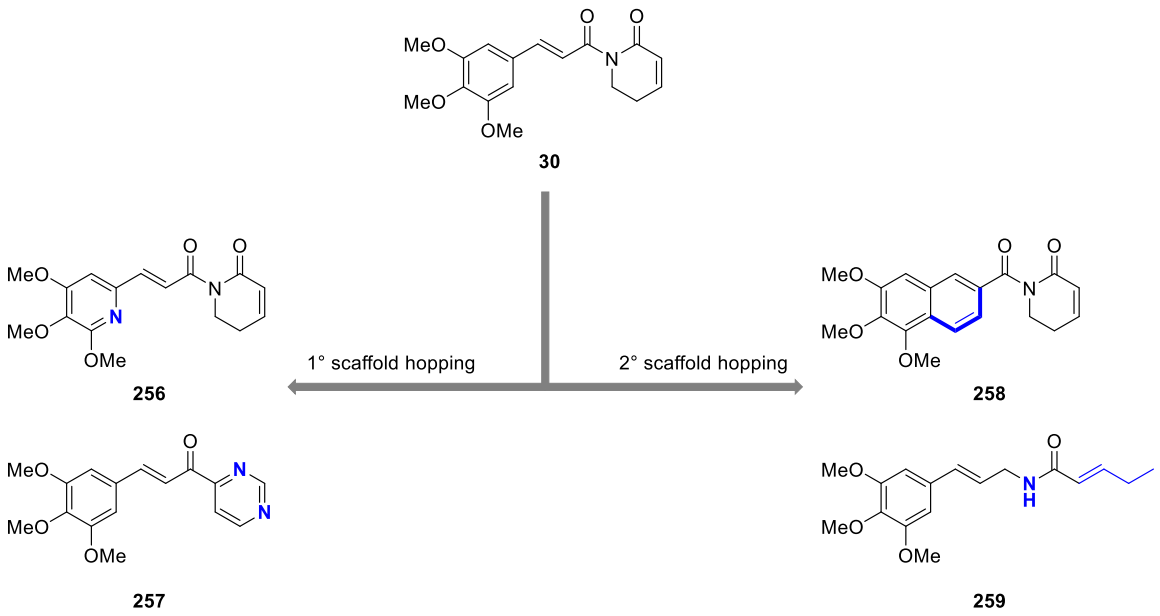

Figure 60: Potential 1° and 2° scaffold hopping of piperlongumine **30**, with heterocyclic replacement, ring closing and ring opening highlighted in **blue**.

1° scaffold hopping could take the form of heterocyclic replacement of either the phenyl ring or lactam. This could give a pyridine as shown in **256**, or pyrimidine as shown in **257**. In a similar manner, potential 2° scaffold hopping could involve ring closing to afford a naphthalene as shown in **258**, or ring opening to give the amide as shown in **259**. It may not be possible to perform 3° scaffold hopping on **30**, as it does not possess peptidic structures required to undertake such a methodology. Nonetheless, the realm of possibilities can be expanded even further by considering 4° scaffold hops undertaken in **Chapter 3**.

5.2.3. PROTAC Design

In recent years, proteolysis-targeting chimera (PROTAC) design become one of the most exciting and rapidly advancing fields within medicinal chemistry research.[450] PROTACs generally consist of three sections: (1) a ligand binding to the target protein; (2) a linker; and (3) a ligand binding to an E3 ligase. By forming a ternary complex between the target protein and an E3 ligase, the target protein is ubiquitinylated and subsequently degraded by the ubiquitin-proteosome system.[450] This is in part due to the fundamental problems that PROTACs were initially purported to address, and the promising biological data observed throughout literature. Indeed, Zhou and coworkers have already reported DT2216 **260** (**Figure 61**), a PROTAC which has shown effective degradation of BCL-X_L.[451] **260** is derived from the aforementioned ABT-263 **47** and the VHL ligand.

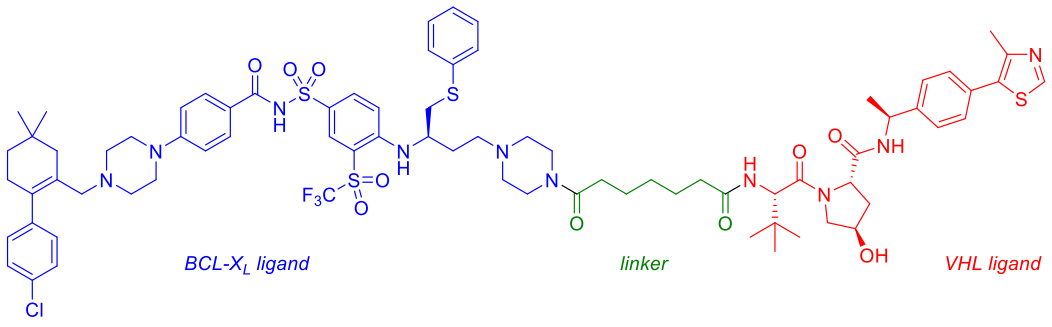

260

Figure 61: Structure of DT2216 **260**, a known degrader of BCL-X_L. The BCL-X_L ligand ABT-263 is shown in **blue**, the linker is shown in **green**, and the VHL ligand is shown in **red**.

If any of the newly developed MCL-1 ligands synthesised in **Chapter 4** possess greater binding affinity than their lead compound **215**, then this may encourage the design of new PROTACs for this member of the BCL-2 family. Some proposed structures of these PROTACs are shown in **Figure 62**, showing MCL-1 as a representative example of the target protein ligand and the common E3 ligase recruiting units lenalidomide **261**, pomalidomide **262** and VHL ligand 1 **263**. While this exploration is only speculative, however inducing senolysis *via* use of PROTACs could create exciting new therapeutic opportunities.

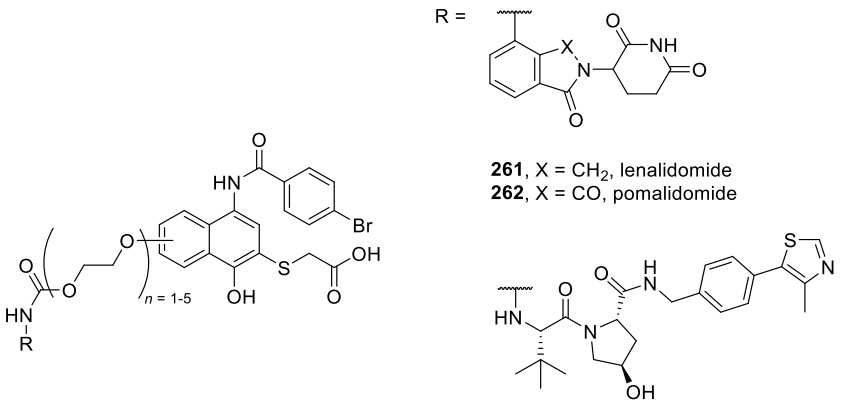

261, X = CH_2, lenalidomide
262, X = CO, pomalidomide

263, VHL ligand 1

Figure 62: Proposed structures of PROTACs derived from UMI-77 **51**.

The drug discovery of senolytics is still an emerging field, although it is encouraging to see the vast array of identified compounds that have been observed to carry out this function. The continued investigation into small-molecule senolytic chemotypes, as well as SCAPs that are yet unknown, will play a crucial role in the treatment of neurodegeneration.

5.3. Final Concluding Remarks

The effect and burden of dementias on patients, carers and healthcare systems worldwide cannot be understated.[452] As global life expectancies increase, these issues are only poised to grow in magnitude and scale. This work has attempted to tackle just one facet of this enormous challenge. The body of work represents different ways in which medicinal chemistry may propose solutions to neurodegenerative disease, namely through techniques which generate novel and unexplored structures. These include the iterative reconstruction of **Chapter 2**; scaffold hopping in **Chapter 3**; and traditional SAR probing in **Chapter 4**. Alongside this, molecular docking studies have been applied to supplant and inform the selection of compounds within libraries. If these structures demonstrate biological activity, they represent exciting opportunities to further knowledge in the medical field, but also in organic chemistry through the implementation of synthetic methodologies. Future investigations should utilise this work as laying the ground for new efforts towards treatments for neurodegenerative disease. It is hoped that this research will also provide inspiration for how medicinal chemistry methods may be applied to existing structures in literature to generate novel scaffolds for other disease models, such as cancer, social dysfunction or cardiovascular disease.

Neurodegeneration has affected people since antiquity[6] and despite more than 100 years of modern medical research, massive gaps are still present in our understanding of the genesis and progression of these disease states. The conditions will no doubt be with us for the long-term future, continuing to affect millions of people and adding costs to economies worldwide. The research discussed in this thesis is but one step in the marathon of tackling such an enormous challenge.

This Page Intentionally Left Blank

This Page Intentionally Left Blank

Chapter 6

Experimental

Chapter 6 – Experimental

6.1. General Experimental

Unless otherwise stated, all solvents and reagents were purchased and used from commercial sources. Anhydrous solvents were obtained from an Innovative Technology PureSolv7 purification system. Tetrahydrofuran, dichloromethane, toluene and 1,4-dioxane were dried on 4 Å molecular sieves, while methanol and ethanol were dried on 3 Å molecular sieves. All reagents were weighed out under ambient conditions. All reactions were performed under nitrogen or argon, unless otherwise stated.

Analytical thin-layer chromatography (TLC) was performed using Merck aluminium backed silica gel 60 F254 (0.2 mm) plates, which were visualised with shortwave (254 nm) ultraviolet light. Products were also visualised with potassium permanganate, vanillin, cerium molybdate, bromocresol green or ninhydrin stains. Flash column chromatography was performed using Merck Kieselgel 60 (230-400 mesh) silica gel or using a Biotage® Selekt flash purification system, using Biotage® Sfär HC, Biotage Sfär C18 or Velocity Silica pre-packed columns, with the eluent mixture reported as the volume:volume ratio.

IR spectra were recorded neat using a Bruker ALPHA FT-IR spectrometer and peaks are expressed in wavenumbers (cm^{-1}). Low-resolution mass spectra (LRMS) were recorded using electrospray ionisation (ESI) recorded on a Bruker AmaZon SL ion trap spectrometer. High-resolution mass spectrometry (HRMS) was performed on a Bruker Apex Qe 7T Fourier Transform Ion Cyclotron Resonance mass spectrometer equipped with an Apollo II ESI/MALDI dual source. Samples were run with syringe infusion at 150 μL/h on a Cole Palmer syringe pump into the ESI source. HRMS samples were run by Dr. Nicholas Proschogo. Nuclear magnetic resonance spectra were recorded at 300 K using either a Bruker AVANCE DRX300 (300 MHz), AVANCE DRX400 (400 MHz) or AVANCE DRX500 (500 MHz) spectrometer. ^{1}H chemical shifts are expressed as parts per million (ppm) with residual chloroform (δ 7.26), dimethyl sulfoxide (δ 2.50) and acetone (δ 2.05) as reference and are reported as chemical shift (δ); multiplicity (s = singlet, br s = broad singlet, d = doublet, dd = doublet of doublets, dt = doublet of triplets, dp = doublet of pentets, ddd = doublet of doublets of doublets, dddd = doublet of doublets of doublets of doublets, dtd = doublet of triplets of doublets, dtt = doublet of triplets of triplets, t = triplet, td = triplet of doublets, tdd = triplet of doublet of doublets, tt = triplet of triplets, q = quartet, p = pentet, hept = heptet, m = multiplet); coupling constants (*J*) reported in Hz; relative integral. Proton decoupled ^{13}C chemical shifts

are expressed as parts per million (ppm) with residual chloroform (δ 77.16), dimethyl sulfoxide (δ 39.52) and acetone (δ 29.84) as reference and reported as chemical shift (δ); multiplicity (d = doublet, m = multiplet); coupling constants (*J*) reported in Hz. Proton decoupled ^{19}F chemical shifts are reported as parts per million (ppm) with no reference. High performance liquid chromatography (HPLC) analysis of organic purity was conducted on a Waters Alliance 2695 instrument using a SunFire™ C18 column (5 μm, 2.1 × 150 mm) and detected using a Waters 2996 photodiode array detector set at 254 nm. Separation was achieved using H_2O + 0.1% TFA (solvent A) and MeCN + 0.1% TFA (solvent B) at a flow rate of 0.2 mL/min and a gradient of 0% B to 100% B over 30 minutes. HPLC data are reported as percentage purity and retention time (R_T) in minutes.

6.2. General Procedures

General Procedure A: *Sulfonamide Coupling*

A solution of carboxylic acid (1.0 equiv.), primary sulfonamide (1.2 equiv.), 1-ethyl-3-(3-dimethylaminopropyl)carbodiimide HCl salt (EDC·HCl, 1.2 equiv.) and 4-(dimethylamino)pyridine (DMAP, 0.5 equiv.) in CH_2Cl_2 (5 mL) was stirred at RT for 16 h. The solvent was evaporated under a gentle stream of N_2, then the crude residue was partitioned between EtOAc and 1 M HCl. The mixture was extracted with EtOAc (×3), then the combined organic layers were washed with brine, then dried ($MgSO_4$). The solvent was evaporated under reduced pressure. Purification procedures are described for each compound.

General Procedure B: *Nucleophilic Aromatic Substitution*

A solution of aryl chloride (1 equiv.) and primary amine (5 equiv.) in DMSO (2 mL) was heated at 100 °C in a sealed tube for 16 h. The solution was diluted with H_2O and extracted with EtOAc (×3). The combined organic layers were washed with brine, then dried ($MgSO_4$). The solvent was evaporated under reduced pressure. Purification procedures are described for each compound.

General Procedure C: *Bechamp Reduction*

To a solution of nitro compound (1 equiv.) in ethanol (5 mL) was added Fe powder (0.10 g) and a solution of NH_4Cl (0.10 g) in H_2O (0.5 mL). The mixture was stirred vigorously at reflux for 1 h. The mixture was concentrated, then partitioned between H_2O and EtOAc, then filtered through a plug of celite. The filtrate was extracted with EtOAc (×3). The combined organic

layers were washed with brine, then dried ($MgSO_4$). The solvent was evaporated under reduced pressure. Purification procedures are described for each compound.

General Procedure D: *Amide Coupling*

A solution of carboxylic acid (1 equiv.), hexafluorophosphate azabenzotriazole tetramethyl uranium (HATU, 1.2–1.5 equiv.) and diisopropylethylamine (DIPEA, 2–3 equiv.) in CH_2Cl_2 (10 mL) was pre-stirred at RT for 15 min, then primary amine (2 equiv.) was added. The reaction was stirred for 1 h at RT, then the solution was concentrated under a gentle stream of N_2, then the crude residue was partitioned between EtOAc and 1 M HCl. The mixture was extracted with EtOAc (×3), then the combined organic layers were washed with brine, then dried ($MgSO_4$). The solvent was evaporated under reduced pressure. Purification procedures are described for each compound.

General Procedure E: *Ester Hydrolysis*

A solution of ester (1 equiv.) and LiOH (5 equiv.) in 1:1 THF/H_2O (5 mL) was stirred at RT for 30 min. When the reaction was complete, 1 M HCl was added, then the solution was extracted with EtOAc (×3). The combined organic layers were washed with brine, then dried ($MgSO_4$). The solvent was evaporated under reduced pressure to yield the product with no further purification.

General Procedure F: *Miyaura Borylation*

A mixture of aryl bromide (1 equiv.), bis(pinacolato)diboron (B_2pin_2, 1.2 equiv.), KOAc (3 equiv.) and bis(diphenylphosphino)ferrocene)palladium(II) dichloride ($Pd(dppf)Cl_2$, 5 mol %) were dried under vacuum. Concurrently, DMF (5 mL) was degassed under N_2. The solvent was then added to the solvents, and the mixture was heated at 100 °C for 16 h. When the reaction was complete, the mixture was diluted with 3 M aq. NaCl solution, then the solution was extracted with EtOAc (×3). The combined organic layers were washed with brine, then dried ($MgSO_4$). The solvent was evaporated under reduced pressure. Purification procedures are described for each compound.

General Procedure G: *Sulfonamide coupling*

To a solution of amine (1 equiv.) and sulfonyl chloride (1–1.5 equiv.) in CH_2Cl_2 (2.5 mL) was added pyridine (1.5 equiv.), then the solution was stirred at RT for 16 h. When the reaction was

complete, the reaction mixture was diluted with 1 M aq. HCl solution and extracted with EtOAc (×3). The combined organic layers were washed with brine, then dried ($MgSO_4$). The solvent was evaporated under reduced pressure. Purification procedures are described for each compound.

General Procedure H: *Demethylation*

A solution of methoxy compound (1 equiv.) in CH_2Cl_2 (1.5 mL) was cooled in an ice-water bath, then BBr_3 (3–5 equiv.) was added dropwise. The solution was allowed to warm to RT and stirred for 1 h. When the reaction was complete, the reaction mixture was carefully poured in sat. aq. NH_4Cl solution to quench excess BBr_3, then extracted with EtOAc (×3). The combined organic layers were washed brine, then dried ($MgSO_4$). The solvent was evaporated under reduced pressure. Purification procedures are described for each compound.

6.3. Experimental and Characterisation for Chapter 2

4-Chlorobenzenesulfonamide **72**

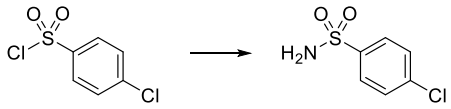

71 **72**

A solution of 4-chlorobenzenesulfonyl chloride **71** (3.5 g, 16.6 mmol) in 26-28% aq. NH_3 (30 mL) was heated at 50 °C for 2 h. The solvent was evaporated, and to the crude residue was added cold H_2O to dissolve any NH_4Cl. The mixture was filtered and the residue collected to yield sulfonamide **72** as a white solid (3.12 g, 98%). **LRMS** (−ESI) *m/z* 190 $[M-H]^-$; **^{1}H NMR** (300 MHz, DMSO-d_6) δ 7.86 – 7.81 (m, 2H), 7.67 – 7.63 (m, 2H), 7.39 (br s, 2H) ppm; **^{13}C NMR** (75 MHz, DMSO-d_6) δ 143.0, 136.6, 129.1, 127.6 ppm. Characterisation data were consistent with literature.[453]

2,4-Dichloro-N-((4-chlorophenyl)sulfonyl)benzamide **58**

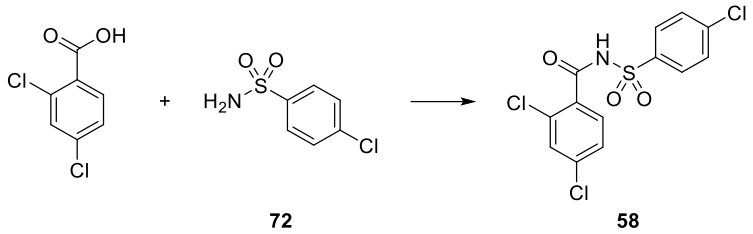

72 **58**

Using **General Procedure A**, 2,4-dichlorobenzoic acid (0.19 g, 1.0 mmol) and 4-chlorobenzenesulfonamide **72** (0.23 g, 1.2 mmol) gave the title compound. The crude residue was purified by flash column chromatography (20-40% EtOAc/hexanes), then recrystallised from EtOH to yield *N*-acylsulfonamide **71** as white crystals (0.26 g, 72%). **IR** (neat, diamond cell) ν 3243, 3094, 3087, 1719, 1583, 1421, 1341, 1177, 1167, 1100, 1080, 1044, 890, 822, 784, 753, 614 cm^{-1}; **LRMS** (−ESI) *m/z* 362, 364 $[M-H]^-$*;* **HRMS** Calcd for $C_{13}H_7Cl_3NO_3S^-$ $[M-H]^-$: *m/z* 361.92177, 363.91882, 365.91587, found *m/z* 361.92180, 363.91885, 365.91590; ^{1}**H NMR** (400 MHz, $CDCl_3$) δ 8.87 (br s, 1H), 8.09 (d, *J* = 8.0 Hz, 2H), 7.21 (d, *J* = 6.8 Hz, 1H), 7.56 (d, *J* = 8.0 Hz, 2H), 7.45 (d, *J* = 2.1 Hz, 1H), 7.35 (dd, *J* = 6.8 Hz, 2.1 Hz, 1H) ppm; **^{13}C NMR** (101 MHz, $CDCl_3$) δ 169.4, 139.0, 137.4, 135.5, 130.9, 130.0, 129.8, 129.6, 129.6, 129.1, 129.0 ppm; **HPLC** (254 nm) R_T = 25.96 min, 98.45%. Characterisation data were consistent with literature.[344]

N-((4-Chlorophenyl)sulfonyl)-4-methylbenzamide **59**

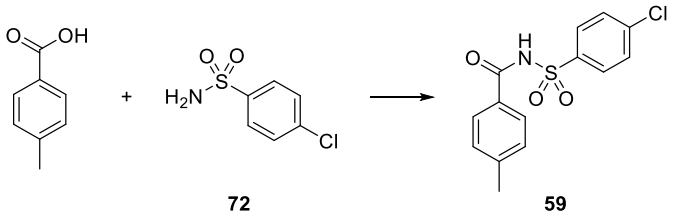

72 **59**

Using **General Procedure A**, *p*-toluic acid (0.14 g, 1.0 mmol) and 4-chlorobenzenesulfonamide **72** (0.23 g, 1.2 mmol) gave the title compound. The crude residue was purified by flash column chromatography (20-40% EtOAc/hexanes), then recrystallised from EtOH to yield *N*-acylsulfonamide **59** as white crystals (0.19 g, 60%). **IR** (neat, diamond cell) ν 3178, 3116, 3096, 1670, 1442, 1361, 1180, 1078, 820, 750, 613 cm^{-1}; **LRMS** (−ESI) *m/z* 308 $[M-H]^-$*;* **HRMS** Calcd for $C_{14}H_{11}{}^{35}ClNO_3S^-$ $[M-H]^-$: *m/z* 308.01537, found *m/z* 308.01523; ^{1}**H NMR** (400 MHz, $CDCl_3$) δ 9.26 (br s, 1H), 8.13 – 8.05 (m, 2H), 7.74 – 7.66 (m, 2H), 7.55 – 7.47 (m, 2H), 7.22 (d, *J* = 8.0 Hz, 2H), 2.37 (s, 3H) ppm; **^{13}C NMR** (101 MHz,

$CDCl_3$) δ 164.3, 144.7, 140.8, 137.0, 130.2, 129.7, 129.3, 128.1, 127.9, 21.6 ppm; **HPLC** (254 nm) R_T = 24.71 min, 98.36%.

N-((4-Chlorophenyl)sulfonyl)-4-isopropylbenzamide **60**

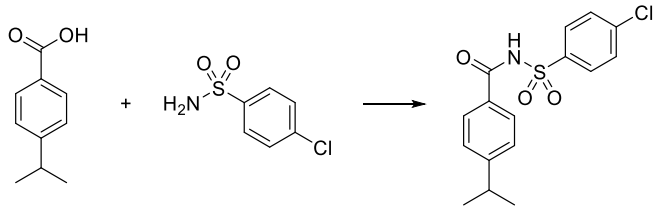

72 **60**

Using **General Procedure A**, cumic acid (0.16 g, 0.97 mmol) and 4-chlorobenzenesulfonamide **72** (0.23 g, 1.2 mmol) gave the title compound. The residue was recrystallised from EtOH to yield *N*-acylsulfonamide **60** as white crystals (0.073 g, 22%). **IR** (neat, diamond cell) ν 3273, 3099, 2967, 2872, 1688, 1427, 1408, 1342, 1171, 1083, 1054, 1015, 826, 766, 753, 618 cm^{-1}; **LRMS** (−ESI) *m/z* 336 $[M-H]^-$; **HRMS** Calcd for $C_{16}H_{15}{}^{35}ClNO_3S^-$ $[M-H]^-$: *m/z* 336.04667, found *m/z* 336.04657; **^{1}H NMR** (400 MHz, $CDCl_3$) δ 8.95 (br s, 1H), 8.14 – 8.06 (m, 2H), 7.75 – 7.67 (m, 2H), 7.56 – 7.48 (m, 2H), 7.29 (d, *J* = 8.2 Hz, 2H), 2.94 (hept, *J* = 6.9 Hz, 1H), 1.24 (d, *J* = 7.0 Hz, 6H) ppm; **^{13}C NMR** (101 MHz, $CDCl_3$) δ 164.0, 155.5, 140.8, 137.0, 131.0, 129.3, 128.4, 128.0, 127.2, 34.2, 23.6 ppm. **HPLC** (254 nm) R_T = 17.14 min, 97.33%.

N-((4-Chlorophenyl)sulfonyl)-4-propylbenzamide **61**

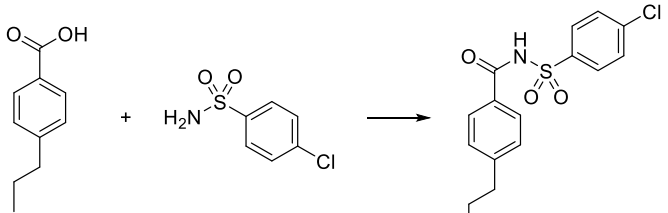

72 **61**

Using **General Procedure A**, 4-propylbenzoic acid (0.16 g, 0.97 mmol) and 4-chlorobenzenesulfonamide **72** (0.23 g, 1.2 mmol) gave the title compound. The crude residue was recrystallised from EtOH to yield *N*-acylsulfonamide **61** as white crystals (0.11 g, 33%). **IR** (neat, diamond cell) ν 3280, 3104, 2961, 2932, 2864, 1686, 1426, 1346, 1169, 1051, 823, 758, 749, 619, 611 cm^{-1}; **LRMS** (−ESI) *m/z* 336 $[M-H]^-$; **HRMS** Calcd for $C_{16}H_{15}{}^{35}ClNO_3S^-$ $[M-H]^-$: *m/z* 336.04667, found *m/z* 336.04669; **^{1}H NMR** (400 MHz, $CDCl_3$) δ 9.14 (br s, 1H), 8.14 – 8.05 (m, 2H), 7.75 – 7.67 (m, 2H), 7.56 – 7.47 (m, 2H), 7.23 (d, *J* =

8.3 Hz, 2H), 2.63 – 2.59 (t, *J* = 7.6 Hz, 2H), 1.67 – 1.59 (sextet, *J* = 7.5 Hz, 2H), 0.93 – 0.89 (t, *J* = 7.3 Hz, 3H) ppm; **^{13}C NMR** (101 MHz, $CDCl_3$) δ 164.2, 149.3, 140.8, 137.0, 130.2, 129.3, 129.1, 128.3, 127.9, 37.9, 24.1, 13.7 ppm; **HPLC** (254 nm) R_T = 27.72 min, 98.80%.

[1,1'-Biphenyl]−4-carboxylic acid **69**

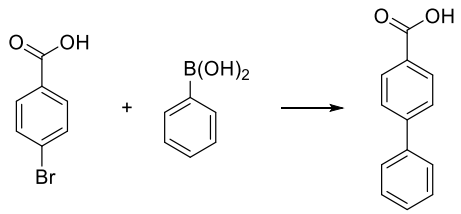

68 **239** **69**

A solution of 4-bromobenzoic acid **68** (2.00 g, 9.95 mmol) and phenylboronic acid **239** (1.33 g, 10.94 mmol) in 1,4-dioxane (20 mL) and 2 M aq. K_2CO_3 solution (20 mL) was degassed with N_2, then [1,1′-bis(diphenylphosphino)ferrocene]dichloropalladium(II) (0.25 g, 0.34 mmol) was added and the solution heated at 80 ºC for 16 h. The reaction mixture was diluted with H_2O and adjusted to pH 1 with 6 M HCl. The aqueous layer was extracted with EtOAc (×3) and the combined organic layers were washed with brine and dried ($MgSO_4$). The solvent was evaporated to yield the crude residue, which was purified by flash column chromatography (30% Et_2O/hexanes) to yield acid **69** as a white solid (1.23 g, 62%). **LRMS** (−ESI) *m/z* 197 $[M-H]^-$; **^{1}H NMR** (300 MHz, $CDCl_3$) δ 8.20 – 8.17 (m, 2H), 7.72 – 7.69 (m, 2H), 7.66 – 7.63 (m, 2H), 7.51 – 7.46 (m, 2H), 7.43 – 7.39 (m, 1H) ppm; **^{13}C NMR** (75 MHz, $CDCl_3$) δ 167.1, 144.3, 139.0, 130.0, 129.7, 129.1, 128.3, 127.0, 126.8 ppm. Characterisation data were consistent with literature.[454]

N-((4-Chlorophenyl)sulfonyl)-[1,1'-biphenyl]−4-carboxamide **62**

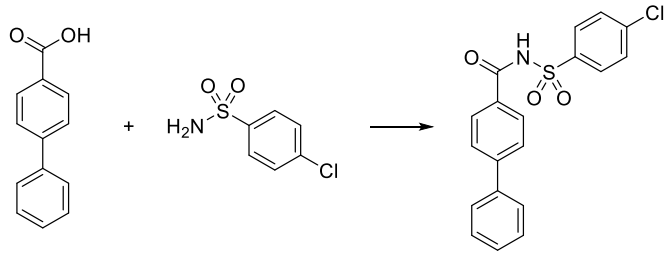

69 **72** **62**

Using **General Procedure A**, 4-chlorobenzenesulfonamide **72** (0.39 g, 2.0 mmol) and biphenyl-4-carboxylic acid **69** (0.40 g, 2.0 mmol) gave the title compound. The crude residue was recrystallised to yield *N*-acylsulfonamide **62** as white crystals (0.12 g, 16%). **IR** (neat,

diamond cell) ν 3261, 3095, 3078, 3033, 1683, 1170, 740, 614, 554 cm^{-1}; **LRMS** (−ESI) *m/z* 370 $[M-H]^-$; **HRMS** Calcd for $C_{19}H_{13}{}^{35}ClNO_3S$ $[M-H]^-$: *m/z* 370.03102, found *m/z* 370.03083; **^{1}H NMR** (400 MHz, DMSO-d_6) δ 8.00 – 7.93 (m, 2H), 7.87 – 7.79 (m, 2H), 7.72 – 7.65 (m, 2H), 7.61 (d, *J* = 8.4 Hz, 2H), 7.50 – 7.41 (m, 4H), 7.40 – 7.32 (m, 1H) ppm; **^{13}C NMR** (101 MHz, DMSO-d_6) 165.3, 144.7, 138.6, 138.6, 138.4, 130.2, 129.7, 129.3, 129.2, 129.1, 128.5, 127.0, 126.8 ppm; **HPLC** (254 nm) R_T = 27.38 min, 99.72%.

4'-Fluoro-[1,1'-biphenyl]−4-carboxylic acid **70**

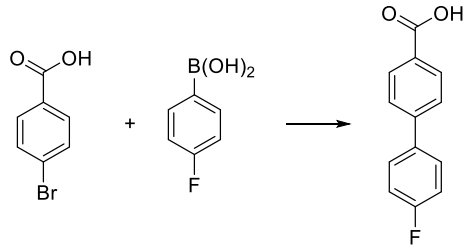

68 **70**

A solution of 4-bromobenzoic acid **68** (1.0 g, 5.0 mmol) and 4-fluorophenylboronic acid (0.77 g, 5.5 mmol) in 1,4-dioxane (10 mL) and 2 M aq. K_2CO_3 (10 mL) was degassed with N_2, then [1,1'-bis(diphenylphosphino)ferrocene]palladium(II) dichloride (0.090 g, 2.5 mol %) was added and the solution heated at 80 °C for 16 h. The reaction mixture was diluted with H_2O and adjusted to pH 1 with 6 M HCl. The aqueous layer was extracted with EtOAc (×3) and the combined organic layers were washed with brine and dried ($MgSO_4$). The solvent was evaporated to yield the crude residue, which was purified by flash column chromatography (30-60% EtOAc/hexanes) to yield acid **70** as an off-white solid (0.83 g, 77%). **LRMS** (−ESI) *m/z* 215 $[M-H]^-$; **^{1}H NMR** (400 MHz, DMSO-d_6) δ 8.02 – 8.00 (m, 2H), 7.80 – 7.77 (m, 4H), 7.34 – 7.30 (m, 2H) ppm; **^{13}C NMR** (101 MHz, DMSO-d_6) δ 167.1, 162.33 (d, $^1J_{CF}$ = 245.6 Hz), 143.2, 135.5, 130.0, 129.6, 129.1 (d, $^3J_{CF}$ = 8.3 Hz), 126.7, 115.9 (d, $^2J_{CF}$ = 21.5 Hz) ppm; **^{19}F NMR** (376 MHz, DMSO-d_6) δ −114.2 ppm. Characterisation data were consistent with literature.[455]

N-((4-Chlorophenyl)sulfonyl)-4'-fluoro-[1,1'-biphenyl]−4-carboxamide **62**

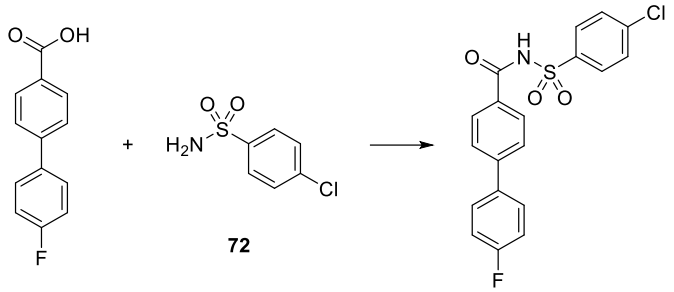

70 **72** **62**

Using **General Procedure A**, 4'-fluorobiphenyl-4-carboxylic acid **62** (0.22 g, 1.0 mmol) and 4-chlorobenzenesulfonamide **72** (0.23 g, 1.2 mmol) gave the title compound. The crude residue was recrystallised from EtOH to yield *N*-acylsulfonamide **62** as white cystals (0.23 g, 58%). **IR** (neat, diamond cell) ν 3270, 3097, 3078, 1682, 1435, 1314, 1171, 1162, 1070, 829, 814, 766, 752, 617 cm^{-1}; **LRMS** (−ESI) *m/z* 388 $[M-H]^-$; **HRMS** Calcd for $C_{19}H_{12}{}^{35}ClFNO_3S^-$ $[M-H]^-$: *m/z* 388.02159, found *m/z* 388.02197; **^{1}H NMR** (400 MHz, $(CD_3)_2CO$) δ 8.15 – 8.12 (m, 2H), 8.03 – 8.01 (m, 2H), 7.79 – 7.75 (m, 4H), 7.70 – 7.68 (m, 2H), 7.28 – 7.23 (m, 2H) ppm; **^{13}C NMR** (101 MHz, $(CD_3)_2CO$) 165.5, 164.0 (d, $^1J_{CF}$ = 246.4 Hz), 145.5, 140.4, 139.6, 136.7 (d, $^4J_{CF}$ = 3.4 Hz), 131.4, 131.1, 130.1 (d, $^3J_{CF}$ = 8.6 Hz), 130.0, 129.9, 127.9, 116.7 (d, $^2J_{CF}$ = 21.8 Hz); **^{19}F NMR** (376 MHz, $CDCl_3$) δ −115.6 ppm; **HPLC** (254 nm) R_T = 27.72 min, 99.19%.

3-Nitrobenzenesulfonamide **74**

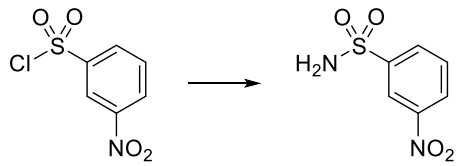

73 **74**

A solution of 3-nitrobenzenesulfonyl chloride **73** (0.86 g, 3.9 mmol) in Et_2O (17 mL) was cooled to 0 °C, then 26-28% aq. NH_3 solution (8 mL) was added dropwise, then the solution was stirred vigorously at RT for 1 h. The solution was diluted with brine and H_2O, then extracted with EtOAc (×3). The organic layers were combined and washed with brine, then dried ($MgSO_4$). The solvent was evaporated to yield sulfonamide **74** as a pale-yellow solid (0.63 g, 80%). **LRMS** (−ESI) *m/z* 201 $[M-H]^-$; **^{1}H NMR** (300 MHz, $CDCl_3$) δ 8.61 – 8.60 (m, 1H), 8.48 – 8.44 (m, 1H), 8.27 – 8.23 (m, 1H), 7.93 – 7.87 (m, 1H) ppm; **^{13}C NMR** (75 MHz,

$CDCl_3$) δ 148.2, 146.1, 132.2, 131.6, 127.0, 121.0 ppm. Characterisation data were consistent with literature.[456]

4′-Fluoro-N-((3-nitrophenyl)sulfonyl)-[1,1′-biphenyl]−4-carboxamide **64**

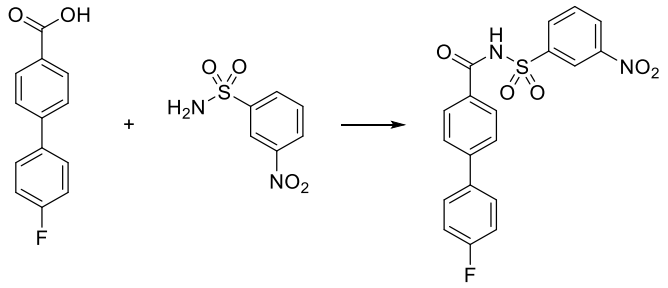

70 **74** **64**

Using **General Procedure A**, 4′-fluorobiphenyl-4-carboxylic acid **70** (0.21 g, 0.97 mmol) and 3-nitrobenzenesulfonamide **74** (0.22 g, 1.1 mmol) gave the title compound. The crude residue was purified by flash column chromatography (1-5% MeOH/CH_2Cl_2) to yield *N*-acylsulfonamide **64** as a white solid (0.29 g, 75%). **IR** (neat, diamond cell) ν 3269, 3225, 3102, 3086, 2870, 1686, 1604, 1528, 1448, 1433, 1348, 1249, 1174, 1161, 1065, 898, 826, 764 cm^{-1}; **LRMS** (−ESI) *m/z* 399 $[M-H]^-$; **HRMS** Calcd for $C_{19}H_{12}FN_2O_5S^-$ $[M-H]^-$: *m/z* 399.04564, found *m/z* 399.04568; **^{1}H NMR** (400 MHz, DMSO-d_6) δ 8.73 (t, *J* = 2.0 Hz, 1H), 8.59 – 8.52 (m, 1H), 8.44 (dt, *J* = 8.1, 1.3 Hz, 1H), 7.97 (dd, *J* = 8.2, 4.6 Hz, 4H), 7.79 (dd, *J* = 8.4, 5.1 Hz, 5H) ppm; **^{13}C NMR** (101 MHz, DMSO-d_6) δ 165.5, 162.4 (d, $^1J_{CF}$ = 246.0 Hz), 147.7, 143.7, 141.1, 135.1 (d, $^4J_{CF}$ = 3.1 Hz), 133.7, 131.2, 130.0, 129.3, 129.1 (d, $^3J_{CF}$ = 8.3 Hz), 128.2, 126.7, 122.6, 115.9 (d, $^2J_{CF}$ = 21.5 Hz) ppm; **^{19}F NMR** (376 MHz, DMSO-d_6) δ −113.9 ppm; **HPLC** (254 nm) R_T = 26.62 min, 98.51%.

4-Nitrobenzenesulfonamide **76**

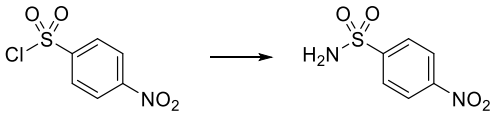

75 **76**

A solution of 4-nitrobenzenesulfonyl chloride **75** (0.86 g, 3.9 mmol) in Et_2O (17 mL) was cooled to 0 °C, then 26-28% aq. NH_3 solution (8 mL) was added dropwise, then the solution was stirred vigorously at RT for 1 h. The solution was diluted with brine and H_2O, then extracted with EtOAc (×3). The organic layers were combined and washed with brine, then dried ($MgSO_4$). The solvent was evaporated to yield the product sulfonamide **76** as a pale-yellow solid (0.55 g, 70%). **LRMS** (−ESI) *m/z* 399 $[M-H]^-$; **^{1}H NMR** (300 MHz, $CDCl_3$) δ

8.41 – 8.38 (m, 2H), 8.14 – 8.11 (m, 2H) ppm; **^{13}C NMR** (75 MHz, $CDCl_3$) δ 149.8, 149.4, 127.2, 123.9 ppm. Characterisation data were consistent with literature.[457]

4′-Fluoro-N-((4-nitrophenyl)sulfonyl)-[1,1′-biphenyl]−4-carboxamide **77**

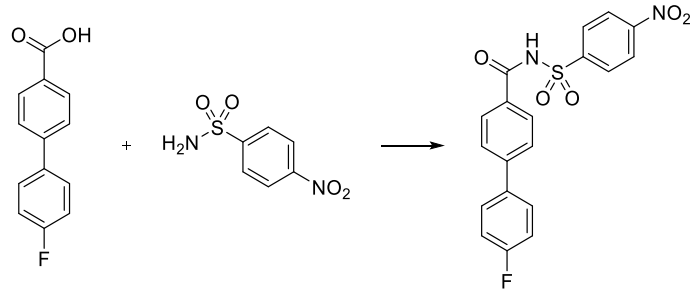

70 **76** **77**

Using **General Procedure A**, 4′-fluorobiphenyl-4-carboxylic acid **70** (0.22 g, 1.0 mmol) and 4-nitrobenzenesulfonamide **76** (0.22 g, 1.1 mmol) gave the title compound. The crude residue was purified by flash column chromatography (0.5-2% MeOH/CH_2Cl_2) to yield *N*-acylsulfonamide **77** as an off-white solid (0.21 g, 52%). **IR** (neat, diamond cell) ν 3247, 3109, 3048, 1716, 1532, 1432, 1421, 1350, 1249, 1164, 1061, 842, 832, 815, 759, 735, 608 cm^{-1}; **LRMS** (−ESI) *m/z* 399 $[M-H]^-$; **HRMS** Calcd for $C_{19}H_{12}FN_2O_5S^-$ $[M-H]^-$: *m/z* 399.04564, found *m/z* 399.04610; **^{1}H NMR** (400 MHz, DMSO) δ 8.94 (d, *J* = 8.7 Hz, 1H), 8.85 (d, *J* = 8.9 Hz, 1H), 8.48 (d, *J* = 8.4 Hz, 1H), 8.28 – 8.17 (m, 2H), 7.71 (t, *J* = 8.8 Hz, 1H) ppm; **^{13}C NMR** (101 MHz, DMSO-d_6) δ 165.7, 164.0 (d, $^1J_{CF}$ = 246.4 Hz), 151.8, 146.1, 145.7, 136.6 (d, $^4J_{CF}$ = 3.2 Hz), 131.2, 130.9, 130.1 (d, $^3J_{CF}$ = 8.2 Hz), 123.0, 127.9, 125.0, 116.7 (d, $^2J_{CF}$ = 21.6 Hz) ppm; **^{19}F NMR** (376 MHz, DMSO-d_6) δ −115.1 ppm.

N-((4-Aminophenyl)sulfonyl)-4′-fluoro-[1,1′-biphenyl]−4-carboxamide **65**

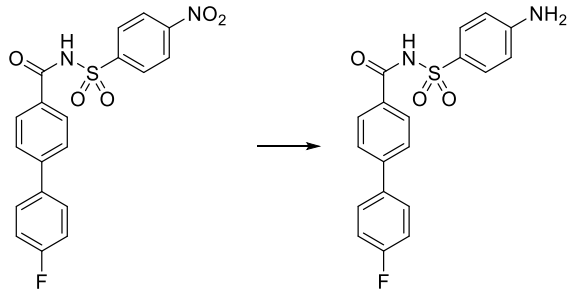

77 **65**

Using **General Procedure C,** *N*-acylsulfonamide **72** (0.10 g, 0.25 mmol) gave the title compound **65** without further purification (0.071 g, 77%). **IR** (neat, diamond cell) ν 3477, 3378, 3241, 1682, 1625, 1593, 1499, 1433, 1415, 1340, 1324, 1244, 1153, 1071, 828, 810, 764,

676 cm^{-1}; **LRMS** (−ESI) *m/z* 369 $[M-H]^-$; **HRMS** Calcd for $C_{19}H_{14}FN_2O_3S^-$ $[M-H]^-$: *m/z* 369.07147, found *m/z* 369.07142; **^{1}H NMR** (400 MHz, DMSO-d_6) δ 12.11 (br s, 1H), 7.94 (d, *J* = 8.1 Hz, 2H), 7.78 (td, *J* = 8.4, 5.1 Hz, 4H), 7.64 (d, *J* = 8.5 Hz, 2H), 7.32 (t, *J* = 8.8 Hz, 2H), 6.62 (d, *J* = 8.7 Hz, 2H), 6.14 (s, 2H) ppm; **^{13}C NMR** (101 MHz, DMSO-d_6) δ 164.7, 162.4 (d, $^1J_{CF}$ = 245.9 Hz), 153.6, 143.2, 135.2 (d, $^4J_{CF}$ = 2.9 Hz), 130.7, 130.0, 129.0 (d, $^3J_{CF}$ = 8.3 Hz), 128.9, 126.6, 123.9, 115.9 (d, $^2J_{CF}$ = 21.5 Hz), 112.2 ppm; **^{19}F NMR** (376 MHz, DMSO-d_6) δ −114.1 ppm; **HPLC** (254 nm) R_T = 23.40 min, 97.88%.

4-Chloro-3-nitrobenzenesulfonamide **80**

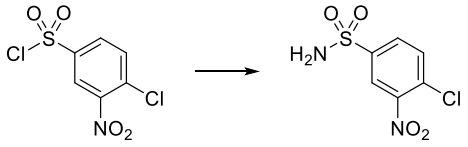

79 **80**

A solution of 4-chloro-3-nitrobenzenesulfonyl chloride **79** (1.0 g, 3.9 mmol) in Et_2O (17 mL) was cooled to 0 °C, then 26-28% aq. NH_3 solution (8 mL) was added dropwise, then the solution was stirred vigorously at RT for 1 h. The solution was diluted with brine and H_2O, then extracted with EtOAc (×3). The organic layers were combined and washed with brine, then dried ($MgSO_4$). The solvent was evaporated to yield sulfonamide **80** as a pale-yellow solid (0.74 g, 80%). **LRMS** (−ESI) *m/z* 235 $[M-H]^-$; **^{1}H NMR** (400 MHz, DMSO-d_6) δ 8.46 (d, *J* = 2.1 Hz, 1H), 8.08 (dd, *J* = 8.5, 2.1 Hz, 1H), 8.02 (d, *J* = 8.5 Hz, 1H), 7.74 (br s, 3H) ppm; **^{13}C NMR** (101 MHz, $CDCl_3$) δ 147.2, 144.1, 132.9, 130.6, 128.6, 123.1 ppm. Characterisation data were consistent with literature.[334]

N-((4-Chloro-3-nitrophenyl)sulfonyl)-4'-fluoro-[1,1'-biphenyl]−4-carboxamide **81**

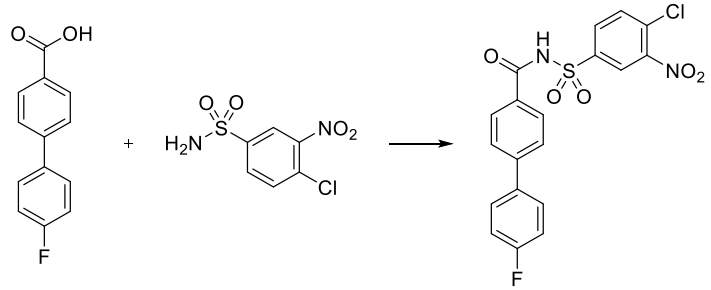

70 **80** **81**

Using **General Procedure A**, 4'-fluorobiphenyl-4-carboxylic acid **70** (0.21 g, 0.97 mmol) and 4-chloro-3-nitrobenzenesulfonamide **80** (0.26 g, 1.1 mmol) gave the title compound. The crude residue was recrystallised from EtOH to yield *N*-acylsulfonamide **81** as a white solid (0.25 g,

59%). **LRMS** (−ESI) *m/z* 433 $[M-H]^-$; **^{1}H NMR** (400 MHz, DMSO-d_6) δ 8.60 (d, *J* = 2.2 Hz, 1H), 8.25 (dd, *J* = 8.5, 2.2 Hz, 1H), 8.03 (d, *J* = 8.5 Hz, 1H), 7.97 (d, *J* = 8.3 Hz, 2H), 7.78 (ddd, *J* = 8.6, 6.3, 2.0 Hz, 4H), 7.37 – 7.26 (m, 2H) ppm; **^{13}C NMR** (101 MHz, DMSO-d_6) δ 166.2, 162.4 (d, $^1J_{CF}$ = 245.8 Hz), 147.1, 143.3, 140.6, 135.2 (d, $^4J_{CF}$ = 3.1 Hz), 132.8, 132.5, 131.1, 130.0, 129.3, 129.1 (d, $^3J_{CF}$ = 8.2 Hz), 126.5, 125.1, 115.9 (d, $^2J_{CF}$ = 21.4 Hz) ppm; **^{19}F NMR** (376 MHz, DMSO-d_6) δ −114.1 ppm. Characterisation data were consistent with literature.[334]

4'-Fluoro-N-((4-(methylamino)-3-nitrophenyl)sulfonyl)-[1,1'-biphenyl]−4-carboxamide **66**

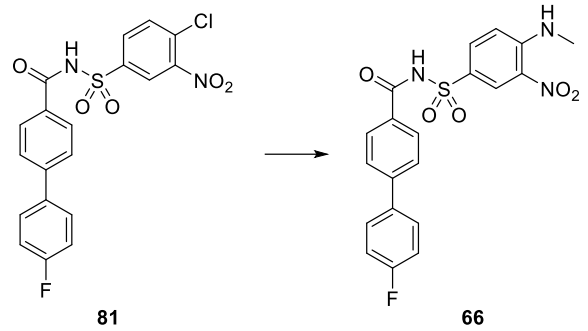

Using **General Procedure B**, *N*-acylsulfonamide **81** (0.050 g, 0.11 mmol) and 40% aq. $MeNH_2$ solution (0.05 mL) gave the title compound. The crude residue was purified *via* flash column chromatography (5% MeOH/CH_2Cl_2) to yield *N*-acylsulfonamide **65** as a yellow solid (0.041 g, 83%). **IR** (neat, diamond cell) ν 3389, 3347, 3307, 3079, 2917, 1687, 1616, 1601, 1518, 1342, 1236, 1222, 1157, 1023, 1004, 828, 763 cm^{-1}; **LRMS** (−ESI) *m/z* 428 $[M-H]^-$; **HRMS** Calcd for $C_{20}H_{15}FN_3O_5S^-$ $[M-H]^-$: *m/z* 428.07219, found *m/z* 428.07255; **^{1}H NMR** (400 MHz, DMSO-d_6) δ 8.58 (d, *J* = 2.2 Hz, 1H), 8.49 (d, *J* = 5.4 Hz, 1H), 7.98 (d, *J* = 2.2 Hz, 1H), 7.96 – 7.93 (m, 2H), 7.79 – 7.70 (m, 2H), 7.66 (d, *J* = 8.1 Hz, 2H), 7.34 – 7.24 (m, 2H), 7.06 (d, *J* = 9.2 Hz, 1H), 2.99 (d, *J* = 5.0 Hz, 3H) ppm; **^{13}C NMR** (101 MHz, DMSO-d_6) δ 167.4, 162.7 (d, $^1J_{CF}$ = 245.3 Hz), 147.9, 142.6, 136.1 (d, $^4J_{CF}$ = 3.0 Hz), 135.0, 134.1, 130.0, 129.5, 129.4 (d, $^3J_{CF}$ = 8.2 Hz), 128.4, 127.3, 126.7, 116.3 (d, $^2J_{CF}$ = 21.6 Hz), 114.8, 30.4 ppm; **^{19}F NMR** (376 MHz, DMSO-d_6) δ −114.5 ppm; **HPLC** (254 nm) R_T = 26.29 min, 95.64%.

N-((4-(Ethylamino)-3-nitrophenyl)sulfonyl)-4'-fluoro-[1,1'-biphenyl]−4-carboxamide **67**

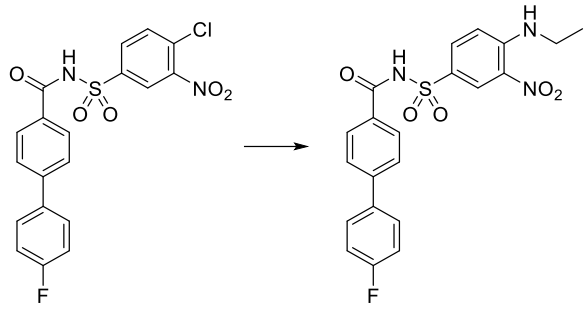

81 **67**

Using **General Procedure B**, *N*-acylsulfonamide **81** (0.05 g, 0.11 mmol) and 70% aq. $EtNH_2$ solution (0.05 mL) gave the title compound. The crude residue was purified ***via*** flash column chromatography (5% MeOH/CH_2Cl_2) to yield *N*-acylsulfonamide **67** as a yellow **solid** (0.029 g, 57%). **IR** (neat, diamond cell) ν 3351, 3305, 2921, 2852, 1689, 1615, 1561, 1515, 1442, 1342, 1228, 1157, 1072, 831, 816, 763, 655 cm^{-1}; **LRMS** (−ESI) *m/z* 442 $[M-H]^-$; **HRMS** Calcd for $C_{21}H_{17}FN_3O_5S^-$ $[M-H]^-$: *m/z* 442.08784, found *m/z* 442.08771; **^{1}H NMR** (400 MHz, DMSO-d_6) δ 8.64 (d, *J* = 2.2 Hz, 1H), 8.54 (t, *J* = 5.8 Hz, 1H), 7.96 (dd, *J* = 9.7, 6.6 Hz, 3H), 7.76 (dt, *J* = 11.0, 6.9 Hz, 4H), 7.30 (t, *J* = 8.8 Hz, 2H), 7.20 (d, *J* = 9.3 Hz, 1H), 3.45 (t, *J* = 6.7 Hz, 2H), 1.22 (t, *J* = 7.1 Hz, 3H) ppm; **^{13}C NMR** (101 MHz, DMSO-d_6) δ 166.0, 162.2 (d, $^1J_{CF}$ = 245.5 Hz), 146.8, 142.7, 135.3 (d, $^4J_{CF}$ = 3.2 Hz), 134.2, 132.0, 129.4, 129.0, 128.9 (d, $^3J_{CF}$ = 8.4 Hz), 127.4, 126.3, 126.2, 115.8 (d, $^2J_{CF}$ = 21.6 Hz), 114.6, 37.3, 13.8 ppm; **^{19}F NMR** (376 MHz, DMSO-d_6) δ −114.3 ppm; **HPLC** (254 nm) R_T = 27.50 min, 96.27%.

2-(Phenylthio)ethan-1-amine **86**

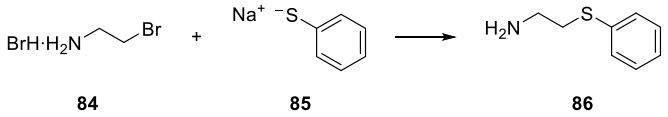

84 **85** **86**

A solution of 2-bromoethylamine hydrobromide **84** (0.39 g, 1.9 mmol), K_2CO_3 (0.61 g, 4.4 mmol) and sodium thiophenolate **85** (0.19 g, 1.5 mmol) in CH_2Cl_2 (6 mL) was stirred for 24 h at RT. When the reaction was complete, the reaction mixture was diluted with H_2O and extracted with CH_2Cl_2 (×3). The combined organic extracts were washed with brine, then dried ($MgSO_4$). The solvent was evaporated under reduced pressure to yield amine **86** as a pale yellow oil (0.12 g, 40%) which was used immediately without characterisation.

4'-Fluoro-N-((3-nitro-4-((2-(phenylthio)ethyl)amino)phenyl)sulfonyl)-[1,1'-biphenyl]−4-carboxamide **57**

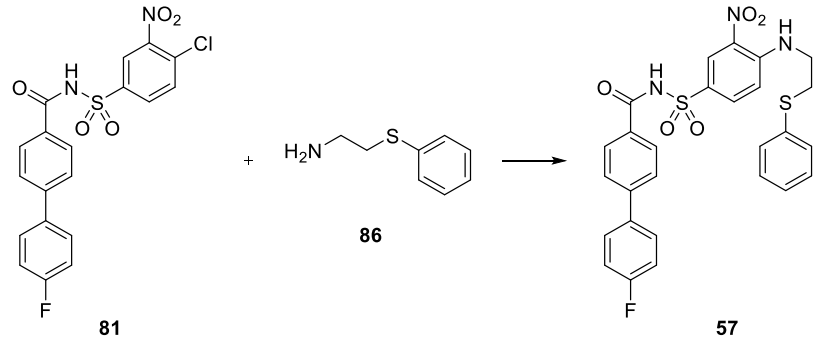

Using **General Procedure B**, *N*-acylsulfonamide **81** (0.05 g, 0.11 mmol) and amine **86** (0.088 g, 0.57 mmol) gave the title compound. The crude residue was purified *via* flash column chromatography (1-5% MeOH/CH_2Cl_2) to yield *N*-acylsulfonamide **57** as a yellow solid (0.046 g, 73%). **IR** (neat, diamond cell) ν 3354, 3247, 3106, 3076, 2923, 2855, 1684, 1613, 1519, 1433, 1345, 1239, 1160, 1073, 905, 830, 813, 764, 741 cm^{-1}; **LRMS** (−ESI) *m/z* 550 $[M-H]^-$; **HRMS** Calcd for $C_{27}H_{21}FN_3O_5S_2^-$ $[M-H]^-$: *m/z* 550.09121, found *m/z* 550.09181; **^{1}H NMR** (500 MHz, DMSO-d_6) δ 8.77 (t, *J* = 6.0 Hz, 1H), 8.62 (d, *J* = 2.3 Hz, 1H), 7.99 – 7.89 (m, 3H), 7.82 – 7.73 (m, 4H), 7.42 – 7.35 (m, 2H), 7.34 – 7.29 (m, 2H), 7.29 – 7.24 (m, 2H), 7.23 – 7.14 (m, 2H), 3.67 (q, *J* = 6.6 Hz, 2H), 3.28 (t, *J* = 6.9 Hz, 2H) ppm; **^{13}C NMR** (126 MHz, DMSO-d_6) δ 165.5, 162.4 (d, $^1J_{CF}$ = 245.8 Hz), 147.0, 143.3, 135.2 (d, $^4J_{CF}$ = 3.1 Hz), 135.0, 134.1, 130.9, 129.8, 129.1, 129.1 (d, $^3J_{CF}$ = 9.0 Hz), 129.0, 128.7, 127.8, 126.6, 126.1, 125.5, 115.9 (d, $^2J_{CF}$ = 21.5 Hz), 115.1, 42.0, 31.1 ppm; **^{19}F NMR** (471 MHz, DMSO-d_6) δ −114.1 ppm; **HPLC** (254 nm) R_T = 29.88 min, 96.49%. Characterisation data were consistent with literature.[334]

N-((3-Nitrophenyl)sulfonyl)adamantane-1-carboxamide **87**

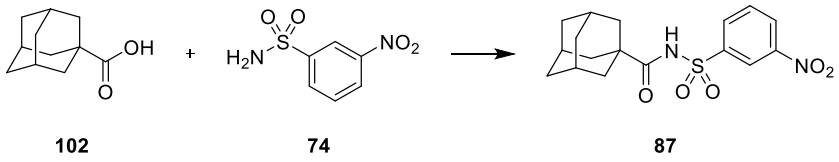

Using **General Procedure A**, adamantane-1-carboxylic acid **102** (0.18 g, 1.0 mmol) and 3-nitrobenzenesulfonamide **74** (0.22 g, 1.1 mmol) gave the title compound. The crude residue was purified by flash column chromatography (10-50% EtOAc/hexane) to yield *N*-acylsulfonamide **87** as a white solid (0.17 g, 47%). **IR** (neat, diamond cell) ν 3203, 3104, 2905, 2853, 1681, 1537, 1422, 1348, 1184, 1160, 1058, 884, 859, 734, 660 cm^{-1}; **LRMS** (−ESI) *m/z*

363 [M−H]⁻; **HRMS** Calcd for $C_{17}H_{19}N_2O_5S^-$ [M−H]⁻: *m/z* 363.10202, found *m/z* 363.10184; **^{1}H NMR** (300 MHz, $CDCl_3$) δ 8.86 (t, *J* = 2.0 Hz, 1H), 8.53 – 8.42 (m, 2H), 7.78 (t, *J* = 8.0 Hz, 1H), 2.04 (s, 3H), 1.79 – 1.61 (m, 12H) ppm; **^{13}C NMR** (75 MHz, $CDCl_3$) δ 175.6, 148.2, 140.6, 134.6, 130.5, 128.5, 123.7, 42.2, 38.4, 36.1, 27.7 ppm; **HPLC** (254 nm) R_T = 26.69 min, 97.54%.

N-((4-Nitrophenyl)sulfonyl)adamantane-1-carboxamide **107**

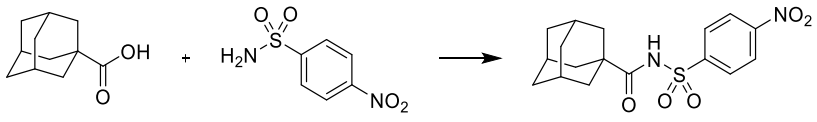

102 **76** **107**

Using **General Procedure A**, adamantane-1-carboxylic acid **102** (0.18 g, 1.0 mmol) and 4-nitrobenzenesulfonamide **76** (0.22 g, 1.1 mmol) gave the title compound. The crude residue was purified by flash column chromatography (10-50% EtOAc/hexane) to yield *N*-acylsulfonamide **107** as a white solid (0.14 g, 38%). **IR** (neat, diamond cell) ν 3291, 2904, 2851, 1719, 1530, 1413, 1344, 1176, 1158, 1040, 876, 852, 737, 604 cm^{-1}; **LRMS** (−ESI) *m/z* 363 [M−H]⁻; **HRMS** Calcd for $C_{17}H_{19}N_2O_5S^-$ [M−H]⁻: *m/z* 363.10202, found *m/z* 363.10189; **^{1}H NMR** (300 MHz, DMSO-d_6) δ 12.04 (br s, 1H), 8.44 – 8.41 (m, 2H), 8.13 – 8.10 (m, 2H), 1.92 (s, 3H), 1.77 – 1.60 (m, 12H) ppm; **^{13}C NMR** (75 MHz, DMSO-d_6) δ 176.7, 150.2, 145.0, 129.1, 124.6, 41.6, 37.0, 35.7, 27.3 ppm.

N-((4-Aminophenyl)sulfonyl)adamantane-1-carboxamide **90**

107 **90**

Using **General Procedure C**, *N*-acylsulfonamide **107** (0.10 g, 0.27 mmol) gave the title compound. The crude residue was purified by flash column chromatography (10-80% EtOAc/hexane) to yield *N*-acylsulfonamide **90** as a white solid (0.073 g, 80%). **IR** (neat, diamond cell) ν 3482, 3383, 3175, 2902, 2851, 1682, 1636, 1598, 1446, 1326, 1150, 1063, 868, 684 cm^{-1}; **LRMS** (−ESI) *m/z* 333 [M−H]⁻; **HRMS** Calcd for $C_{17}H_{21}N_2O_3S^-$ [M−H]⁻: *m/z* 333.12784, found *m/z* 333.12776; **^{1}H NMR** (400 MHz, DMSO-d_6) δ 11.14 (br s, 1H), 7.50 – 7.48 (m, 2H), 6.59 – 6.57 (m, 2H), 6.07 (br s, 2H), 1.91 (s, 3H), 1.71 – 1.60 (m, 12H) ppm; **^{13}C**

NMR (101 MHz, DMSO-d_6) δ 175.5, 153.3, 129.6, 124.2, 112.2, 41.3, 37.0, 35.6, 27.3 ppm; **HPLC** (254 nm) R_T = 22.77 min, 97.61%.

N-((4-Chloro-3-nitrophenyl)sulfonyl)adamantane-1-carboxamide **110**

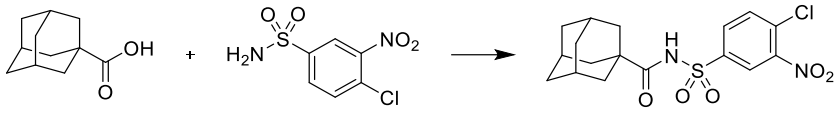

102 **80** **110**

Using **General Procedure A**, adamantane-1-carboxylic acid **102** (0.18 g, 1.0 mmol) and 4-chloro-3-nitrobenzenesulfonamide **80** (0.26 g, 1.1 mmol) gave the title compound. The crude residue was purified by flash column chromatography (20-60% EtOAc/hexane) to yield *N*-acylsulfonamide **110** as a white solid (0.27 g, 68%). **IR** (neat, diamond cell) ν 3310, 3081, 2917, 2854, 1703, 1537, 1402, 1346, 1181, 1164, 1148, 1052, 1040, 891, 865, 792 cm^{-1}; **LRMS** (−ESI) *m/z* 397 $[M-H]^-$; **HRMS** Calcd for $C_{17}H_{18}{}^{35}ClN_2O_5S^-$ $[M-H]^-$: *m/z* 397.06304, found *m/z* 397.06283; **^{1}H NMR** (400 MHz, DMSO-d_6) δ 12.03 (br s, 1H), 8.50 (d, *J* = 2.2 Hz, 1H), 8.13 (dd, *J* = 8.5, 2.2 Hz, 1H), 8.05 (d, *J* = 8.5 Hz, 1H) 1.94 (s, 3H), 1.75 – 1.74 (m, 6H), 1.66 – 1.59 (m, 6H) ppm; **^{13}C NMR** (101 MHz, DMSO-d_6) δ 176.5, 147.1, 139.6, 133.1, 132.1, 130.5, 124.9, 41.6, 36.9, 35.6, 27.2 ppm.

N-((4-(Methylamino)-3-nitrophenyl)sulfonyl)adamantane-1-carboxamide **93**

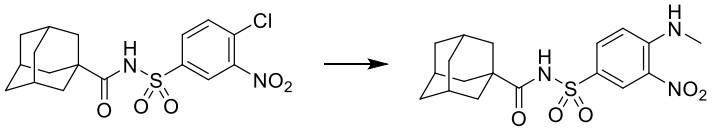

110 **93**

Using **General Procedure B**, *N*-acylsulfonamide **110** (0.050 g, 0.13 mmol) and 40% methylamine solution (0.05 mL) gave the title compound. The crude residue was purified by flash column chromatography (0.25-0.5% MeOH/CH_2Cl_2) to yield *N*-acylsulfonamide **93** as a yellow solid (0.020 g, 41%). **IR** (neat, diamond cell) ν 3348, 3243, 2929, 2906, 2889, 2851, 1712, 1624, 1417, 1338, 1313, 1260, 1243, 1178, 1157, 1129, 1100, 1060, 1043, 900, 863, 789, 658 cm^{-1}; **LRMS** (−ESI) *m/z* 392 $[M-H]^-$; **HRMS** Calcd for $C_{18}H_{22}N_3O_5S^-$ $[M-H]^-$: *m/z* 392.12857, found *m/z* 392.12923; **^{1}H NMR** (400 MHz, DMSO-d_6) δ 11.55 (br s, 1H), 8.67 (q, *J* = 5.0 Hz, 1H), 8.54 (d, *J* = 2.3 Hz, 1H), 7.86 (dd, *J* = 9.3, 2.3 Hz, 1H), 7.15 (d, *J* = 9.3 Hz, 1H), 3.02 – 3.01 (d, *J* = 4.8 Hz, 3H), 1.92 (s, 3H), 1.72 – 1.60 (m, 12H) ppm; **^{13}C NMR** (101 MHz, DMSO-d_6) δ 76.1, 147.9, 133.7, 129.5, 127.5, 124.3, 115.1, 41.4, 36.9, 35.6, 30.0, 27.3 ppm; **HPLC** (254 nm) R_T = 26.32 min, 96.75%.

N-((4-(Ethylamino)-3-nitrophenyl)sulfonyl)adamantane-1-carboxamide **96**

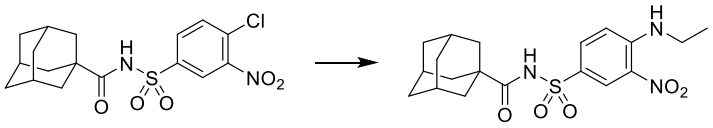

110 **96**

Using **General Procedure B**, *N*-acylsulfonamide **110** (0.075 g, 0.19 mmol) and 70% ethylamine solution (0.05 mL) gave the title compound. The crude residue was purified by flash column chromatography (0.25-0.5% MeOH/CH_2Cl_2) to yield *N*-acylsulfonamide **96** as a yellow solid (0.033 g, 43%). **IR** (neat, diamond cell) ν 3335, 2923, 2906, 2852, 1696, 1617, 1561, 1519, 1450, 1340, 1321, 1258, 1240, 1220, 1157, 1132, 1097, 1062, 1021, 997, 978, 891, 861 cm^{-1}; **LRMS** (−ESI) *m/z* 406 $[M-H]^-$; **HRMS** Calcd for $C_{19}H_{24}N_3O_5S^-$ $[M-H]^-$: *m/z* 406.14422, found *m/z* 406.14443; **^{1}H NMR** (300 MHz, DMSO-d_6) δ 11.55 (br s, 1H), 8.59 (t, *J* = 5.8 Hz, 1H), 8.54 (d, *J* = 2.3 Hz, 1H), 7.84 (dd, *J* = 9.2, 2.4 Hz, 1H), 7.22 (d, *J* = 9.3 Hz, 1H), 3.46 (p, *J* = 6.9 Hz, 2H), 1.92 (s, 3H), 1.72 – 1.71 (m, 6H), 1.60 (m, 6H), 1.25 – 1.20 (t, 3H, *J* = 7.1 Hz) 1.23 (t, *J* = 7.1 Hz, 3H) ppm; **^{13}C NMR** (75 MHz, DMSO-d_6) δ 176.2, 147.1, 133.7, 129.6, 127.7, 124.6, 115.2, 41.4, 37.3, 37.0, 35.6, 27.3, 13.9 ppm; **HPLC** (254 nm) R_T = 27.80 min, 98.63%.

N-((3-Nitro-4-((3-(phenylthio)propyl)amino)phenyl)sulfonyl)adamantane-1-carboxamide **99**

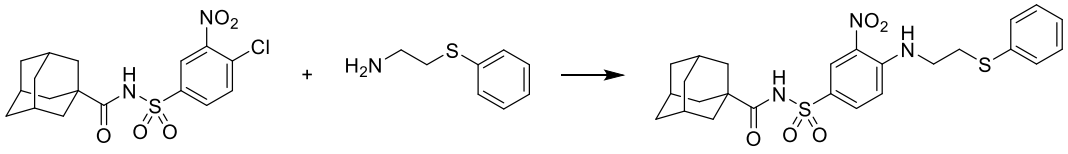

110 **86** **99**

Using **General Procedure B**, *N*-acylsulfonamide **110** (0.050 g, 0.13 mmol) and amine **86** (0.090 g, 0.59 mmol) gave the title compound. The crude residue was purified by flash column chromatography (10-50% EtOAc/hexane), then preparatory TLC (30% EtOAc/hexane, eluting twice) to yield *N*-acylsulfonamide **99** as a yellow solid (0.041 g, 63%). **IR** (neat, diamond cell) ν 3327, 2920, 2851, 1692, 1614, 1565, 1519, 1459, 1335, 1149, 1063, 1050, 1021, 1001, 900, 864, 737, 690, 655 cm^{-1}; **LRMS** (−ESI) *m/z* 514 $[M-H]^-$; **HRMS** Calcd for $C_{25}H_{28}N_3O_5S_2^-$ $[M-H]^-$: *m/z* 514.14759, found *m/z* 514.14851; **^{1}H NMR** (300 MHz, DMSO-d_6) δ 11.57 (br s, 1H), 8.76 (t, *J* = 6.0 Hz, 1H), 8.50 (d, *J* = 2.4 Hz, 1H), 7.80 (dd, *J* = 9.2, 2.3 Hz, 1H), 7.37 (d, *J* = 7.3 Hz, 2H), 7.28 (t, *J* = 7.6 Hz, 2H), 7.23 – 7.15 (m, 2H), 3.70 – 3.63 (q, *J* = 6.4 Hz, 2H), 3.31 – 3.27 (t, *J* = 6.4 Hz, 2H), 1.92 (s, 3H), 1.73 (m, 6H), 1.60 (m, 6H) ppm; **^{13}C NMR** (75

MHz, DMSO-d_6) δ 176.1, 147.0, 135.0, 133.6, 129.7, 129.1, 128.7, 127.6, 126.1, 124.9, 115.3, 42.0, 41.5, 37.0, 35.6, 31.1, 27.3 ppm. **HPLC** (254 nm) R_T = 30.58 min, 95.33%.

2-(Adamantan-1-yl)-N-((3-nitrophenyl)sulfonyl)acetamide **88**

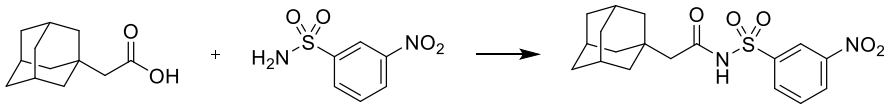

74 **88**

Using **General Procedure A**, adamantane-1-acetic acid (0.19 g, 0.98 mmol) and 3-nitrobenzenesulfonamide **74** (0.22 g, 1.1 mmol) gave the title compound. The crude residue was purified by flash column chromatography (10-50% EtOAc/hexane) to yield *N*-acylsulfonamide **88** as a white solid (0.32 g, 86%). **IR** (neat, diamond cell) ν 3111, 2900, 2847, 1688, 1534, 1436, 1348, 1176, 1113, 1095, 852, 665 cm^{-1}; **LRMS** (−ESI) *m/z* 377 $[M-H]^-$; **HRMS** Calcd for $C_{18}H_{21}N_2O_5S^-$ *m/z* 377.11767 $[M-H]^-$, found *m/z* 377.11746; **^{1}H NMR** (400 MHz, $CDCl_3$) δ 12.30 (br s, 1H), 8.60 (t, *J* = 2.0 Hz, 1H), 8.56 (ddd, *J* = 8.2, 2.3, 1.0 Hz, 1H), 8.33 (ddd, *J* = 7.9, 1.8, 1.1 Hz, 1H), 7.95 (t, *J* = 8.0 Hz, 1H), 1.93 (s, 3H),1.72 – 1.53 (m, 12H) ppm; **^{13}C NMR** (101 MHz, $CDCl_3$) δ 169.0, 148.2, 140.7, 134.7, 130.5, 128.5, 123.8, 51.2, 42.5, 36.6, 33.8, 28.6 ppm; **HPLC** (254 nm) R_T = 27.38 min, 99.52%.

2-(Adamantan-1-yl)-N-((4-nitrophenyl)sulfonyl)acetamide **108**

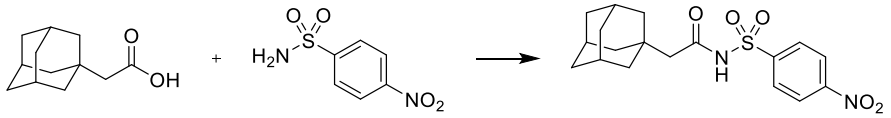

108 **76**

Using **General Procedure A**, adamantane-1-acetic acid (0.19 g, 0.98 mmol) and 4-nitrobenzenesulfonamide **76** (0.22 g, 1.1 mmol) gave the title compound. The crude residue was purified by flash column chromatography (10-50% EtOAc/hexane) to yield *N*-acylsulfonamide **108** as a white solid (0.22 g, 58%). **IR** (neat, diamond cell) ν 3065, 2904, 2850, 1676, 1530, 1444, 1347, 1308, 1163, 1086, 856, 847, 736, 684 cm^{-1}; **LRMS** (−ESI) *m/z* 377 $[M-H]^-$; **HRMS** Calcd for $C_{18}H_{21}N_2O_5S^-$ $[M-H]^-$: *m/z* 377.11767, found *m/z* 377.11746; **^{1}H NMR** (400 MHz, DMSO-d_6) δ 12.26 (br s, 1H), 8.48 – 8.40 (m, 1H), 8.20 – 8.12 (m, 1H), 1.95 (s, 2H), 1.85 (s, 3H), 1.61 – 1.42 (m, 12H) ppm; **^{13}C NMR** (101 MHz, DMSO-d_6) δ 169.9, 150.2, 144.6, 129.3, 124.3, 49.1, 41.6, 36.1, 33.0, 27.8 ppm.

2-(Adamantan-1-yl)-N-((4-aminophenyl)sulfonyl)acetamide **91**

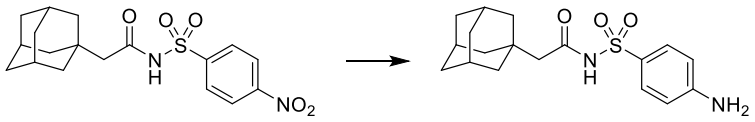

108 **91**

Using **General Procedure C**, *N*-acylsulfonamide **108** (0.13 g, 0.34 mmol) gave the title compound. The crude residue was purified by flash column chromatography (10-80% EtOAc/hexane) to yield *N*-acylsulfonamide **91** as a white solid (0.073 g, 61%). **IR** (neat, diamond cell) ν 3466, 3367, 3214, 2900, 2846, 1703, 1642, 1595, 1505, 1450, 1434, 1329, 1254, 1146, 1120, 1084, 849, 831, 686 cm^{-1}; **LRMS** (−ESI) *m/z* 347 $[M-H]^-$; **HRMS** Calcd for $C_{18}H_{23}N_2O_3S^-$ $[M-H]^-$: *m/z* 347.14349, found *m/z* 347.14332; **^{1}H NMR** (400 MHz, DMSO-d_6) δ 11.44 (br s, 1H), 7.52 – 7.50 (m, 2H), 6.60 – 6.58 (m, 2H), 6.09 (s, 2H), 1.85 (s, 2H), 1.83 (s, 3H), 1.61 – 1.40 (m, 12H) ppm; **^{13}C NMR** (101 MHz, DMSO-d_6) δ 169.2, 153.6, 129.9, 124.1, 112.2, 49.3, 41.7, 36.3, 32.9, 28.0 ppm; **HPLC** (254 nm) R_T = 23.69 min, 96.33%.

2-(Adamantan-1-yl)-N-((4-chloro-3-nitrophenyl)sulfonyl)acetamide **111**

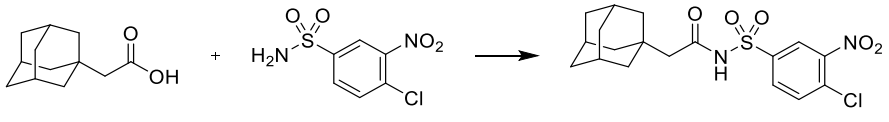

80 **111**

Using **General Procedure A**, adamantane-1-acetic acid (0.19 g, 0.98 mmol) and 4-chloro-3-nitrobenzenesulfonamide **80** (0.26 g, 1.1 mmol) gave the title compound. The crude residue was purified by flash column chromatography (10-50% EtOAc/hexane) to yield *N*-acylsulfonamide **111** as a white solid (0.29 g, 72%). **IR** (neat, diamond cell) ν 3168, 3097, 2906, 2850, 1683, 1541, 1428, 1356, 1173, 1088, 1048, 896, 851, 665, 624 cm^{-1}; **LRMS** (−ESI) *m/z* 411 $[M-H]^-$; **HRMS** Calcd for $C_{18}H_{20}{}^{35}ClN_2O_5S^-$ $[M-H]^-$: *m/z* 411.07869, found *m/z* 411.07850; **^{1}H NMR** (400 MHz, DMSO-d_6) δ 12.34 (br s, 1H), 8.52 (d, *J* = 2.2 Hz, 1H), 8.17 (dd, *J* = 8.5, 2.2 Hz, 1H), 8.07 (d, *J* = 8.5 Hz, 1H), 1.95 (s, 2H), 1.85 (s, 3H), 1.63 – 1.41 (m, 12H) ppm; **^{13}C NMR** (101 MHz, DMSO-d_6) δ 170.0, 147.2, 139.3, 132.8, 132.4, 130.5, 124.9, 49.1, 41.6, 36.1, 33.0, 27.8 ppm.

2-(Adamantan-1-yl)-N-((4-(methylamino)-3-nitrophenyl)sulfonyl)acetamide **94**

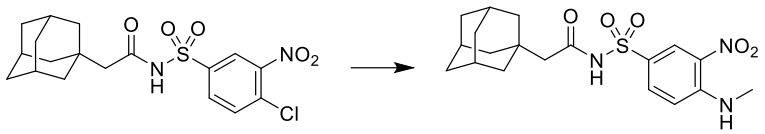

111 **94**

Using **General Procedure B**, *N*-acylsulfonamide **111** (0.050 g, 0.12 mmol) and 40% methylamine solution (0.05 mL) gave the title compound. The crude residue was purified by flash column chromatography (10-50% EtOAc/hexane) to yield *N*-acylsulfonamide **94** as a yellow solid (0.043 g, 87%). **IR** (neat, diamond cell) ν 3370, 3242, 2900, 2847, 1710, 1625, 1419, 1342, 1313, 1158, 1114, 1101, 1088, 1046, 898, 845, 803, 663, 624 cm^{-1}; **LRMS** (−ESI) *m/z* 406 $[M-H]^-$; **HRMS** Calcd for $C_{19}H_{24}N_3O_5S^-$ $[M-H]^-$: *m/z* 406.14422, found *m/z* 406.14443; **^{1}H NMR** (400 MHz, DMSO-d_6) δ 8.67 – 8.66 (q, *J* = 5.0 Hz, 1H), 8.54 (d, *J* = 2.2 Hz, 1H), 7.88 (dd, *J* = 9.2, 2.3 Hz, 1H), 7.15 (d, *J* = 9.3 Hz, 1H), 3.00 (d, *J* = 5.0 Hz, 3H), 1.89 (s, 2H), 1.83 (s, 3H), 1.61 – 1.40 (m, 12H) ppm; **^{13}C NMR** (101 MHz, DMSO-d_6) δ 169.8, 148.1, 134.2, 129.6, 127.7, 124.3, 115.0, 49.2, 41.8, 36.3, 33.1, 30.1, 28.0 ppm. **HPLC** (254 nm) R_T = 26.78 min, 96.14%.

2-(Adamantan-1-yl)-N-((4-(ethylamino)-3-nitrophenyl)sulfonyl)acetamide **97**

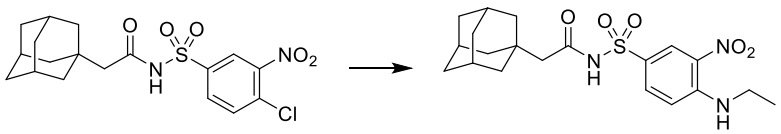

111 **97**

Using **General Procedure B**, *N*-acylsulfonamide **111** (0.050 g, 0.12 mmol) and 70% ethylamine solution (0.05 mL) gave the title compound. The crude residue was purified by flash column chromatography (10-50% EtOAc/hexane) to yield *N*-acylsulfonamide **97** as a yellow solid (0.037 g, 72%). **IR** (neat, diamond cell) ν 3364, 3240, 3097, 2901, 2846, 1714, 1623, 1561, 1421, 1340, 1322, 1252, 1234, 1157, 1114, 1100, 1088, 894, 847, 805, 664, 624 cm^{-1}; **LRMS** (−ESI) *m/z* 420 $[M-H]^-$; **HRMS** Calcd for $C_{20}H_{26}N_3O_5S^-$ $[M-H]^-$: *m/z* 420.15987, found *m/z* 420.16034; **^{1}H NMR** (300 MHz, DMSO-d_6) δ 11.89 (br s, 1H), 8.64 – 8.61 (t, *J* = 5.9 Hz, 1H), 8.55 (d, *J* = 2.1 Hz, 1H), 7.86 (d, *J* = 9.3, 2.2 Hz, 1H), 7.24 (d, *J* = 9.4 Hz, 1H), 3.51 – 3.42 (quintet, 2H, *J* = 7.1 Hz), 1.83 (s, 3H), 1.62 – 1.41 (m, 12H), 1.23 – 1.18 (t, *J* = 7.1 Hz, 3H) ppm; **^{13}C NMR** (75 MHz, DMSO-d_6) δ 169.6, 147.2, 134.0, 129.5, 127.9,

124.2, 115.0, 49.1, 41.7, 37.4, 36.2, 33.0, 27.9, 13.8 ppm. **HPLC** (254 nm) R_T = 28.02 min, 96.88%.

2-(Adamantan-1-yl)-N-((3-nitro-4-((2-(phenylthio)ethyl)amino)phenyl)sulfonyl)acetamide **100**

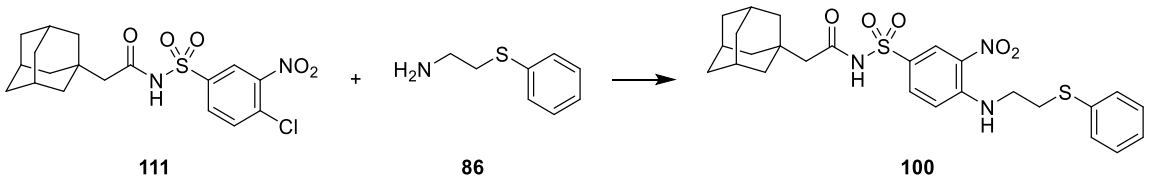

111 **86** **100**

Using **General Procedure B**, *N*-acylsulfonamide **111** (0.050 g, 0.12 mmol) and amine **86** (0.079 g, 0.52 mmol) gave the title compound. The crude residue was purified by flash column chromatography (10-50% EtOAc/hexane), then preparatory TLC (30% EtOAc/hexane, eluting twice) to yield *N*-acylsulfonamide **100** as a yellow solid (0.036 g, 56%). **IR** (neat, diamond cell) ν 3339, 3237, 3078, 2897, 2849, 1712, 1620, 1561, 1522, 1424, 1340, 1240, 1159, 1118, 1104, 1091, 899, 848, 733, 685, 664, 624 cm^{-1}; **LRMS** (−ESI) *m/z* 528 $[M-H]^-$; **HRMS** Calcd for $C_{26}H_{30}N_3O_5S_2^-$ $[M-H]^-$: *m/z* 528.16324, found *m/z* 528.16412; **^{1}H NMR** (500 MHz, DMSO-d_6) δ 11.91 (br s, 1H), 8.78 – 8.76 (t, *J* = 6.0 Hz, 1H), 8.52 – 8.51 (d, *J* = 2.4 Hz, 1H), 7.85 – 7.81 (dd, *J* = 9.5, 2.3 Hz, 1H), 7.18 – 7.38 (m, 6H), 3.68 – 3.64 (q, *J* = 6.5 Hz, 2H), 3.28 – 3.26 (t, *J* = 6.5 Hz, 2H), 1.90 (s, 2H), 1.82 (m, 3H), 1.59 – 1.41 (m, 12H); **^{13}C NMR** (126 MHz, DMSO-d_6) δ 169.68, 147.04, 134.98, 133.94, 129.74, 129.08, 128.66, 127.76, 126.10, 124.72, 115.16, 49.13, 41.90, 41.68, 36.17, 32.99, 31.08, 27.89 ppm; **HPLC** (254 nm) R_T = 30.65 min, 95.62%.

(Adamantan-1-yl)methanol **103**

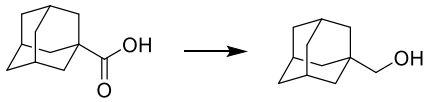

102 **103**

A solution of adamantane-1-carboxylic acid **102** (2.00 g, 11.1 mmol) in THF (30 mL) was cooled to 0 °C, then lithium aluminium hydride (1.05 g, 27.7 mmol) was added portionwise, then the suspension was then refluxed for 3 h. The suspension was then cooled to 0 °C, then H_2O (1 mL) was added, followed by 15% aq. KOH (1 mL), then H_2O again (3 mL). The mixture was stirred at RT for 15 min, then dried ($MgSO_4$) and filtered through a plug of celite. The

filtrate was evaporated to yield the alcohol **103** as a white solid (1.74 g, 95%). **IR** (neat, diamond cell) ν 3206, 2893, 2842, 1448, 1342, 1152, 1043, 695 cm^{-1}; **^{1}H NMR** (300 MHz, $CDCl_3$) δ 3.21 – 3.19 (d, *J* = 5.1 Hz, 2H), 1.99 (s, 3H), 1.76 – 1.63 (m, 6H), 1.51 (m, 6H), 1.28 – 1.25 (t, *J* = 5.1 Hz, 1H) ppm; **^{13}C NMR** (75 MHz, $CDCl_3$) δ 74.0, 39.2, 37.3, 34.6, 28.1 ppm.

Adamantane-1-carbaldehyde **104**

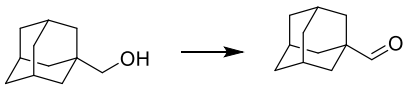

103 **104**

To a solution of (adamantan-1-yl)methanol **103** (1.0 g, 6.0 mmol) in CH_2Cl_2 (50 mL) was added Dess-Martin periodinane (2.8 g, 6.6 mmol), then the mixture was stirred at RT for 1 h. To the mixture was added sat. aq. $NaHCO_3$, then sat. aq. $NaHSO_3$ (1 mL). The mixture was extracted with diethyl ether (×3). The organic layers were combined and washed with brine, then dried ($MgSO_4$). The solvent was evaporated under reduced pressure. The crude residue was purified by flash column chromatography (CH_2Cl_2) to yield aldehyde **104** as a colourless, waxy solid (0.71 g, 72%). **IR** (neat, diamond cell) ν 2911, 2852, 1718, 1453, 649 cm^{-1}; **^{1}H NMR** (400 MHz, $CDCl_3$) δ 9.30 (s, 1H), 2.06 (s, 3H), 1.80 – 1.66 (m, 12H) ppm; **^{13}C NMR** (101 MHz, $CDCl_3$) δ 206.5, 85.4, 77.2, 76.5, 68.0 ppm.

Benzyl (E)-3-(adamantan-1-yl)acrylate **105**

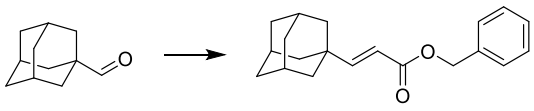

104 **105**

To a solution of adamantane-1-carbaldehyde **104** (1.0 g, 6.1 mmol) in toluene (20 mL) was added benzyl(triphosphoranylidene)acetate (3.0 g, 7.3 mmol), then the solution was heated at reflux for 16 h. The solution was concentrated and then purified by column chromatography (0-5% EtOAc/hexane) to yield acrylate **105** as a colourless oil (0.93 g), which was telescoped to the next step without characterisation.

3-(Adamantan-1-yl)propanoic acid **106**

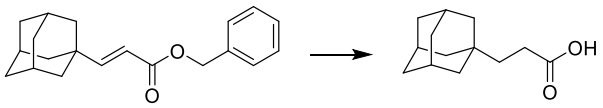

105 **106**

To a solution of crude benzyl (*E*)-3-(adamantan-1-yl)acrylate **105** (0.93 g) in MeOH (20 mL) was added palladium on carbon (0.090 g, 10% by mass), then the suspension was hydrogenated *via* H_2 balloon for 16 h. The mixture was filtered through a plug of celite, then the solvent was evaporated under reduced pressure. The crude residue was purified by column chromatography (5% MeOH/CH_2Cl_2) to yield acid **106** as an off-white solid (0.48 g, 38% over 2 steps). **LRMS** (−ESI) *m/z* 207.09 $[M-H]^-$; **^{1}H NMR** (300 MHz, $CDCl_3$) δ 2.34 – 2.28 (m, 2H), 1.96 (s, 3H), 1.73 – 1.60 (m, 6H), 1.47 – 1.41 (m, 8H) ppm; **^{13}C NMR** (75 MHz, $CDCl_3$) δ 181.1, 42.1, 38.8, 37.2, 32.1, 28.7, 28.1 ppm.

3-(Adamantan-1-yl)-N-((3-nitrophenyl)sulfonyl)propenamide **89**

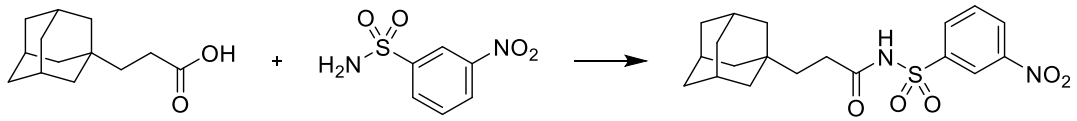

106 **74** **89**

Using **General Procedure A**, 3-(adamantan-1-yl)propanoic acid **106** (0.10 g, 0.48 mmol) and 3-nitrobenzenesulfonamide **74** (0.11 g, 0.54 mmol) gave the title compound. The crude residue was purified by flash column chromatography (10-50% EtOAc/hexanes) to yield *N*-acylsulfonamide **89** as an off-white solid (0.16 g, 85%). **IR** (neat, diamond cell) ν 3256, 3078, 2898, 2847, 1717, 1533, 1422, 1404, 1349, 1188, 1178, 1111, 1099, 1071, 885, 856, 661 cm^{-1}; **LRMS** (−ESI) *m/z* 391 $[M-H]^-$; **HRMS** Calcd for $C_{19}H_{23}N_2O_5S^-$ $[M-H]^-$: *m/z* 391.13332, found *m/z* 391.13325; **^{1}H NMR** (500 MHz, DMSO-d_6) δ 12.32 (br s, 1H), 8.60 (t, *J* = 2.0 Hz, 1H), 8.54 (ddd, *J* = 8.3, 2.4, 1.0 Hz, 1H), 8.35 – 8.30 (m, 1H), 7.94 (t, *J* = 8.1 Hz, 1H), 2.18 (t, *J* = 7.8 Hz, 2H), 1.81 (s, 3H), 1.60 – 1.48 (m, 6H), 1.26 (m, 6H), 1.19 (t, *J* = 7.8 Hz, 2H) ppm; **^{13}C NMR** (126 MHz, DMSO-d_6) δ 172.7, 147.6, 140.7, 133.6, 131.3, 128.2, 122.5, 41.4, 37.8, 36.4, 31.5, 29.5, 27.9 ppm; **HPLC** (254 nm) R_T = 29.17 min, 96.64%.

3-(Adamantan-1-yl)-N-((4-nitrophenyl)sulfonyl)propenamide **109**

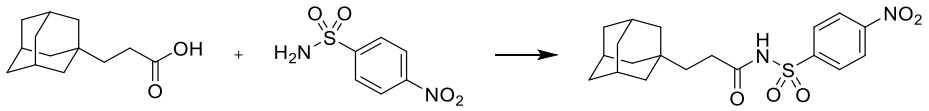

106 **76** **109**

Using **General Procedure A**, 3-(adamantan-1-yl)propanoic acid **106** (0.10 g, 0.48 mmol) and 4-nitrobenzenesulfonamide **76** (0.11 g, 0.54 mmol) gave the title compound. The crude residue was purified by flash column chromatography (10-50% EtOAc/hexane) to yield *N*-acylsulfonamide **109** as an off-white solid (0.17 g, 90%). **IR** (neat, diamond cell) ν 3266, 3111, 3100, 2895, 2845, 1735, 1530, 1422, 1402, 1347, 1186, 1177, 1086, 869, 850, 737, 610 cm^{-1}; **LRMS** (−ESI) *m/z* 391 $[M-H]^-$; **HRMS** Calcd for $C_{19}H_{23}N_2O_5S^-$ $[M-H]^-$: *m/z* 391.1332, found *m/z* 391.13301; **^{1}H NMR** (500 MHz, $(CD_3)_2CO$) δ 8.47 – 8.45 (m, 2H), 8.30 – 8.28 (m, 2H), 2.34 – 2.31 (t, *J* = 8.1 Hz, 2H), 1.87 (s, 3H), 1.69 – 1.57 (m, 6H), 1.39 – 1.38 (m, 6H), 1.33 – 1.30 (t, *J* = 8.1 Hz, 2H) ppm; **^{13}C NMR** (126 MHz, $(CD_3)_2CO$) δ 172.8, 151.7, 145.9, 130.6, 124.9, 42.6, 39.0, 37.6, 32.6, 30.6, 29.4 ppm.

3-(Adamantan-1-yl)-N-((4-aminophenyl)sulfonyl)propenamide **92**

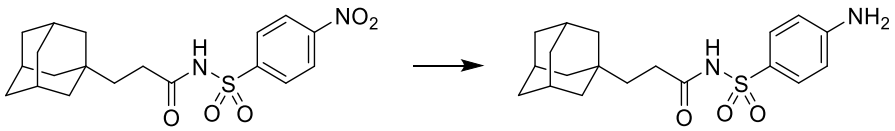

109 **92**

Using **General Procedure C**, *N*-acylsulfonamide **109** (0.050 g, 0.13 mmol) gave the title compound. The crude residue was purified by flash column chromatography (10-80% EtOAc/hexanes) to yield *N*-acylsulfonamide **92** as a white solid (0.041 g, 89%). **IR** (neat, diamond cell) ν 3482, 3377, 3240, 3218, 2901, 2845, 1714, 1625, 1593, 1434, 1317, 1154, 1125, 1082, 846, 832, 679 cm^{-1}; **LRMS** (−ESI) *m/z* 361 $[M-H]^-$; **HRMS** Calcd for $C_{19}H_{25}N_2O_3S^-$ $[M-H]^-$: *m/z* 361.15914, found *m/z* 361.15898; **^{1}H NMR** (500 MHz, $(CD_3)_2CO$) δ 10.19 (br s, 1H), 7.69 – 7.67 (m, 2H), 7.63 – 7.61 (m, 2H), 5.60 (br s, 1H), 2.24 – 2.21 (t, *J* = 8.1 Hz, 2H), 1.88 (s, 3H), 1.69 – 1.58 (m, 6H), 1.40 – 1.39 (m, 6H), 1.32 – 1.28 (t, *J* = 8.1 Hz, 2H) ppm; **^{13}C NMR** (126 MHz, $(CD_3)_2CO$) δ 172.1, 154.3, 131.2, 126.5, 113.5, 42.6, 39.3, 37.7, 32.6, 30.5, 29.5 ppm; **HPLC** (254 nm) R_T = 25.87 min, 96.08%.

3-(Adamantan-1-yl)-N-((4-chloro-3-nitrophenyl)sulfonyl)propenamide **112**

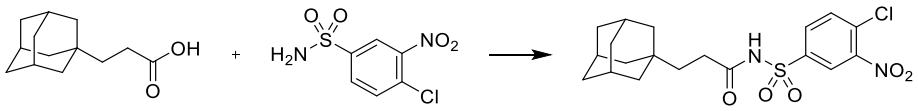

106 **80** **112**

Using **General Procedure A**, 3-(adamantan-1-yl)propanoic acid **106** (0.21 g, 1.0 mmol) and 4-chloro-3-nitrobenzenesulfonamide **80** (0.26 g, 1.1 mmol) gave the title compound. The crude residue was purified *via* flash column chromatography (30-50% EtOAc/hexanes) to yield *N*-acylsulfonamide **112** as a white solid (0.25 g, 58%). **IR** (neat, diamond cell) ν 3275, 3105, 3063, 2895, 2845, 1720, 1542, 1412, 1349, 1189, 1179, 1116, 1093, 1049, 892, 854, 832, 775, 612 cm^{-1}; **LRMS** (−ESI) *m/z* 425 $[M-H]^-$; **HRMS** Calcd for $C_{19}H_{23}{}^{35}ClN_2O_5S$ $[M-H]^-$: *m/z* 425.09325, found *m/z* 425.09256; **^{1}H NMR** (500 MHz, DMSO-d_6) δ 8.51 (d, *J* = 2.2 Hz, 1H), 8.16 (dd, *J* = 8.5, 2.2 Hz, 1H), 8.05 (d, *J* = 8.5 Hz, 1H), 2.19 (t, *J* = 7.8 Hz, 2H), 1.84 (t, *J* = 3.2 Hz, 3H), 1.68 – 1.46 (m, 6H), 1.28 (d, *J* = 2.8 Hz, 6H), 1.21 (t, *J* = 7.8 Hz, 2H) ppm; **^{13}C NMR** (126 MHz, DMSO-d_6) δ 172.9, 147.2, 139.2, 132.9, 132.4, 130.6, 125.0, 41.4, 37.8, 36.5, 31.6, 29.5, 27.9 ppm.

3-(Adamantan-1-yl)-N-((4-(methylamino)-3-nitrophenyl)sulfonyl)propenamide **95**

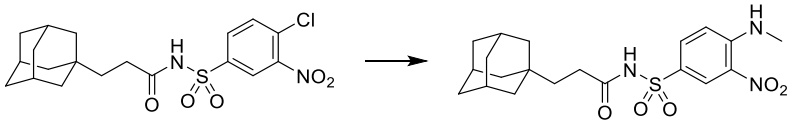

112 **95**

Using **General Procedure B**, *N*-acylsulfonamide **112** (0.075 g, 0.18 mmol) and 40% aq. $MeNH_2$ (0.2 mL) solution gave the title compound. The crude residue was purified *via* flash column chromatography (20-50% acetone/hexane) to yield *N*-acylsulfonamide **95** as a yellow solid (0.042 g, 57%). **IR** (neat, diamond cell) ν 3364, 3226, 3085, 2904, 2846, 1725, 1618, 1420, 1346, 1266, 1229, 1182, 1166, 1132, 1120, 1088, 1048, 900, 854, 813, 663 cm^{-1}; **LRMS** (−ESI) *m/z* 420 $[M-H]^-$; **HRMS** Calcd for $C_{20}H_{26}N_3O_5S^-$ $[M-H]^-$: *m/z* 420.15987, found *m/z* 420.15979; **^{1}H NMR** (400 MHz, DMSO-d_6) δ 8.66 (q, *J* = 4.9 Hz, 1H), 8.54 (d, *J* = 2.3 Hz, 1H), 7.89 (dd, *J* = 9.2, 2.3 Hz, 1H), 7.15 (d, *J* = 9.3 Hz, 1H), 3.01 (d, *J* = 4.9 Hz, 3H), 2.13 (t, *J* = 7.8 Hz, 2H), 2.08 (s, 1H), 1.82 (dd, *J* = 5.9, 3.1 Hz, 3H), 1.68 – 1.46 (m, 6H), 1.27 (d, *J* = 2.8 Hz, 6H), 1.19 (t, *J* = 7.8 Hz, 2H) ppm; **^{13}C NMR** (101 MHz, DMSO-d_6) δ 172.4, 148.0,

134.0, 129.6, 127.5, 124.2, 115.0, 41.4, 38.0, 36.5, 31.6, 30.0, 29.4, 27.9 ppm; **HPLC** (254 nm) R_T = 28.60 min, 96.32%.

3-(Adamantan-1-yl)-N-((4-(ethylamino)-3-nitrophenyl)sulfonyl)propenamide **98**

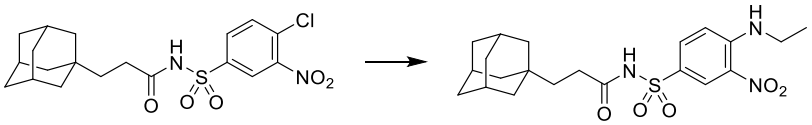

112 **98**

Using **General Procedure B**, *N*-acylsulfonamide **112** (0.075 g, 0.18 mmol) and 70% aq. $EtNH_2$ solution (0.5 mL) gave the title compound. The crude residue was purified *via* flash column chromatography (20-50% acetone/hexane) to yield *N*-acylsulfonamide **98** as a yellow solid (0.043 g, 56%). **IR** (neat, diamond cell) ν 3373, 3323, 3096, 2900, 2848, 1719, 1614, 1565, 1516, 1430, 1338, 1321, 1262, 1237, 1166, 1118, 1091, 1070, 1053, 917, 886, 850, 810, 659 cm^{-1}; **LRMS** (−ESI) *m/z* 434 $[M-H]^-$; **HRMS** Calcd for $C_{21}H_{28}N_3O_5S^-$ $[M-H]^-$: *m/z* 434.17552, found *m/z* 434.17466; **^{1}H NMR** (400 MHz, DMSO-d_6) δ 11.96 (br s, 1H), 8.62 (t, *J* = 5.9 Hz, 1H), 8.54 (d, *J* = 2.3 Hz, 1H), 7.86 (dd, *J* = 9.2, 2.3 Hz, 1H), 7.22 (d, *J* = 9.3 Hz, 1H), 3.46 (pentet, *J* = 6.5 Hz, 2H), 2.14 (t, *J* = 7.7 Hz, 2H), 1.84 – 1.78 (m, 3H), 1.67 – 1.43 (m, 6H), 1.26 (d, *J* = 2.8 Hz, 6H), 1.23 – 1.17 (m, 5H) ppm; **^{13}C NMR** (101 MHz, DMSO-d_6) δ 172.5, 147.1, 134.0, 129.5, 127.7, 124.3, 115.0, 41.4, 38.0, 37.4, 36.5, 31.6, 29.4, 27.9, 13.8 ppm; **HPLC** (254 nm) R_T = 29.79 min, 96.74%.

3-(Adamantan-1-yl)-N-((3-nitro-4-((2-(phenylthio)ethyl)amino)phenyl)sulfonyl)propenamide **101**

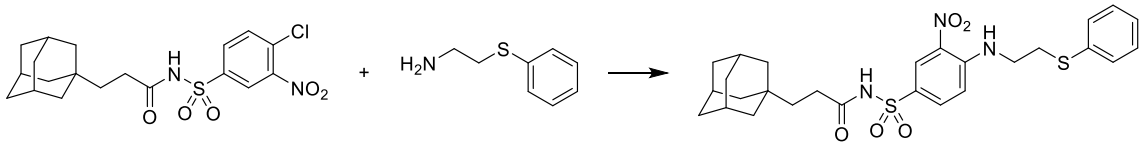

112 **86** **101**

Using **General Procedure B**, *N*-acylsulfonamide **112** (0.050 g, 0.11 mmol) and amine **86** (0.085 g, 0.55 mmol) gave the title compound. The crude residue was purified *via* flash column chromatography (20-50% acetone/hexane), then preparatory TLC (0.5% MeOH/CH_2Cl_2) to yield *N*-acylsulfonamide **101** as a yellow solid (0.041 g, 64%). **IR** (neat, diamond cell) ν 3355, 3247, 3232, 3099, 3076, 2899, 2846, 1714, 1614, 1566, 1519, 1437, 1411, 1345, 1272, 1241, 1164, 1128, 1092, 901, 847, 811, 739, 659 cm^{-1}; **LRMS** (−ESI) *m/z* 542

$[M-H]^-$; **HRMS** Calcd for $C_{27}H_{32}N_3O_5S_2^-$ $[M-H]^-$: *m/z* 542.17779, found *m/z* 542.17662; **^{1}H NMR** (400 MHz, DMSO-d_6) δ 8.73 (t, *J* = 6.0 Hz, 1H), 8.50 (d, *J* = 2.3 Hz, 1H), 7.82 (dd, *J* = 9.2, 2.3 Hz, 1H), 7.43 – 7.34 (m, 2H), 7.34 – 7.25 (m, 2H), 7.23 – 7.17 (m, 1H), 7.16 (d, *J* = 9.3 Hz, 1H), 3.65 (q, *J* = 6.6 Hz, 2H), 3.27 (t, *J* = 6.9 Hz, 3H), 2.10 (t, *J* = 7.8 Hz, 2H), 1.81 (q, *J* = 3.2 Hz, 3H), 1.73 – 1.43 (m, 6H), 1.27 (d, *J* = 2.8 Hz, 6H), 1.24 – 1.15 (t, *J* = 7.8 Hz, 2H) ppm; **^{13}C NMR** (101 MHz, DMSO-d_6) δ 173.1, 146.8, 135.0, 134.0, 129.8, 129.1, 128.7, 127.4, 126.1, 125.7, 114.9, 41.9, 41.4, 38.2, 36.5, 31.6, 31.2, 29.8, 27.9 ppm; **HPLC** (254 nm) R_T = 32.07 min, 98.08%.

6.4. Experimental and Characterisation for Chapter 3

7-(4,4,5,5-Tetramethyl-1,3,2-dioxaborolan-2-yl)-3,4-dihydronaphthalen-1(2H)-one **147**

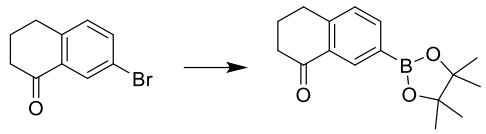

146 **147**

A mixture of aryl bromide **146** (0.39 g, 1.7 mmol), B_2pin_2 (0.57 g, 2.3 mmol), KOAc (0.34 g, 2.5 mmol) and Pd(dppf)Cl_2 (0.051 g, 0.69 mmol) was dried under vacuum. Concurrently, MeOH (7 mL) was degassed under N_2. MeOH was then added to the solid mixture, which was heated at 60 ºC for 16 h. When the reaction was complete, the mixture was filtered over a plug of celite and the filter cake washed with EtOAc. The solvent was evaporated under reduced pressure and the crude residue was purified by flash column chromatography (5-15% EtOAc/hexanes) to yield pinacol boronate **147** as a pale yellow oil (0.12 g, 25%). **LRMS** (+ESI) *m/z* 295 $[M+Na]^+$, 567 $[2M+Na]^+$; **^{1}H NMR** (400 MHz, $CDCl_3$) δ 8.50 (s, 1H), 7.87 (dd, *J* = 7.6, 1.5 Hz, 1H), 7.28 – 7.22 (m, 1H), 2.98 (t, *J* = 6.1 Hz, 2H), 2.66 (t, *J* = 6.5 Hz, 2H), 2.13 (p, *J* = 6.3 Hz, 2H), 1.34 (s, 12H) ppm; **^{13}C NMR** (101 MHz, $CDCl_3$) δ 198.4, 147.5, 139.5, 134.2, 132.2, 128.3, 84.1, 39.4, 30.2, 25.0, 23.3 ppm. The carbon bonded to boron could not be detected. Characterisation data were consistent with literature.[376]

6-(8-Oxo-5,6,7,8-tetrahydronaphthalen-2-yl)picolinic acid **148**

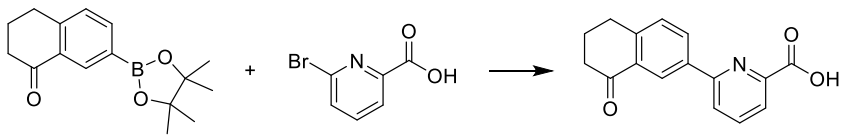

147 **210** **148**

A mixture of pinacol boronate **147** (0.12 g, 0.43 mmol), 6-bromopicolinic acid **210** (0.067 g, 0.33 mmol), K_2CO_3 (0.12 g, 0.90 mmol), TBAB (0.010 g, 0.030 mmol) and bis(triphenylphosphine)palladium(II) dichloride ($Pd(PPh_3)_2Cl_2$, 0.011 g, 0.017 mmol) was dried under vacuum. Concurrently, 1,4-dioxane/H_2O (2:1, 3.6 mL) was degassed under N_2. The solution was then added to the solid mixture, which was heated in a microwave reactor for 2 h. When the reaction was complete, the mixture was partitioned between EtOAc and H_2O, then the organic layer was extracted. The aqueous layer was acidified to pH 3, at which point a precipitate formed. The mixture was filtered and the residue was dried under vacuum. The residue was redissolved in 10% aq. K_2CO_3 solution, then acidified to pH 4, at which point a precipitate formed. The mixture was again filtered and the residue was dried under vacuum to yield ketone **148** as a white solid (0.055 g, 62%). **LRMS** (+ESI) *m/z* 266, $[M+Na]^+$, 555 $[2M+Na]^+$; **^{1}H NMR** (500 MHz, DMSO-d_6) δ 8.62 (d, *J* = 2.1 Hz, 1H), 8.34 (dd, *J* = 8.1, 2.1 Hz, 1H), 8.17 (d, *J* = 7.8 Hz, 1H), 8.04 (t, *J* = 7.8 Hz, 1H), 7.97 (d, *J* = 7.6 Hz, 1H), 7.51 (d, *J* = 8.1 Hz, 1H), 3.02 (t, *J* = 6.0 Hz, 2H), 2.66 (t, *J* = 6.5 Hz, 2H), 2.08 (p, *J* = 6.2 Hz, 2H); **^{13}C NMR** (126 MHz, DMSO-d_6) δ 197.6, 166.5, 155.0, 149.8, 145.9, 138.5, 136.4, 132.5, 131.5, 129.8, 124.5, 123.3, 122.7, 38.7, 28.8, 22.7 ppm. Characterisation data were consistent with literature.[376]

2-Hydrazineylbenzo[d]thiazole **150**

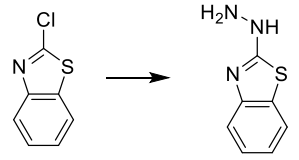

149 **150**

A solution of 2-chlorobenzothiazole **149** (0.25 g, 1.5 mmol) and 60% aq. hydrazine hydrate (0.7 mL) was refluxed at 80 °C for 2 h. When the reaction was complete, the mixture was filtered and the crude residue washed with EtOH. The residue was collected and recrystallised from EtOH to yield hydrazine **150** as a white solid (0.23 g, 94%). **LRMS** (+ESI) *m/z* 188

$[M+Na]^+$, 353 $[2M+Na]^+$; **^{1}H NMR** (500 MHz, $(CD_3)_2CO$) δ 7.67 (dd, *J* = 8.0, 1.3 Hz, 1H), 7.41 (dd, *J* = 8.1, 1.1 Hz, 1H), 7.29 – 7.22 (m, 1H), 7.07 (td, *J* = 7.5, 1.2 Hz, 1H) ppm; **^{13}C NMR** (126 MHz, $(CD_3)_2CO$) δ 168.4, 151.3, 130.8, 126.5, 122.3, 122.0, 118.5 ppm. Characterisation data were consistent with literature.[376]

(Z)-6-(8-(2-(Benzo[d]thiazol-2-yl)hydrazineylidene)-5,6,7,8-tetrahydronaphthalen-2-yl)picolinic acid **126**

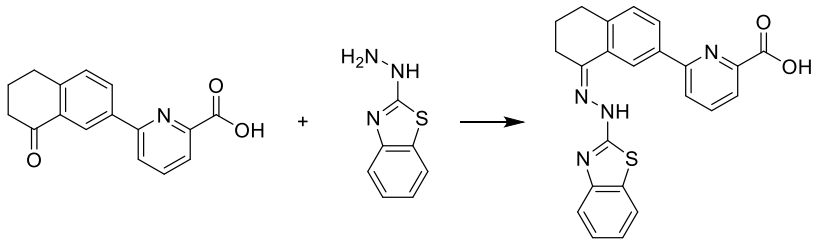

148 **150** **126**

A solution of ketone **148** (0.060 g, 0.36 mmol) in EtOH (4 mL) was gently heated to dissolve the solid. To this was added a solution of hydrazine **150** (0.060 g, 0.22 mmol) in EtOH (4 mL). The solution was heated at 80 °C for 1 h, at which point a precipitate had formed. The mixture was filtered and the residue dried under vacuum to yield hydrazone **126** as an off-white solid (0.028 g, 30%). **IR** (neat, diamond cell) ν 3520, 3060, 2959, 2938, 2880, 2872, 2422, 1883, 1682, 1603, 1587, 1572, 1558, 1443, 1410, 1388, 1328, 1310, 1267, 1243, 1152, 1120, 1087, 1070, 1048, 1030, 1018, 990, 900, 882, 822, 765, 749, 725, 714, 696, 643 cm^{-1}; **LRMS** (−ESI) *m/z* 413 $[M-H]^-$; **^{1}H NMR** (500 MHz, DMSO-d_6) δ 8.81 (d, *J* = 1.9 Hz, 1H), 8.17 – 8.04 (m, 4H), 8.04 – 7.98 (m, 1H), 7.74 (d, *J* = 7.8 Hz, 1H), 7.40 – 7.34 (m, 2H), 7.28 (t, *J* = 7.6 Hz, 1H), 7.10 (t, *J* = 7.5 Hz, 1H), 2.87 – 2.79 (m, 4H), 1.90 (p, *J* = 6.3 Hz, 2H) ppm; **HPLC** (254 nm) R_T = 22.88 min, 96.70%. Characterisation data were consistent with literature.[376]

Methyl 2-bromothiazole-4-carboxylate **152**

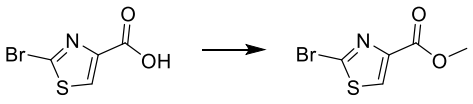

151 **152**

A solution of acid **151** (0.50 g, 2.4 mmol) and H_2SO_4 (0.25 mL) in MeOH (5 mL) was refluxed for 2 h. When the reaction was complete, the solution was concentrated under a gentle stream of N_2. The mixture was then quenched by addition of sat. aq. $NaHCO_3$ (50 mL), then extracted

with CH_2Cl_2 (×3). The combined organic layers were washed with brine, then dried ($MgSO_4$). The solvent was evaporated under reduced pressure to yield the aryl bromide **152** as a cream yellow solid (0.48 g, 89%), which was used without further purification. **LRMS** (+ESI) *m/z* 244, 246 $[M+Na]^+$; **^{1}H NMR** (400 MHz, DMSO-d_6) δ 8.12 (s, 1H), 3.94 (s, 3H) ppm; **^{13}C NMR** (101 MHz, DMSO-d_6) δ 160.7, 147.0, 137.0, 131.1, 52.8 ppm.

Tert-butyl 8-(benzo[d]thiazol-2-ylcarbamoyl)-3,4-dihydroisoquinoline-2(1H)-carboxylate **155**

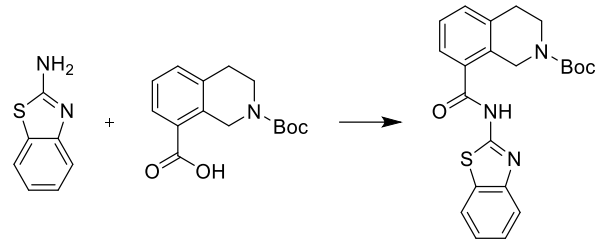

154 **153** **155**

Using **General Procedure D**, 2-aminobenzothiazole **154** (0.16 g, 1.1 mmol) and 2-(*tert*-butoxycarbonyl)-1,2,3,4-tetrahydroisoquinoline-8-carboxylic acid **153** (0.20 g, 0.72 mmol) gave the title compound. The crude residue was purified by flash column chromatography (20-50% EtOAc/hexanes) to yield amide **155** as a white solid (0.31 g, 71%). **IR** (neat, diamond cell) ν 3122, 3066, 2976, 2935, 2883, 2832, 1683, 1669, 1599, 1545, 1477, 1445, 1421, 1364, 1296, 1278, 1251, 1223, 1162, 1145, 1111, 916, 907, 874, 856, 841, 785, 755, 743, 731, 684, 441 cm^{-1}; **LRMS** (+ESI) *m/z* 432 $[M+Na]^+$, (−ESI) *m/z* 408 $[M-H]^-$; **^{1}H NMR** (500 MHz, DMSO-d_6) δ 11.89 (br s, 1H), 7.79 (dd, *J* = 7.9, 1.2 Hz, 1H), 7.47 (dd, *J* = 7.6, 1.2 Hz, 1H), 7.25 – 7.22 (m, 1H), 7.20 (d, *J* = 7.7 Hz, 1H), 7.18 – 7.12 (m, 1H), 7.08 – 7.02 (m, 1H), 6.94 (d, *J* = 8.1 Hz, 1H), 4.90 (s, 2H), 3.63 (s, 2H), 2.87 (s, 2H), 1.45 (s, 9H) ppm. Characterisation data were consistent with literature.[378]

N-(Benzo[d]thiazol-2-yl)-1,2,3,4-tetrahydroisoquinoline-8-carboxamide **156**

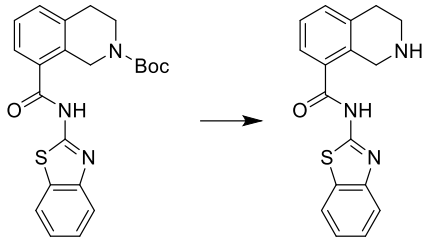

155 **156**

A solution of amide **155** (0.19 g, 0.46 mmol) in CH_2Cl_2 (2 mL) was cooled in an ice-water bath, then 4 M HCl in 1,4-dioxane (1 mL) was added dropwise. The solution was allowed to warm to RT and stirred for 16 h. When the reaction was complete, the solvent was evaporated under a gentle stream to N_2 to yield amine **156** as a white powder (0.14 g, 99%). **IR** (neat, diamond cell) ν 3498, 3345, 3162, 3034, 2977, 2926, 2829, 2748, 2674, 2594, 2500, 2469, 2405, 1689, 1588, 1561, 1539, 1464, 1453, 1427, 1362, 1347, 1318, 1290, 1266, 1235, 1215, 1201, 1129, 1101, 1064, 1017, 821, 807, 777, 762, 740, 722 cm^{-1}; **LRMS** (+ESI) *m/z* 310, (−ESI) *m/z* 308 $[M-H]^-$; **^{1}H NMR** (400 MHz, DMSO-d_6) δ 9.85 (s, 2H), 8.01 (dd, *J* = 7.9, 1.2 Hz, 1H), 7.82 – 7.76 (m, 1H), 7.74 (dd, *J* = 6.9, 2.1 Hz, 1H), 7.51 – 7.39 (m, 3H), 7.34 (ddd, *J* = 8.2, 7.2, 1.1 Hz, 1H), 4.49 – 4.42 (m, 2H), 3.35 (dt, *J* = 7.6, 3.9 Hz, 2H), 3.11 (t, *J* = 6.2 Hz, 2H) ppm. Characterisation data were consistent with literature.[378]

Methyl 2-(8-(benzo[d]thiazol-2-ylcarbamoyl)-3,4-dihydroisoquinolin-2(1H)-yl)thiazole-4-carboxylate **157**

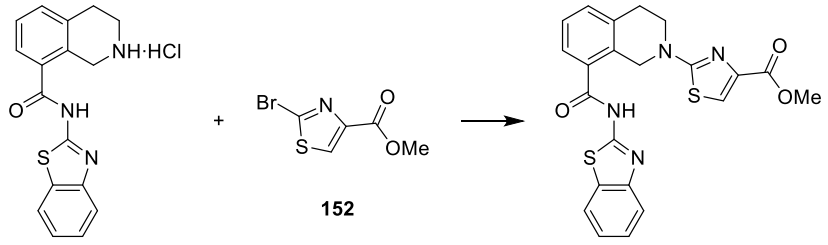

156 **152** **157**

To solution of amine **156** (0.050 g, 0.16 mmol) and aryl bromide **152** (0.036 g, 0.16 mmol) in dimethylacetamide (0.75 mL) was added Cs_2CO_3 (0.26 g, 0.81 mmol), then the solution was heated at 50 °C for 16 h. When the reaction was complete, the solution was acidified with 1 M HCl, then extracted with CH_2Cl_2 (×3). The organic layers were combined and washed with brine, then dried ($MgSO_4$). The solvent was evaporated under reduced pressure to yield the crude residue, which was purified by column chromatography (1-5% MeOH/CH_2Cl_2) to yield

ester **157** as a white solid (0.046 g, 63%), which was telescoped to the next step without characterisation.

2-(8-(Benzo[d]thiazol-2-ylcarbamoyl)-3,4-dihydroisoquinolin-2(1H)-yl)thiazole-4-carboxylic acid **127**

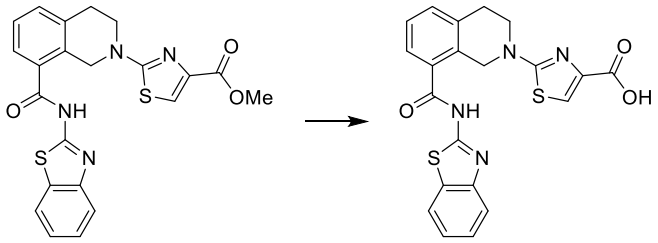

157 **127**

Using **General Procedure E**, ester **157** (0.046 g, 0.10 mmol) and LiOH (0.012 g, 0.51 mmol) gave the title compound. The crude residue was purified by column chromatography (1-5% MeOH/CH_2Cl_2) to yield acid **127** as a white solid (0.044 g, 99%). **IR** (neat, diamond cell) ν 3128, 2955, 2924, 2871, 2852, 1670, 1597, 1533, 1443, 1415, 1355, 1296, 1278, 1203, 1140, 784, 755, 727, 682, 633 cm^{-1} **LRMS** (−ESI) *m/z* 435 $[M-H]^-$; **^{1}H NMR** (500 MHz, DMSO-d_6) δ 8.01 (dd, *J* = 7.9, 1.2 Hz, 1H), 7.77 (d, *J* = 8.0 Hz, 1H), 7.67 (dd, *J* = 7.5, 1.5 Hz, 1H), 7.50 – 7.29 (m, 5H), 4.86 (s, 2H), 3.75 (t, *J* = 6.0 Hz, 2H), 3.04 (t, *J* = 6.0 Hz, 2H) ppm; **HPLC** (254 nm) R_T = 21.93 min, 96.73%. Characterisation data were consistent with literature.[378]

N-(Benzo[d]thiazol-2-yl)-1-(3-bromophenyl)cyclopropane-1-carboxamide **158**

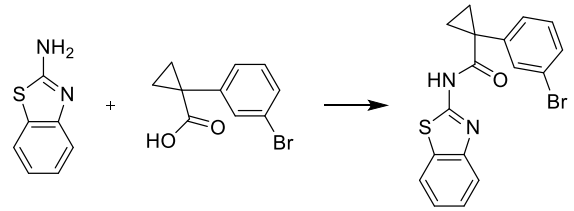

154 **159** **158**

Using **General Procedure D**, 2-aminobenzothiazole **154** (0.75 g, 5.0 mmol) and 1-(3-bromophenyl)cyclopropane-1-carboxylic acid **159** (0.60 g, 2.5 mmol) gave the title compound. The crude residue was purified by flash column chromatography (30-50% EtOAc/hexanes) to yield amide **158** as a white solid (0.77 g, 83%). **IR** (neat, diamond cell) ν 3149, 3100, 3064, 3013, 2954, 2695, 1673, 1596, 1523, 1478, 1447, 1411, 1308, 1279, 1266, 1208, 1151, 1069, 961, 879, 817, 779, 753, 728, 694, 664, 635 cm^{-1}; **LRMS** (−ESI) *m/z* 371, 373 $[M-H]^-$; **HRMS** Calcd for $C_{17}H_{12}BrN_2OS^-$ $[M-H]^-$: *m/z* 370.98592, 372.98387, found *m/z* 370.98565, 372.98374; **^{1}H NMR** (400 MHz, $CDCl_3$) δ 8.61 (br s, 1H), 7.80 (ddd, *J* = 7.9, 1.3,

0.6 Hz, 1H), 7.71 – 7.62 (m, 2H), 7.54 (ddd, *J* = 8.0, 2.0, 1.1 Hz, 1H), 7.47 – 7.36 (m, 2H), 7.33 – 7.27 (m, 2H), 1.85 (q, *J* = 4.0 Hz, 2H), 1.31 (q, *J* = 4.0 Hz, 2H) ppm; **^{13}C NMR** (101 MHz, $CDCl_3$) δ 171.8, 157.8, 148.4, 139.9, 134.4, 132.4, 132.3, 131.3, 130.1, 126.4, 124.2, 123.8, 121.5, 121.0, 30.7, 18.1 ppm.

N-(Benzo[d]thiazol-2-yl)-1-(3-(4,4,5,5-tetramethyl-1,3,2-dioxaborolan-2-yl)phenyl)cyclopropane-1-carboxamide **162**

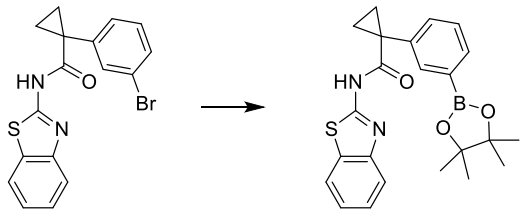

158 **162**

Using **General Procedure F**, aryl bromide **158** (0.25 g, 0.67 mmol) gave the title compound. The crude residue was purified by flash column chromatography (5-10% acetone/hexanes) to yield amide **162** as a white solid (0.21 g, 75%). **IR** (neat, diamond cell) ν 3394, 2981, 2923, 1679, 1531, 1447, 1431, 1418, 1385, 1361, 1325, 1275, 1141, 1111, 1094, 1073, 966, 859, 760, 732, 714, 681, 669 cm^{-1}; **LRMS** (+ESI) *m/z* 443 $[M+Na]^+$, (−ESI) *m/z* 419 $[M-H]^-$; **HRMS** Calcd for $C_{23}H_{24}BN_2O_3S^-$ $[M-H]^-$: *m/z* 419.16062, found *m/z* 419.16027; **^{1}H NMR** (400 MHz, $CDCl_3$) δ 8.54 (br s, 1H), 7.91 (d, *J* = 1.7 Hz, 1H), 7.85 (dt, *J* = 7.3, 1.3 Hz, 1H), 7.79 (dd, *J* = 7.9, 1.1 Hz, 1H), 7.66 (dt, *J* = 8.1, 0.9 Hz, 1H), 7.58 (ddd, *J* = 7.7, 2.0, 1.4 Hz, 1H), 7.45 (t, *J* = 7.5 Hz, 1H), 7.39 (ddd, *J* = 8.2, 7.2, 1.3 Hz, 1H), 7.31 – 7.27 (m, 1H), 1.83 (q, *J* = 3.9 Hz, 2H), 1.37 (s, 12H), 1.34 (q, *J* = 4.0 Hz, 2H) ppm; **^{13}C NMR** (101 MHz, $CDCl_3$) δ 172.7, 158.0, 148.5, 137.6, 136.8, 135.6, 134.3, 132.4, 131.4, 129.9, 129.2, 126.3, 124.0, 121.5, 120.9, 84.3, 30.9, 25.0, 18.1 ppm.

Methyl 2-(3-(1-(benzo[d]thiazol-2-ylcarbamoyl)cyclopropyl)phenyl)thiazole-4-carboxylate **161**

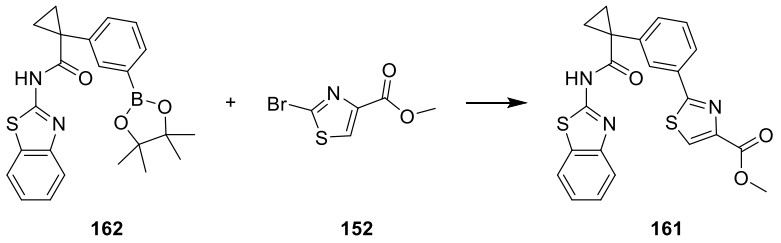

A mixture of pinacol boronate **162** (0.15 g, 0.36 mmol), aryl bromide **152** (0.12 g, 0.54 mmol), $Pd(PPh_3)_4$ (0.021 g, 0.018 mmol) and Na_2CO_3 (0.11 g, 1.1 mmol) was dried under vacuum. Concurrently, a mixture of 1,4-dioxane (0.75 mL) and H_2O (0.25 mL) was degassed with N_2. The solution was added to the solids and the mixture heated at 80 °C for 16 h. When the reaction was complete, the mixture was diluted with 1 M HCl. The aqueous layer was extracted with EtOAc (×3) and the combined organic layers were washed with brine and dried ($MgSO_4$). The solvent was evaporated to yield the crude residue, which was purified by flash column chromatography (5-10% acetone/hexanes, then 20-30% acetone/hexanes) to yield ester **161** as a white solid (0.019 g, 12%), which was telescoped to the next step without characterisation.

2-(3-(1-(Benzo[d]thiazol-2-ylcarbamoyl)cyclopropyl)phenyl)thiazole-4-carboxylic acid **139**

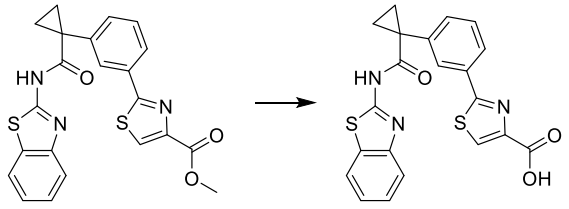

Using **General Procedure E**, ester **161** (0.019 g, 0.044 mmol) and LiOH (0.005 g, 0.2 mmol) gave the title compound. The residue was purified by reverse phase column chromatography (0-100% MeCN/H_2O) to yield acid **139** as an off-white solid (0.018 g, 99%). **IR** (neat, diamond cell) ν 3474, 3474, 3157, 3120, 3059, 2958, 2921, 2851, 1692, 1667, 1537, 1454, 1438, 1362, 1343, 1310, 1284, 1258, 1245, 1228, 1177, 1164, 1120, 1093, 1027, 989, 961, 943, 900, 828, 809, 773, 756, 739, 728, 705, 696, 679, 640 cm^{-1}; **LRMS** (−ESI) *m/z* 420 $[M-H]^-$; **HRMS** Calcd for $C_{21}H_{14}N_3O_3S_2^-$ $[M-H]^-$: *m/z* 420.04821, found *m/z* 420.04826; **^{1}H NMR** (400 MHz, $(CD_3)_2CO$) δ 8.44 (s, 1H), 8.26 (t, *J* = 1.9 Hz, 1H), 8.02 (dt, *J* = 7.9, 1.4 Hz, 1H), 7.94 – 7.87 (m, 1H), 7.75 (dt, *J* = 7.6, 1.4 Hz, 1H), 7.63 – 7.54 (m, 2H), 7.37 (td, *J* = 7.7, 1.3 Hz, 1H), 7.31 – 7.25 (m, 1H), 1.79 (q, *J* = 4.1 Hz, 2H), 1.43 (q, *J* = 4.1 Hz, 2H) ppm; **^{13}C**

NMR (101 MHz, $(CD_3)_2CO$) δ 172.82, 168.58, 162.21, 158.81, 149.64, 148.64, 140.29, 136.97, 134.64, 134.19, 133.05, 130.84, 129.93, 129.05, 127.35, 126.81, 124.52, 122.15, 121.72, 31.52, 17.53 ppm; **HPLC** (254 nm) R_T = 27.28 min, 99.66%.

1-(3-Bromophenyl)cyclobutane-1-carbonitrile **167**

166 **167**

To a solution of nitrile **166** (0.66 mL, 5.1 mmol) in DMF (12 mL) was added NaH (0.45 g, 11.2 mmol), at which point the solution turned deep red. After 30 minutes, the solution was cooled in an ice-water bath and 1,3-dibromopropane (0.55 mL 5.4 mmol) was added dropwise, and then the solution was stirred for 16 h at RT. When the reaction was complete, the solution was diluted with H_2O and extracted with EtOAc (×3). The organic layers were combined and washed with brine, then dried ($MgSO_4$). The crude residue was purified by flash column chromatography (10-30% EtOAc/hexane) to yield nitrile **167** as a colourless oil (0.55 g, 46%). **LRMS** (−ESI) *m/z* 258, 260 $[M-H]^-$; **^{1}H NMR** (500 MHz, $CDCl_3$) δ 7.53 (t, *J* = 1.9 Hz, 1H), 7.43 (ddd, *J* = 7.9, 1.9, 1.1 Hz, 1H), 7.32 (ddd, *J* = 7.8, 1.9, 1.1 Hz, 1H), 7.25 – 7.19 (m, 1H), 2.80 (dddd, *J* = 12.8, 6.1, 3.3, 1.5 Hz, 2H), 2.62 – 2.53 (m, 2H), 2.48 – 2.35 (m, 1H), 2.06 (dtt, *J* = 11.7, 9.0, 4.4 Hz, 1H) ppm; **^{13}C NMR** (125 MHz, $CDCl_3$) δ 142.1, 131.2, 130.6, 129.0, 124.5, 123.9, 123.2, 39.9, 34.7, 17.2 ppm. Characterisation data were consistent with literature.[458]

1-(3-Bromophenyl)cyclobutane-1-carboxylic acid **165**

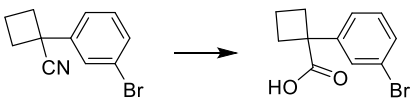

167 **165**

To a solution of nitrile **167** (0.55 g, 2.34 mmol) in 1:1 EtOH/H_2O (5 mL) was added KOH (0.66 g, 11.7 mmol), and then solution was refluxed for 16 h. When the reaction was complete, the mixture was concentrated under a gentle stream of N_2, then acidified by addition of 1 M HCl and extracted with EtOAc (×3). The organic layers were combined and washed with brine, then dried ($MgSO_4$). The solvent was evaporated under reduced pressure to yield acid **165** with no further purification (0.47 g, 79%). **LRMS** (−ESI) *m/z* 253, 255 $[M-H]^-$, 529, 531, 533

$[2M-2H+Na]^-$; **^{1}H NMR** (400 MHz, $CDCl_3$) δ 7.44 (d, *J* = 1.9 Hz, 1H), 7.38 (dt, *J* = 7.1, 1.9 Hz, 1H), 7.25 – 7.15 (m, 2H), 2.90 – 2.78 (m, 2H), 2.57 – 2.45 (m, 2H), 2.10 (dp, *J* = 11.3, 8.6 Hz, 1H), 1.88 (dtt, *J* = 10.7, 9.1, 4.8 Hz, 1H) ppm; **^{13}C NMR** (101 MHz, $CDCl_3$) δ 181.5, 145.5, 130.2, 130.0, 129.9, 125.3, 122.6, 52.1, 32.4, 16.8 ppm. Characterisation data were consistent with literature.[459]

N-(Benzo[d]thiazol-2-yl)-1-(3-bromophenyl)cyclobutane-1-carboxamide **164**

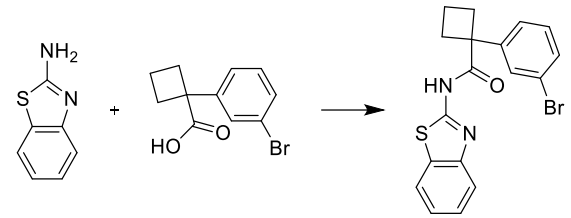

154 **165** **164**

Using **General Procedure D**, 2-aminobenzothiazole **154** (0.59 g, 3.9 mmol) and acid **165** (0.50 g, 2.0 mmol) gave the title compound. The crude residue was purified by flash column chromatography (30-50% EtOAc/hexanes) to yield amide **164** as a white solid (0.61 g, 80%). **IR** (neat, diamond cell) ν 3252, 3208, 3082, 3054, 2985, 2944, 2865, 1666, 1595, 1532, 1476, 1451, 1438, 1287, 1255, 1228, 1118, 962, 848, 823, 780, 760, 733, 699, 691, 676 cm^{-1}; **LRMS** (−ESI) *m/z* 385, 387 $[M-H]^-$; **HRMS** Calcd for $C_{18}H_{14}BrN_2OS^-$ $[M-H]^-$: *m/z* 385.00157, 386.99952, found *m/z* 385.00197, 386.99973; **^{1}H NMR** (400 MHz, $CDCl_3$) δ 8.76 (br s, 1H), 7.81 (d, *J* = 7.9 Hz, 1H), 7.67 (d, *J* = 8.1 Hz, 1H), 7.48 (d, *J* = 1.7 Hz, 1H), 7.44 (ddd, *J* = 7.4, 6.2, 1.5 Hz, 1H), 7.41 – 7.37 (m, 1H), 7.35 – 7.17 (m, 3H), 2.94 (ddd, *J* = 11.5, 9.0, 5.2 Hz, 2H), 2.55 (ddd, *J* = 12.2, 9.4, 7.3 Hz, 2H), 2.21 (dddd, *J* = 16.3, 11.3, 9.1, 7.3 Hz, 1H), 1.97 (dddd, *J* = 14.7, 11.1, 9.4, 5.5 Hz, 1H) ppm; **^{13}C NMR** (101 MHz, $CDCl_3$) δ 173.5, 158.2, 148.3, 144.6, 131.1, 131.0, 129.7, 128.1, 126.4, 125.1, 124.2, 123.7, 121.5, 121.0, 53.1, 32.1, 16.6 ppm.

N-(Benzo[d]thiazol-2-yl)-1-(3-(4,4,5,5-tetramethyl-1,3,2-dioxaborolan-2-yl)phenyl)cyclobutane-1-carboxamide **163**

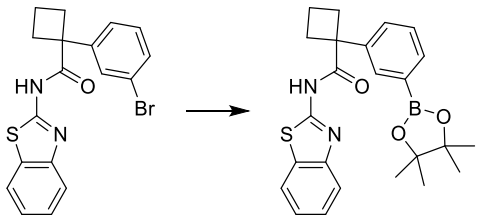

164 **163**

Using **General Procedure F**, aryl bromide **164** (0.25 g, 0.65 mmol) gave the title compound. The crude residue was purified by flash column chromatography to yield pinacol boronate **163** as a white solid (0.18 g, 63%). **IR** (neat, diamond cell) ν 3388, 3244, 2976, 2944, 2868, 1688, 1598, 1530, 1444, 1419, 1380, 1355, 1316, 1291, 1260, 1190, 1166, 1142, 1081, 963, 937, 862, 846, 756, 730, 707, 675 cm^{-1}; **LRMS** (−ESI) *m/z* 433 $[M-H]^-$; **HRMS** Calcd for $C_{24}H_{27}BN_2NaO_3S^-$ $[M+Na]^+$: *m/z* 457.17277, found *m/z* 457.17277; **^{1}H NMR** (500 MHz, $CDCl_3$) δ 8.37 (br s, 1H), 7.79 (tdd, *J* = 6.7, 2.1, 1.0 Hz, 3H), 7.69 – 7.63 (m, 1H), 7.47 – 7.34 (m, 3H), 7.30 – 7.27 (m, 1H), 3.02 – 2.92 (m, 2H), 2.65 (tdd, *J* = 9.4, 7.5, 2.3 Hz, 2H), 2.27 (dtt, *J* = 11.3, 9.1, 7.5 Hz, 1H), 1.97 (dtt, *J* = 11.0, 9.3, 5.3 Hz, 1H), 1.36 (s, 12H) ppm; **^{13}C NMR** (126 MHz, $CDCl_3$) δ 174.3, 158.1, 148.5, 141.5, 134.5, 132.4, 132.4, 129.6, 129.0, 126.3, 124.0, 121.5, 120.9, 84.2, 53.2, 32.2, 25.0, 16.7 ppm. The carbon bonded to boron could not be detected.

N-(Benzo[d]thiazol-2-yl)-1-(3-cyanophenyl)cyclobutane-1-carboxamide **170**

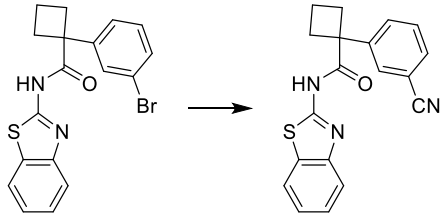

164 **170**

A mixture of aryl bromide **164** (0.10 g, 0.26 mmol), $Zn(CN)_2$ (0.061 g, 0.52 mmol) and $Pd(PPh_3)_4$ (0.060 g, 0.0052 mmol) was dried under vacuum. Concurrently, DMF (1 mL) was degassed under N_2. The solvent was added to the solids and the mixture solution was heated at 100 ºC for 3 h. When the reaction was complete, the mixture was diluted with 1 aq. M NH_3 solution. The aqueous layer was extracted with EtOAc (×3) and the combined organic layers were washed with brine and dried ($MgSO_4$). The solvent was evaporated under a gentle stream

of N_2 to yield the crude residue, which was purified by flash column chromatography (10-40% EtOAc/hexanes) to yield nitrile **170** as a white solid (0.071 g, 91%). **IR** (neat, diamond cell) ν 3340, 3134, 2989, 2890, 2226, 1698, 1587, 1570, 1435, 11376, 1342, 1310, 1287, 1216, 1190, 1139, 1085, 971, 947, 859, 840, 756, 745, 701, 667 cm^{-1}; **LRMS** (−ESI) *m/z* 332 $[M-H]^-$, 687 $[2M-2H+Na]^-$; **HRMS** Calcd for $C_{19}H_{14}N_3OS^-$ $[M-H]^-$ *m/z* 332.08631, found *m/z* 332.08632; **^{1}H NMR** (500 MHz, $CDCl_3$) δ 9.56 (br s, 1H), 7.81 (dd, *J* = 8.0, 1.3 Hz, 1H), 7.66 – 7.59 (m, 2H), 7.56 (dt, *J* = 7.4, 1.5 Hz, 1H), 7.49 – 7.36 (m, 3H), 7.30 (ddd, *J* = 8.2, 7.2, 1.1 Hz, 1H), 2.95 (dtd, *J* = 12.1, 5.6, 2.6 Hz, 2H), 2.49 (tdd, *J* = 9.3, 7.1, 2.5 Hz, 2H), 2.14 (dddd, *J* = 16.3, 9.1, 7.2, 3.8 Hz, 1H), 1.94 (dtt, *J* = 11.5, 9.2, 5.7 Hz, 1H) ppm; **^{13}C NMR** (126 MHz, $CDCl_3$) δ 173.2, 158.5, 148.2, 143.8, 132.2, 131.2, 130.8, 130.0, 129.9, 126.4, 124.2, 121.6, 120.9, 118.4, 113.3, 53.0, 32.0, 16.4 ppm.

N-(Benzo[d]thiazol-2-yl)-1-(3-carbamothioylphenyl)cyclobutane-1-carboxamide **169**

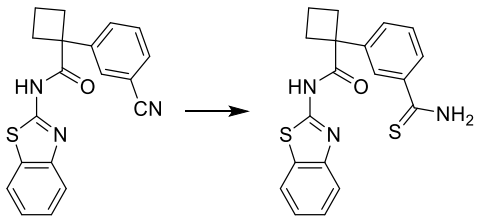

170 **169**

A solution of nitrile **170** (0.10 g, 0.30 mmol) and $Na_2S·9H_2O$ (0.17 g, 0.71 mmol) in DMF (1 mL) was heated at 130 °C for 2 h. The reaction mixture was subsequently poured into H_2O. The aqueous layer was extracted with EtOAc (×3) and the combined organic layers were washed with brine and dried ($MgSO_4$). The solvent was evaporated under reduced pressure to yield the crude residue, which was purified by column chromatography (20-60% EtOAc/hexanes) to yield thioamide **169** as a brown solid (0.054 g, 49%), which was telescoped to the next step without characterisation.

Ethyl 2-(3-(1-(benzo[d]thiazol-2-ylcarbamoyl)cyclobutyl)phenyl)thiazole-4-carboxylate **168**

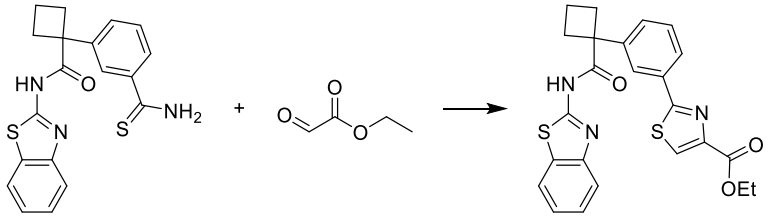

169 **168**

A solution of thioamide **169** (0.050 g, 0.14 mmol) and ethyl glyoxalate (0.020 mL, 0.16 mmol) in EtOH (2 mL) was heated at reflux for 2 h. When the reaction was complete, the mixture was concentrated under a gentle stream of N_2, then diluted with H_2O. The aqueous layer was extracted with EtOAc (×3) and the combined organic layers were washed with brine, then dried ($MgSO_4$). The solvent was evaporated under reduced pressure to yield the crude residue, which was purified by column chromatography to yield ester **168** as an off-white solid (0.052 g, 83%). **IR** (neat, diamond cell) ν 3569, 3256, 3114, 3072, 3042, 2952, 2921, 2852, 1708, 1686, 1598, 1537, 1475, 1452, 1441, 1408, 1371, 1342, 1292, 1268, 1224, 1156, 1123, 1112, 1094, 1020, 1006, 943, 943, 863, 843, 795, 753, 728, 714, 693 cm^{-1}; **LRMS** (+ESI) *m/z* 486 $[M+Na]^+$; (−ESI) *m/z* 462.10 $[M-H]^-$; **HRMS** Calcd for $C_{24}H_{21}N_3NaO_3S_2^-$ $[M+Na]^+$: *m/z* 486.09165, found *m/z* 486.09181; **^{1}H NMR** (400 MHz, $(CD_3)_2CO$) δ 10.86 (br s, 1H), 8.37 (s, 1H), 8.20 (d, *J* = 1.9 Hz, 1H), 7.86 (td, *J* = 7.8, 1.4 Hz, 2H), 7.65 – 7.56 (m, 2H), 7.50 (t, *J* = 7.8 Hz, 1H), 7.38 – 7.30 (m, 1H), 7.30 – 7.18 (m, 1H), 4.34 (q, *J* = 7.1 Hz, 2H), 3.10 (ddd, *J* = 12.3, 8.8, 5.9 Hz, 2H), 2.70 (tdd, *J* = 9.3, 7.1, 2.4 Hz, 2H), 2.03 – 1.92 (m, 2H), 1.34 (t, *J* = 7.1 Hz, 3H) ppm; **^{13}C NMR (**101 MHz, $(CD_3)_2CO$) δ 175.1, 168.8, 161.7, 159.1, 149.9, 149.0, 145.2, 134.3, 133.1, 130.6, 129.6, 128.8, 126.8, 126.4, 125.1, 124.4, 122.1, 121.6, 61.7, 54.6, 54.5, 32.8, 16.9, 14.6 ppm.

2-(3-(1-(Benzo[d]thiazol-2-ylcarbamoyl)cyclobutyl)phenyl)thiazole-4-carboxylic acid **140**

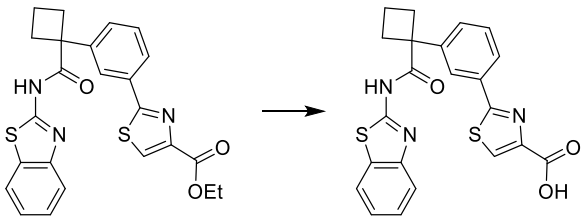

168 **140**

Using **General Procedure E**, ester **168** (0.025 g, 0.054 mmol) and LiOH (0.006 g, 0.3 mmol) gave the title compound as a white solid (0.023 g, 99%). **IR** (neat, diamond cell) ν 3550, 3509,

3245, 3111, 3069, 2944, 2911, 2860, 1699, 1681, 1604, 1466, 1460, 1439, 1420, 1368, 1335, 1301, 1278, 1219, 1160, 1124, 1119, 1081, 1031, 951, 865, 849, 799, 742, 726, 689 cm^{-1}; **LRMS** (−ESI) *m/z* 434.05 $[M-H]^-$; **HRMS** Calcd for $C_{22}H_{17}N_3O_3S_2^-$ $[M-H]^-$ *m/z* 458.06035, found *m/z* 458.06084; **^{1}H NMR** (500 MHz, DMSO-d_6) δ 12.43 (br s, 1H), 8.49 (s, 1H), 8.14 (s, 1H), 7.95 (d, J = 7.9 Hz, 1H), 7.85 (d, J = 7.6 Hz, 1H), 7.68 (d, J = 8.1 Hz, 1H), 7.60 (d, J = 7.8 Hz, 1H), 7.54 (t, J = 7.7 Hz, 1H), 7.40 (t, J = 7.7 Hz, 1H), 7.28 (t, J = 7.6 Hz, 1H), 3.01 – 2.92 (m, 2H), 2.60 (dt, J = 12.0, 8.5 Hz, 2H), 1.96 – 1.81 (m, 1H) ppm; **^{13}C NMR** (126 MHz, DMSO-d_6) δ 174.6, 167.2, 162.1, 158.5, 148.4, 148.4, 144.1, 132.7, 131.4, 129.6, 128.7, 128.7, 126.1, 125.3, 124.0, 123.6, 121.6, 120.3, 53.1, 31.9, 15.9 ppm; **HPLC** (254 nm) 24.47 min, 95.30%.

N-(Benzo[d]thiazol-2-yl)-2-iodobenzamide **172**

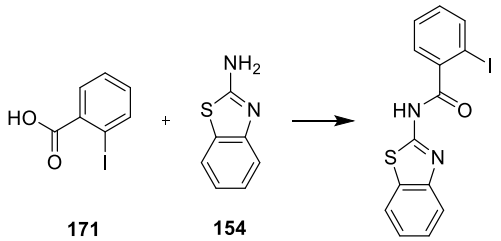

171 **154** **172**

Using **General Procedure D**, 2-iodobenzoic acid **171** (0.83 g, 3.4 mmol) and 2-aminobenzothiazole **154** (1.0 g, 6.7 mmol) gave the title compound. The crude residue was purified *via* flash column chromatography (20-50% EtOAc/hexane) to yield amide **172** as an off-white solid (0.51 g, 40%). **IR** (neat, diamond cell) ν 3046, 3122, 2917, 2887, 2836, 2771, 2690, 2690, 1689, 1680, 1599, 1579, 1551, 1477, 1453, 1442, 1431, 1230, 1279, 1260, 1136, 1108, 1016, 914, 867, 845, 769, 755, 739, 726, 712, 702, 679, 655, 636 cm^{-1}; **LRMS** (+ESI) *m/z* 403 $[M+Na]^+$, (−ESI) *m/z* 378.92 $[M-H]^-$; **HRMS** Calcd for $C_{14}H_8IN_2O_5S^-$ $[M-H]^-$: *m/z* 378.94075, found *m/z* 378.94052; **^{1}H NMR** (400 MHz, $CDCl_3$) δ 7.78 (d, *J* = 7.9 Hz, 1H), 7.71 (d, *J* = 8.0 Hz, 1H), 7.51 (dd, *J* = 7.7, 1.7 Hz, 1H), 7.27 (t, *J* = 7.6 Hz, 1H), 7.22 (t, *J* = 7.6 Hz, 1H), 7.16 – 7.07 (m, 1H), 7.01 (td, *J* = 7.7, 1.7 Hz, 1H), 6.86 (d, *J* = 8.1 Hz, 1H) ppm; **^{13}C NMR** (101 MHz, $CDCl_3$) δ 167.4, 159.3, 147.9, 140.6, 139.5, 132.6, 131.9, 129.3, 128.5, 126.4, 124.1, 121.4, 120.5, 92.7 ppm.

N-(Benzo[d]thiazol-2-yl)-2-((trimethylsilyl)ethynyl)benzamide **173**

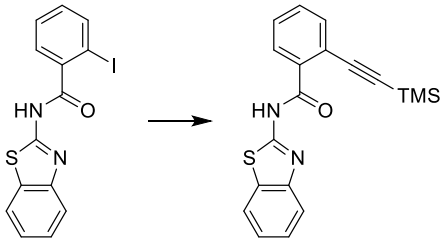

172 **173**

A mixture of aryl iodide **172** (0.050 g, 0.13 mmol), $Pd(PPh_3)_2Cl_2$ (0.009 g, 0.013 mmol) and CuI (0.001 g, 0.007 mmol) were dried under vacuum. Concurrently, a solution of trimethylsilylacetylene (TMSA, 0.028 mL, 0.20 mmol) and Et_3N (0.040 mL, 0.39 mmol) in DMF (1 mL) was degassed under N_2. The solution was added to the solids and the mixture was heated at 30 ºC for 3 h. When the reaction was complete, the mixture was diluted with 1 M HCl solution and extracted with EtOAc (×3). The combined organic layers were washed with brine, then dried ($MgSO_4$). The solvent was evaporated under reduced pressure to yield the crude residue, which was purified by flash column chromatography (5-15% EtOAc/hexane) to yield alkyne **173** as a cream yellow solid (0.072 g, 16%). **IR** (neat, diamond cell) ν 3064, 3012, 2955, 2924, 2852, 1720, 1608, 1594, 1499, 1472, 1440, 1360, 1338, 1303, 1280, 1265, 1249, 1223, 1175, 1150, 1140, 1092, 1073, 1015, 911, 857, 755, 729, 694, 678, 647, 614 cm^{-1}; **LRMS** (+ESI) *m/z* 373 $[M+Na]^+$; **HRMS** Calcd for $C_{19}H_{18}N_2NaOSSi^+$ $[M+Na]^+$: *m/z* 373.08013, found *m/z* 373.08032; **^{1}H NMR** (500 MHz, $CDCl_3$) δ 8.05 (s, 1H), 8.00 (d, *J* = 7.5 Hz, 1H), 7.98 (d, *J* = 8.1 Hz, 1H), 7.91 (d, *J* = 7.9 Hz, 2H), 7.72 (td, *J* = 7.6, 1.2 Hz, 1H), 7.59 (td, *J* = 7.5, 0.9 Hz, 1H), 7.49 (ddd, *J* = 8.3, 7.2, 1.3 Hz, 1H), 7.38 (ddd, *J* = 8.2, 7.2, 1.2 Hz, 1H), 0.44 (s, 9H) ppm; **^{13}C NMR** (101 MHz, DMSO-d_6) δ 166.5, 156.1, 149.0, 143.4, 137.3, 133.6, 132.7, 129.8, 128.2, 126.2, 124.8, 124.5, 123.4, 122.3, 121.2, 116.5, 0.4 ppm.

Methyl 2-((trimethylsilyl)ethynyl)thiazole-4-carboxylate **174**

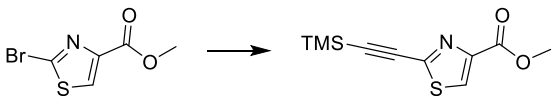

152 **174**

A mixture of aryl bromide **152** (1.0 g, 4.4 mmol), $Pd(PPh_3)_4$ (0.26 g, 0.22 mmol) and CuI (0.042 g, 0.22 mmol) was dried under vacuum. Concurrently, a solution of TMSA (3.2 mL, 23 mmol), Et_3N (5.0 mL, 53 mmol) and DMF (5 mL) was degassed under N_2. The solution was added to the solids and the mixture was stirred at 40 ºC for 1 h. When the reaction was complete, the

mixture was diluted 1 M HCl solution and extracted with EtOAc (×3). The combined organic layers were washed with brine, then dried ($MgSO_4$). The solvent was evaporated to yield the crude residue, which was purified by flash column chromatography (10-30% EtOAc/hexane) to yield alkyne **174** (0.73 g, 68%), which was telescoped to the next step without characterisation.

Methyl 2-ethynylthiazole-4-carboxylate **175**

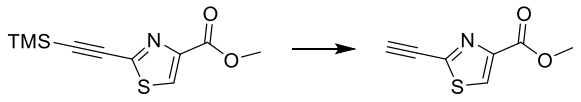

174 **175**

To a solution of alkyne **174** (0.97 g, 4.3 mmol) in THF (5 mL) was added tetrabutylammonium fluoride in THF solution (1 mL), at which point the solution turned black, then the solution was stirred at RT for 30 min. When the reaction was complete, the solution was diluted with H_2O and extracted with EtOAc (×3). The combined organic layers were washed with brine, then dried ($MgSO_4$). The solvent was evaporated under reduced pressure, and the crude residue was purified by flash column chromatography (20-40% EtOAc/hexane) to yield alkyne **175** as a cream yellow solid (0.66 g, 92%). **IR** (neat, diamond cell) ν 3110, 2957, 1716, 1489, 1446, 1317, 1236, 1152, 1084, 986, 870, 841, 781, 761, 706, 650, 631 cm^{-1}; **LRMS** (+ESI) *m/z* 356.95 $[2M+Na]^+$; **^{1}H NMR** (400 MHz, $CDCl_3$) δ 8.19 (s, 1H), 3.97 (s, 3H), 3.51 (s, 1H) ppm; **^{13}C NMR** (101 MHz, $CDCl_3$) δ 161.3, 148.4, 147.5, 129.0, 75.8, 52.8 ppm.

Methyl 2-((2-(benzo[d]thiazol-2-ylcarbamoyl)phenyl)ethynyl)thiazole-4-carboxylate **176**

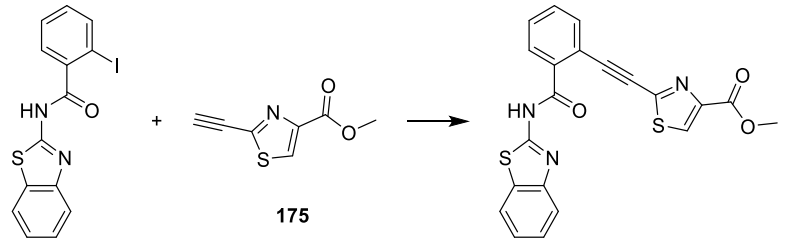

172 **176**

A mixture of aryl iodide **172** (0.10 g, 0.27 mmol), alkyne **175** (0.050 g, 0.30 mmol), $Pd(PPh_3)_4$ (0.010 g, 0.014 mmol) and CuI (0.003 g, 0.014 mmol) were dried under vacuum. Concurrently, a solution of Et_3N (0.50 mL, 6.8 mmol) and DMF (0.5 mL) was degassed under N_2. The solution was added to the solvent and the mixture was heated at 40 °C for 1 h. When the reaction was complete, the mixture was diluted with 1 M HCl solution, then extracted with EtOAc (×3).

The combined organic layers were washed with brine, then dried ($MgSO_4$). The solvent was evaporated under reduced pressure to yield the crude residue, which was purified by column chromatography (5-20% EtOAc/hexanes) to yield ester **176** as a yellow solid, which was telescoped to the next step without characterisation (0.026 g, 24%).

2-((2-(Benzo[d]thiazol-2-ylcarbamoyl)phenyl)ethynyl)thiazole-4-carboxylic acid **141**

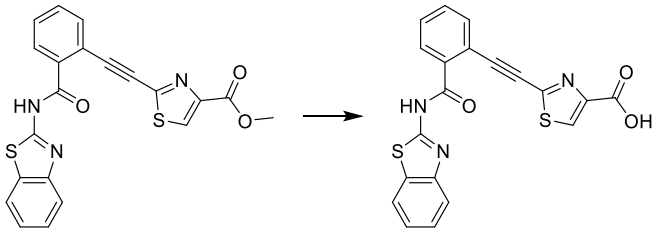

176 **141**

Using **General Procedure E**, ester **176** (0.026 g, 0.062 mmol) and LiOH (0.007 g, 0.3 mmol) gave the title compound as a yellow solid, without further purification (0.025 g, 99%). **IR** (neat, diamond cell) ν 3137, 3119, 3055, 3036, 2945, 2945, 2918, 2895, 2847, 2788, 2758, 1671, 1598, 1535, 1455, 1441, 1319, 1297, 1278, 1246, 1184, 1159, 1110, 1068, 1028, 1017, 916, 871, 748, 725, 695, 653 cm^{-1}; **LRMS** (−ESI) *m/z* 404 $[M-H]^-$; **HRMS** Calcd for $C_{20}H_{10}N_3O_3S_2^-$ $[M-H]^-$: *m/z* 404.01691, found *m/z* 404.01679; **^{1}H NMR** (400 MHz, $CDCl_3$) δ 8.03 (d, *J* = 7.7 Hz, 2H), 7.86 (d, *J* = 7.7 Hz, 1H), 7.60 (t, *J* = 7.4 Hz, 1H), 7.55 – 7.43 (m, 3H), 7.41 – 7.28 (m, 2H) ppm; **^{13}C NMR** (101 MHz, DMSO-d_6) δ 165.57, 161.73, 159.44, 149.32, 148.00, 147.47, 140.61, 139.66, 133.32, 132.02, 129.21, 128.62, 127.95, 126.41, 124.25, 121.60, 120.82, 102.80, 96.82, 93.42 ppm; **HPLC** (254 nm) R_T = 23.47 min, 95.82%.

1-(7-Fluoronaphthalen-1-yl)ethan-1-one **178**

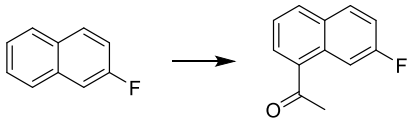

177 **178**

A solution of 2-fluoronaphthalene **177** (0.25 g, 1.7 mmol) in CH_2Cl_2 (2.5 mL), then cooled to −78 °C. To the solution was added $AlCl_3$ (0.68 g, 5.1 mmol), then acetyl chloride (AcCl, 0.24 mL, 3.4 mmol) dropwise, at which point the solution turned green. The solution was then stirred for 4 h, with the cooling bath allowed to warm to RT. When the reaction was complete, the reaction was quenched by addition of 1 M HCl, then extracted with CH_2Cl_2 (×3). The combined organic layers were washed with brine and dried ($MgSO_4$). The solvent was evaporated to yield

the crude residue, which was purified by flash column chromatography (20-40% EtOAc/hexanes) to yield ketone **178** as a colourless oil (0.21 g, 63%). **LRMS** (+ESI) *m/z* 211 $[M+Na]^+$, 399 $[2M+Na]^+$; **^{1}H NMR** (300 MHz, $CDCl_3$) δ 8.61 (dd, *J* = 12.2, 2.6 Hz, 1H), 8.09 – 7.96 (m, 2H), 7.48 (t, *J* = 7.7 Hz, 1H), 7.32 (ddd, *J* = 9.0, 7.9, 2.6 Hz, 1H), 2.75 (s, 3H) ppm; **^{13}C NMR** (75 MHz, $CDCl_3$) δ 201.1, 162.6 (d, $^1J_{CF}$ = 247.1 Hz), 134.2 (d, $^4J_{CF}$ = 5.9 Hz), 133.4 (d, $^5J_{CF}$ = 1.3 Hz), 131.5 (d, $^3J_{CF}$ = 10.9 Hz), 131.2 (d, $^5J_{CF}$ = 1.1 Hz), 130.8 (d, $^3J_{CF}$ = 9.4 Hz), 130.5, 123.7 (d, $^4J_{CF}$ = 2.5 Hz), 117.0 (d, $^2J_{CF}$ = 25.6 Hz), 110.5 (d, $^2J_{CF}$ = 23.9 Hz), 29.8 ppm; **^{19}F NMR** (282 MHz, $CDCl_3$) δ −110.6 (m) ppm. Characterisation data were consistent with literature.[409]

1-(7-Fluoronaphthalen-1-yl)ethan-1-one **179**

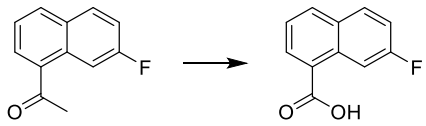

178 **179**

To a solution of ketone **178** (0.54 g, 2.9 mmol) in MeOH (2 mL) was added 12.5% aq NaOCl solution (3 mL) and the mixture was stirred at RT for 72 h. When the reaction was complete, the mixture was diluted with sat. aq. $NaHCO_3$, then extracted with EtOAc. The aqueous layer was then acidified with 1 M HCl, then extracted with EtOAc (×3). The combined organic layers were washed with brine and dried ($MgSO_4$). The solvent was evaporated to yield the crude residue, which was purified by flash column chromatography (20-40% acetone/hexanes) to yield acid **179** as a white solid (0.19 g, 35%). **LRMS** (−ESI) *m/z* 189 $[M-H]^-$, 401 $[2M-2H+Na]^-$; **^{1}H NMR** (500 MHz, DMSO-d_6) δ 8.67 (dd, *J* = 12.5, 2.7 Hz, 1H), 8.32 – 8.25 (m, 1H), 8.23 (d, *J* = 8.3 Hz, 1H), 8.13 (dd, *J* = 9.1, 6.2 Hz, 1H), 7.59 (dd, *J* = 8.2, 7.3 Hz, 1H), 7.53 (ddd, *J* = 9.0, 8.3, 2.7 Hz, 1H) ppm; **^{13}C NMR** (126 MHz, DMSO-d_6) δ 168.3, 161.1 (d, $^1J_{CF}$ = 244.2 Hz), 133.3, 131.8, 131.7 (d, $^3J_{CF}$ = 9.7 Hz), 131.5, 130.8, 126.6 (d, $^4J_{CF}$ = 5.8 Hz), 124.4 (d, $^4J_{CF}$ = 2.4 Hz), 116.4 (d, $^2J_{CF}$ = 25.5 Hz), 109.2 (d, $^2J_{CF}$ = 23.8 Hz) ppm; **^{19}F NMR** (471 MHz, DMSO-d_6) −111.2 ppm. Characterisation data were consistent with literature.[460]

N-(Benzo[d]thiazol-2-yl)-7-fluoro-1-naphthamide **142**

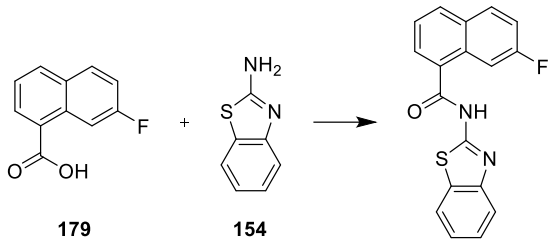

179 **154** **142**

Using **General Procedure D**, acid **179** (0.010 g, 0.053 mmol) and 2-aminobenzothiazole **154** (0.009 g, 0.058 mmol) gave the title compound. The crude residue was purified by flash column chromatography (20-40% acetone/hexanes) to yield amide **142** as a white solid (0.011 g, 65%). **IR** (neat, diamond cell) ν 3477, 3216, 3163, 3061, 3036, 2955, 2918, 2850, 1933, 1894, 1679, 1630, 1596, 1583, 1542, 1514, 1473, 1441, 1295, 1282, 1266, 1248, 1207, 1168, 1135, 1121, 933, 894, 866, 828, 809, 779, 748, 725, 709, 685, 658 cm^{-1}; **LRMS** (−ESI) *m/z* 321 $[M-H]^-$, 665 $[2M-2H+Na]^-$; **HRMS** Calcd for $C_{18}H_{10}FN_2OS^-$ $[M-H]^-$: *m/z* 321.05034, found *m/z* 321.05031; **^{1}H NMR** (400 MHz, DMSO-d_6) δ 13.03 (br s, 1H), 8.23 (d, *J* = 8.3 Hz, 1H), 8.17 (dd, *J* = 9.1, 6.1 Hz, 1H), 8.12 – 8.02 (m, 3H), 7.80 (d, *J* = 8.1 Hz, 1H), 7.64 (t, *J* = 7.7 Hz, 1H), 7.56 (td, *J* = 8.3, 2.3 Hz, 1H), 7.48 (t, *J* = 7.6 Hz, 1H), 7.36 (t, *J* = 7.6 Hz, 1H) ppm; **^{13}C NMR** (101 MHz, DMSO-d_6) δ 167.4, 160.9 (d, $^1J_{CF}$ = 244.7 Hz), 158.5, 132.0, 131.6 (d, $^3J_{CF}$ = 9.6 Hz), 131.5, 130.7 (d, $^3J_{CF}$ = 10.1 Hz), 130.5, 130.0 (d, $^4J_{CF}$ = 6.1 Hz), 128.8, 126.2, 124.4 (d, $^4J_{CF}$ = 2.0 Hz), 123.8, 121.8, 120.5, 116.8 (d, $^2J_{CF}$ = 25.3 Hz), 108.6 (d, $^2J_{CF}$ = 23.1 Hz) ppm; **^{19}F NMR** (376 MHz, DMSO-d_6) −111.5 ppm; **HPLC** (254 nm) R_T = 27.49 min, 96.79%.

Methyl 2-(benzo[d]thiazol-2-ylcarbamoyl)benzoate **181**

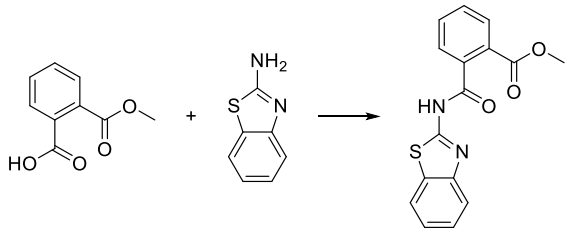

180 **154** **181**

Using **General Procedure D**, monomethyl phthalate **180** (0.50 g, 2.8 mmol) and 2-aminobenzothiazole **154** (0.83 g, 5.5 mmol) gave the title compound. The crude residue was purified by flash column chromatography (30-50% EtOAc/hexanes) to yield ester **181** as a white solid (0.66 g, 76%). **IR** (neat, diamond cell) ν 3217, 3157, 3121, 3069, 3035, 2954, 2843,

1720, 1671, 1599, 1530, 1447, 1435, 1294, 1277, 1262, 1222, 1190, 1164, 1135, 1116, 1079, 1071, 963, 910, 866, 803, 761, 728, 709, 681, 663, 644 cm^{-1}; **LRMS** (+ESI) *m/z* 335 $[M+Na]^+$, (−ESI) *m/z* 311 $[M-H]^-$; **HRMS** Calcd for $C_{16}H_{12}N_2NaO_3S^+$ $[M+Na]^+$: *m/z* 335.04608, found *m/z* 335.04634, calcd for $C_{16}H_{11}N_2O_3S^-$ *m/z* 311.04959 $[M-H]^-$, found *m/z* 311.04902; **^{1}H NMR** (500 MHz, $CDCl_3$) δ 12.48 (br s, 1H), 7.77 (ddd, *J* = 8.0, 1.3, 0.6 Hz, 1H), 7.70 – 7.65 (m, 1H), 7.55 – 7.50 (m, 1H), 7.33 (td, *J* = 7.5, 1.5 Hz, 1H), 7.29 (td, *J* = 7.6, 1.5 Hz, 1H), 7.20 (ddd, *J* = 8.1, 7.2, 1.1 Hz, 1H), 7.07 (ddd, *J* = 8.3, 7.2, 1.2 Hz, 1H), 6.78 (dt, *J* = 8.1, 0.9 Hz, 1H), 3.81 (s, 3H) ppm; **^{13}C NMR** (126 MHz, $CDCl_3$) δ 168.1, 166.3, 160.2, 147.6, 136.1, 132.3, 131.6, 130.6, 130.3, 129.0, 127.9, 126.1, 123.8, 121.2, 120.0, 52.8 ppm.

2-(Benzo[d]thiazol-2-ylcarbamoyl)benzoic acid **182**

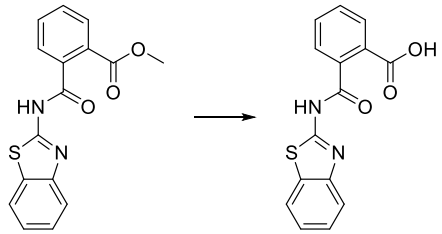

181 **182**

Using **General Procedure E**, ester **181** (0.050 g, 0.16 mmol) gave the title compound **182** as a white solid (0.046 g, 96%). **IR** (neat, diamond cell) ν 3243, 3169, 3065, 2965, 2932, 2851, 2805, 2616, 2423, 1868, , 1847, 1689, 1595, 1581, 1552, 1448, 1303, 1284, 1251, 1229, 1149, 1080, 1066, 988, 920, 881, 872, 804, 781, 758, 733, 719, 705, 662, 643 cm^{-1}; **LRMS** (−ESI) *m/z* 297 $[M-H]^-$; **HRMS** Calcd for $C_{15}H_9N_2O_3S^-$ $[M-H]^-$: *m/z* 297.03394, found *m/z* 297.03382; **^{1}H NMR** (500 MHz, DMSO-d_6) δ 12.81 (br s, 1H), 8.01 (d, *J* = 7.8 Hz, 1H), 7.96 – 7.91 (m, 1H), 7.76 (d, *J* = 8.1 Hz, 1H), 7.69 (td, *J* = 7.5, 1.4 Hz, 1H), 7.66 – 7.58 (m, 2H), 7.48 – 7.41 (m, 1H), 7.33 (t, *J* = 7.6 Hz, 1H), 4.07 (br s, 1H) ppm; **^{13}C NMR** (126 MHz, DMSO-d_6) δ 168.4, 167.1, 158.3, 148.6, 136.3, 132.0, 131.6, 130.3, 130.1, 129.8, 128.1, 126.2, 123.6, 121.7, 120.6 ppm.

1H-Tetrazol-5-amine **184**

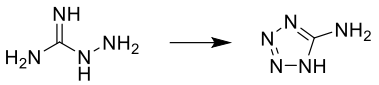

183 **183**

A solution of aminoguanidine bicarbonate **183** (1.36 g, 10.0 mmol) in 32% HCl (3 mL) solution and H_2O (6 mL) was cooled in an ice-water bath, then a solution of $NaNO_2$ (0.720 g, 10.0 mmol) in H_2O (2 mL) was added dropwise. The solution was stirred for 30 min, then basified to pH 9 using sat. aq. Na_2CO_3 solution, then heated at 85 °C for 3 h. The solution was then adjusted to pH 5 using 1 M HCl, at which point a precipitate formed. The mixture was left to cool at −20 °C for 16 h, then filtered. The crude residue was washed with sat. aq. NH_4Cl to afford tetrazole **184**, which was recrystallised from MeOH (0.34 g, 40%). **IR** (neat, diamond cell) ν 3470, 3376, 3335, 3186, 2799, 2609, 2459, 1637, 1447, 1399, 1296, 1156, 1052, 993, 909, 755, 740 cm^{-1}; **LRMS** (+ESI) *m/z* 86 $[M+H]^+$, 171 $[2M+Na]^+$; **^{1}H NMR** (400 MHz, DMSO-d_6) δ 6.45 (br s, 2H) ppm. Characterisation data were consistent with literature.[461]

Benzyl 2-(2-ethoxy-2-oxoethoxy)benzoate **198**

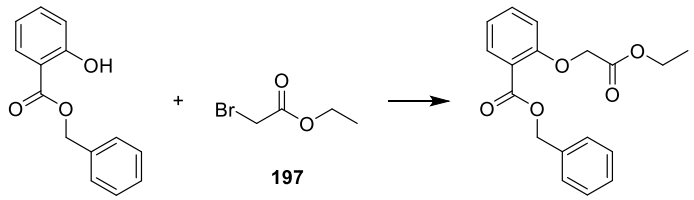

196 **197** **198**

To a solution of benzyl salicylate **196** (0.46 g, 2.0 mmol) in acetone (10 mL) was added ethyl bromoacetate **197** (0.27 mL, 2.4 mmol) and K_2CO_3 (0.97 g, 7.0 mmol), then the mixture was refluxed for 16 h, after which the solution had turned pink. The mixture was concentrated under a gentle stream of N_2, then diluted with H_2O and sat. aq. Na_2CO_3 and extracted with EtOAc (×4). The combined organic layers were washed with brine and dried ($MgSO_4$). The solvent was evaporated to yield the crude residue, which was purified by flash column chromatography (10-30% EtOAc/hexanes) to yield ester **196** as a colourless oil (0.51 g, 81%). **IR** (neat, diamond cell) ν 3066, 3034, 2981, 2981, 2939, 2908, 1755, 1725, 1601, 1489, 1453, 1376, 1297, 1244, 1193, 1167, 1132, 1074, 1027, 752, 734, 696, 660 cm^{-1}; **LRMS** (+ESI) *m/z* 337 $[M+Na]^+$, 651 $[2M+Na]^+$; **HRMS** Calcd for $C_{18}H_{18}NaO_5^+$ $[M+Na]^+$: *m/z* 337.10464, found *m/z* 337.10417; **^{1}H NMR** (300 MHz, $CDCl_3$) δ 7.86 (dd, *J* = 7.8, 1.8 Hz, 1H), 7.51 – 7.26 (m, 7H), 7.04 (td, *J* = 7.6, 1.0 Hz, 1H), 6.90 (dd, *J* = 8.4, 1.0 Hz, 1H), 5.36 (s, 2H), 4.70 (s, 2H), 4.24 (q,

J = 7.1 Hz, 2H), 1.27 (t, *J* = 7.1 Hz, 3H) ppm; **^{13}C NMR** (75 MHz, $CDCl_3$) δ 168.7, 165.8, 157.9, 136.3, 133.6, 132.1, 128.7, 128.3, 128.2, 121.8, 121.4, 114.5, 66.8, 61.5, 14.3 ppm.

2-(2-Ethoxy-2-oxoethoxy)benzoic acid **199**

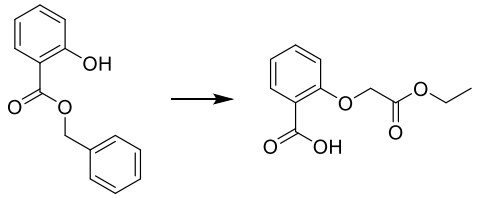

196 **199**

To a solution of ester **198** (0.1 g, 0.32 mmol) in MeOH (5 mL) was added Pd/C (0.1 g), then the suspension was hydrogenated *via* H_2 balloon for 16 h. When the reaction was complete, the mixture was filtered through a plug of celite and washed with EtOAc. The solvent was evaporated under reduced pressure, then the crude residue was purified by flash column chromatography (1-3% MeOH/CH_2Cl_2) to yield acid **199** as a white solid (0.039 g, 55%). **IR** (neat, diamond cell) ν 3264, 2994, 2943, 2913, 1739, 1720, 1602, 1583, 1486, 1458, 1436, 1418, 1377, 1342, 1297, 1262, 1236, 1160, 1126, 1098, 1059, 1020, 959, 839, 797, 753, 736, 686, 640, 597, 528 cm^{-1}; **LRMS** (−ESI) *m/z* 223 $[M-H]^-$, 469 $[2M-2H+Na]^-$; **HRMS** Calcd for $C_{11}H_{11}O_5^-$ $[M-H]^-$: *m/z* 223.06120, found *m/z* 223.06087; **^{1}H NMR** (300 MHz, $CDCl_3$) δ 8.20 (dd, *J* = 7.8, 1.8 Hz, 1H), 7.56 (ddd, *J* = 8.3, 7.4, 1.8 Hz, 1H), 7.19 (td, *J* = 7.6, 1.0 Hz, 1H), 6.94 (dd, *J* = 8.3, 1.0 Hz, 1H), 4.82 (s, 2H), 4.34 (q, *J* = 7.2 Hz, 2H), 1.34 (t, *J* = 7.1 Hz, 3H) ppm; **^{13}C NMR** (75 MHz, $CDCl_3$) δ 167.7, 165.2, 156.3, 135.0, 134.3, 123.4, 119.1, 113.0, 66.5, 62.7, 14.2 ppm.

Ethyl 2-(2-(benzo[d]thiazol-2-ylcarbamoyl)phenoxy)acetate **200**

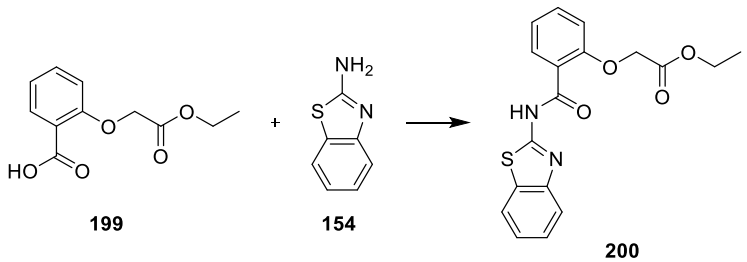

199 **154** **200**

Using **General Procedure D**, ester **199** (0.039 g, 0.17 mmol) and 2-aminobenzothiazole **154** (0.039 g, 0.26 mmol) gave the title compound. The crude residue was purified by flash column chromatography (10-50% EtOAc/hexanes) to yield amide **200** as a white solid (0.030 g, 48%). **IR** (neat, diamond cell) ν 3290, 3062, 2990, 2967, 2906, 2852, 1739, 1653, 1600, 1535, 1472,

1445, 1365, 1295, 1265, 1232, 1161, 1126, 1105, 1061, 1015, 918, 866, 855, 758, 750, 727, 708, 678, 521 cm^{-1}; **LRMS** (+ESI) *m/z* 379 $[M+Na]^+$, (−ESI) *m/z* 355 $[M-H]^-$, 733 $[2M-2H+Na]^-$; **HRMS** Calcd for $C_{18}H_{16}N_2NaO_4S^+$ $[M+Na]^+$: *m/z* 379.07230, found *m/z* 379.07203, calcd for $C_{18}H_{15}N_2O_4S^-$ *m/z* 355.07580, found *m/z* 35507522; **^{1}H NMR** (300 MHz, $CDCl_3$) δ 11.62 (br s, 1H), 8.36 (dd, *J* = 7.9, 1.9 Hz, 1H), 7.90 – 7.79 (m, 2H), 7.56 (ddd, *J* = 8.3, 7.3, 1.9 Hz, 1H), 7.44 (ddd, *J* = 8.3, 7.2, 1.3 Hz, 1H), 7.31 (ddd, *J* = 8.2, 7.3, 1.1 Hz, 1H), 7.26 – 7.16 (m, 1H), 6.95 (dd, *J* = 8.3, 1.0 Hz, 1H), 4.89 (s, 2H), 4.50 (q, *J* = 7.1 Hz, 2H), 1.39 (t, *J* = 7.1 Hz, 3H) ppm; **^{13}C NMR** (75 MHz, $CDCl_3$) δ 167.9, 163.2, 158.3, 156.1, 149.2, 134.7, 133.3, 132.7, 126.1, 123.8, 122.9, 121.4, 121.4, 120.1, 112.6, 66.2, 62.6, 14.4 ppm.

2-(2-(Benzo[d]thiazol-2-ylcarbamoyl)phenoxy)acetic acid **201**

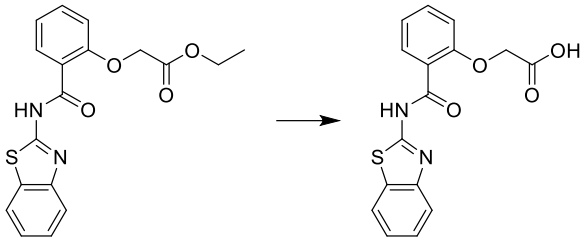

200 **201**

Using **General Procedure E**, ester **200** (0.030 g, 0.084 mmol) and LiOH (0.010 g, 0.42 mmol) gave the title compound **201** as a white solid (0.027 g, 99%). **IR** (neat, diamond cell) ν 3291, 3087, 3062, 2951, 2920, 2850, 2346, 1675, 1599, 1534, 1483, 1451, 1297, 1285, 1202, 1159, 1118, 1106, 1073, 1058, 1015, 944, 918, 889, 878, 758, 745, 728, 710, 679, 662, 648, 609, 520 cm^{-1}; **LRMS** (−ESI) *m/z* 327 $[M-H]^-$, 677 $[2M-2H+Na]^-$; **HRMS** Calcd for $C_{16}H_{11}N_2O_4S^-$ $[M-H]^-$: *m/z* 327.04450, found *m/z* 327.04416; **^{1}H NMR** (500 MHz, DMSO-d_6) δ 12.31 (br s, 1H), 8.02 (d, *J* = 7.9 Hz, 1H), 7.90 (dd, *J* = 7.8, 1.8 Hz, 1H), 7.77 (d, *J* = 8.1 Hz, 1H), 7.61 (ddd, *J* = 8.8, 7.4, 1.8 Hz, 1H), 7.49 – 7.43 (m, 1H), 7.34 (t, *J* = 7.6 Hz, 1H), 7.26 (d, *J* = 8.4 Hz, 1H), 7.18 (t, *J* = 7.5 Hz, 1H), 4.99 (s, 2H) ppm; **^{13}C NMR** (126 MHz, DMSO-d_6) δ 170.6, 164.3, 157.6, 156.0, 148.7, 134.1, 131.7, 131.1, 126.2, 123.7, 121.8, 121.8, 121.2, 120.7, 114.1, 66.0 ppm.

N-(Benzo[d]thiazol-2-yl)-2-(2-(methylamino)-2-oxoethoxy)benzamide **144**

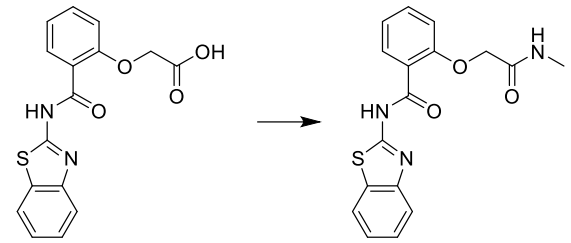

201 **144**

Using **General Procedure D**, acid **201** (0.030 g, 0.091 mmol) and 2 M $MeNH_2$ in THF solution (0.23 mL) gave the title compound. The crude residue was purified by flash column chromatography (1-5% MeOH/CH_2Cl_2) to yield amide **144** as a white solid (0.019 g, 61%). **IR** (neat, diamond cell) ν 3281, 3244, 3126, 2919, 2851, 1686, 1655, 1598, 1586, 1523, 1489, 1465, 1438, 1415, 1296, 1277, 1262, 1244, 1227, 1165, 1122, 1102, 1029, 915, 761, 741, 731, 684, 674, 591, 530, 516, 437 cm^{-1}; **LRMS** (+ESI) *m/z* 364 $[M+Na]^+$, (−ESI) *m/z* 340 $[M-H]^-$; **HRMS** Calcd for $C_{17}H_{15}N_3NaO_3S^+$ $[M+Na]^+$: *m/z* 364.07263, found *m/z* 364.07297; calcd for $C_{17}H_{14}N_3O_3S$ $[M-H]^-$: *m/z* 340.07614, found *m/z* 340.07595; **^{1}H NMR** (300 MHz, DMSO-d_6) δ 8.26 (d, *J* = 5.0 Hz, 1H), 8.02 (d, *J* = 7.9 Hz, 1H), 7.84 – 7.74 (m, 2H), 7.65 – 7.53 (m, 1H), 7.46 (t, *J* = 7.6 Hz, 1H), 7.34 (t, *J* = 7.5 Hz, 1H), 7.23 – 7.10 (m, 2H), 4.80 (s, 2H), 2.69 (d, *J* = 4.6 Hz, 3H) ppm; **^{13}C NMR** (75 MHz, DMSO-d_6) δ 168.6, 165.0, 157.9, 155.8, 148.7, 133.9, 131.7, 131.0, 126.3, 123.8, 122.5, 122.0, 121.8, 120.7, 114.0, 67.9, 25.5 ppm; **HPLC** (254 nm) R_T = 22.27 min, 98.34%.

N-(Benzo[d]thiazol-2-yl)-6-bromo-1H-indole-1-carboxamide **204**

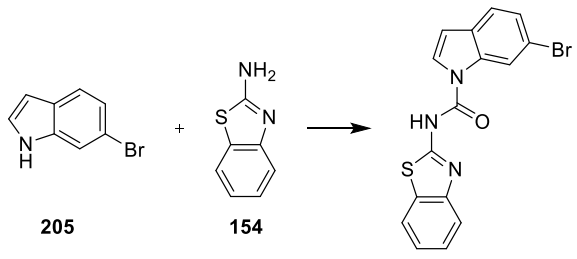

205 **154** **204**

A solution of 6-bromoindole **205** (0.5 g, 2.6 mmol) and 1,1′-carbonyldiimidazole (0.62 g, 3.8 mmol) in MeCN (7 mL) was refluxed for 16 h, then 2-aminobenzothiazole **154** (0.77 g, 5.1 mmol) was added and the mixture refluxed for 6 h. When the reaction was complete, the solvent was evaporated under a gentle stream of N_2. The crude residue was purified by flash column chromatography (10-30% EtOAc/hexane) to yield aryl bromide **204** as a white solid. (0.47 g,

50%). **IR** (neat, diamond cell) ν 3157, 3100, 2906, 2853, 2771, 2749, 1653, 1555, 1524, 1465, 1444, 1430, 1421, 1400, 1376, 1341, 1307, 1267, 1250, 1223, 1199, 1169, 1119, 1068, 884, 869, 808, 799, 783, 760, 741, 718, 680, 647 cm^{-1}; **LRMS** (−ESI) *m/z* 370, 372 $[M-H]^-$; **HRMS** Calcd for $C_{16}H_9BrN_3OS^-$ $[M-H]^-$: *m/z* 369.96552, 371.96347, found *m/z* 369.96553, 371.96345; **^{1}H NMR** (500 MHz, $(CD_3)_2CO$) δ 8.82 (d, *J* = 1.9 Hz, 1H), 8.02 (d, *J* = 3.7 Hz, 1H), 7.89 – 7.83 (m, 1H), 7.60 – 7.56 (m, 1H), 7.53 (d, *J* = 8.3 Hz, 1H), 7.51 – 7.44 (m, 1H), 7.35 (ddd, *J* = 8.3, 5.6, 1.6 Hz, 3H), 6.64 (d, *J* = 3.7 Hz, 1H) ppm; **^{13}C NMR** (126 MHz, $(CD_3)_2CO$) δ 171.0, 158.8, 137.2, 137.2, 130.9, 128.1, 128.0, 128.0, 126.1, 124.7, 123.5, 123.0, 119.7, 117.6, 114.2, 106.9 ppm.

Methyl 6-bromopicolinate **202**

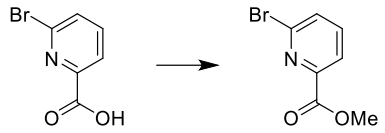

210 **202**

To a solution of 6-bromopicolinic acid **202** (1.0 g, 5.0 mmol) in MeOH (10 mL) was added H_2SO_4 (0.5 mL) and the solution was refluxed for 1 h. When the reaction was complete, the solution was concentrated under a gentle stream of N_2. The mixture was then quenched by addition of sat. aq. $NaHCO_3$ (50 mL), then extracted with CH_2Cl_2 (×3). The combined organic layers were washed with brine, then dried ($MgSO_4$). The solvent was evaporated under reduced pressure to yield the aryl bromide **202** as a cream yellow solid (1.01 g, 94%), which was used without further purification. **LRMS** (+ESI) *m/z* 238, 240 $[M+Na]^+$, 453, 455, 457 $[2M+Na]^+$; **^{1}H NMR** (500 MHz, $CDCl_3$) δ 8.08 (dd, J = 7.1, 1.4 Hz, 1H), 7.73 – 7.64 (m, 2H), 3.99 (s, 3H) ppm; **^{13}C NMR** (101 MHz, DMSO-d_6) δ (126 MHz, $CDCl_3$) δ 164.57, 148.89, 142.25, 139.31, 131.95, 124.18, 53.29 ppm. Characterisation data were consistent with literature.[462]

Methyl 6-(1H-indol-6-yl)picolinate **208**

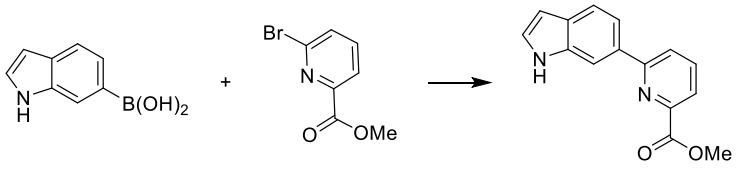

209 **202** **208**

A mixture of boronic acid **209** (0.30 g, 1.9 mmol), aryl bromide **202** (0.37 g, 1.7 mmol), Na_2CO_3 (0.54 g, 5.1 mmol) were dried under vacuum. Concurrently, a mixture of 1,4-dioxane (3 mL) and H_2O (1 mL) was degassed with N_2. The solution was added to the solids and the mixture heated at 80 ºC for 16 h. When the reaction was complete, the mixture was diluted with 1 M HCl. The aqueous layer was extracted with EtOAc (×3) and the combined organic layers were washed with brine and dried ($MgSO_4$). The solvent was evaporated to yield the crude residue, which was purified by flash column chromatography (20-40% acetone/hexanes) to yield indole **208** as a white solid (0.27 g, 57%). **IR** (neat, diamond cell) ν 3365, 3293, 3043, 3027, 3017, 2956, 1731, 1720, 1586, 1508, 1438, 1394, 1326, 1311, 1285, 1245, 1196, 1171, 1148, 1093, 1054, 978, 895, 815, 766, 739, 731, 669, 643, 623 cm^{-1}; **LRMS** (+ESI) *m/z* 275 $[M+Na]^+$, 527 $[2M+Na]^+$, (−ESI) *m/z* 251 $[M-H]^-$; **HRMS** Calcd for $C_{15}H_{11}N_2O_2^-$ $[M-H]^-$: *m/z* 251.08260, found *m/z* 251.08286; **^{1}H NMR** (500 MHz, $CDCl_3$) δ 8.67 (br s, 1H), 8.24 (dt, *J* = 1.7, 0.9 Hz, 1H), 8.01 (dd, *J* = 7.5, 1.0 Hz, 1H), 7.93 (dd, *J* = 8.0, 1.1 Hz, 1H), 7.85 (t, *J* = 7.8 Hz, 1H), 7.74 (dd, *J* = 8.3, 1.6 Hz, 1H), 7.70 (d, *J* = 8.3 Hz, 1H), 7.22 (dd, *J* = 3.2, 2.4 Hz, 1H), 6.54 (ddd, *J* = 3.0, 1.9, 0.9 Hz, 1H), 4.02 (s, 3H) ppm; **^{13}C NMR** (126 MHz, $CDCl_3$) δ 166.4, 158.9, 147.9, 137.7, 136.5, 132.4, 129.2, 126.3, 123.8, 122.8, 120.9, 119.0, 110.6, 102.5, 52.9 ppm.

6.5. Experimental and Characterisation for Chapter 4

2-Iodo-1-methoxy-4-nitronaphthalene **227**

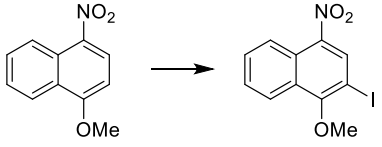

228 **227**

To a mixture of 1-methoxy-4-nitronaphthalene **228** (0.25 g, 1.2 mmol) and *N*-iodosuccinimide (0.31 g, 1.4 mmol) was added trifluoroacetic acid (5 mL), then the solution was refluxed for

24 h. When the reaction was complete, the excess iodine was quenched by addition of sat. aq. $Na_2S_2O_3$ solution, then extracted with EtOAc (×2). The combined organic layers were washed with sat. aq. Na_2CO_3 solution (×2), then brine, then dried ($MgSO_4$). The solvent was evaporated under reduced pressure to yield the crude residue, which was purified by column chromatography (1-5% EtOAc/hexanes) to yield aryl iodide **227** as a yellow solid (0.15 g, 37%). **LRMS** (+ESI) *m/z* 352 $[M+Na]^+$; **^{1}H NMR** (500 MHz, $CDCl_3$) δ 8.63 – 8.58 (m, 2H), 8.22 (dd, J = 8.5, 1.2 Hz, 1H), 7.76 (ddd, J = 8.5, 6.8, 1.3 Hz, 1H), 7.67 (ddd, J = 8.1, 6.8, 1.1 Hz, 1H), 4.04 (s, 3H) ppm; **^{13}C NMR** (126 MHz, $CDCl_3$) δ 161.9, 143.1, 134.3, 130.2, 128.8, 128.3, 126.8, 124.1, 123.2, 83.5, 62.4 ppm. Characterisation data were consistent with literature.[419]

Methyl 2-((1-methoxy-4-nitronaphthalen-2-yl)thio)acetate **225**

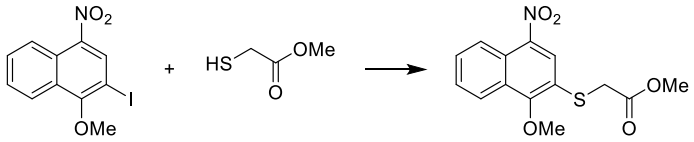

227 **226** **225**

A mixture of aryl iodide **227** (0.25 g, 0.76 mmol), Xantphos (0.13 g, 30 mol %) and tris(dibenzylideneacetone)dipalladium(0) ($Pd_2(dba)_3$, 0.17 g, 20 mol %) were dried under vacuum. Concurrently, a solution of DIPEA (0.26 mL, 1.5 mmol) and methyl thioglycolate **226** (0.14 mL, 1.5 mmol) in 1,4-dioxane (2.5 mL) was degassed under N_2. The solution was added to the solid mixture, which was then heated at reflux for 4 h. When the reaction was complete, the mixture was filtered through a plug of celite. The filtrate was evaporated under reduced pressure to yield the crude residue, which was purified by column chromatography (40-100% EtOAc/hexanes) to yield thioether **225** as a yellow oil which solidified (0.22 g, 94%). **LRMS** (+ESI) *m/z* 330 $[M+Na]^+$; **^{1}H NMR** (400 MHz, $CDCl_3$) δ 8.62 (dt, *J* = 8.8, 0.9 Hz, 1H), 8.39 (s, 1H), 8.21 (ddd, *J* = 8.4, 1.5, 0.8 Hz, 1H), 7.72 (ddd, *J* = 8.6, 6.9, 1.5 Hz, 1H), 7.66 (ddd, *J* = 8.2, 6.9, 1.2 Hz, 1H), 4.09 (s, 3H), 3.79 (s, 2H), 3.72 (s, 3H) ppm; **^{13}C NMR** (101 MHz, $CDCl_3$) δ 169.7, 162.6, 160.2, 129.9, 129.1, 128.1, 127.5, 126.2, 123.9, 123.1, 122.9, 62.1, 52.9, 35.3 ppm. Characterisation data were consistent with literature.[419]

Methyl 2-((4-amino-1-methoxynaphthalen-2-yl)thio)acetate **223**

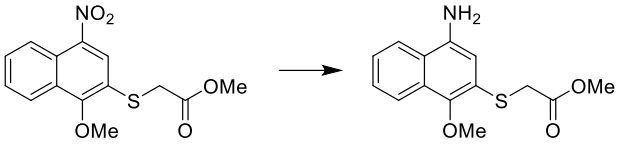

225 **223**

A solution of nitroarene **225** (0.050 g, 0.16 mmol) and 4,4′-bipyridine (0.0005 g, 0.003 mmol) in DMF (1 mL) was cooled in an ice-water bath, then tetrahydroxydiboron (0.088 g, 0.98 mmol) was added. The solution was allowed to warm to RT and stirred for 16 h. When the reaction was complete, the solution was diluted with water and extracted with EtOAc (×3). The combined organic extracts were washed with brine, then dried ($MgSO_4$). The solvent was evaporated to yield amine **223** as a light brown oil, which was used immediately without further purification (0.044 g, 98%). **LRMS** (+ESI) *m/z* 278 $[M+H]^+$, 300 $[M+Na]^+$, 577 $[2M+Na]^+$; **^{1}H NMR** (400 MHz, $CDCl_3$) δ 8.07 – 8.02 (m, 1H), 7.77 (dt, *J* = 8.1, 1.1 Hz, 1H), 7.51 (ddd, *J* = 8.3, 6.8, 1.3 Hz, 1H), 7.45 (ddd, *J* = 8.3, 6.8, 1.4 Hz, 1H), 6.78 (s, 1H), 3.93 (s, 3H), 3.75 (s, 2H), 3.70 (s, 3H) ppm; **^{13}C NMR** (101 MHz, $CDCl_3$) δ 170.5, 147.9, 139.1, 128.8, 126.7, 125.5, 124.4, 123.6, 122.7, 121.5, 111.0, 61.6, 52.6, 35.6 ppm. Characterisation data were consistent with literature.[419]

Methyl 2-((4-((4-bromophenyl)sulfonamido)-1-methoxynaphthalen-2-yl)thio)acetate **230**

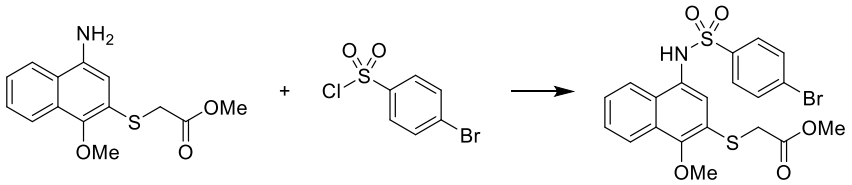

223 **230**

Using **General Procedure G**, aniline **223** (0.044 g, 0.16 mmol) and 4-bromobenzenesulfonyl chloride (0.042 g, 0.16 mmol) gave the title compound. The crude residue was purified by column chromatography (5-30% EtOAc/hexanes) to yield sulfonamide **230** as a brown oil (0.070 g, 89%). **LRMS** (+ESI) *m/z* 518, 520 $[M+Na]^+$, (−ESI) *m/z* 494, 496 $[M-H]^-$; **^{1}H NMR** (400 MHz, $CDCl_3$) δ 8.06 (dd, *J* = 8.3, 1.2 Hz, 1H), 7.73 (d, *J* = 8.4 Hz, 1H), 7.60 (d, *J* = 8.7 Hz, 2H), 7.55 – 7.48 (m, 3H), 7.42 (ddd, *J* = 8.2, 6.8, 1.3 Hz, 1H), 7.36 (s, 1H), 6.76 (s, 1H), 3.99 (s, 3H), 3.72 (s, 3H), 3.65 (s, 2H) ppm; **^{13}C NMR** (101 MHz, $CDCl_3$) δ 170.0, 154.5, 138.5, 132.5, 130.1, 129.1, 128.9, 128.2, 127.6, 127.3, 127.3, 126.2, 123.7, 122.7, 122.2, 61.7, 52.8, 35.2 ppm. Characterisation data were consistent with literature.[419]

2-((4-((4-Bromophenyl)sulfonamido)-1-hydroxynaphthalen-2-yl)thio)acetic acid **51**

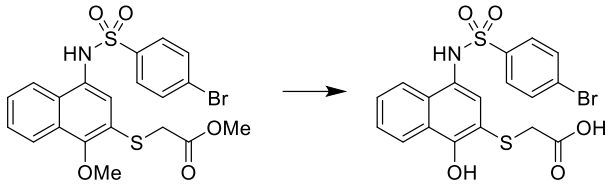

230 **51**

Using **General Procedure H**, ester **230** (0.070 g, 0.14 mmol) and BBr_3 (0.70 mL, 0.70 mmol) gave the title compound. The crude residue was purified by reverse phase column chromatography (0-100% MeCN/H_2O) to yield acid **51** as an off-white solid (0.026 g, 39%). **LRMS** (+ESI) *m/z* 490, 492 $[M+Na]^+$, (−ESI) *m/z* 465.90, 467.86 $[M-H]^-$; **^{1}H NMR** (400 MHz, DMSO-d_6) δ 10.02 (br s, 1H), 8.18 – 8.11 (m, 1H), 7.88 – 7.79 (m, 1H), 7.70 (d, *J* = 8.6 Hz, 2H), 7.54 (d, *J* = 8.5 Hz, 2H), 7.51 – 7.39 (m, 2H), 7.03 (s, 1H), 3.52 (s, 2H) ppm; **^{13}C NMR** (101 MHz, DMSO-d_6) δ 171.1, 152.6, 139.1, 132.1, 131.1, 129.4, 128.8, 126.7, 126.4, 125.8, 125.1, 123.7, 123.2, 122.5, 112.9, 36.9 ppm; **HPLC** (254 nm) 22.72 min, 97.54%. Characterisation data were consistent with literature.[419]

4-Phenoxybenzenesulfonic acid **232**

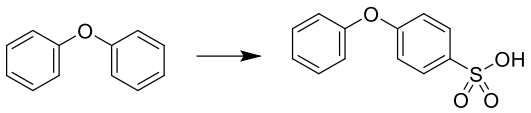

231 **232**

A solution of diphenyl ether **231** (0.93 mL, 5.9 mmol) in CH_2Cl_2 (30 mL) was cooled in an ice-water bath, then chlorosulfonic acid (0.39 mL, 5.9 mmol) was added dropwise. The solution was stirred for 2 h, then the solvent was evaporated under a gentle stream of N_2 to yield sulfonic acid **232** as a pale pink solid (1.47 g, 99%). **LRMS** *m/z* 249 $[M-H]^-$; **^{1}H NMR** (500 MHz, $CDCl_3$) δ 10.54 (s, 1H), 7.89 – 7.82 (m, 2H), 7.46 – 7.37 (m, 2H), 7.27 – 7.20 (m, 1H), 7.11 – 7.01 (m, 4H) ppm; **^{13}C NMR** (126 MHz, $CDCl_3$) δ 162.6, 154.8, 130.6, 130.3, 129.3, 125.3, 120.5, 117.6 ppm. Characterisation data were consistent with literature.[463]

4-Phenoxybenzenesulfonyl chloride **233**

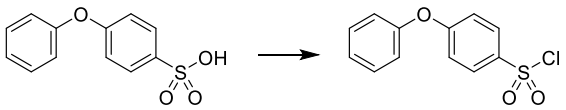

232 **233**

To a solution of sulfonic acid **232** (1.47 g, 5.9 mmol) in thionyl chloride (10 mL) was added DMF (3 drops), then the solution was refluxed for 2 h. When the reaction was complete, the solvent was evaporated under a gentle stream of N_2, then the residue was diluted with Et_2O. The organic layer was washed with 5% aq. NaOH solution (×2), then H_2O (×2), then dried ($MgSO_4$). The solvent was evaporated under reduced pressure to yield sulfonyl chloride **233** as a brown oil (1.46 g, 93%). **LRMS** (+ESI) *m/z* 291 $[M+Na]^+$; **^{1}H NMR** (400 MHz, $CDCl_3$) δ 7.98 (d, *J* = 9.1 Hz, 2H), 7.45 (t, *J* = 7.5 Hz, 2H), 7.28 (t, *J* = 7.4 Hz, 1H), 7.14 – 7.04 (m, 4H) ppm; **^{13}C NMR** (101 MHz, $CDCl_3$) δ 164.0, 154.5, 137.8, 130.6, 129.8, 125.9, 120.8, 117.6 ppm. Characterisation data were consistent with literature.[463]

2-((1-Hydroxy-4-((4-phenoxyphenyl)sulfonamido)naphthalen-2-yl)thio)acetic acid **234**

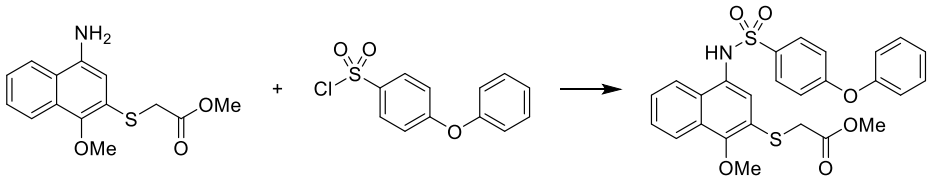

223 **233** **234**

Using **General Procedure G**, aniline **223** (0.090 g, 0.33 mmol) and sulfonyl chloride **233** (0.11 g, 0.41 mmol) gave the title compound. The crude residue was purified by column chromatography (10-40% EtOAc/hexanes) to yield sulfonamide **234** as an off-white solid (0.13 g, 76%). **LRMS** (+ESI) *m/z* 532 $[M+Na]^+$; (−ESI) *m/z* 508 $[M-H]^-$; **^{1}H NMR** (400 MHz, $CDCl_3$) δ 8.04 (dt, *J* = 8.4, 1.0 Hz, 1H), 7.80 (dt, *J* = 8.4, 0.9 Hz, 1H), 7.72 – 7.64 (m, 2H), 7.50 (ddd, *J* = 8.3, 6.8, 1.2 Hz, 1H), 7.45 – 7.32 (m, 4H), 7.22 – 7.15 (m, 1H), 7.06 (s, 1H), 6.95 (dd, *J* = 8.6, 1.2 Hz, 1H), 6.89 (d, *J* = 8.9 Hz, 1H), 3.97 (s, 3H), 3.70 (s, 3H), 3.67 (s, 2H) ppm; **^{13}C NMR** (101 MHz, $CDCl_3$) δ 170.0, 161.8, 155.3, 154.2, 132.9, 130.2, 130.1, 129.8, 128.8, 128.2, 127.1, 127.0, 125.8, 125.0, 123.6, 122.5, 122.5, 120.2, 117.8, 61.6, 52.8, 35.3 ppm. Characterisation data were consistent with literature.[419]

2-((1-Hydroxy-4-((4-phenoxyphenyl)sulfonamido)naphthalen-2-yl)thio)acetic acid **215**

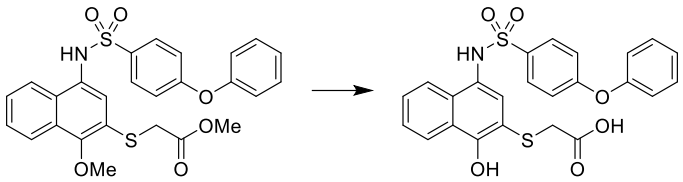

234 **215**

Using **General Procedure H**, ester **234** (0.12 g, 0.24 mmol) and BBr_3 (0.71 mL, 0.71 mmol) gave the title compound. The crude residue was purified by reverse phase column chromatography (0-100% MeCN/H_2O) to yield acid **215** as an off-white solid (0.046 g, 41%). **LRMS** (−ESI) *m/z* 480 $[M-H]^-$; **^{1}H NMR** (500 MHz, DMSO-d_6) δ 9.85 (s, 1H), 8.18 – 8.12 (m, 1H), 7.90 – 7.84 (m, 1H), 7.63 – 7.57 (m, 2H), 7.53 – 7.47 (m, 1H), 7.48 – 7.36 (m, 3H), 7.22 (tt, *J* = 7.4, 1.1 Hz, 1H), 7.07 – 6.98 (m, 5H), 3.54 (s, 2H) ppm; **^{13}C NMR** (126 MHz, DMSO-d_6) δ 206.5, 171.2, 160.4, 155.2, 152.4, 133.8, 131.2, 130.3, 129.5, 126.7, 125.7, 125.1, 124.7, 124.1, 123.4, 122.4, 119.6, 117.9, 113.0, 36.9 ppm; **HPLC** (254 nm) 24.28 min, 97.30%. Characterisation data were consistent with literature.[419]

Methyl 2-((4-(2-cyclohexylacetamido)-1-methoxynaphthalen-2-yl)thio)acetate **236**

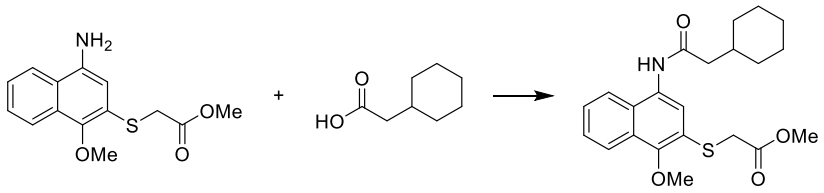

223 **236**

Using **General Procedure D**, aniline **223** (0.045 g, 0.16 mmol) and cyclohexaneacetic acid (0.035 mL, 0.24 mmol) gave the title compound. The crude residue was purified by column chromatography, (1-2% MeOH/CH_2Cl_2) to yield amide **236** as a brown solid (0.048 g, 74%). **IR** (neat, diamond cell) ν 3255, 2919, 2851, 1743, 1646, 1622, 1536, 1499, 1439, 1396, 1363, 1297, 1220, 1201, 1190, 1149, 1122, 1074, 995, 979, 897, 857, 761, 721, 711, 677, 655, 589 cm^{-1} **LRMS** (+ESI) *m/z* 424 $[M+Na]^+$, 825 $[2M+Na]^+$; (−ESI) *m/z* 400.16 $[M-H]^-$, 800.99 $[2M-H]^-$; **HRMS** Calcd for $C_{22}H_{27}NNaO_4S^+$ $[M+Na]^+$: *m/z* 424.15530, found *m/z* 424.15521; calcd for $C_{22}H_{27}NO_4S$ $[M-H]^-$: *m/z* 400.15880, found *m/z* 400.15918; **^{1}H NMR** (400 MHz, $CDCl_3$) δ 8.15 – 8.08 (m, 1H), 7.92 (s, 1H), 7.80 – 7.74 (m, 1H), 7.58 – 7.48 (m, 2H), 7.34 (s, 1H), 3.99 (s, 3H), 3.78 (s, 2H), 3.71 (s, 3H), 2.37 (d, *J* = 7.1 Hz, 2H), 2.03 – 1.83 (m, 3H), 1.79 – 1.64 (m, 3H), 1.46 – 1.02 (m, 5H) ppm; **^{13}C NMR** (101 MHz, $CDCl_3$) δ 171.6, 170.2, 152.8,

129.3, 128.6, 128.2, 126.7, 126.6, 123.6, 123.5, 122.7, 121.6, 61.5, 52.7, 45.5, 35.7, 35.4, 33.3, 30.4, 29.8, 26.3, 26.2 ppm.

2-((4-(2-Cyclohexylacetamido)-1-hydroxynaphthalen-2-yl)thio)acetic acid **219**

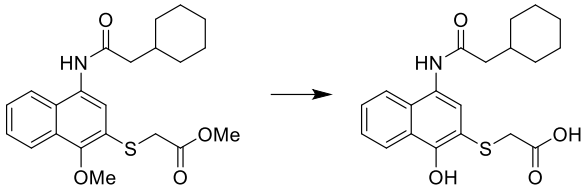

236 **219**

Using **General Procedure H**, ester **236** (0.053 g, 0.13 mmol mmol) and BBr_3 (0.53 mL, 0.53 mmol) gave the title compound. The crude residue was purified by reverse phase column chromatography (0-100% MeCN/H_2O) to yield acid **219** as a white solid (0.025 g, 51%). **IR** (neat, diamond cell) ν 3471, 3264, 3062, 2915, 2848, 2663, 1724, 1647, 1534, 1501, 1450, 1439, 1372, 1360, 1347, 1291, 1248, 1216, 1185, 1169, 1158, 1123, 1074, 866, 760, 749, 722, 709, 666, 646 cm^{-1} **LRMS** (+ESI) *m/z* 396 $[M+Na]^+$; (−ESI) *m/z* 372 $[M-H]^-$; **HRMS** Calcd for $C_{20}H_{23}NO_4S^-$ $[M-H]^-$: *m/z* 372.12750, found *m/z* 372.12770; **^{1}H NMR** (500 MHz, $(CD_3)_2CO$) δ 9.39 (s, 1H), 8.73 (d, *J* = 8.2 Hz, 1H), 8.44 (d, *J* = 8.3 Hz, 1H), 8.28 (d, *J* = 6.8 Hz, 1H), 7.99 (dt, *J* = 15.1, 7.6 Hz, 2H), 4.19 (s, 2H), 2.85 (d, *J* = 7.0 Hz, 2H), 2.38 (s, 1H), 2.31 (d, *J* = 13.0 Hz, 2H), 2.18 (d, *J* = 13.1 Hz, 2H), 2.12 (d, *J* = 12.8 Hz, 1H), 1.76 (q, *J* = 12.7 Hz, 2H), 1.66 (t, *J* = 12.5 Hz, 1H), 1.54 (q, *J* = 11.0 Hz, 2H) ppm; **^{13}C NMR** (126 MHz, $(CD_3)_2CO$) δ 173.6, 171.9, 154.2, 131.5, 129.5, 128.2, 127.1, 126.4, 125.7, 124.2, 123.3, 111.8, 45.1, 39.7, 36.3, 33.9, 27.1, 26.9 ppm; **HPLC** (254 nm) 22.84 min, 96.41%.

Methyl 2-(4-phenoxyphenyl)acetate **240**

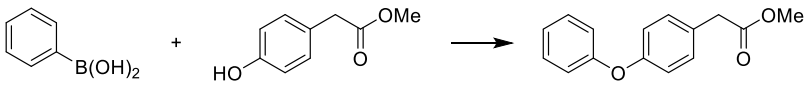

239 **238** **240**

To a solution of phenylboronic acid **239** (0.37 g, 3.0 mmol), methyl 4-hydroxyphenylacetate **238** (0.25 g, 1.5 mmol), copper(II) acetate hydrate (0.30 g, 1.5 mmol) in CH_2Cl_2 (7.5 mL) was added 4 Å molecular sieves (0.25 g) and pyridine (0.61 mL, 7.5 mmol), and the solution was stirred at RT for 16 h. When the reaction was complete, the solution was diluted with 1 M HCl solution and extracted with CH_2Cl_2 (×3). The combined organic layers were washed with brine and dried ($MgSO_4$). The solvent was evaporated under reduced pressure to yield the crude residue, which was purified by column chromatography (5-50% EtOAc/hexanes) to yield ester

240 as a clear oil (0.065 g, 18%). **LRMS** (+ESI) *m/z* 265 $[M+Na]^+$, *m/z* 507 $[2M+Na]^+$; **^{1}H NMR** (400 MHz, $CDCl_3$) δ 7.38 – 7.28 (m, 2H), 7.24 (d, *J* = 8.6 Hz, 2H), 7.14 – 7.06 (m, 1H), 7.06 – 6.99 (m, 2H), 6.97 (d, *J* = 8.6 Hz, 2H), 3.71 (s, 3H), 3.61 (s, 2H); **^{13}C NMR** (101 MHz, $CDCl_3$) δ 172.3, 157.3, 156.6, 130.7, 129.9, 128.9, 123.4, 119.1, 119.1, 52.2, 40.5 ppm. Characterisation data were consistent with literature.[464]

2-(4-Phenoxyphenyl)acetic acid **241**

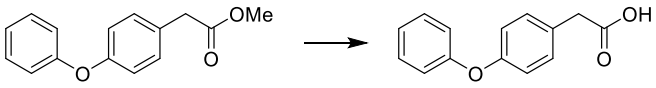

240 **241**

Using **General Procedure E**, ester **240** (0.065 g, 0.27 mmol) and LiOH (0.032 g, 1.3 mmol) gave the title compound **241** as a white solid, which was used without further purification (0.060 g, 98%). **LRMS** (+ESI) *m/z* 273 $[M-H+2Na]^+$, (−ESI) *m/z* 227 $[M-H]^-$, 477 $[2M-2H+Na]^-$; **^{1}H NMR** (400 MHz, $CDCl_3$) δ 7.31 – 7.21 (m, 2H), 7.20 – 7.13 (m, 2H), 7.03 (t, *J* = 7.4 Hz, 1H), 6.97 – 6.91 (m, 2H), 6.89 (d, *J* = 8.6 Hz, 2H), 3.55 (s, 2H) ppm; **^{13}C NMR** (101 MHz, $CDCl_3$) δ 177.5, 157.2, 156.8, 130.9, 129.9, 128.1, 123.5, 119.2, 119.0, 40.4 ppm. Characterisation data were consistent with literature.[465]

Methyl 2-((1-methoxy-4-(2-(4-phenoxyphenyl)acetamido)naphthalen-2-yl)thio)acetate **242**

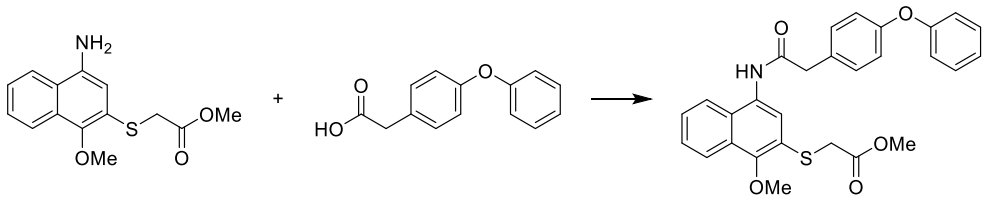

223 **241** **242**

Using **General Procedure D**, aniline **223** (0.090 g, 0.33 mmol), acid **241** (0.096 g, 0.42 mmol), HATU (0.19 g, 0.49 mmol) and DIPEA (0.11 mL, 0.65 mmol) gave the title compound. The crude residue was purified by flash column chromatography (5-40% EtOAc/hexanes) to yield ester **242** as an off-white solid (0.082 g, 52%). **IR** (neat, diamond cell) ν 3284, 3047, 2997, 2960, 2939, 2926, 2844, 1737, 1651, 1590, 1533, 1508, 1500, 1486, 1454, 1442, 1390, 1363, 1293, 1244, 1222, 1196, 1170, 1146, 1073, 1000, 976, 875, 863, 852, 816, 780, 763, 733, 710, 692, 676 cm^{-1}; **LRMS** (+ESI) *m/z* 510 $[M+Na]^+$; (−ESI) *m/z* 486 $[M-H]^-$; **HRMS** Calcd for $C_{28}H_{25}NNaO_5S^+$ $[M+Na]^+$: *m/z* 510.13456, found *m/z* 510.13439; calcd for $C_{28}H_{24}NO_5S^-$ *m/z* 486.13807, found *m/z* 486.13876; **^{1}H NMR** (400 MHz, $CDCl_3$) δ 8.08 (d, *J* = 8.4 Hz, 1H), 7.94 (s, 1H), 7.50 (t, *J* = 7.6 Hz, 1H), 7.46 – 7.29 (m, 7H), 7.18 – 6.92 (m, 5H), 3.96 (s, 3H),

3.84 (s, 2H), 3.77 (s, 2H), 3.70 (s, 3H) ppm; **^{13}C NMR** (101 MHz, $CDCl_3$) δ 170.2, 169.9, 157.4, 152.8, 131.2, 130.8, 130.0, 129.9, 129.3, 128.9, 127.8, 126.8, 123.8, 122.9, 122.7, 120.9, 119.8, 119.2, 119.1, 119.0, 61.6, 52.7, 44.1, 35.4 ppm.

2-((1-Hydroxy-4-(2-(4-phenoxyphenyl)acetamido)naphthalen-2-yl)thio)acetic acid **220**

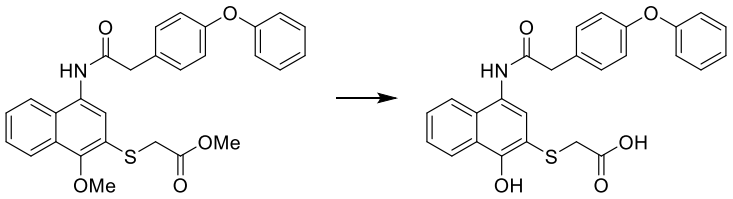

242 **220**

Using **General Procedure H**, ester **242** (0.045 mg, 0.092 mmol) and BBr_3 (0.37 mL, 0.37 mmol) gave the title compound. The crude residue was purified by reverse phase flash column chromatography (0-100% H_2O/MeCN) to yield acid **220** as an off-white solid (0.023 g, 54%). **IR** (neat, diamond cell) ν 3603, 3451, 3391, 3284, 3035, 2923, 2852, 2659, 1697, 1654, 1610, 1591, 1532, 1500, 1489, 1452, 1410, 1384, 1338, 1276, 1244, 1218, 1195, 1164, 1074, 966, 874, 854, 842, 764, 753, 691, 663, 607 cm^{-1}; **LRMS** (+ESI) *m/z* 482 $[M+Na]^+$; (−ESI) *m/z* 458 $[M-H]^-$; **HRMS** Calcd for $C_{26}H_{21}NNaO_5S^+$ $[M+Na]^+$: *m/z* 482.10326, found *m/z* 482.10367; calcd for $C_{26}H_{20}NO_5S$ $[M-H]^-$: *m/z* 458.10677, found *m/z* 458.10738; **^{1}H NMR** (500 MHz, DMSO-d_6) δ 9.93 (s, 1H), 8.24 – 8.17 (m, 1H), 7.88 – 7.80 (m, 1H), 7.56 – 7.48 (m, 3H), 7.46 – 7.35 (m, 4H), 7.13 (t, J = 7.4 Hz, 1H), 7.05 – 6.97 (m, 4H), 3.75 (s, 2H), 3.63 (s, 2H) ppm; **^{13}C NMR** (126 MHz, DMSO-d_6) δ 171.5, 169.9, 156.9, 155.2, 151.4, 131.5, 130.8, 130.0, 129.4, 127.0, 126.5, 125.6, 125.5, 125.1, 123.3, 122.8, 122.7, 118.7, 118.4, 113.1, 41.9, 37.2 ppm; **HPLC** (254 nm) 24.34 min, 96.13%.

Methyl 2-((4-((4-(1H-pyrazol-1-yl)phenyl)sulfonamido)-1-methoxynaphthalen-2-yl)thio)acetate **244**

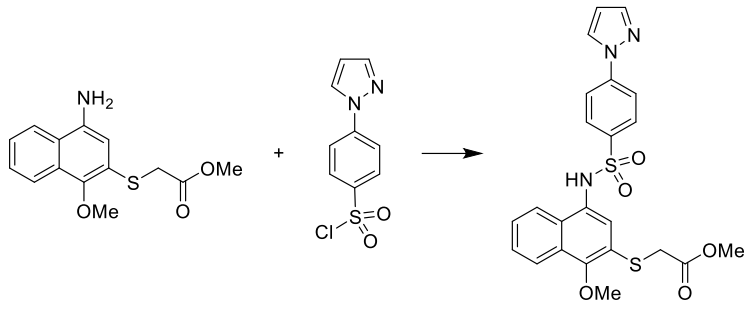

223 **243** **244**

To a solution of aniline **223** (0.090 g, 0.33 mmol) and 4-(1*H*-pyrazol-1-yl)benzenesulfonyl chloride **243** (0.079 g, 0.33 mmol) in CH_2Cl_2 (2.5 mL) was added pyridine (0.039 mL, 0.49 mmol) and the solution stirred at RT for 3 h. When the reaction was complete, the solution was diluted with aq. 1 M HCl solution, then extracted with EtOAc (×3). The combined organic extracts were washed with brine, then dried ($MgSO_4$). The solvent was evaporated to yield the crude residue, which was purified by column chromatography (10-40% EtOAc/hexanes) to yield sulfonamide **244** as a pale green solid (0.13 g, 86%). **IR** (neat, diamond cell) ν 3243, 3126, 2955, 2853, 2642, 2525, 1723, 1595, 1569, 1524, 1503, 1395, 1371, 1338, 1321, 1306, 1270, 1158, 1091, 1074, 1061, 1026, 950, 912, 901, 882, 841, 752, 672, 634, 606 cm^{-1}; **LRMS** (+ESI) *m/z* 506 $[M+Na]^+$; (−ESI) *m/z* 482 $[M-H]^-$; **HRMS** Calcd for $C_{23}H_{21}N_3NaO_5S_2^+$ $[M+Na]^+$: *m/z* 506.08148, found *m/z* 506.08127; calcd for $C_{23}H_{20}N_3O_5S_2$ $[M-H]^-$: *m/z* 482.08499, found *m/z* 482.08550; **^{1}H NMR** (400 MHz, $CDCl_3$) δ 8.05 (dt, *J* = 8.4, 1.0 Hz, 1H), 7.94 (d, *J* = 2.6 Hz, 1H), 7.83 (d, *J* = 8.9 Hz, 2H), 7.77 (d, *J* = 8.4 Hz, 1H), 7.76 – 7.72 (m, 3H), 7.48 (ddd, *J* = 8.3, 6.8, 1.3 Hz, 1H), 7.44 – 7.36 (m, 2H), 6.78 (s, 1H), 6.50 (dd, *J* = 2.6, 1.7 Hz, 1H), 3.98 (s, 3H), 3.68 (s, 3H), 3.65 (s, 2H) ppm; **^{13}C NMR** (101 MHz, $CDCl_3$) δ 170.0, 154.4, 143.4, 142.4, 136.6, 130.1, 129.2, 128.9, 127.8, 127.3, 127.2, 127.0, 126.0, 123.6, 122.7, 122.2, 118.8, 109.0, 61.7, 52.8, 35.3 ppm.

2-((4-((4-(1H-Pyrazol-1-yl)phenyl)sulfonamido)-1-hydroxynaphthalen-2-yl)thio)acetic acid **221**

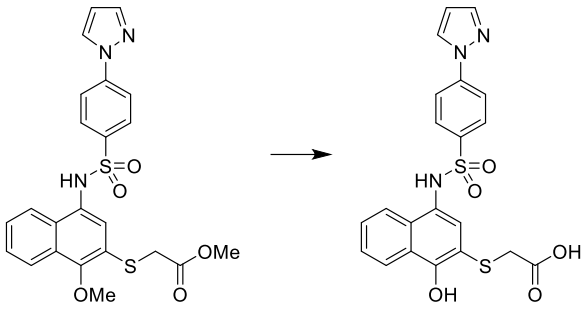

244 **221**

Using **General Procedure H**, ester **244** (0.042 g, 0.087 mmol) and BBr_3 (0.26 mL, 0.26 mmol) gave the title compound. The crude residue was purified by reverse phase column chromatography (0-100% MeCN/H_2O) to yield acid **221** as a white solid (0.019 g, 47%). **IR** (neat, diamond cell) ν 3243, 3126, 2955, 2922, 2853, 2642, 2525, 1723, 1595, 1569, 1524, 1503, 1395, 1371, 1338, 1321, 1306, 1269, 1226, 1158, 1091, 1074, 1061, 1026, 950, 912, 901, 882, 841, 752, 672, 634, 606 cm^{-1}; **LRMS** (−ESI) *m/z* 454 $[M-H]^-$; **HRMS** Calcd for $C_{21}H_{16}N_3O_5S_2^-$ $[M-H]^-$: *m/z* 454.05369, found *m/z* 454.05434; **^{1}H NMR** (500 MHz, DMSO-d_6) δ 9.96 (s, 1H), 8.56 (d, *J* = 2.6 Hz, 1H), 8.14 (dd, *J* = 8.1, 1.5 Hz, 1H), 7.99 – 7.93 (m, 2H), 7.89 (dd, *J* = 8.1, 1.5 Hz, 1H), 7.81 (d, *J* = 1.7 Hz, 1H), 7.75 – 7.69 (m, 2H), 7.43 (dddd, *J* = 16.6, 8.2, 6.8, 1.4 Hz, 2H), 7.08 (s, 1H), 6.59 (t, *J* = 2.1 Hz, 1H), 3.49 (s, 2H) ppm; **^{13}C NMR (**126 MHz, DMSO-d_6) δ 171.2, 152.8, 142.3, 142.1, 136.9, 131.2, 129.5, 128.6, 128.3, 126.7, 125.7, 125.2, 123.8, 123.3, 122.5, 118.2, 112.9, 108.8, 37.2 ppm; **HPLC** (254 nm) 21.22 min, 98.11%.

1-Nitro-4-phenoxybenzene **247**

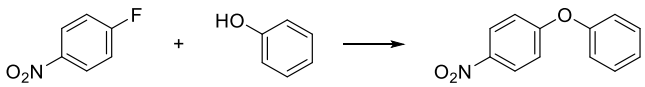

245 **246** **247**

4-fluoronitrobenzene **245** (0.25 g, 1.8 mmol) and phenol **246** (0.17 g, 1.8 mmol) were dissolved in DMF (12 mL), then K_2CO_3 (0.29 g, 2.1 mmol) was added. The solution was stirred at RT for 16 h. When the reaction was complete, the mixture was diluted with H_2O and extracted with EtOAc (×3). The combined organic layers were washed with brine, then dried ($MgSO_4$). The solvent was evaporated under reduced pressure to yield the crude residue, which was purified by flash column chromatography (1–5% EtOAc/hexanes) to yield nitroarene **247** as a yellow oil (0.24 g, 63%). **LRMS** (+ESI) *m/z* 238 $[M+Na]^+$; **^{1}H NMR** (400 MHz, $CDCl_3$) δ

8.23 – 8.12 (m, 2H), 7.48 – 7.38 (m, 2H), 7.29 – 7.23 (m, 1H), 7.13 – 7.06 (m, 2H), 7.05 – 6.95 (m, 2H) ppm; **^{13}C NMR** (101 MHz, $CDCl_3$) δ 163.5, 154.9, 142.8, 130.5, 126.1, 125.6, 120.7, 117.3 ppm. Characterisation data were consistent with literature.[466]

4-Phenoxyaniline **248**

247 **248**

A solution of nitroarene **247** (0.22 g, 1.0 mmol) and 4,4′-bipyridine (0.0005 g, 0.003 mmol) in DMF (1.5 mL) was cooled in an ice-water bath, then tetrahydroxydiboron (0.27 g, 3.0 mmol) was added. The solution was allowed to warm to RT and stirred for 30 min. When the reaction was complete, the solution was diluted with water and extracted with EtOAc (×3). The combined organic extracts were washed with brine, then dried ($MgSO_4$). The solvent was evaporated to yield aniline **248** as an off-white solid (0.19 g, 99%). **LRMS** (+ESI) *m/z* 186 $[M+H]^+$; **^{1}H NMR** (400 MHz, $CDCl_3$) δ 7.33 – 7.24 (m, 2H), 7.02 (tt, *J* = 7.2, 1.1 Hz, 1H), 6.94 (dt, *J* = 7.8, 1.1 Hz, 2H), 6.90 – 6.85 (m, 2H), 6.74 – 6.65 (m, 2H), 3.58 (s, 2H) ppm; **^{13}C NMR** (101 MHz, CDCl3) δ 159.0, 148.8, 142.8, 129.7, 122.2, 121.3, 117.4, 116.4 ppm. Characterisation data were consistent with literature.[467]

Methyl 2-((1-methoxy-4-(3-(4-phenoxyphenyl)ureido)naphthalen-2-yl)thio)acetate **251**

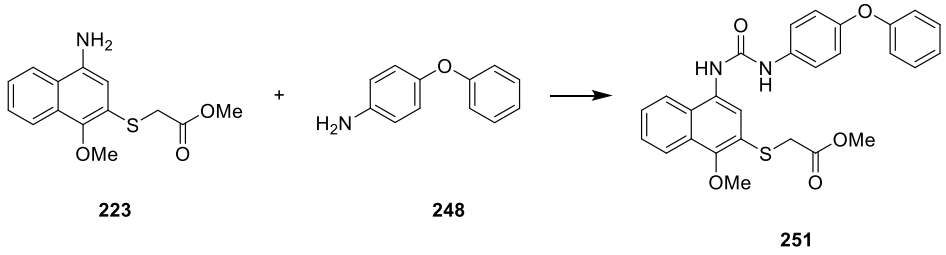

223 **248** **251**

A solution of aniline **223** (0.045 g, 0.16 mmol) in CH_2Cl_2 (1 mL) was cooled in an ice-water bath, then a solution of triphosgene (0.019 g, 0.065 mmol) in CH_2Cl_2 (2 mL) was added dropwise. The solution was allowed to warm to RT and stirred for 4 h. When the reaction was complete, the solvent was evaporated under a gentle stream of N_2. The residue was subsequently redissolved in CH_2Cl_2 (2 mL), then aniline **248** (0.038 g, 0.20 mmol) and Et_3N (0.034 mL, 0.24 mmol) were added, and the solution was stirred at RT for 16 h. When the reaction was complete, the solution was diluted with H_2O, then extracted with EtOAc (×3). The combined organic extracts were washed with brine, then dried ($MgSO_4$). The solvent was

evaporated to yield the crude residue, which was purified by column chromatography (20-50% EtOAc/hexanes) to yield urea **251** as a brown solid (0.017 g, 11%). **IR** (neat, diamond cell) **ν** 3326, 3094, 2950, 2930, 2874, 1735, 1653, 1608, 1591, 1534, 1506, 1486, 1438, 1410, 1359, 1336, 1305, 1220, 1159, 1123, 1069, 975, 955, 852, 778, 731, 692, 653 cm^{-1}; **LRMS** (+ESI) *m/z* 511 $[M+Na]^+$; (−ESI) *m/z* 487 $[M-H]^-$; **HRMS** Calcd for $C_{27}H_{24}N_2NaO_5S$ $[M+Na]^+$: *m/z* 511.12981, found *m/z* 511.12938; calcd for $C_{27}H_{23}N_2O_5S$ $[M-H]^-$: *m/z* 487.13332, found *m/z* 487.13423; **^{1}H NMR** (400 MHz, $CDCl_3$) δ 8.04 (d, *J* = 8.4 Hz, 1H), 7.89 (d, *J* = 8.4 Hz, 1H), 7.68 (s, 1H), 7.49 (t, *J* = 7.6 Hz, 1H), 7.39 (t, *J* = 7.6 Hz, 1H), 7.28 (d, *J* = 7.7 Hz, 2H), 7.19 (s, 1H), 7.10 (s, 1H), 7.06 (t, *J* = 7.4 Hz, 1H), 6.93 (d, *J* = 8.0 Hz, 2H), 6.88 (s, 2H), 3.94 (s, 3H), 3.72 (s, 2H), 3.63 (s, 3H) ppm; **^{13}C NMR** (101 MHz, $CDCl_3$) δ 170.4, 157.8, 154.9, 153.7, 153.3, 133.8, 129.8, 129.4, 129.0, 127.2, 127.2, 125.3, 123.3, 123.1, 122.7, 122.5, 122.4, 119.8, 118.5, 61.7, 52.8, 35.1 ppm. The peak corresponding to the urea carbon could not be detected.

6.6. Experimental for Scaffold Hopping Using Spark™ Software

The Spark™ software package (10.7.1, Cresset®, Litlington, Cambridgeshire, UK; http://www.cresset-group.com/spark/) was used to visualise and perform scaffold hopping of the lead molecules. This software package utilises Cresset's field technology which condenses the molecular fields into a set of points around the molecule, called "field points". The electrostatic, van der Waals and hydrophobic potentials of the molecule are therefore represented as field points, which are generated using the eXtended Electron Distribution (XED) forcefield. The field types are represented as follows: red (postive), blue (negative), orange (hydrophobic), and yellow (van der Waals attractive forces). The size of the field or spheres indicates whether more energetically favourable interactions can be made.

Structures of **126** and **127** were drawn using ChemDraw Professional 23.0.1 and energy minimised using MM2 calculation within Chem3D 23.0.1. Minimised structures were loaded into the R-group replacement workflow of Spark and the regions to be replaced were selected as shown in **Chapter 3.5.** The experiment was run using commercial databases based on eMolecules screening compounds, VeryCommon (67,888 fragments; appearing in at least 725 molecules), Common (112,949 fragments; appearing in 215–724 molecules), LessCommon (211,480 fragments; appearing in 65–214 molecules) and Rare (279,658 fragments; appearing in 25–64 molecules). All other parameters were left as default settings. The scoring criteria for replacement fragments was weighted based on 50% field score and 50% shape score. The

results of the Spark search showed 500 possible R-group replacements, which were ranked according to the scoring criteria above.

6.7. Experimental for Docking Studies

All molecular docking studies were performed with the Maestro software package (2024-1, Schrodinger Inc., New York, USA) within the Drug Discovery Initiative *In Silico* Drug Design Facility at the School of Pharmacy, University of Sydney.

The homology models and crystal structures of BCL-X_L (PDB: 2O2N and 3ZLN) and MCL-1 (PDB: 2NLA) were imported from PDB and prepared using Protein Preparation Wizard embedded in Maestro. This program assigns bond orders, adds hydrogen atoms, and creates zero-order bonds to metals and disulfide bonds, among other tasks. The hydrogen bond networks within the proteins were optimized with all het groups within the receptor grid bounding box previously removed and the protein structure minimized to a root-mean-square deviation of 0.3 Å using the OPLS3 force field.[468, 469] The structures of desired ligands were drawn using ChemDraw Professional 23.0.1 and energy minimisation was completed using MM2 calculations in Chem3D 23.0.1. The ligands were prepared using LigPrep to generate potential ionisation states at pH 7.0 ± 2.0. ConfGen was utilized to obtain up to 64 different conformers for each ligand.[470]

The Receptor Grid Generation tool in Glide was used to characterize the binding site for the docking studies.[367, 471] Binding sites were defined by a 20 Å bounding box centred at the ligand within the active site of each crystal structure. All other settings were left as the default.

Finally, ligands were docked into the receptor grids using Glide.[367, 471] Molecular docking was carried out using Glide's Extra Precision (XP) setting to refine binding energy estimates.[472] All other settings were left as the default for docking.

6.8. Experimental for Biological Evaluation

All biological evaluation was performed by Dr. Alexandra Maximova within the Faculty of Health Sciences, University of Sydney.

6.8.1. Time-Resolved Fluorescence Resonance Energy Transfer (TR-FRET) Assay

To explore compound binding to the BCL-X_L protein as a potential drug target, a TR-FRET assay (50223, BPS Bioscience) was performed according to the manufacturer's protocol. Compounds were incubated at 10 μM in anti-His Tb-labelled donor, dye-labelled acceptor, BCL-X_L peptide ligand (BCL-2 interacting mediator of cell death, BIM) and BCL-X_L protein

in 96-well polypropylene V-bottom microplates while protected from light for 3 h at RT. A negative control representing non-specific binding was performed by incubating all reagents in the absence of BIM and test compounds. A positive control for binding of BIM to the BCL-X_L protein was performed by incubating all reagents in test compound vehicle (0.1% DMSO) with the absence of test compounds. A sample (17 μL) from each well was transferred to a 384-well white proxy plate (Thermo Fisher Scientific) and fluorescence was read on a PHERAstar microplate reader (BMG LABTECH) at 620 nm and 665 nm. Values were calculated for each wavelength corrected for non-specific binding by subtracting the negative control value and then expressing values in the presence of each drug as a percentage of the positive control.

6.8.2. AlphaScreen® Assay

The ability of compounds to bind to BCL-2 was explored using a protocol adapted from a modified AlphaScreen® approach by Lv and co-workers.[451] Compounds were incubated at 10 μM in BCL-2 (9 nM, SRP0186, Sigma-Aldrich) and biotin-tagged BIM (52 nM, sequence biotin-MRPEIWIAQELRRIGDEFNA, AnaSpec) in 96-well polypropylene V-bottom microplates (Greiner Bio-One) for 2 h at RT. Following incubation, AlphaLISA™ anti-6xHis acceptor beads (5 μg/mL, AL178C, PerkinElmer) were added to all wells and incubated for 1 h at RT. Lastly, AlphaScreen® streptavidin donor beads (5 μg/mL) (67600025, PerkinElmer) were added to all wells and incubated while protecting from light for 45 min at RT. A negative control to determine non-specific binding was represented by incubating all reagents with non-biotin-tagged BIM (5.2 μM) in absence of test compounds. A positive control to determine binding between biotin-tagged BIM and BCL-2 was performed by incubating all reagents in test vehicle compound with the absence of test compounds. A sample (17 μL) from each well was transferred to a 384-well white proxy plate (Thermo Fisher Scientific) and fluorescence was read on a PHERAstar microplate reader at 620 nm and 665 nm. Values were calculated for each wavelength, corrected for non-specific binding by subtracting the negative control value, and expressed as a percentage of the positive control.

6.8.3. Statistical Analysis

Data collected from experiments examining drug binding was analysed to determine significant differences between positive control and drug (10 μM) treatment conditions, for compounds which inhibited binding by more than 50%. The false discovery rate was set to 5%.

Statistical significance for all experiments was determined using a cut-off p-value < 0.05 in Prism using one-way ANOVA and Dunnett's test.

This Page Intentionally Left Blank

This Page Intentionally Left Blank

Chapter 7

References

Chapter 7 – References

1. World Health Organization, *Dementia*, **2023**. Available at: https://www.who.int/news-room/fact-sheets/detail/dementia (accessed 25 December 2023).
2. Zahn, R.; Burns, A. Dementia disorders: an overview. In *Alzheimer's Disease*; Oxford University Press, **2017**, Oxford, UK.
3. World Health Organization, *Ageing and health*, **2022**. Available at: https://www.who.int/news-room/fact-sheets/detail/ageing-and-health (accessed 25 December 2023).
4. Prince, M.; Wimo, A.; Guerchet, M.; Ali, G.-C.; Wu, Y.-T.; Prina, M., *World Alzheimer Report 2015: The global impact of dementia: an analysis of prevalence, incidence, cost and trends. Alzheimer's Disease International: London, 2015*
5. Australian Government, *Dementia in Australia*, **2023**. Available at: https://www.aihw.gov.au/reports/dementia/dementia-in-aus/contents/summary (accessed 25 December 2023).
6. Vatanabe, I. P.; Manzine, P. R.; Cominetti, M. R. Historic concepts of dementia and Alzheimer's disease: From ancient times to the present. *Revue Neurologique* **2020**, *176* (3), 140-147.
7. Irwin, K.; Sexton, C.; Daniel, T.; Lawlor, B.; Naci, L. Healthy Aging and Dementia: Two Roads Diverging in Midlife? *Front. Aging Neurosci.* **2018**, *10*, 275.
8. Um, Y. H.; Choi, W. H.; Jung, W. S.; Park, Y. H.; Lee, C.-U.; Lim, H. K. A Case Report of a 37-Year-Old Alzheimer's Disease Patient with Prominent Striatum Amyloid Retention. *Psychiatry Investig.* **2017**, *14* (4), 521-524.
9. Bakker, C.; Koopmans, R. T. C. M.; Pijnenburg, Y. A. L.; Verhey, F. R. J.; Vernooij-Dassen, M. J. F. J.; de Vugt, M. E.; van Vliet, D. Time to diagnosis in young-onset dementia as compared with late-onset dementia. *Psych. Med.* **2013**, *43* (2), 423-432.
10. Prince, M. K., M.; Guerchet, M.; McCrone, P.; Prina, M.; Comas-Herrera, A.; Wittenberg, R.; Adelaja, B.; Hu, B.; King, D.; Rehill, A.; Salimkumar, D. *Dementia UK: Update*; London, UK, 2014.
11. Mesulam, M. M. Primary progressive aphasia. *Ann. Neurol.* **2001**, *49* (4), 425-432.
12. Outeiro, T. F.; Koss, D. J.; Erskine, D.; Walker, L.; Kurzawa-Akanbi, M.; Burn, D.; Donaghy, P.; Morris, C.; Taylor, J.-P.; Thomas, A.; et al. Dementia with Lewy bodies: an update and outlook. *Mol. Neurodegener.* **2019**, *14* (1), 5.

13. Goedert, M.; Spillantini, M. G. A Century of Alzheimer's Disease. *Science* **2006**, *314* (5800), 777-781.
14. Davie, C. A. A review of Parkinson's disease. *British Medical Bulletin* **2008**, *86* (1), 109-127. DOI: 10.1093/bmb/ldn013 (acccessed 3/6/2023).
15. Mejzini, R.; Flynn, L. L.; Pitout, I. L.; Fletcher, S.; Wilton, S. D.; Akkari, P. A. ALS Genetics, Mechanisms, and Therapeutics: Where Are We Now? *Front. Neurosci.* **2019**, *13*, 1310.
16. Walker, Z.; Possin, K. L.; Boeve, B. F.; Aarsland, D. Lewy body dementias. *The Lancet* **2015**, *386* (10004), 1683-1697.
17. Bang, J.; Spina, S.; Miller, B. L. Frontotemporal dementia. *The Lancet* **2015**, *386* (10004), 1672-1682.
18. Gorno-Tempini, M. L.; Hillis, A. E.; Weintraub, S.; Kertesz, A.; Mendez, M.; Cappa, S. F.; Ogar, J. M.; Rohrer, J. D.; Black, S.; Boeve, B. F.; et al. Classification of primary progressive aphasia and its variants. *Neurology* **2011**, *76* (11), 1006.
19. Iwasaki, Y. Creutzfeldt-Jakob disease. *Neuropathology* **2017**, *37* (2), 174-188.
20. Müller-Spahn, F. Behavioral disturbances in dementia. *Dialogues Clin. Neurosci.* **2003**, *5* (1), 49-59.
21. Cerejeira, J.; Lagarto, L.; Mukaetova-Ladinska, E. Behavioral and Psychological Symptoms of Dementia. *Front. Neurol.* **2012**, *3*, 73.
22. Duong, S.; Patel, T.; Chang, F. Dementia: What pharmacists need to know. *Can. Pharm. J.* **2017**, *150* (2), 118-129.
23. Gottesman, R. T.; Stern, Y. Behavioral and Psychiatric Symptoms of Dementia and Rate of Decline in Alzheimer's Disease. *Front. Pharmacol.* **2019**, *10*, 1062.
24. Folstein, M. F.; Folstein, S. E.; McHugh, P. R. "Mini-mental state": A practical method for grading the cognitive state of patients for the clinician. *J. Psych. Res.* **1975**, *12* (3), 189-198.
25. Bradshaw, J. R.; Thomson, J. L.; Campbell, M. J. Computed tomography in the investigation of dementia. *BMJ* **1983**, *286* (6361), 277.
26. Shivamurthy, V. K. N.; Tahari, A. K.; Marcus, C.; Subramaniam, R. M. Brain FDG PET and the Diagnosis of Dementia. *Am. J. Roentgenol.* **2014**, *204* (1), W76-W85.
27. Harper, L.; Fumagalli, G. G.; Barkhof, F.; Scheltens, P.; O'Brien, J. T.; Bouwman, F.; Burton, E. J.; Rohrer, J. D.; Fox, N. C.; Ridgway, G. R.; et al. MRI visual rating scales in

the diagnosis of dementia: evaluation in 184 post-mortem confirmed cases. *Brain* **2016**, *139* (4), 1211-1225.

28. Chen, J.-H.; Lin, K.-P.; Chen, Y.-C. Risk Factors for Dementia. *J. Formos. Med. Assoc.* **2009**, *108* (10), 754-764.
29. Tanzi, R. E.; Kovacs, D. M.; Kim, T.-W.; Moir, R. D.; Guenette, S. Y.; Wasco, W. REVIEWThe Gene Defects Responsible for Familial Alzheimer's Disease. *Neurobiol. Dis.* **1996**, *3* (3), 159-168.
30. Haaksma, M. L.; Eriksdotter, M.; Rizzuto, D.; Leoutsakos, J.-M. S.; Olde Rikkert, M. G. M.; Melis, R. J. F.; Garcia-Ptacek, S. Survival time tool to guide care planning in people with dementia. *Neurology* **2020**, *94* (5), e538-e548.
31. Zanetti, O.; Solerte, S. B.; Cantoni, F. Life Expectancy in Alzheimer's Disease (AD). *Arch. Gerontol. Geriatr.* **2009**, *49*, 237-243.
32. Qiu, C.; Fratiglioni, L. Epidemiology of Alzheimer's disease. In *Alzheimer's Disease*; Oxford University Press, **2009**, Oxford, UK.
33. Cheng, S.-T.; Chow, P. K.; Song, Y.-Q.; Yu, E. C. S.; Chan, A. C. M.; Lee, T. M. C.; Lam, J. H. M. *Am. J. Geriatr. Psychiatry* **2014**, *22* (1), 63-74.
34. Hoffmann, K.; Sobol, N. A.; Frederiksen, K. S.; Beyer, N.; Vogel, A.; Vestergaard, K.; Brændgaard, H.; Gottrup, H.; Lolk, A.; Wermuth, L.; et al. Moderate-to-High Intensity Physical Exercise in Patients with Alzheimer's Disease: A Randomized Controlled Trial. *J. Alzheimer's Dis.* **2016**, *50*, 443-453.
35. Jia, R.-x.; Liang, J.-h.; Xu, Y.; Wang, Y.-q. Effects of physical activity and exercise on the cognitive function of patients with Alzheimer disease: a meta-analysis. *BMC Geriatr.* **2019**, *19* (1), 181.
36. Mitra, S.; Muni, M.; Shawon, N. J.; Das, R.; Emran, T. B.; Sharma, R.; Chandran, D.; Islam, F.; Hossain, M. J.; Safi, S. Z.; et al. Tacrine Derivatives in Neurological Disorders: Focus on Molecular Mechanisms and Neurotherapeutic Potential. *Oxid. Med. Cell Longev.* **2022**, *2022*, 7252882.
37. H. Ferreira-Vieira, T.; M. Guimaraes, I.; R. Silva, F.; M. Ribeiro, F. Alzheimer's disease: Targeting the Cholinergic System. *Curr. Neuropharm.* **2016**, *14* (1), 101-115.
38. Silman, I.; Sussman, J. L. Acetylcholinesterase: 'classical' and 'non-classical' functions and pharmacology. *Curr. Opin. Pharmacol.* **2005**, *5* (3), 293-302.
39. Shen, T.; Tai, K.; Henchman, R. H.; McCammon, J. A. Molecular Dynamics of Acetylcholinesterase. *Acc. Chem. Res.* **2002**, *35* (6), 332-340.

40. Millard, C. B.; Broomfield, C. A. Anticholinesterases: Medical Applications of Neurochemical Principles. *J. Neurochem.* **1995**, *64* (5), 1909-1918.
41. Rotundo, R. L. Expression and localization of acetylcholinesterase at the neuromuscular junction. *J. Neurocytol.* **2003**, *32* (5), 743-766.
42. Qaseem, A.; Snow, V.; Cross, J. T.; Forciea, M. A.; Hopkins, R.; Shekelle, P.; Adelman, A.; Mehr, D.; Schellhase, K.; Campos-Outcalt, D.; et al. Current Pharmacologic Treatment of Dementia: A Clinical Practice Guideline from the American College of Physicians and the American Academy of Family Physicians. *Ann. Intern. Med.* **2008**, *148* (5), 370-378.
43. Kryger, G.; Silman, I.; Sussman, J. L. *Structure* **1999**, *7* (3), 297-307.
44. Kasper, B. H.; Lonnie, P. W.; Derek, B.; Hiro, F.; Frank, S. M.; Alexander, I. S.; Geoffrey, T. S.; Sharon, A. S.; Ingo, H. G.; Terunaga, N.; et al. Structure, Function, and Pharmacology of Glutamate Receptor Ion Channels. *Pharmacol. Rev.* **2021**, *73* (4), 1469.
45. Tajima, N.; Karakas, E.; Grant, T.; Simorowski, N.; Diaz-Avalos, R.; Grigorieff, N.; Furukawa, H. Activation of NMDA receptors and the mechanism of inhibition by ifenprodil. *Nature* **2016**, *534* (7605), 63-68.
46. Twomey, E. C.; Sobolevsky, A. I. Structural Mechanisms of Gating in Ionotropic Glutamate Receptors. *Biochem.* **2018**, *57* (3), 267-276.
47. McShane, R.; Westby, M. J.; Roberts, E.; Minakaran, N.; Schneider, L.; Farrimond, L. E.; Maayan, N.; Ware, J.; Debarros, J. Memantine for dementia. *Cochrane Database Syst. Rev.* **2019**, (3).
48. Onyike, C. U. Psychiatric Aspects of Dementia. *Continuum (Minneap. Minn.)* **2016**, *22* (2 Dementia), 600-614.
49. Gustafsson, M.; Karlsson, S.; Gustafson, Y.; Lövheim, H. Psychotropic drug use among people with dementia – a six-month follow-up study. *BMC Pharmacol. Toxicol.* **2013**, *14* (1), 56.
50. Tampi, R. R.; Tampi, D. J.; Balachandran, S.; Srinivasan, S. Antipsychotic use in dementia: a systematic review of benefits and risks from meta-analyses. *Ther. Adv. Chronic Dis.* **2016**, *7* (5), 229-245.
51. Giron, M. S. T.; Forsell, Y.; Bernsten, C.; Thorslund, M.; Winblad, B.; Fastbom, J. Psychotropic drug use in elderly people with and without dementia. *Int. J. Geriatr. Psychiatry* **2001**, *16* (9), 900-906.

52. Gustafson, Y.; Kallin, K.; Karlsson, S.; Lövheim, H.; Sandman, P.-O. Relationship between antipsychotic drug use and behavioral and psychological symptoms of dementia in old people with cognitive impairment living in geriatric care. *Int. Psychogeriatr.* **2006**, *18* (4), 713-726.
53. Orgeta, V.; Tabet, N.; Nilforooshan, R.; Howard, R. Efficacy of Antidepressants for Depression in Alzheimer's Disease: Systematic Review and Meta-Analysis. *J. Alzheimer's Dis.* **2017**, *58*, 725-733.
54. Farina, N.; Morrell, L.; Banerjee, S. What is the therapeutic value of antidepressants in dementia? A narrative review. *Int. J. Geriatr. Psychiatry* **2017**, *32* (1), 32-49.
55. Walsh, S.; Merrick, R.; Milne, R.; Brayne, C. Aducanumab for Alzheimer's disease? *BMJ* **2021**, *374*, n1682.
56. Cummings, J. Anti-Amyloid Monoclonal Antibodies are Transformative Treatments that Redefine Alzheimer's Disease Therapeutics. *Drugs* **2023**, *83* (7), 569-576.
57. Tiller, K. E.; Tessier, P. M. Advances in Antibody Design. *Annu. Rev. Biomed. Eng.* **2015**, *17*, 191-216.
58. Rabinovici, G. D.; La Joie, R. Amyloid-Targeting Monoclonal Antibodies for Alzheimer Disease. *JAMA* **2023**, *330* (6), 507-509.
59. Selkoe, D. J. Treatments for Alzheimer's disease emerge. *Science* **2021**, *373* (6555), 624-626.
60. Ackley, S. F.; Zimmerman, S. C.; Brenowitz, W. D.; Tchetgen Tchetgen, E. J.; Gold, A. L.; Manly, J. J.; Mayeda, E. R.; Filshtein, T. J.; Power, M. C.; Elahi, F. M.; et al. Effect of reductions in amyloid levels on cognitive change in randomized trials: instrumental variable meta-analysis. *BMJ* **2021**, *372*, n156.
61. Budd Haeberlein, S.; Aisen, P. S.; Barkhof, F.; Chalkias, S.; Chen, T.; Cohen, S.; Dent, G.; Hansson, O.; Harrison, K.; von Hehn, C.; et al. Two Randomized Phase 3 Studies of Aducanumab in Early Alzheimer's Disease. *J. Prev. Alzheimer's Dis.* **2022**, *9* (2), 197-210.
62. Sevigny, J.; Chiao, P.; Bussière, T.; Weinreb, P. H.; Williams, L.; Maier, M.; Dunstan, R.; Salloway, S.; Chen, T.; Ling, Y.; et al. The antibody aducanumab reduces Aβ plaques in Alzheimer's disease. *Nature* **2016**, *537* (7618), 50-56.
63. van Dyck Christopher, H.; Swanson Chad, J.; Aisen, P.; Bateman Randall, J.; Chen, C.; Gee, M.; Kanekiyo, M.; Li, D.; Reyderman, L.; Cohen, S.; et al. Lecanemab in Early Alzheimer's Disease. *N. Engl. J. Med.* **2023**, *388* (1), 9-21.

64. Michod, R. E. Evolution of individuality during the transition from unicellular to multicellular life. *Proc. Natl. Acad. Sci. USA* **2007**, *104 Suppl 1* (Suppl 1), 8613-8618.
65. Pichugin, Y.; Park, H. J.; Traulsen, A. Evolution of simple multicellular life cycles in dynamic environments. *J. R. Soc. Interface* **2019**, *16* (154), 20190054.
66. Di Leonardo, A.; Linke, S. P.; Clarkin, K.; Wahl, G. M. DNA damage triggers a prolonged p53-dependent G1 arrest and long-term induction of Cip1 in normal human fibroblasts. *Genes Dev.* **1994**, *8* (21), 2540-2551.
67. Gire, V.; Dulić, V. Senescence from G2 arrest, revisited. *Cell Cycle* **2015**, *14* (3), 297-304.
68. Serrano, M.; Lin, A. W.; McCurrach, M. E.; Beach, D.; Lowe, S. W. Oncogenic Ras Provokes Premature Cell Senescence Associated with Accumulation of p53 and $p16^{INK4a}$. *Cell* **1997**, *88* (5), 593-602.
69. Di Micco, R.; Fumagalli, M.; Cicalese, A.; Piccinin, S.; Gasparini, P.; Luise, C.; Schurra, C.; Garre', M.; Giovanni Nuciforo, P.; Bensimon, A.; et al. Oncogene-induced senescence is a DNA damage response triggered by DNA hyper-replication. *Nature* **2006**, *444* (7119), 638-642.
70. Bartkova, J.; Rezaei, N.; Liontos, M.; Karakaidos, P.; Kletsas, D.; Issaeva, N.; Vassiliou, L.-V. F.; Kolettas, E.; Niforou, K.; Zoumpourlis, V. C.; et al. Oncogene-induced senescence is part of the tumorigenesis barrier imposed by DNA damage checkpoints. *Nature* **2006**, *444* (7119), 633-637.
71. Lee, S.; Schmitt, C. A. The dynamic nature of senescence in cancer. *Nat. Cell Biol.* **2019**, *21* (1), 94-101.
72. Hayflick, L.; Moorhead, P. S. The serial cultivation of human diploid cell strains. *Exp. Cell Res.* **1961**, *25* (3), 585-621.
73. Gorgoulis, V.; Adams, P. D.; Alimonti, A.; Bennett, D. C.; Bischof, O.; Bishop, C.; Campisi, J.; Collado, M.; Evangelou, K.; Ferbeyre, G.; et al. Cellular Senescence: Defining a Path Forward. *Cell* **2019**, *179* (4), 813-827.
74. Marescal, O.; Cheeseman, I. M. Cellular Mechanisms and Regulation of Quiescence, *Dev. Cell* **2020**, *55* (3), 259-271.
75. Rodier, F.; Campisi, J. Four faces of cellular senescence. *J. Cell Biol.* **2011**, *192* (4), 547-556.
76. Galanos, P.; Vougas, K.; Walter, D.; Polyzos, A.; Maya-Mendoza, A.; Haagensen, E. J.; Kokkalis, A.; Roumelioti, F.-M.; Gagos, S.; Tzetis, M.; et al. Chronic p53-independent

p21 expression causes genomic instability by deregulating replication licensing. *Nat. Cell Biol.* **2016**, *18* (7), 777-789.

77. Milanovic, M.; Fan, D. N. Y.; Belenki, D.; Däbritz, J. H. M.; Zhao, Z.; Yu, Y.; Dörr, J. R.; Dimitrova, L.; Lenze, D.; Monteiro Barbosa, I. A.; et al. Senescence-associated reprogramming promotes cancer stemness. *Nature* **2018**, *553* (7686), 96-100.
78. Patel, P. L.; Suram, A.; Mirani, N.; Bischof, O.; Herbig, U. Derepression of hTERT gene expression promotes escape from oncogene-induced cellular senescence. *Proc. Natl. Acad. Sci. USA* **2016**, *113* (34), E5024-E5033.
79. Saleh, T.; Tyutyunyk-Massey, L.; Gewirtz, D. A. Tumor Cell Escape from Therapy-Induced Senescence as a Model of Disease Recurrence after Dormancy. *Cancer Res.* **2019**, *79* (6), 1044-1046.
80. Hayflick, L. The limited in vitro lifetime of human diploid cell strains. *Exp. Cell Res.***1965**, *37* (3), 614-636.
81. Campisi, J. The biology of replicative senescence. *Eur. J. Cancer* **1997**, *33* (5), 703-709.
82. Lee, B. Y.; Han, J. A.; Im, J. S.; Morrone, A.; Johung, K.; Goodwin, E. C.; Kleijer, W. J.; DiMaio, D.; Hwang, E. S. Senescence-associated β-galactosidase is lysosomal β-galactosidase. *Aging Cell* **2006**, *5* (2), 187-195.
83. Alcorta, D. A.; Xiong, Y.; Phelps, D.; Hannon, G.; Beach, D.; Barrett, J. C. Involvement of the cyclin-dependent kinase inhibitor p16 (INK4a) in replicative senescence of normal human fibroblasts. *Proc. Natl. Acad. Sci. USA* **1996**, *93* (24), 13742-13747.
84. Hara, E.; Smith, R.; Parry, D.; Tahara, H.; Stone, S.; Peters, G. Regulation of p16CDKN2 Expression and Its Implications for Cell Immortalization and Senescence. *Mol. Cell. Biol.* **1996**, *16* (3), 859-867.
85. Brenner, A. J.; Stampfer, M. R.; Aldaz, C. M. Increased p16 expression with first senescence arrest in human mammary epithelial cells and extended growth capacity with p16 inactivation. *Oncogene* **1998**, *17* (2), 199-205.
86. Stein, G. H.; Drullinger, L. F.; Soulard, A.; Dulić, V. Differential Roles for Cyclin-Dependent Kinase Inhibitors p21 and p16 in the Mechanisms of Senescence and Differentiation in Human Fibroblasts. *Mol. Cell. Biol.* **1999**, *19* (3), 2109-2117.
87. Acosta, J. C.; O'Loghlen, A.; Banito, A.; Guijarro, M. V.; Augert, A.; Raguz, S.; Fumagalli, M.; Da Costa, M.; Brown, C.; Popov, N.; et al. Chemokine Signaling via the CXCR2 Receptor Reinforces Senescence. *Cell* **2008**, *133* (6), 1006-1018.

88. Coppé, J.-P.; Patil, C. K.; Rodier, F.; Sun, Y.; Muñoz, D. P.; Goldstein, J.; Nelson, P. S.; Desprez, P.-Y.; Campisi, J. Senescence-Associated Secretory Phenotypes Reveal Cell-Nonautonomous Functions of Oncogenic RAS and the p53 Tumor Suppressor. *PLOS Biol.* **2008**, *6* (12), e301.
89. Kuilman, T.; Michaloglou, C.; Vredeveld, L. C. W.; Douma, S.; van Doorn, R.; Desmet, C. J.; Aarden, L. A.; Mooi, W. J.; Peeper, D. S. Oncogene-Induced Senescence Relayed by an Interleukin-Dependent Inflammatory Network. *Cell* **2008**, *133* (6), 1019-1031.
90. González-Gualda, E.; Ou, H.-L.; Macías, D.; Muñoz-Espín, D. Chapter 1 - Cellular senescence: from old to new testament. In *Cellular Senescence in Disease*, Serrano, M., Muñoz-Espín, D. Eds.; Elsevier Inc., **2022**; Amsterdam, Netherlands.
91. Chau, B. N.; Wang, J. Y. Coordinated regulation of life and death by RB. *Nature Rev. Cancer* **2003**, *3* (2), 130-138.
92. Levine, A. J.; Oren, M. The first 30 years of p53: growing ever more complex, *Nature Rev. Cancer*, Vol. 9; 2009; pp 749-758.
93. Takeuchi, S.; Takahashi, A.; Motoi, N.; Yoshimoto, S.; Tajima, T.; Yamakoshi, K.; Hirao, A.; Yanagi, S.; Fukami, K.; Ishikawa, Y.; et al. Intrinsic cooperation between p16INK4a and p21Waf1/Cip1 in the onset of cellular senescence and tumor suppression in vivo. *Cancer Res.* **2010**, *70* (22), 9381-9390.
94. Zhang, J.; Pickering, C. R.; Holst, C. R.; Gauthier, M. L.; Tlsty, T. D. p16INK4a modulates p53 in primary human mammary epithelial cells. *Cancer Res.* **2006**, *66* (21), 10325-10331.
95. Yamakoshi, K.; Takahashi, A.; Hirota, F.; Nakayama, R.; Ishimaru, N.; Kubo, Y.; Mann, D. J.; Ohmura, M.; Hirao, A.; Saya, H.; et al. Real-time in vivo imaging of p16Ink4a reveals cross talk with p53. *J. Cell Biol.* **2009**, *186* (3), 393-407.
96. Ohtani, N.; Zebedee, Z.; Huot, T. J. G.; Stinson, J. A.; Sugimoto, M.; Ohashi, Y.; Sharrocks, A. D.; Peters, G.; Hara, E. Opposing effects of Ets and Id proteins on p16INK4a expression during cellular senescence. *Nature* **2001**, *409* (6823), 1067-1070.
97. Weinberg, R. A. The retinoblastoma protein and cell cycle control. *Cell* **1995**, *81* (3), 323-330.
98. Coppé, J. P.; Desprez, P. Y.; Krtolica, A.; Campisi, J. The senescence-associated secretory phenotype: the dark side of tumor suppression. *Annu. Rev. Pathol.* **2010**, *5*, 99-118.
99. Ohtani, N. The roles and mechanisms of senescence-associated secretory phenotype (SASP): can it be controlled by senolysis? *Inflamm. Regener.* **2022**, *42* (1), 11.

100. Cuollo, L.; Antonangeli, F.; Santoni, A.; Soriani, A. The Senescence-Associated Secretory Phenotype (SASP) in the Challenging Future of Cancer Therapy and Age-Related Diseases. *Biology* **2020**, *9* (12).
101. Lopes-Paciencia, S.; Saint-Germain, E.; Rowell, M.-C.; Ruiz, A. F.; Kalegari, P.; Ferbeyre, G. The senescence-associated secretory phenotype and its regulation. *Cytokine* **2019**, *117*, 15-22.
102. Langhi Prata, L. G. P.; Tchkonia, T.; Kirkland, J. L. Cell senescence, the senescence-associated secretory phenotype, and cancers. *PLOS Biol.* **2023**, *21* (9), e3002326.
103. Basisty, N.; Kale, A.; Jeon, O. H.; Kuehnemann, C.; Payne, T.; Rao, C.; Holtz, A.; Shah, S.; Sharma, V.; Ferrucci, L.; et al. A proteomic atlas of senescence-associated secretomes for aging biomarker development. *PLOS Biol.* **2020**, *18* (1), e3000599.
104. Harley, C. B.; Futcher, A. B.; Greider, C. W. Telomeres shorten during ageing of human fibroblasts. *Nature* **1990**, *345* (6274), 458-460.
105. Sedivy, J. M. Can ends justify the means?: Telomeres and the mechanisms of replicative senescence and immortalization in mammalian cells. *Proc. Natl. Acad. Sci. USA* **1998**, *95* (16), 9078-9081.
106. Lundberg, A. S.; Hahn, W. C.; Gupta, P.; Weinberg, R. A. Genes involved in senescence and immortalization. *Curr. Opin. Cell Biol.* **2000**, *12* (6), 705-709.
107. Höhn, A.; Weber, D.; Jung, T.; Ott, C.; Hugo, M.; Kochlik, B.; Kehm, R.; König, J.; Grune, T.; Castro, J. P. Happily (n)ever after: Aging in the context of oxidative stress, proteostasis loss and cellular senescence. *Redox Biol.* **2017**, *11*, 482-501.
108. Nyström, T. Role of oxidative carbonylation in protein quality control and senescence. *EMBO J.* **2005**, *24* (7), 1311-1317-1317.
109. Ogrodnik, M.; Salmonowicz, H.; Gladyshev, V. N. Integrating cellular senescence with the concept of damage accumulation in aging: Relevance for clearance of senescent cells. *Aging Cell* **2019**, *18* (1), e12841.
110. Kaushik, S.; Cuervo, A. M. Proteostasis and aging. *Nat. Med.* **2015**, *21* (12), 1406-1415. DOI: 10.1038/nm.4001.
111. van Meer, G.; Voelker, D. R.; Feigenson, G. W. Membrane lipids: where they are and how they behave. *Nat. Rev. Mol. Cell Biol.* **2008**, *9* (2), 112-124.
112. Ademowo, O. S.; Dias, H. K. I.; Burton, D. G. A.; Griffiths, H. R. Lipid (per) oxidation in mitochondria: an emerging target in the ageing process? *Biogerontology* **2017**, *18* (6), 859-879.

113. Correia-Melo, C.; Marques, F. D. M.; Anderson, R.; Hewitt, G.; Hewitt, R.; Cole, J.; Carroll, B. M.; Miwa, S.; Birch, J.; Merz, A.; et al. Mitochondria are required for pro-ageing features of the senescent phenotype. *EMBO J.* **2016**, *35* (7), 724-742.
114. Ogrodnik, M.; Miwa, S.; Tchkonia, T.; Tiniakos, D.; Wilson, C. L.; Lahat, A.; Day, C. P.; Burt, A.; Palmer, A.; Anstee, Q. M.; et al. Cellular senescence drives age-dependent hepatic steatosis. *Nat. Commun.* **2017**, *8* (1), 15691.
115. Gorgoulis, V. G.; Pefani, D.-E.; Pateras, I. S.; Trougakos, I. P. Integrating the DNA damage and protein stress responses during cancer development and treatment. *J. Pathol.* **2018**, *246* (1), 12-40.
116. Jiang, P.; Du, W.; Mancuso, A.; Wellen, K. E.; Yang, X. Reciprocal regulation of p53 and malic enzymes modulates metabolism and senescence. *Nature* **2013**, *493* (7434), 689-693.
117. Kaplon, J.; Zheng, L.; Meissl, K.; Chaneton, B.; Selivanov, V. A.; Mackay, G.; van der Burg, S. H.; Verdegaal, E. M. E.; Cascante, M.; Shlomi, T.; et al. A key role for mitochondrial gatekeeper pyruvate dehydrogenase in oncogene-induced senescence. *Nature* **2013**, *498* (7452), 109-112.
118. Miwa, S.; Jow, H.; Baty, K.; Johnson, A.; Czapiewski, R.; Saretzki, G.; Treumann, A.; von Zglinicki, T. Low abundance of the matrix arm of complex I in mitochondria predicts longevity in mice. *Nat. Commun.* **2014**, *5* (1), 3837.
119. Moiseeva, O.; Bourdeau, V.; Roux, A.; Deschênes-Simard, X.; Ferbeyre, G. Mitochondrial dysfunction contributes to oncogene-induced senescence. *Mol. Cell Biol.* **2009**, *29* (16), 4495-4507.
120. Park, Y.-Y.; Lee, S.; Karbowski, M.; Neutzner, A.; Youle, R. J.; Cho, H. Loss of MARCH5 mitochondrial E3 ubiquitin ligase induces cellular senescence through dynamin-related protein 1 and mitofusin 1. *J. Cell Sci.* **2010**, *123* (4), 619-626.
121. Wiley, Christopher D.; Velarde, Michael C.; Lecot, P.; Liu, S.; Sarnoski, Ethan A.; Freund, A.; Shirakawa, K.; Lim, Hyung W.; Davis, Sonnet S.; Ramanathan, A.; et al. Mitochondrial Dysfunction Induces Senescence with a Distinct Secretory Phenotype. *Cell Metab.* **2016**, *23* (2), 303-314.
122. Passos, J. F.; Nelson, G.; Wang, C.; Richter, T.; Simillion, C.; Proctor, C. J.; Miwa, S.; Olijslagers, S.; Hallinan, J.; Wipat, A.; et al. Feedback between p21 and reactive oxygen production is necessary for cell senescence. *Mol. Syst. Biol.* **2010**, *6*, 347.

123. Birch, J.; Passos, J. F. Targeting the SASP to combat ageing: Mitochondria as possible intracellular allies? *BioEssays* **2017**, *39* (5), 1600235.
124. Korolchuk, V. I.; Miwa, S.; Carroll, B.; von Zglinicki, T. Mitochondria in Cell Senescence: Is Mitophagy the Weakest Link? *EBioMedicine* **2017**, *21*, 7-13.
125. Robbins, E.; Levine, E. M.; Eagle, H. Morphologic Changes Accompanying Senescence of Cultured Human Diploid Cells. *J. Exp. Med* **1970**, *131* (6), 1211-1222.
126. Levine, B.; Kroemer, G. Autophagy in the Pathogenesis of Disease. *Cell* **2008**, *132* (1), 27-42.
127. Rovira, M.; Sereda, R.; Pladevall-Morera, D.; Ramponi, V.; Marin, I.; Maus, M.; Madrigal-Matute, J.; Díaz, A.; García, F.; Muñoz, J.; et al. The lysosomal proteome of senescent cells contributes to the senescence secretome. *Aging Cell* **2022**, *21* (10), e13707.
128. Knaś, M.; Zalewska, A.; Krętowski, R.; Niczyporuk, M.; Waszkiewicz, N.; Cechowska-Pasko, M.; Waszkiel, D.; Zwierz, K. The profile of lysosomal exoglycosidases in replicative and stress-induced senescence in early passage human fibroblasts. *Folia Histochem. Cytobiol.* **2012**, *50* (2), 220-227.
129. He, S.; Sharpless, N. E. Senescence in Health and Disease. *Cell* **2017**, *169* (6), 1000-1011.
130. Hoenicke, L.; Zender, L. Immune surveillance of senescent cells—biological significance in cancer- and non-cancer pathologies. *Carcinogenesis* **2012**, *33* (6), 1123-1126.
131. Donehower, L. A. Does p53 affect organismal aging? *J. Cell. Physiol.* **2002**, *192* (1), 23-33.
132. Faragher, R. G. A. Cell senescence and human aging: where's the link? *Biochem. Soc. Trans.* **2000**, *28* (2), 221-226.
133. Kortlever, R. M.; Bernards, R. Senescence, Wound Healing, and Cancer: the PAI-1 Connection. *Cell Cycle* **2006**, *5* (23), 2697-2703.
134. Kirkwood, T. B. L.; Austad, S. N. Why do we age? *Nature* **2000**, *408* (6809), 233-238.
135. Mitteldorf, J. What Is Antagonistic Pleiotropy? *Biochemistry (Moscow)* **2019**, *84* (12), 1458-1468.
136. Muñoz-Espín, D.; Cañamero, M.; Maraver, A.; Gómez-López, G.; Contreras, J.; Murillo-Cuesta, S.; Rodríguez-Baeza, A.; Varela-Nieto, I.; Ruberte, J.; Collado, M.; et al.

Programmed Cell Senescence during Mammalian Embryonic Development. *Cell* **2013**, *155* (5), 1104-1118.

137. Storer, M.; Mas, A.; Robert-Moreno, A.; Pecoraro, M.; Ortells, M. C.; Di Giacomo, V.; Yosef, R.; Pilpel, N.; Krizhanovsky, V.; Sharpe, J.; et al. Senescence Is a Developmental Mechanism that Contributes to Embryonic Growth and Patterning. *Cell* **2013**, *155* (5), 1119-1130.
138. Kumari, R.; Jat, P. Mechanisms of Cellular Senescence: Cell Cycle Arrest and Senescence Associated Secretory Phenotype. *Front. Cell Dev. Biol.* **2021**, *9*, 645593.
139. Xue, W.; Zender, L.; Miething, C.; Dickins, R. A.; Hernando, E.; Krizhanovsky, V.; Cordon-Cardo, C.; Lowe, S. W. Senescence and tumour clearance is triggered by p53 restoration in murine liver carcinomas. *Nature* **2007**, *445* (7128), 656-660.
140. Mohamad Kamal, N. S.; Safuan, S.; Shamsuddin, S.; Foroozandeh, P. Aging of the cells: Insight into cellular senescence and detection Methods. *Eur. J. Cell Biol.* **2020**, *99* (6), 151108.
141. von Kobbe, C. Cellular senescence: a view throughout organismal life. *Cell Mol. Life Sci.* **2018**, *75* (19), 3553-3567.
142. Tasdemir, N.; Banito, A.; Roe, J. S.; Alonso-Curbelo, D.; Camiolo, M.; Tschaharganeh, D. F.; Huang, C. H.; Aksoy, O.; Bolden, J. E.; Chen, C. C.; et al. BRD4 Connects Enhancer Remodeling to Senescence Immune Surveillance. *Cancer Discov.* **2016**, *6* (6), 612-629.
143. Iannello, A.; Thompson, T. W.; Ardolino, M.; Lowe, S. W.; Raulet, D. H. p53-dependent chemokine production by senescent tumor cells supports NKG2D-dependent tumor elimination by natural killer cells. *J. Exp. Med.* **2013**, *210* (10), 2057-2069.
144. Kang, T. W.; Yevsa, T.; Woller, N.; Hoenicke, L.; Wuestefeld, T.; Dauch, D.; Hohmeyer, A.; Gereke, M.; Rudalska, R.; Potapova, A.; et al. Senescence surveillance of pre-malignant hepatocytes limits liver cancer development. *Nature* **2011**, *479* (7374), 547-551.
145. Demaria, M.; Ohtani, N.; Youssef, Sameh A.; Rodier, F.; Toussaint, W.; Mitchell, James R.; Laberge, R.-M.; Vijg, J.; Van Steeg, H.; Dollé, Martijn E. T.; et al. An Essential Role for Senescent Cells in Optimal Wound Healing through Secretion of PDGF-AA. *Dev. Cell* **2014**, *31* (6), 722-733.
146. Jun, J.-I.; Lau, L. F. The matricellular protein CCN1 induces fibroblast senescence and restricts fibrosis in cutaneous wound healing. *Nat. Cell Biol.* **2010**, *12* (7), 676-685.

147. Sorrentino, J. A.; Krishnamurthy, J.; Tilley, S.; Alb, J. G., Jr.; Burd, C. E.; Sharpless, N. E. p16INK4a reporter mice reveal age-promoting effects of environmental toxicants. *J. Clin. Investig.* **2014**, *124* (1), 169-173.
148. Baker, D. J.; Childs, B. G.; Durik, M.; Wijers, M. E.; Sieben, C. J.; Zhong, J.; A. Saltness, R.; Jeganathan, K. B.; Verzosa, G. C.; Pezeshki, A.; et al. Naturally occurring p16Ink4a-positive cells shorten healthy lifespan. *Nature* **2016**, *530* (7589), 184-189.
149. Prata, L. G. P. L.; Ovsyannikova, I. G.; Tchkonia, T.; Kirkland, J. L. Senescent cell clearance by the immune system: Emerging therapeutic opportunities. *Semin. Immunol.* **2018**, *40*, 101275.
150. Brighton, P. J.; Maruyama, Y.; Fishwick, K.; Vrljicak, P.; Tewary, S.; Fujihara, R.; Muter, J.; Lucas, E. S.; Yamada, T.; Woods, L.; et al. Clearance of senescent decidual cells by uterine natural killer cells in cycling human endometrium. *eLife* **2017**, *6*, e31274.
151. Coppé, J.-P.; Desprez, P.-Y.; Krtolica, A.; Campisi, J. The Senescence-Associated Secretory Phenotype: The Dark Side of Tumor Suppression. *Annu. Rev. Pathol.* **2010**, *5* (1), 99-118.
152. Franceschi, C.; Bonafè, M.; Valensin, S.; Olivieri, F.; De Luca, M.; Ottaviani, E.; De Benedictis, G. Inflamm-aging. An evolutionary perspective on immunosenescence. *Ann. NY Acad. Sci.* **2000**, *908*, 244-254.
153. He, Y.; Zhang, X.; Chang, J.; Kim, H.-N.; Zhang, P.; Wang, Y.; Khan, S.; Liu, X.; Zhang, X.; Lv, D.; et al. Using proteolysis-targeting chimera technology to reduce navitoclax platelet toxicity and improve its senolytic activity. *Nat. Commun.* **2020**, *11* (1), 1996.
154. Jeyapalan, J. C.; Ferreira, M.; Sedivy, J. M.; Herbig, U. Accumulation of senescent cells in mitotic tissue of aging primates. *Mech. Ageing Dev.* **2007**, *128* (1), 36-44.
155. Krishnamurthy, J.; Ramsey, M. R.; Ligon, K. L.; Torrice, C.; Koh, A.; Bonner-Weir, S.; Sharpless, N. E. p16INK4a induces an age-dependent decline in islet regenerative potential. *Nature* **2006**, *443* (7110), 453-457.
156. Lawless, C.; Wang, C.; Jurk, D.; Merz, A.; Zglinicki, T. v.; Passos, J. F. Quantitative assessment of markers for cell senescence. *Exp. Gerontol.* **2010**, *45* (10), 772-778.
157. Xu, M.; Pirtskhalava, T.; Farr, J. N.; Weigand, B. M.; Palmer, A. K.; Weivoda, M. M.; Inman, C. L.; Ogrodnik, M. B.; Hachfeld, C. M.; Fraser, D. G.; et al. Senolytics improve physical function and increase lifespan in old age. *Nature Med.* **2018**, *24* (8), 1246-1256.
158. Baker, D. J.; Perez-Terzic, C.; Jin, F.; Pitel, K. S.; Niederländer, N. J.; Jeganathan, K.; Yamada, S.; Reyes, S.; Rowe, L.; Hiddinga, H. J.; et al. Opposing roles for p16Ink4a and

p19Arf in senescence and ageing caused by BubR1 insufficiency. *Nat. Cell Biol.* **2008**, *10* (7), 825-836.

159. Baker, D. J.; Wijshake, T.; Tchkonia, T.; LeBrasseur, N. K.; Childs, B. G.; van de Sluis, B.; Kirkland, J. L.; van Deursen, J. M. Clearance of p16Ink4a-positive senescent cells delays ageing-associated disorders. *Nature* **2011**, *479* (7372), 232-236.
160. Jeon, O. H.; Wilson, D. R.; Clement, C. C.; Rathod, S.; Cherry, C.; Powell, B.; Lee, Z.; Khalil, A. M.; Green, J. J.; Campisi, J.; et al. Senescence cell-associated extracellular vesicles serve as osteoarthritis disease and therapeutic markers. *JCI Insight* **2019**, *4* (7).
161. Coryell, P. R.; Diekman, B. O.; Loeser, R. F. Mechanisms and therapeutic implications of cellular senescence in osteoarthritis. *Nat. Rev. Rheumatol.* **2021**, *17* (1), 47-57.
162. McCulloch, K.; Litherland, G. J.; Rai, T. S. Cellular senescence in osteoarthritis pathology. *Aging Cell* **2017**, *16* (2), 210-218.
163. Schneider, J. L.; Rowe, J. H.; Garcia-de-Alba, C.; Kim, C. F.; Sharpe, A. H.; Haigis, M. C. The aging lung: Physiology, disease, and immunity. *Cell* **2021**, *184* (8), 1990-2019.
164. Kellogg, D. L.; Kellogg, D. L., Jr.; Musi, N.; Nambiar, A. M. Cellular Senescence in Idiopathic Pulmonary Fibrosis. *Curr. Mol. Biol. Rep.* **2021**, *7* (3), 31-40.
165. Minamino, T.; Miyauchi, H.; Yoshida, T.; Ishida, Y.; Yoshida, H.; Komuro, I. Endothelial cell senescence in human atherosclerosis: role of telomere in endothelial dysfunction. *Circulation* **2002**, *105* (13), 1541-1544.
166. Bennett, M. R.; Clarke, M. C. H. Killing the old: cell senescence in atherosclerosis. *Nat. Rev. Cardiol.* **2017**, *14* (1), 8-9.
167. Wu, C.-M.; Zheng, L.; Wang, Q.; Hu, Y.-W. The emerging role of cell senescence in atherosclerosis, *Clin. Chem. Lab. Med.* **2021**, *59* (1), 27-38.
168. Guo, N.; Parry, E. M.; Li, L. S.; Kembou, F.; Lauder, N.; Hussain, M. A.; Berggren, P. O.; Armanios, M. Short telomeres compromise β-cell signaling and survival. *PLoS One* **2011**, *6* (3), e17858.
169. Minamino, T.; Orimo, M.; Shimizu, I.; Kunieda, T.; Yokoyama, M.; Ito, T.; Nojima, A.; Nabetani, A.; Oike, Y.; Matsubara, H.; et al. A crucial role for adipose tissue p53 in the regulation of insulin resistance. *Nature Med.* **2009**, *15* (9), 1082-1087.
170. Childs, B. G.; Durik, M.; Baker, D. J.; van Deursen, J. M. Cellular senescence in aging and age-related disease: from mechanisms to therapy. *Nat. Med.* **2015**, *21* (12), 1424-1435.

171. Yang, G.; Rosen, D. G.; Zhang, Z.; Bast, R. C.; Mills, G. B.; Colacino, J. A.; Mercado-Uribe, I.; Liu, J. The chemokine growth-regulated oncogene 1 (Gro-1) links RAS signaling to the senescence of stromal fibroblasts and ovarian tumorigenesis. *Proc. Natl. Acad. Sci. USA* **2006**, *103* (44), 16472-16477.
172. Alimirah, F.; Pulido, T.; Valdovinos, A.; Alptekin, S.; Chang, E.; Jones, E.; Diaz, D. A.; Flores, J.; Velarde, M. C.; Demaria, M.; et al. Cellular Senescence Promotes Skin Carcinogenesis through p38MAPK and p44/42MAPK Signaling. *Cancer Res.* **2020**, *80* (17), 3606-3619.
173. Gonçalves, S.; Yin, K.; Ito, Y.; Chan, A.; Olan, I.; Gough, S.; Cassidy, L.; Serrao, E.; Smith, S.; Young, A.; et al. COX2 regulates senescence secretome composition and senescence surveillance through PGE_2. *Cell Rep.* **2021**, *34* (11), 108860.
174. Okamura, K.; Suzuki, T.; Nohara, K. Gestational arsenite exposure augments hepatic tumors of C3H mice by promoting senescence in F1 and F2 offspring via different pathways. *Toxicol. Appl. Pharmacol.* **2020**, *408*, 115259.
175. Krtolica, A.; Parrinello, S.; Lockett, S.; Desprez, P. Y.; Campisi, J. Senescent fibroblasts promote epithelial cell growth and tumorigenesis: a link between cancer and aging. *Proc. Natl. Acad. Sci. USA* **2001**, *98* (21), 12072-12077.
176. Coppé, J. P.; Kauser, K.; Campisi, J.; Beauséjour, C. M. Secretion of vascular endothelial growth factor by primary human fibroblasts at senescence. *J. Biol. Chem.* **2006**, *281* (40), 29568-29574.
177. Yoshimoto, S.; Loo, T. M.; Atarashi, K.; Kanda, H.; Sato, S.; Oyadomari, S.; Iwakura, Y.; Oshima, K.; Morita, H.; Hattori, M.; et al. Obesity-induced gut microbial metabolite promotes liver cancer through senescence secretome. *Nature* **2013**, *499* (7456), 97-101.
178. Di Mitri, D.; Toso, A.; Chen, J. J.; Sarti, M.; Pinton, S.; Jost, T. R.; D'Antuono, R.; Montani, E.; Garcia-Escudero, R.; Guccini, I.; et al. Tumour-infiltrating Gr-1+ myeloid cells antagonize senescence in cancer. *Nature* **2014**, *515* (7525), 134-137.
179. Eggert, T.; Wolter, K.; Ji, J.; Ma, C.; Yevsa, T.; Klotz, S.; Medina-Echeverz, J.; Longerich, T.; Forgues, M.; Reisinger, F.; et al. Distinct Functions of Senescence-Associated Immune Responses in Liver Tumor Surveillance and Tumor Progression. *Cancer Cell* **2016**, *30* (4), 533-547.
180. Demaria, M.; O'Leary, M. N.; Chang, J.; Shao, L.; Liu, S.; Alimirah, F.; Koenig, K.; Le, C.; Mitin, N.; Deal, A. M.; et al. Cellular Senescence Promotes Adverse Effects of Chemotherapy and Cancer Relapse. *Cancer Discov.* **2017**, *7* (2), 165-176.

181. Kim, Y. H.; Choi, Y. W.; Lee, J.; Soh, E. Y.; Kim, J. H.; Park, T. J. Senescent tumor cells lead the collective invasion in thyroid cancer. *Nat. Commun.* **2017**, *8*, 15208.
182. Chen, F.; Long, Q.; Fu, D.; Zhu, D.; Ji, Y.; Han, L.; Zhang, B.; Xu, Q.; Liu, B.; Li, Y.; et al. Targeting SPINK1 in the damaged tumour microenvironment alleviates therapeutic resistance. *Nat. Commun.* **2018**, *9* (1), 4315.
183. Ruhland, M. K.; Loza, A. J.; Capietto, A. H.; Luo, X.; Knolhoff, B. L.; Flanagan, K. C.; Belt, B. A.; Alspach, E.; Leahy, K.; Luo, J.; et al. Stromal senescence establishes an immunosuppressive microenvironment that drives tumorigenesis. *Nat. Commun.* **2016**, *7*, 11762.
184. Schmitt, C. A.; Wang, B.; Demaria, M. Senescence and cancer — role and therapeutic opportunities. *Nat. Rev. Clin. Oncol.* **2022**, *19* (10), 619-636.
185. von Bartheld, C. S.; Bahney, J.; Herculano-Houzel, S. The search for true numbers of neurons and glial cells in the human brain: A review of 150 years of cell counting. *J. Comp. Neurol.* **2016**, *524* (18), 3865-3895.
186. Herbig, U.; Jobling, W. A.; Chen, B. P. C.; Chen, D. J.; Sedivy, J. M. Telomere Shortening Triggers Senescence of Human Cells through a Pathway Involving ATM, p53, and $p21^{CIP1}$, but Not $p16^{INK4a}$. *Mol. Cell* **2004**, *14* (4), 501-513.
187. Sedelnikova, O. A.; Horikawa, I.; Zimonjic, D. B.; Popescu, N. C.; Bonner, W. M.; Barrett, J. C. Senescing human cells and ageing mice accumulate DNA lesions with unrepairable double-strand breaks. *Nat. Cell Biol.* **2004**, *6* (2), 168-170.
188. Jurk, D.; Wang, C.; Miwa, S.; Maddick, M.; Korolchuk, V.; Tsolou, A.; Gonos, E. S.; Thrasivoulou, C.; Jill Saffrey, M.; Cameron, K.; et al. Postmitotic neurons develop a p21-dependent senescence-like phenotype driven by a DNA damage response. *Aging Cell* **2012**, *11* (6), 996-1004.
189. Pertusa, M.; García-Matas, S.; Rodríguez-Farré, E.; Sanfeliu, C.; Cristòfol, R. Astrocytes aged in vitro show a decreased neuroprotective capacity. *J. Neurochem.* **2007**, *101* (3), 794-805.
190. Mansour, H.; Chamberlain, C. G.; Weible Ii, M. W.; Hughes, S.; Chu, Y.; Chan-Ling, T. Aging-related changes in astrocytes in the rat retina: imbalance between cell proliferation and cell death reduces astrocyte availability. *Aging Cell* **2008**, *7* (4), 526-540.
191. Salminen, A.; Ojala, J.; Kaarniranta, K.; Haapasalo, A.; Hiltunen, M.; Soininen, H. Astrocytes in the aging brain express characteristics of senescence-associated secretory phenotype. *Eur. J. Neurosci.* **2011**, *34* (1), 3-11.

192. Bitto, A.; Sell, C.; Crowe, E.; Lorenzini, A.; Malaguti, M.; Hrelia, S.; Torres, C. Stress-induced senescence in human and rodent astrocytes. *Exp. Cell Res.* **2010**, *316* (17), 2961-2968.
193. Evans, R. J.; Wyllie, F. S.; Wynford-Thomas, D.; Kipling, D.; Jones, C. J. A P53-dependent, Telomere-independent Proliferative Life Span Barrier in Human Astrocytes Consistent with the Molecular Genetics of Glioma Development. *Cancer Res.* **2003**, *63* (16), 4854-4861.
194. Flanary, B. E.; Streit, W. J. Progressive telomere shortening occurs in cultured rat microglia, but not astrocytes. *Glia* **2004**, *45* (1), 75-88.
195. Flanary, B. E.; Sammons, N. W.; Nguyen, C.; Walker, D.; Streit, W. J. Evidence That Aging And Amyloid Promote Microglial Cell Senescence. *Rejuvenation Res.* **2007**, *10* (1), 61-74.
196. Al-Mashhadi, S.; Simpson, J. E.; Heath, P. R.; Dickman, M.; Forster, G.; Matthews, F. E.; Brayne, C.; Ince, P. G.; Wharton, S. B.; Medical Research Council Cognitive Function and Ageing, S. Oxidative Glial Cell Damage Associated with White Matter Lesions in the Aging Human Brain. *Brain Pathol.* **2015**, *25* (5), 565-574.
197. Donnini, S.; Solito, R.; Cetti, E.; Corti, F.; Giachetti, A.; Carra, S.; Beltrame, M.; Cotelli, F.; Ziche, M. Aß peptides accelerate the senescence of endothelial cells in vitro and in vivo, impairing angiogenesis. *FASEB J.* **2010**, *24* (7), 2385-2395.
198. Ferrón, S.; Mira, H.; Franco, S.; Cano-Jaimez, M.; Bellmunt, E.; Ramírez, C.; Fariñas, I.; Blasco, M. a. A. Telomere shortening and chromosomal instability abrogates proliferation of adult but not embryonic neural stem cells. *Development* **2004**, *131* (16), 4059-4070.
199. He, N.; Jin, W. L.; Lok, K. H.; Wang, Y.; Yin, M.; Wang, Z. J. Amyloid-β1–42 oligomer accelerates senescence in adult hippocampal neural stem/progenitor cells via formylpeptide receptor 2. *Cell Death Dis.* **2013**, *4* (11), e924-e924.
200. Li, W.-Q.; Wang, Z.-j.; Liu, S.; Hu, Y.; Yin, M.; Lu, Y. N-Stearoyl-L-Tyrosine Inhibits the Senescence of Neural Stem/Progenitor Cells Induced by $A\beta_{1-42}$ via the CB2 Receptor. *Stem Cells Int.* **2016**, *2016*, 7419389.
201. Streit, W. J.; Braak, H.; Xue, Q.-S.; Bechmann, I. Dystrophic (senescent) rather than activated microglial cells are associated with tau pathology and likely precede neurodegeneration in Alzheimer's disease. *Acta Neuropathol.* **2009**, *118* (4), 475-485.

202. Streit, W. J.; Sammons, N. W.; Kuhns, A. J.; Sparks, D. L. Dystrophic microglia in the aging human brain. *Glia* **2004**, *45* (2), 208-212.
203. Conde, J. R.; Streit, W. J. Microglia in the Aging Brain. *J. Neuropathol. Exp. Neurol.* **2006**, *65* (3), 199-203.
204. Bhat, R.; Crowe, E. P.; Bitto, A.; Moh, M.; Katsetos, C. D.; Garcia, F. U.; Johnson, F. B.; Trojanowski, J. Q.; Sell, C.; Torres, C. Astrocyte Senescence as a Component of Alzheimer's Disease. *PLOS ONE* **2012**, *7* (9), e45069.
205. Nasrabady, S. E.; Rizvi, B.; Goldman, J. E.; Brickman, A. M. White matter changes in Alzheimer's disease: a focus on myelin and oligodendrocytes. *Acta Neuropathol. Commun.* **2018**, *6* (1), 22.
206. Biron-Shental, T.; Liberman, M.; Sharvit, M.; Sukenik-Halevy, R.; Amiel, A. Amniocytes from aneuploidy embryos have enhanced random aneuploidy and signs of senescence — Can these findings be related to medical problems? *Gene* **2015**, *562* (2), 232-235.
207. Martínez-Cué, C.; Rueda, N. Cellular Senescence in Neurodegenerative Diseases. *Front. Cell. Neurosci.* **2020**, *14*, 16.
208. Sikora, E.; Bielak-Zmijewska, A.; Dudkowska, M.; Krzystyniak, A.; Mosieniak, G.; Wesierska, M.; Wlodarczyk, J. Cellular Senescence in Brain Aging. *Front. Aging Neurosci.* **2021**, *13*, 646924.
209. Dong, W.; Cheng, S.; Huang, F.; Fan, W.; Chen, Y.; Shi, H.; He, H. Mitochondrial dysfunction in long-term neuronal cultures mimics changes with aging. *Med. Sci. Monit.* **2011**, *17* (4), Br91-96.
210. Bhanu, M. U.; Mandraju, R. K.; Bhaskar, C.; Kondapi, A. K. Cultured cerebellar granule neurons as an in vitro aging model: topoisomerase IIβ as an additional biomarker in DNA repair and aging. *Toxicol. in Vitro* **2010**, *24* (7), 1935-1945.
211. Ishikawa, S.; Ishikawa, F. Proteostasis failure and cellular senescence in long-term cultured postmitotic rat neurons. *Aging Cell* **2020**, *19* (1), e13071.
212. Wong, E. S. M.; Le Guezennec, X.; Demidov, O. N.; Marshall, N. T.; Wang, S. T.; Krishnamurthy, J.; Sharpless, N. E.; Dunn, N. R.; Bulavin, D. V. p38MAPK Controls Expression of Multiple Cell Cycle Inhibitors and Islet Proliferation with Advancing Age. *Dev. Cell* **2009**, *17* (1), 142-149.
213. Si, Z.; Sun, L.; Wang, X. Evidence and perspectives of cell senescence in neurodegenerative diseases. *Biomed. Pharmacother.* **2021**, *137*, 111327.

214. Hayakawa, K.; Esposito, E.; Wang, X.; Terasaki, Y.; Liu, Y.; Xing, C.; Ji, X.; Lo, E. H. Transfer of mitochondria from astrocytes to neurons after stroke. *Nature* **2016**, *535* (7613), 551-555.
215. Tasdemir-Yilmaz, O. E.; Freeman, M. R. Astrocytes engage unique molecular programs to engulf pruned neuronal debris from distinct subsets of neurons. *Genes Dev.* **2014**, *28* (1), 20-33.
216. Takano, T.; Oberheim, N.; Cotrina, M. L.; Nedergaard, M. Astrocytes and ischemic injury. *Stroke* **2009**, *40* (3 Suppl), S8-12.
217. Rachmian, N.; Krizhanovsky, V. Senescent cells in the brain and where to find them. *FEBS J.* **2023**, *290* (5), 1256-1266.
218. Colonna, M.; Butovsky, O. Microglia Function in the Central Nervous System During Health and Neurodegeneration. *Annu. Rev. Immunol.* **2017**, *35*, 441-468.
219. Lull, M. E.; Block, M. L. Microglial Activation and Chronic Neurodegeneration. *Neurotherapeutics* **2010**, *7* (4), 354-365.
220. Damani, M. R.; Zhao, L.; Fontainhas, A. M.; Amaral, J.; Fariss, R. N.; Wong, W. T. Age-related alterations in the dynamic behavior of microglia. *Aging Cell* **2011**, *10* (2), 263-276.
221. Greenwood, E. K.; Brown, D. R. Senescent Microglia: The Key to the Ageing Brain? *Int. J. Mol. Sci.* **2021**, *22* (9), 4402.
222. Wong, W. T. Microglial aging in the healthy CNS: phenotypes, drivers, and rejuvenation. *Front. Cell. Neurosci.* **2013**, *7*, 22.
223. Lupo, G.; Gaetani, S.; Cacci, E.; Biagioni, S.; Negri, R. Molecular Signatures of the Aging Brain: Finding the Links Between Genes and Phenotypes. *Neurotherapeutics* **2019**, *16* (3), 543-553.
224. Sams, E. C. Oligodendrocytes in the aging brain. *Neuronal Signal.* **2021**, *5* (3), Ns20210008.
225. Tse, K.-H.; Herrup, K. DNA damage in the oligodendrocyte lineage and its role in brain aging. *Mech. Ageing Dev.* **2017**, *161*, 37-50.
226. Burton, D. G. A.; Stolzing, A. Cellular senescence: Immunosurveillance and future immunotherapy. *Ageing Res. Rev.* **2018**, *43*, 17-25.
227. Justice, J. N.; Gregory, H.; Tchkonia, T.; LeBrasseur, N. K.; Kirkland, J. L.; Kritchevsky, S. B.; Nicklas, B. J. Cellular Senescence Biomarker p16INK4a+ Cell Burden in Thigh

Adipose is Associated With Poor Physical Function in Older Women. *J. Geront.: Series A* **2018**, *73* (7), 939-945.

228. Gasek, N. S.; Kuchel, G. A.; Kirkland, J. L.; Xu, M. Strategies for targeting senescent cells in human disease. *Nat. Aging* **2021**, *1* (10), 870-879.
229. Amor, C.; Feucht, J.; Leibold, J.; Ho, Y.-J.; Zhu, C.; Alonso-Curbelo, D.; Mansilla-Soto, J.; Boyer, J. A.; Li, X.; Giavridis, T.; et al. Senolytic CAR T cells reverse senescence-associated pathologies. *Nature* **2020**, *583* (7814), 127-132.
230. Zhai, B.-T.; Tian, H.; Sun, J.; Zou, J.-B.; Zhang, X.-F.; Cheng, J.-X.; Shi, Y.-J.; Fan, Y.; Guo, D.-Y. Urokinase-type plasminogen activator receptor (uPAR) as a therapeutic target in cancer. *J. Trans. Med.* **2022**, *20* (1), 135.
231. Tavassoly, I.; Parmar, J.; Shajahan-Haq, A. N.; Clarke, R.; Baumann, W. T.; Tyson, J. J. Dynamic Modeling of the Interaction Between Autophagy and Apoptosis in Mammalian Cells. *CPT: Pharmacometrics Syst. Pharmacol.* **2015**, *4* (4), 263-272.
232. Nogueira-Recalde, U.; Lorenzo-Gómez, I.; Blanco, F. J.; Loza, M. I.; Grassi, D.; Shirinsky, V.; Shirinsky, I.; Lotz, M.; Robbins, P. D.; Domínguez, E.; et al. Fibrates as drugs with senolytic and autophagic activity for osteoarthritis therapy. *EBioMedicine* **2019**, *45*, 588-605.
233. Bharath, L. P.; Agrawal, M.; McCambridge, G.; Nicholas, D. A.; Hasturk, H.; Liu, J.; Jiang, K.; Liu, R.; Guo, Z.; Deeney, J.; et al. Metformin Enhances Autophagy and Normalizes Mitochondrial Function to Alleviate Aging-Associated Inflammation. *Cell Metabol.* **2020**, *32* (1), 44-55.e46.
234. Kucheryavenko, O.; Nelson, G.; von Zglinicki, T.; Korolchuk, V. I.; Carroll, B. The mTORC1-autophagy pathway is a target for senescent cell elimination. *Biogerontol.* **2019**, *20* (3), 331-335.
235. Wakita, M.; Takahashi, A.; Sano, O.; Loo, T. M.; Imai, Y.; Narukawa, M.; Iwata, H.; Matsudaira, T.; Kawamoto, S.; Ohtani, N.; et al. A BET family protein degrader provokes senolysis by targeting NHEJ and autophagy in senescent cells. *Nat. Commun.* **2020**, *11* (1), 1935.
236. Kang, H. T.; Park, J. T.; Choi, K.; Kim, Y.; Choi, H. J. C.; Jung, C. W.; Lee, Y.-S.; Park, S. C. Chemical screening identifies ATM as a target for alleviating senescence. *Nat. Chem. Biol.* **2017**, *13* (6), 616-623.
237. Cai, Y.; Zhou, H.; Zhu, Y.; Sun, Q.; Ji, Y.; Xue, A.; Wang, Y.; Chen, W.; Yu, X.; Wang, L.; et al. Elimination of senescent cells by β-galactosidase-targeted prodrug attenuates

inflammation and restores physical function in aged mice. *Cell Res.* **2020**, *30* (7), 574-589.

238. Muñoz-Espín, D.; Rovira, M.; Galiana, I.; Giménez, C.; Lozano-Torres, B.; Paez-Ribes, M.; Llanos, S.; Chaib, S.; Muñoz-Martín, M.; Ucero, A. C.; et al. A versatile drug delivery system targeting senescent cells. *EMBO Mol. Med.* **2018**, *10* (9), e9355.
239. Hall, B. M.; Balan, V.; Gleiberman, A. S.; Strom, E.; Krasnov, P.; Virtuoso, L. P.; Rydkina, E.; Vujcic, S.; Balan, K.; Gitlin, I.; et al. Aging of mice is associated with p16(Ink4a)- and β-galactosidase-positive macrophage accumulation that can be induced in young mice by senescent cells. *Aging (Albany NY)* **2016**, *8* (7), 1294-1315.
240. Triana-Martínez, F.; Picallos-Rabina, P.; Da Silva-Álvarez, S.; Pietrocola, F.; Llanos, S.; Rodilla, V.; Soprano, E.; Pedrosa, P.; Ferreirós, A.; Barradas, M.; et al. Identification and characterization of Cardiac Glycosides as senolytic compounds. *Nat. Commun.* **2019**, *10* (1), 4731.
241. Pivovarov, A. S.; Calahorro, F.; Walker, R. J. Na(+)/K(+)-pump and neurotransmitter membrane receptors. *Invert. Neurosci.* **2018**, *19* (1), 1.
242. Guerrero, A.; Herranz, N.; Sun, B.; Wagner, V.; Gallage, S.; Guiho, R.; Wolter, K.; Pombo, J.; Irvine, E. E.; Innes, A. J.; et al. Cardiac glycosides are broad-spectrum senolytics. *Nat. Metabol.* **2019**, *1* (11), 1074-1088.
243. Johmura, Y.; Yamanaka, T.; Omori, S.; Wang, T.-W.; Sugiura, Y.; Matsumoto, M.; Suzuki, N.; Kumamoto, S.; Yamaguchi, K.; Hatakeyama, S.; et al. Senolysis by glutaminolysis inhibition ameliorates various age-associated disorders. *Science* **2021**, *371* (6526), 265-270.
244. Zhu, Y.; Tchkonia, T.; Pirtskhalava, T.; Gower, A. C.; Ding, H.; Giorgadze, N.; Palmer, A. K.; Ikeno, Y.; Hubbard, G. B.; Lenburg, M.; et al. The Achilles' heel of senescent cells: from transcriptome to senolytic drugs. *Aging Cell* **2015**, *14* (4), 644-658.
245. Tchkonia, T.; Morbeck, D. E.; Von Zglinicki, T.; Van Deursen, J.; Lustgarten, J.; Scrable, H.; Khosla, S.; Jensen, M. D.; Kirkland, J. L. Fat tissue, aging, and cellular senescence. *Aging Cell* **2010**, *9* (5), 667-684.
246. Fuhrmann-Stroissnigg, H.; Ling, Y. Y.; Zhao, J.; McGowan, S. J.; Zhu, Y.; Brooks, R. W.; Grassi, D.; Gregg, S. Q.; Stripay, J. L.; Dorronsoro, A.; et al. Identification of HSP90 inhibitors as a novel class of senolytics. *Nat. Commun.* **2017**, *8* (1), 422.

247. He, Y.; Sun, M. M.; Zhang, G. G.; Yang, J.; Chen, K. S.; Xu, W. W.; Li, B. Targeting PI3K/Akt signal transduction for cancer therapy. *Signal Transduct. Target. Ther.* **2021**, *6* (1), 425.

248. Hemmings, B. A.; Restuccia, D. F. PI3K-PKB/Akt pathway. *Cold Spring Harb. Perspect. Biol.* **2012**, *4* (9), a011189.

249. Thorpe, L. M.; Yuzugullu, H.; Zhao, J. J. PI3K in cancer: divergent roles of isoforms, modes of activation and therapeutic targeting. *Nat. Rev. Cancer* **2015**, *15* (1), 7-24.

250. Hanker, A. B.; Kaklamani, V.; Arteaga, C. L. Challenges for the Clinical Development of PI3K Inhibitors: Strategies to Improve Their Impact in Solid Tumors. *Cancer Discov.* **2019**, *9* (4), 482-491.

251. Manning, B. D.; Cantley, L. C. AKT/PKB Signaling: Navigating Downstream. *Cell* **2007**, *129* (7), 1261-1274.

252. Liu, S.; Liu, S.; Wang, X.; Zhou, J.; Cao, Y.; Wang, F.; Duan, E. The PI3K-Akt pathway inhibits senescence and promotes self-renewal of human skin-derived precursors in vitro. *Aging Cell* **2011**, *10* (4), 661-674.

253. Kregel, K. C. Heat shock proteins: modifying factors in physiological stress responses and acquired thermotolerance. *J. Appl. Physiol. (1985)* **2002**, *92* (5), 2177-2186.

254. Fuhrmann-Stroissnigg, H.; Niedernhofer, L. J.; Robbins, P. D. Hsp90 inhibitors as senolytic drugs to extend healthy aging. *Cell Cycle* **2018**, *17* (9), 1048-1055.

255. Taipale, M.; Jarosz, D. F.; Lindquist, S. HSP90 at the hub of protein homeostasis: emerging mechanistic insights. *Nat. Rev. Mol. Cell Biol.* **2010**, *11* (7), 515-528.

256. Fuhrmann-Stroissnigg, H.; Ling, Y. Y.; Zhao, J.; McGowan, S. J.; Zhu, Y.; Brooks, R. W.; Grassi, D.; Gregg, S. Q.; Stripay, J. L.; Dorronsoro, A.; et al. Identification of HSP90 inhibitors as a novel class of senolytics. *Nat. Commun.* **2017**, *8* (1), 422.

257. Sato, S.; Fujita, N.; Tsuruo, T. Modulation of Akt kinase activity by binding to Hsp90. *Proc. Natl. Acad. Sci. USA* **2000**, *97* (20), 10832-10837.

258. Pennisi, R.; Ascenzi, P.; di Masi, A. Hsp90: A New Player in DNA Repair? *Biomolecules* **2015**, *5* (4), 2589-2618.

259. Stecklein, S. R.; Kumaraswamy, E.; Behbod, F.; Wang, W.; Chaguturu, V.; Harlan-Williams, L. M.; Jensen, R. A. BRCA1 and HSP90 cooperate in homologous and non-homologous DNA double-strand-break repair and G2/M checkpoint activation. *Proc. Natl. Acad. Sci. USA* **2012**, *109* (34), 13650-13655.

260. Noguchi, M.; Yu, D.; Hirayama, R.; Ninomiya, Y.; Sekine, E.; Kubota, N.; Ando, K.; Okayasu, R. Inhibition of homologous recombination repair in irradiated tumor cells pretreated with Hsp90 inhibitor 17-allylamino-17-demethoxygeldanamycin. *Biochem. Biophys. Res. Commun.* **2006**, *351* (3), 658-663.
261. Tilstra, J. S.; Robinson, A. R.; Wang, J.; Gregg, S. Q.; Clauson, C. L.; Reay, D. P.; Nasto, L. A.; St Croix, C. M.; Usas, A.; Vo, N.; et al. NF-κB inhibition delays DNA damage-induced senescence and aging in mice. *J. Clin. Invest.* **2012**, *122* (7), 2601-2612.
262. Maximova, A.; Werry, E. L.; Kassiou, M. Senolytics: A Novel Strategy for Neuroprotection in ALS? *Int. J. Mol. Sci.* **2021**; Vol. 22(21): 12078
263. Chilosi, M.; Carloni, A.; Rossi, A.; Poletti, V. Premature lung aging and cellular senescence in the pathogenesis of idiopathic pulmonary fibrosis and COPD/emphysema. *Transl. Res.* **2013**, *162* (3), 156-173.
264. Rossignol, P.; Luttun, A.; Martin-Ventura, J. L.; Lupu, F.; Carmeliet, P.; Collen, D.; Anglès-Cano, E.; Lijnen, H. R. Plasminogen activation: a mediator of vascular smooth muscle cell apoptosis in atherosclerotic plaques. *J. Thromb. Haemost.* **2006**, *4* (3), 664-670.
265. Reijerkerk, A.; Mosnier, L. O.; Kranenburg, O.; Bouma, B. N.; Carmeliet, P.; Drixler, T.; Meijers, J. C.; Voest, E. E.; Gebbink, M. F. Amyloid endostatin induces endothelial cell detachment by stimulation of the plasminogen activation system. *Mol. Cancer. Res.* **2003**, *1* (8), 561-568.
266. Lindstedt, K. A.; Leskinen, M. J.; Kovanen, P. T. Proteolysis of the pericellular matrix: a novel element determining cell survival and death in the pathogenesis of plaque erosion and rupture. *Arterioscler. Thromb. Vasc. Biol.* **2004**, *24* (8), 1350-1358.
267. Porter, A. G.; Jänicke, R. U. Emerging roles of caspase-3 in apoptosis. *Cell Death Differ* **1999**, *6* (2), 99-104.
268. Balsara, R. D.; Castellino, F. J.; Ploplis, V. A. A novel function of plasminogen activator inhibitor-1 in modulation of the AKT pathway in wild-type and plasminogen activator inhibitor-1-deficient endothelial cells. *J. Biol. Chem.* **2006**, *281* (32), 22527-22536.
269. Fernández Pérez, E. R.; Daniels, C. E.; St. Sauver, J.; Hartman, T. E.; Bartholmai, B. J.; Yi, E. S.; Ryu, J. H.; Schroeder, D. R. Incidence, Prevalence, and Clinical Course of Idiopathic Pulmonary Fibrosis: A Population-Based Study. *CHEST* **2010**, *137* (1), 129-137.

270. Eren, M.; Boe, A. E.; Klyachko, E. A.; Vaughan, D. E. Role of Plasminogen Activator Inhibitor-1 in Senescence and Aging. *Semin. Thromb. Hemost.* **2014**, *40* (06), 645-651.
271. Eren, M.; Boe, A. E.; Murphy, S. B.; Place, A. T.; Nagpal, V.; Morales-Nebreda, L.; Urich, D.; Quaggin, S. E.; Budinger, G. R. S.; Mutlu, G. M.; et al. PAI-1–regulated extracellular proteolysis governs senescence and survival in Klotho mice. *Proc. Natl. Acad. Sci. USA* **2014**, *111* (19), 7090-7095.
272. Ghosh, A. K.; Rai, R.; Park, K. E.; Eren, M.; Miyata, T.; Wilsbacher, L. D.; Vaughan, D. E. A small molecule inhibitor of PAI-1 protects against doxorubicin-induced cellular senescence. *Oncotarget* **2016**, *7*, 72443-72457.
273. Schneider, D. J.; Chen, Y.; Sobel, B. E. The effect of plasminogen activator inhibitor type 1 on apoptosis. *Thromb. Haemost.* **2008**, *100* (12), 1037-1040.
274. Negulescu, A.-M.; Mehlen, P. Dependence receptors – the dark side awakens. *FEBS J.* **2018**, *285* (21), 3909-3924.
275. Rabizadeh, S.; Oh, J.; Zhong, L. T.; Yang, J.; Bitler, C. M.; Butcher, L. L.; Bredesen, D. E. Induction of apoptosis by the low-affinity NGF receptor. *Science* **1993**, *261* (5119), 345-348.
276. Lomonosova, E.; Chinnadurai, G. BH3-only proteins in apoptosis and beyond: an overview. *Oncogene* **2008**, *27* (1), S2-S19.
277. Kale, J.; Osterlund, E. J.; Andrews, D. W. BCL-2 family proteins: changing partners in the dance towards death. *Cell Death Differ.* **2018**, *25* (1), 65-80.
278. Shamas-Din, A.; Kale, J.; Leber, B.; Andrews, D. W. Mechanisms of action of Bcl-2 family proteins. *Cold Spring Harb. Perspect. Biol.* **2013**, *5* (4), a008714.
279. Moldoveanu, T.; Grace, C. R.; Llambi, F.; Nourse, A.; Fitzgerald, P.; Gehring, K.; Kriwacki, R. W.; Green, D. R. BID-induced structural changes in BAK promote apoptosis. *Nat. Struct. Mol. Biol.* **2013**, *20* (5), 589-597.
280. Czabotar, Peter E.; Westphal, D.; Dewson, G.; Ma, S.; Hockings, C.; Fairlie, W. D.; Lee, Erinna F.; Yao, S.; Robin, Adeline Y.; Smith, Brian J.; et al. Bax Crystal Structures Reveal How BH3 Domains Activate Bax and Nucleate Its Oligomerization to Induce Apoptosis. *Cell* **2013**, *152* (3), 519-531.
281. Tait, S. W. G.; Green, D. R. Mitochondria and cell death: outer membrane permeabilization and beyond. *Nat. Rev. Mol. Cell Biol.* **2010**, *11* (9), 621-632.
282. Petros, A. M.; Nettesheim, D. G.; Wang, Y.; Olejniczak, E. T.; Meadows, R. P.; Mack, J.; Swift, K.; Matayoshi, E. D.; Zhang, H.; Fesik, S. W.; et al. Rationale for Bcl-XL/Bad

peptide complex formation from structure, mutagenesis, and biophysical studies. *Protein Sci.* **2000**, *9* (12), 2528-2534.

283. Zhu, Y.; Tchkonia, T.; Fuhrmann-Stroissnigg, H.; Dai, H. M.; Ling, Y. Y.; Stout, M. B.; Pirtskhalava, T.; Giorgadze, N.; Johnson, K. O.; Giles, C. B.; et al. Identification of a novel senolytic agent, navitoclax, targeting the Bcl-2 family of anti-apoptotic factors. *Aging Cell* **2016**, *15* (3), 428-435.
284. Martin, N.; Popgeorgiev, N.; Ichim, G.; Bernard, D. BCL-2 proteins in senescence: beyond a simple target for senolysis? *Nat. Rev. Mol. Cell Biol.* **2023**, *24* (8), 517-518.
285. Zhang, L.; Pitcher, L. E.; Prahalad, V.; Niedernhofer, L. J.; Robbins, P. D. Targeting cellular senescence with senotherapeutics: senolytics and senomorphics. *FEBS J.* **2023**, *290* (5), 1362-1383.
286. Song, S.; Tchkonia, T.; Jiang, J.; Kirkland, J. L.; Sun, Y. Targeting Senescent Cells for a Healthier Aging: Challenges and Opportunities. *Adv. Sci.* **2020**, *7* (23), 2002611.
287. Lagoumtzi, S. M.; Chondrogianni, N. Senolytics and senomorphics: Natural and synthetic therapeutics in the treatment of aging and chronic diseases. *Free Radic. Biol. Med.* **2021**, *171*, 169-190.
288. Yang, X.-D.; Corvalan, J. R. F.; Wang, P.; Roy, C. M. N.; Davis, C. G. Fully human anti-interleukin-8 monoclonal antibodies: potential therapeutics for the treatment of inflammatory disease states. *J. Leukoc. Biol.* **1999**, *66* (3), 401-410.
289. Laberge, R.-M.; Sun, Y.; Orjalo, A. V.; Patil, C. K.; Freund, A.; Zhou, L.; Curran, Samuel C.; Davalos, A. R.; Wilson-Edell, K. A.; Liu, S.; et al. MTOR regulates the pro-tumorigenic senescence-associated secretory phenotype by promoting IL1A translation. *Nat. Cell Biol.* **2015**, *17* (8), 1049-1061.
290. Harrison, D. E.; Strong, R.; Sharp, Z. D.; Nelson, J. F.; Astle, C. M.; Flurkey, K.; Nadon, N. L.; Wilkinson, J. E.; Frenkel, K.; Carter, C. S.; et al. Rapamycin fed late in life extends lifespan in genetically heterogeneous mice. *Nature* **2009**, *460* (7253), 392-395.
291. Correia-Melo, C.; Birch, J.; Fielder, E.; Rahmatika, D.; Taylor, J.; Chapman, J.; Lagnado, A.; Carroll, B. M.; Miwa, S.; Richardson, G.; et al. Rapamycin improves healthspan but not inflammaging in nfκb1−/− mice. *Aging Cell* **2019**, *18* (1), e12882.
292. Szaniawski, M. A.; Spivak, A. M. Senotherapeutics and HIV-1 Persistence. *Curr. HIV/AIDS Rep.* **2020**, *17* (3), 219-225.

293. Al-Khayri, J. M.; Sahana, G. R.; Nagella, P.; Joseph, B. V.; Alessa, F. M.; Al-Mssallem, M. Q. Flavonoids as Potential Anti-Inflammatory Molecules: A Review. *Molecules* **2022**, *27* (9), 2901.
294. Panche, A. N.; Diwan, A. D.; Chandra, S. R. Flavonoids: an overview. *J. Nutr. Sci.* **2016**, *5*, e47.
295. Xu, L.; Botchway, B. O. A.; Zhang, S.; Zhou, J.; Liu, X. Inhibition of NF-κB Signaling Pathway by Resveratrol Improves Spinal Cord Injury. *Front. Neurosci.* **2018**, *12*, 690.
296. Chien, Y.; Scuoppo, C.; Wang, X.; Fang, X.; Balgley, B.; Bolden, J. E.; Premsrirut, P.; Luo, W.; Chicas, A.; Lee, C. S.; et al. Control of the senescence-associated secretory phenotype by NF-κB promotes senescence and enhances chemosensitivity. *Genes Dev.* **2011**, *25* (20), 2125-2136.
297. Menicacci, B.; Laurenzana, A.; Chillà, A.; Margheri, F.; Peppicelli, S.; Tanganelli, E.; Fibbi, G.; Giovannelli, L.; Del Rosso, M.; Mocali, A. Chronic Resveratrol Treatment Inhibits MRC5 Fibroblast SASP-Related Protumoral Effects on Melanoma Cells. *J. Gerontol: Series A* **2017**, *72* (9), 1187-1195.
298. Menicacci, B.; Margheri, F.; Laurenzana, A.; Chillà, A.; Del Rosso, M.; Giovannelli, L.; Fibbi, G.; Mocali, A. Chronic Resveratrol Treatment Reduces the Pro-angiogenic Effect of Human Fibroblast "Senescent-Associated Secretory Phenotype" on Endothelial Colony-Forming Cells: The Role of IL8. *J. Gerontol: Series A* **2019**, *74* (5), 625-633.
299. Lim, H.; Park, H.; Kim, H. P. Effects of flavonoids on senescence-associated secretory phenotype formation from bleomycin-induced senescence in BJ fibroblasts. *Biochem. Pharmacol.* **2015**, *96* (4), 337-348.
300. Lee, Y. R.; Cho, H. M.; Park, E. J.; Zhang, M.; Doan, T. P.; Lee, B. W.; Cho, K. A.; Oh, W. K. Metabolite Profiling of Rambutan (*Nephelium lappaceum*) Seeds Using UPLC-qTOF-MS/MS and Senomorphic Effects in Aged Human Dermal Fibroblasts. *Nutrients*, 2020; Vol. 12.
301. Han, D.-W.; Lee, M. H.; Kim, B.; Lee, J. J.; Hyon, S.-H.; Park, J.-C. Preventive Effects of Epigallocatechin-3-O-Gallate against Replicative Senescence Associated with p53 Acetylation in Human Dermal Fibroblasts. *Oxid. Med. Cell. Longev.* **2012**, *2012* (1), 850684.
302. Moiseeva, O.; Deschênes-Simard, X.; St-Germain, E.; Igelmann, S.; Huot, G.; Cadar, A. E.; Bourdeau, V.; Pollak, M. N.; Ferbeyre, G. Metformin inhibits the senescence-

associated secretory phenotype by interfering with IKK/NF-κB activation. *Aging Cell* **2013**, *12* (3), 489-498.

303. Xu, M.; Tchkonia, T.; Ding, H.; Ogrodnik, M.; Lubbers, E. R.; Pirtskhalava, T.; White, T. A.; Johnson, K. O.; Stout, M. B.; Mezera, V.; et al. JAK inhibition alleviates the cellular senescence-associated secretory phenotype and frailty in old age. *Proc. Natl. Acad. Sci. USA* **2015**, *112* (46), E6301-E6310.
304. Kang, C.; Xu, Q.; Martin, T. D.; Li, M. Z.; Demaria, M.; Aron, L.; Lu, T.; Yankner, B. A.; Campisi, J.; Elledge, S. J. The DNA damage response induces inflammation and senescence by inhibiting autophagy of GATA4. *Science* **2015**, *349* (6255), aaa5612.
305. Wang, E. Senescent human fibroblasts resist programmed cell death, and failure to suppress bcl2 is involved. *Cancer Res.* **1995**, *55* (11), 2284-2292.
306. Chen, L. S.; Balakrishnan, K.; Gandhi, V. Inflammation and survival pathways: Chronic lymphocytic leukemia as a model system. *Biochem. Pharmacol.* **2010**, *80* (12), 1936-1945.
307. Bessler, H.; Bergman, M.; Salman, H.; Cohen, A. M.; Fenig, E.; Djaldetti, M. Factor(s) released from irradiated B-CLL cells induce apoptosis in leukemic lymphocytes. *Cancer Lett.* **2002**, *179* (1), 103-108.
308. Chaib, S.; Tchkonia, T.; Kirkland, J. L. Cellular senescence and senolytics: the path to the clinic. *Nat. Med.* **2022**, *28* (8), 1556-1568.
309. Cho, H. J.; Hwang, J. A.; Yang, E. J.; Kim, E. C.; Kim, J. R.; Kim, S. Y.; Kim, Y. Z.; Park, S. C.; Lee, Y. S. Nintedanib induces senolytic effect via STAT3 inhibition. *Cell Death Dis.* **2022**, *13* (9), 760.
310. Cho, H. J.; Yang, E. J.; Park, J. T.; Kim, J. R.; Kim, E. C.; Jung, K. J.; Park, S. C.; Lee, Y. S. Identification of SYK inhibitor, R406 as a novel senolytic agent. *Aging (Albany NY)* **2020**, *12* (9), 8221-8240.
311. Kusumoto, D.; Seki, T.; Sawada, H.; Kunitomi, A.; Katsuki, T.; Kimura, M.; Ito, S.; Komuro, J.; Hashimoto, H.; Fukuda, K.; et al. Anti-senescent drug screening by deep learning-based morphology senescence scoring. *Nat. Commun.* **2021**, *12* (1), 257.
312. Fraga, C. G.; Croft, K. D.; Kennedy, D. O.; Tomás-Barberán, F. A. The effects of polyphenols and other bioactives on human health. *Food Funct.* **2019**, *10* (2), 514-528.
313. Zhu, Y.; Doornebal, E. J.; Pirtskhalava, T.; Giorgadze, N.; Wentworth, M.; Fuhrmann-Stroissnigg, H.; Niedernhofer, L. J.; Robbins, P. D.; Tchkonia, T.; Kirkland, J. L. New

agents that target senescent cells: the flavone, fisetin, and the BCL-X(L) inhibitors, A1331852 and A1155463. *Aging (Albany NY)* **2017**, *9* (3), 955-963.

314. Yousefzadeh, M. J.; Zhu, Y.; McGowan, S. J.; Angelini, L.; Fuhrmann-Stroissnigg, H.; Xu, M.; Ling, Y. Y.; Melos, K. I.; Pirtskhalava, T.; Inman, C. L.; et al. Fisetin is a senotherapeutic that extends health and lifespan. *EBioMedicine* **2018**, *36*, 18-28.
315. Li, W.; He, Y.; Zhang, R.; Zheng, G.; Zhou, D. The curcumin analog EF24 is a novel senolytic agent. *Aging (Albany NY)* **2019**, *11* (2), 771-782.
316. Xu, Q.; Fu, Q.; Li, Z.; Liu, H.; Wang, Y.; Lin, X.; He, R.; Zhang, X.; Ju, Z.; Campisi, J.; et al. The flavonoid procyanidin C1 has senotherapeutic activity and increases lifespan in mice. *Nat. Metab.* **2021**, *3* (12), 1706-1726.
317. Moaddel, R.; Rossi, M.; Rodriguez, S.; Munk, R.; Khadeer, M.; Abdelmohsen, K.; Gorospe, M.; Ferrucci, L. Identification of gingerenone A as a novel senolytic compound. *PLoS One* **2022**, *17* (3), e0266135.
318. Wang, Y.; Chang, J.; Liu, X.; Zhang, X.; Zhang, S.; Zhang, X.; Zhou, D.; Zheng, G. Discovery of piperlongumine as a potential novel lead for the development of senolytic agents. *Aging (Albany NY)* **2016**, *8* (11), 2915-2926.
319. Liu, X.; Wang, Y.; Zhang, X.; Gao, Z.; Zhang, S.; Shi, P.; Zhang, X.; Song, L.; Hendrickson, H.; Zhou, D.; et al. Senolytic activity of piperlongumine analogues: Synthesis and biological evaluation. *Bioorg. Med. Chem.* **2018**, *26* (14), 3925-3938.
320. Limbad, C.; Doi, R.; McGirr, J.; Ciotlos, S.; Perez, K.; Clayton, Z. S.; Daya, R.; Seals, D. R.; Campisi, J.; Melov, S. Senolysis induced by 25-hydroxycholesterol targets CRYAB in multiple cell types. *iScience* **2022**, *25* (2), 103848.
321. Go, S.; Kang, M.; Kwon, S. P.; Jung, M.; Jeon, O. H.; Kim, B. S. The Senolytic Drug JQ1 Removes Senescent Cells via Ferroptosis. *J. Tissue Eng. Regen. Med.* **2021**, *18* (5), 841-850.
322. He, Y.; Li, W.; Lv, D.; Zhang, X.; Zhang, X.; Ortiz, Y. T.; Budamagunta, V.; Campisi, J.; Zheng, G.; Zhou, D. Inhibition of USP7 activity selectively eliminates senescent cells in part via restoration of p53 activity. *Aging Cell* **2020**, *19* (3), e13117.
323. Cherif, H.; Bisson, D. G.; Mannarino, M.; Rabau, O.; Ouellet, J. A.; Haglund, L. Senotherapeutic drugs for human intervertebral disc degeneration and low back pain. *Elife* **2020**, *9*, e54693.
324. Fouad, Y. A.; Aanei, C. Revisiting the hallmarks of cancer. *Am. J. Cancer Res.* **2017**, *7* (5), 1016-1036.

325. Yang, D.; Tian, X.; Ye, Y.; Liang, Y.; Zhao, J.; Wu, T.; Lu, N. Identification of GL-V9 as a novel senolytic agent against senescent breast cancer cells. *Life Sci.* **2021**, *272*, 119196.
326. Moore, D. Panobinostat (Farydak): A Novel Option for the Treatment of Relapsed Or Relapsed and Refractory Multiple Myeloma. *Pharm. Ther.* **2016**, *41* (5), 296-300.
327. Ozsvari, B.; Nuttall, J. R.; Sotgia, F.; Lisanti, M. P. Azithromycin and Roxithromycin define a new family of "senolytic" drugs that target senescent human fibroblasts. *Aging (Albany NY)* **2018**, *10* (11), 3294-3307.
328. Chang, J.; Wang, Y.; Shao, L.; Laberge, R. M.; Demaria, M.; Campisi, J.; Janakiraman, K.; Sharpless, N. E.; Ding, S.; Feng, W.; et al. Clearance of senescent cells by ABT263 rejuvenates aged hematopoietic stem cells in mice. *Nat. Med.* **2016**, *22* (1), 78-83.
329. Yosef, R.; Pilpel, N.; Tokarsky-Amiel, R.; Biran, A.; Ovadya, Y.; Cohen, S.; Vadai, E.; Dassa, L.; Shahar, E.; Condiotti, R.; et al. Directed elimination of senescent cells by inhibition of BCL-W and BCL-XL. *Nat. Commun.* **2016**, *7* (1), 11190.
330. Miura, Y.; Endo, K.; Komori, K.; Sekiya, I. Clearance of senescent cells with ABT-263 improves biological functions of synovial mesenchymal stem cells from osteoarthritis patients. *Stem Cell Res. Ther.* **2022**, *13* (1), 222.
331. Troiani, M.; Colucci, M.; D'Ambrosio, M.; Guccini, I.; Pasquini, E.; Varesi, A.; Valdata, A.; Mosole, S.; Revandkar, A.; Attanasio, G.; et al. Single-cell transcriptomics identifies Mcl-1 as a target for senolytic therapy in cancer. *Nat. Commun.* **2022**, *13* (1), 2177.
332. Park, C.-M.; Bruncko, M.; Adickes, J.; Bauch, J.; Ding, H.; Kunzer, A.; Marsh, K. C.; Nimmer, P.; Shoemaker, A. R.; Song, X.; et al. Discovery of an Orally Bioavailable Small Molecule Inhibitor of Prosurvival B-Cell Lymphoma 2 Proteins. *J. Med. Chem.* **2008**, *51* (21), 6902-6915.
333. Bruncko, M.; Oost, T. K.; Belli, B. A.; Ding, H.; Joseph, M. K.; Kunzer, A.; Martineau, D.; McClellan, W. J.; Mitten, M.; Ng, S.-C.; et al. Studies Leading to Potent, Dual Inhibitors of Bcl-2 and Bcl-xL. *J. Med. Chem.* **2007**, *50* (4), 641-662.
334. Petros, A. M.; Dinges, J.; Augeri, D. J.; Baumeister, S. A.; Betebenner, D. A.; Bures, M. G.; Elmore, S. W.; Hajduk, P. J.; Joseph, M. K.; Landis, S. K.; et al. Discovery of a Potent Inhibitor of the Antiapoptotic Protein Bcl-xL from NMR and Parallel Synthesis. *J. Med. Chem.* **2006**, *49* (2), 656-663.
335. Schembri, L. S.; Eriksson, J.; Odell, L. R. Palladium(0)-Catalyzed Carbonylative Synthesis of N-Acylsulfonamides via Regioselective Acylation. *The Journal of Organic Chemistry* **2019**, *84* (11), 6970-6981.

336. Francisco, K. R.; Varricchio, C.; Paniak, T. J.; Kozlowski, M. C.; Brancale, A.; Ballatore, C. Structure property relationships of N-acylsulfonamides and related bioisosteres. *Eur. J. Med. Chem.* **2021**, *218*, 113399.
337. Hansch, C.; Unger, S. H.; Forsythe, A. B. Strategy in drug design. Cluster anlysis as an aid in the selection of substituents. *J. Med. Chem.* **1973**, *16* (11), 1217-1222.
338. Topliss, J. G. A manual method for applying the Hansch approach to drug design. *J. Med. Chem.* **1977**, *20* (4), 463-469
339. Martin, Y. C. Molecular diversity: how we measure it? Has it lived up to its promise? *Il Farmaco* **2001**, *56* (1), 137-139.
340. Brown, R. D.; Martin, Y. C. An evaluation of structural descriptors and clustering methods for use in diversity selection. *SAR QSAR Environ. Res.* **1998**, *8* (1-2), 23-39.
341. Barnard, J. M.; Downs, G. M. Clustering of chemical structures on the basis of two-dimensional similarity measures. *J. Chem. Inf. Comput. Sci.* **1992**, *32* (6), 644-649.
342. Wendt, M. D.; Shen, W.; Kunzer, A.; McClellan, W. J.; Bruncko, M.; Oost, T. K.; Ding, H.; Joseph, M. K.; Zhang, H.; Nimmer, P. M.; et al. Discovery and Structure−Activity Relationship of Antagonists of B-Cell Lymphoma 2 Family Proteins with Chemopotentiation Activity in Vitro and in Vivo. *J. Med. Chem.* **2006**, *49* (3), 1165-1181.
343. Oltersdorf, T.; Elmore, S. W.; Shoemaker, A. R.; Armstrong, R. C.; Augeri, D. J.; Belli, B. A.; Bruncko, M.; Deckwerth, T. L.; Dinges, J.; Hajduk, P. J.; et al. An inhibitor of Bcl-2 family proteins induces regression of solid tumours. *Nature* **2005**, *435* (7042), 677-681.
344. Lobb, K. L.; Hipskind, P. A.; Aikins, J. A.; Alvarez, E.; Cheung, Y.-Y.; Considine, E. L.; De Dios, A.; Durst, G. L.; Ferritto, R.; Grossman, C. S.; et al. Acyl Sulfonamide Anti-Proliferatives: Benzene Substituent Structure−Activity Relationships for a Novel Class of Antitumor Agents. *J. Med. Chem.* **2004**, *47* (22), 5367-5380.
345. Evano, G.; Nitelet, A.; Thilmany, P.; Dewez, D. F. Metal-Mediated Halogen Exchange in Aryl and Vinyl Halides: A Review. *Front. Chem.* **2018**, *6*, 114.
346. Kadam, H. K.; Tilve, S. G. Advancement in methodologies for reduction of nitroarenes. *RSC Adv.* **2015**, *5* (101), 83391-83407.
347. Popat, V. R.; Padhiyar, N. U. Kinetic Study of Bechamp Process for P-Nitrotoluene Reduction to P-Toluidine. *Int. J. Chem. Eng.* **2013**, 401-405.
348. Campbell, C. D.; Stewart, M. I. Reflections on the Teaching Practices for the Reduction of Nitroarenes: Updating Methodologies and Considerations of the Mechanism. *J. Chem. Educ.* **2023**, *100* (9), 3171-3178.

349. Creager, S. 3 - Solvents and Supporting Electrolytes. In *Handbook of Electrochemistry*, Zoski, C. G. Ed.; Elsevier, **2007**; Amsterdam, Netherlands.
350. Chen, J; Ren, Y.; She, J.; Wang, L.; Yu, J.; Zhang, G.; Process for the preparation of N-[(3-aminooxetan-3-yl)methyl]-2-(1,1-dioxo-3,5-dihydro-1,4-benzothiazepin-4-yl)-6-methyl-quinazolin-4-amine, US Patent 20160326160.
351. Katritzky, A. R.; Xu, Y.-J.; He, H.-Y.; Mehta, S. Syntheses of 1,4-Benzothiazepines and 1,4-Benzoxazepines via Cyclizations of 1-[2-Arylthio(oxy)ethyl]-5-benzotriazolyl-2-pyrrolidinones and 3-Benzotriazolyl-2-[2-arylthio(oxy)ethyl]-1-isoindolinones. *J. Org. Chem.* **2001**, *66* (16), 5590-5594.
352. González-Gualda, E.; Baker, A. G.; Fruk, L.; Muñoz-Espín, D. A guide to assessing cellular senescence in vitro and in vivo. *FEBS J.* **2021**, *288* (1), 56-80.
353. Wanka, L.; Iqbal, K.; Schreiner, P. R. The Lipophilic Bullet Hits the Targets: Medicinal Chemistry of Adamantane Derivatives. *Chem. Rev.* **2013**, *113* (5), 3516-3604.
354. Torres, P. H. M.; Sodero, A. C. R.; Jofily, P.; Silva-Jr, F. P. Key Topics in Molecular Docking for Drug Design. *Int. J. Mol. Sci.* **2019**, *20* (18), 4574.
355. Huang, S. Y.; Zou, X. Advances and challenges in protein-ligand docking. *Int. J. Mol. Sci.* **2010**, *11* (8), 3016-3034.
356. Madhavi Sastry, G.; Adzhigirey, M.; Day, T.; Annabhimoju, R.; Sherman, W. Protein and ligand preparation: parameters, protocols, and influence on virtual screening enrichments. *J. Comput. Aided Mol. Des.* **2013**, *27* (3), 221-234.
357. Das, D.R.; Kumar, D.; Kumar, P.; Dash, B.P. Molecular docking and its application in search of antisickling agent from *Carica papaya*, *J. Appl. Biol. Biotech.* **2020**, *8*(1):105-116
358. Kitchen, D. B.; Decornez, H.; Furr, J. R.; Bajorath, J. Docking and scoring in virtual screening for drug discovery: methods and applications. *Nat. Rev. Drug Discov.* **2004**, *3* (11), 935-949.
359. Bajorath, J. Integration of virtual and high-throughput screening. *Nat. Rev. Drug Discov.* **2002**, *1* (11), 882-894.
360. Walters, W. P.; Stahl, M. T.; Murcko, M. A. Virtual screening—an overview. *Drug Discov. Today* **1998**, *3* (4), 160-178.
361. Langer, T.; Hoffmann, D. R. Virtual Screening An Effective Tool for Lead Structure Discovery. *Curr. Pharm. Des.* **2001**, *7* (7), 509-527.

362. Sastry, G. M.; Adzhigirey, M.; Day, T.; Annabhimoju, R.; Sherman, W. Protein and ligand preparation: parameters, protocols, and influence on virtual screening enrichments. *J. Comput. Aided Mol. Des.* **2013**, *27* (3), 221-234.
363. Maestro 13.9, *Schrodinger, Inc*. **2024**, New York, USA.
364. LigPrep, *Schrodinger, Inc*. **2024**, New York, USA.
365. Protein Preparation Wizard, *Schrodinger, Inc*. **2024**, New York, USA.
366. Glide, *Schrodinger, Inc*. **2024**, New York, USA.
367. Halgren, T. A.; Murphy, R. B.; Friesner, R. A.; Beard, H. S.; Frye, L. L.; Pollard, W. T.; Banks, J. L. Glide: A New Approach for Rapid, Accurate Docking and Scoring. 2. Enrichment Factors in Database Screening. *J. Med. Chem.* **2004**, *47* (7), 1750-1759.
368. Meng, X. Y.; Zhang, H. X.; Mezei, M.; Cui, M. Molecular docking: a powerful approach for structure-based drug discovery. *Curr. Comput. Aided Drug Des.* **2011**, *7* (2), 146-157.
369. Warren, G. L.; Andrews, C. W.; Capelli, A.-M.; Clarke, B.; LaLonde, J.; Lambert, M. H.; Lindvall, M.; Nevins, N.; Semus, S. F.; Senger, S.; et al. A Critical Assessment of Docking Programs and Scoring Functions. *J. Med. Chem.* **2006**, *49* (20), 5912-5931.
370. Griffith, W. P.; Ley, S. V.; Whitcombe, G. P.; White, A. D. Preparation and use of tetra-n-butylammonium per-ruthenate (TBAP reagent) and tetra-n-propylammonium per-ruthenate (TPAP reagent) as new catalytic oxidants for alcohols. *J. Chem. Soc. Chem. Commun.* **1987**, (21), 1625-1627.
371. Dess, D. B.; Martin, J. C. Readily accessible 12-I-5 oxidant for the conversion of primary and secondary alcohols to aldehydes and ketones. *J. Org. Chem.* **1983**, *48* (22), 4155-4156.
372. Savignac, P.; Iorga, B.; Savignac, M. 1.16 - One or More CC Bond(s) Formed by Condensation: Condensation of P, As, Sb, Bi, Si, Ge, B, or Metal Functions. In *Comprehensive Organic Functional Group Transformations II*, Katritzky, A. R., Taylor, R. J. K. Eds.; Elsevier, **2005**, Amsterdam, Netherlands.
373. Callis, T. B.; Garrett, T. R.; Montgomery, A. P.; Danon, J. J.; Kassiou, M. Recent Scaffold Hopping Applications in Central Nervous System Drug Discovery. *J. Med. Chem.* **2022**, *65* (20), 13483-13504.
374. Hu, Y.; Stumpfe, D.; Bajorath, J. Recent Advances in Scaffold Hopping. *J. Med. Chem.* **2017**, *60* (4), 1238-1246.

375. Lessene, G.; Czabotar, P. E.; Sleebs, B. E.; Zobel, K.; Lowes, K. N.; Adams, J. M.; Baell, J. B.; Colman, P. M.; Deshayes, K.; Fairbrother, W. J.; et al. Structure-guided design of a selective BCL-XL inhibitor. *Nat. Chem. Biol.* **2013**, *9* (6), 390-397.
376. Sleebs, B. E.; Kersten, W. J. A.; Kulasegaram, S.; Nikolakopoulos, G.; Hatzis, E.; Moss, R. M.; Parisot, J. P.; Yang, H.; Czabotar, P. E.; Fairlie, W. D.; et al. Discovery of Potent and Selective Benzothiazole Hydrazone Inhibitors of Bcl-XL. *J. Med. Chem.* **2013**, *56* (13), 5514-5540.
377. Tian, M.; Peng, Y.; Zheng, J. Metabolic Activation and Hepatotoxicity of Furan-Containing Compounds. *Drug Metab. Dispos.* **2022**, *50* (5), 655.
378. Koehler, M. F. T.; Bergeron, P.; Choo, E. F.; Lau, K.; Ndubaku, C.; Dudley, D.; Gibbons, P.; Sleebs, B. E.; Rye, C. S.; Nikolakopoulos, G.; et al. Structure-Guided Rescaffolding of Selective Antagonists of BCL-XL. *ACS Med. Chem. Lett.* **2014**, *5* (6), 662-667.
379. Schneider, G.; Neidhart, W.; Giller, T.; Schmid, G. "Scaffold-Hopping" by Topological Pharmacophore Search: A Contribution to Virtual Screening. *Angew. Chem. Int. Ed.* **1999**, *38* (19), 2894-2896.
380. Sun, H.; Tawa, G.; Wallqvist, A. Classification of scaffold-hopping approaches. *Drug Discov. Today* **2012**, *17* (7-8), 310-324.
381. Wouters, O. J.; McKee, M.; Luyten, J. Estimated Research and Development Investment Needed to Bring a New Medicine to Market, 2009-2018. *JAMA* **2020**, *323* (9), 844-853.
382. Schneider, G.; Neidhart, W.; Giller, T.; Schmid, G. “Scaffold-Hopping” by Topological Pharmacophore Search: A Contribution to Virtual Screening. *Angew. Chem. Int. Ed.* **1999**, *38* (19), 2894-2896.
383. Kumari, S.; Carmona, A. V.; Tiwari, A. K.; Trippier, P. C. Amide Bond Bioisosteres: Strategies, Synthesis, and Successes. *J. Med. Chem.* **2020**, *63* (21), 12290-12358.
384. Lavey, B. J.; Kozlowski, J. A.; Shankar, B. B.; Spitler, J. M.; Zhou, G.; Yang, D. Y.; Shu, Y.; Wong, M. K.; Wong, S. C.; Shih, N. Y.; et al. Optimization of triaryl bis-sulfones as cannabinoid-2 receptor ligands. *Bioorg. Med. Chem. Lett.* **2007**, *17* (13), 3760-3764.
385. Sun, H. A universal molecular descriptor system for prediction of logP, logS, logBB, and absorption. *J. Chem. Inf. Comput. Sci.* **2004**, *44* (2), 748-757.
386. Ishikawa, M.; Hashimoto, Y. Improvement in aqueous solubility in small molecule drug discovery programs by disruption of molecular planarity and symmetry. *J. Med. Chem.* **2011**, *54* (6), 1539-1554.

387. Vieth, M.; Siegel, M. G.; Higgs, R. E.; Watson, I. A.; Robertson, D. H.; Savin, K. A.; Durst, G. L.; Hipskind, P. A. Characteristic physical properties and structural fragments of marketed oral drugs. *J. Med. Chem.* **2004**, *47* (1), 224-232.

388. Hall, A.; Billinton, A.; Brown, S. H.; Chowdhury, A.; Giblin, G. M. P.; Goldsmith, P.; Hurst, D. N.; Naylor, A.; Patel, S.; Scoccitti, T.; et al. Discovery of a novel indole series of EP1 receptor antagonists by scaffold hopping. *Bioorg. Med. Chem. Lett.* **2008**, *18* (8), 2684-2690.

389. Furet, P.; Caravatti, G.; Guagnano, V.; Lang, M.; Meyer, T.; Schoepfer, J. Entry into a new class of protein kinase inhibitors by pseudo ring design. *Bioorg. Med. Chem. Lett.* **2008**, *18* (3), 897-900.

390. Adessi, C.; Soto, C. Converting a peptide into a drug: strategies to improve stability and bioavailability. *Curr. Med. Chem.* **2002**, *9* (9), 963-978.

391. Rosenström, U.; Sköld, C.; Lindeberg, G.; Botros, M.; Nyberg, F.; Karlén, A.; Hallberg, A. Design, synthesis, and incorporation of a beta-turn mimetic in angiotensin II forming novel pseudopeptides with affinity for AT1 and AT2 receptors. *J. Med. Chem.* **2006**, *49* (20), 6133-6137.

392. Bregman, H.; Simard, J. R.; Andrews, K. L.; Ayube, S.; Chen, H.; Gunaydin, H.; Guzman-Perez, A.; Hu, J.; Huang, L.; Huang, X.; et al. The Discovery and Hit-to-Lead Optimization of Tricyclic Sulfonamides as Potent and Efficacious Potentiators of Glycine Receptors. *J. Med. Chem.* **2017**, *60* (3), 1105-1125.

393. Chakka, N.; Andrews, K. L.; Berry, L. M.; Bregman, H.; Gunaydin, H.; Huang, L.; Guzman-Perez, A.; Plant, M. H.; Simard, J. R.; Gingras, J.; et al. Applications of parallel synthetic lead hopping and pharmacophore-based virtual screening in the discovery of efficient glycine receptor potentiators. *Eur. J. Med. Chem.* **2017**, *137*, 63-75.

394. Spark™ 10.7.1, *Cresset Group*, **2024**, England, UK.

395. Cheeseright, T.; Mackey, M.; Rose, S.; Vinter, A. Molecular Field Extrema as Descriptors of Biological Activity: Definition and Validation. *J. Chem. Inf. Model.* **2006**, *46* (2), 665-676.

396. Meuser, M. E.; Rashad, A. A.; Ozorowski, G.; Dick, A.; Ward, A. B.; Cocklin, S. Field-Based Affinity Optimization of a Novel Azabicyclohexane Scaffold HIV-1 Entry Inhibitor. *Molecules*, **2019**; *24*(8), 1581.

397. Maurya, S.; Jain, A.; Rehman, M. T.; Hakamy, A.; Bantun, F.; AlAjmi, M. F.; Singh, V.; Zehra, A.; Khan, F.; Haque, S.; et al. In Silico Identification of Novel Derivatives of

Rifampicin Targeting Ribonuclease VapC2 of M. tuberculosis H37Rv: Rifampicin Derivatives Target VapC2 of Mtb H37Rv. *Molecules*, **2023**, *28*(4), 1652

398. Ghamari, N.; Kouhi Hargelan, S.; Zivkovic, A.; Leitzbach, L.; Dastmalchi, S.; Stark, H.; Hamzeh-Mivehroud, M. Guided rational design with scaffold hopping leading to novel histamine H3 receptor ligands. *Bioorg. Chem.* **2021**, *117*, 105411.
399. Hillig, R. C.; Sautier, B.; Schroeder, J.; Moosmayer, D.; Hilpmann, A.; Stegmann, C. M.; Werbeck, N. D.; Briem, H.; Boemer, U.; Weiske, J.; et al. Discovery of potent SOS1 inhibitors that block RAS activation via disruption of the RAS–SOS1 interaction. *Proc. Natl. Acad. Sci. USA* **2019**, *116* (7), 2551-2560.
400. Wildman, S. A.; Crippen, G. M. Prediction of Physicochemical Parameters by Atomic Contributions. *J. Chem. Inf. Comput. Sci.* **1999**, *39* (5), 868-873.
401. Fischer, E.; Speier, A. Darstellung der Ester. *Ber. Dtsch. Chem. Ges.* **1895**, *28* (3), 3252-3258.
402. Ishiyama, T.; Murata, M.; Miyaura, N. Palladium(0)-Catalyzed Cross-Coupling Reaction of Alkoxydiboron with Haloarenes: A Direct Procedure for Arylboronic Esters. *J. Org. Chem.* **1995**, *60* (23), 7508-7510.
403. Ishiyama, T.; Ishida, K.; Miyaura, N. Synthesis of pinacol arylboronates via cross-coupling reaction of bis(pinacolato)diboron with chloroarenes catalyzed by palladium(0)–tricyclohexylphosphine complexes. *Tetrahedron* **2001**, *57* (49), 9813-9816.
404. Willis, D. M.; Strongin, R. M. Palladium-catalyzed borylation of aryldiazonium tetrafluoroborate salts. A new synthesis of arylboronic esters. *Tetrahedron Lett.* **2000**, *41* (45), 8683-8686.
405. Fürstner, A.; Seidel, G. Microwave-Assisted Synthesis of Pinacol Boronates from Aryl Chlorides Catalyzed by a Palladium/Imidazolium Salt System. *Org. Lett.* **2002**, *4* (4), 541-543.
406. Yang, L.; Liu, Y.-T.; Park, Y.; Park, S.-W.; Chang, S. Ni-Mediated Generation of "CN" Unit from Formamide and Its Catalysis in the Cyanation Reactions. *ACS Catal.* **2019**, *9* (4), 3360-3365.
407. Tan, Y.; Ni, P.; Jiang, W.-j.; Fu, Y.; Ding, Q. Direct Transamidation of Thioamides with Amines via Acetophenone-Promoted Enamine Catalysis under Metal-Free Conditions. *J. Org. Chem.* **2024**, *89* (5), 2939-2950.

408. Khan, M.-u.-H.; Hameed, S.; Akhtar, T.; Al-Masoudi, N. A.; Al-Masoudi, W. A.; Jones, P. G.; Pannecouque, C. Synthesis, crystal structure, anti-HIV, and antiproliferative activity of new oxadiazole and thiazole analogs. *Med. Chem. Res.* **2016**, *25* (10), 2399-2409.
409. Krülle, T. M.; Barba, O.; Davis, S. H.; Dawson, G.; Procter, M. J.; Staroske, T.; Thomas, G. H. A simple route to 6- and 7-fluoro-substituted naphthalene-1-carboxylic acids. *Tetrahedron Lett.* **2007**, *48* (9), 1537-1540.
410. Demko, Z. P.; Sharpless, K. B. Preparation of 5-Substituted 1H-Tetrazoles from Nitriles in Water. *J. Org. Chem.* **2001**, *66* (24), 7945-7950.
411. Guha, R. On exploring structure-activity relationships. *Methods Mol. Biol.* **2013**, *993*, 81-94.
412. Tantawy, S. I.; Timofeeva, N.; Sarkar, A.; Gandhi, V. Targeting MCL-1 protein to treat cancer: opportunities and challenges. *Front. Oncol.* **2023**, *13*:1226289.
413. Widden, H.; Placzek, W. J. The multiple mechanisms of MCL1 in the regulation of cell fate. *Commun. Biol.* **2021**, *4* (1), 1029.
414. Arbour, N.; Vanderluit, J. L.; Le Grand, J. N.; Jahani-Asl, A.; Ruzhynsky, V. A.; Cheung, E. C.; Kelly, M. A.; MacKenzie, A. E.; Park, D. S.; Opferman, J. T.; et al. Mcl-1 is a key regulator of apoptosis during CNS development and after DNA damage. *J. Neurosci.* **2008**, *28* (24), 6068-6078.
415. Cen, X.; Chen, Y.; Xu, X.; Wu, R.; He, F.; Zhao, Q.; Sun, Q.; Yi, C.; Wu, J.; Najafov, A.; et al. Pharmacological targeting of MCL-1 promotes mitophagy and improves disease pathologies in an Alzheimer's disease mouse model. *Nat. Commun.* **2020**, *11* (1), 5731.
416. Friberg, A.; Vigil, D.; Zhao, B.; Daniels, R. N.; Burke, J. P.; Garcia-Barrantes, P. M.; Camper, D.; Chauder, B. A.; Lee, T.; Olejniczak, E. T.; et al. Discovery of Potent Myeloid Cell Leukemia 1 (Mcl-1) Inhibitors Using Fragment-Based Methods and Structure-Based Design. *J. Med. Chem.* **2013**, *56* (1), 15-30.
417. Bernardo, P. H.; Sivaraman, T.; Wan, K.-F.; Xu, J.; Krishnamoorthy, J.; Song, C. M.; Tian, L.; Chin, J. S. F.; Lim, D. S. W.; Mok, H. Y. K.; et al. Structural Insights into the Design of Small Molecule Inhibitors That Selectively Antagonize Mcl-1. *J. Med. Chem.* **2010**, *53* (5), 2314-2318.
418. Doi, K.; Li, R.; Sung, S.-S.; Wu, H.; Liu, Y.; Manieri, W.; Krishnegowda, G.; Awwad, A.; Dewey, A.; Liu, X.; et al. Discovery of Marinopyrrole A (Maritoclax) as a Selective Mcl-

1 Antagonist that Overcomes ABT-737 Resistance by Binding to and Targeting Mcl-1 for Proteasomal Degradation*. *J. Biol. Chem.* **2012**, *287* (13), 10224-10235.

419. Abulwerdi, F. A.; Liao, C.; Mady, A. S.; Gavin, J.; Shen, C.; Cierpicki, T.; Stuckey, J. A.; Showalter, H. D. H.; Nikolovska-Coleska, Z. 3-Substituted-N-(4-Hydroxynaphthalen-1-yl)arylsulfonamides as a Novel Class of Selective Mcl-1 Inhibitors: Structure-Based Design, Synthesis, SAR, and Biological Evaluation. *J. Med. Chem.* **2014**, *57* (10), 4111-4133.
420. Song, T.; Li, X.; Chang, X.; Liang, X.; Zhao, Y.; Wu, G.; Xie, S.; Su, P.; Wu, Z.; Feng, Y.; et al. 3-Thiomorpholin-8-oxo-8H-acenaphtho [1,2-b] pyrrole-9-carbonitrile (S1) derivatives as pan-Bcl-2-inhibitors of Bcl-2, Bcl-xL and Mcl-1. *Bioorg. Med. Chem.* **2013**, *21* (1), 11-20.
421. Tanaka, Y.; Aikawa, K.; Nishida, G.; Homma, M.; Sogabe, S.; Igaki, S.; Hayano, Y.; Sameshima, T.; Miyahisa, I.; Kawamoto, T.; et al. Discovery of Potent Mcl-1/Bcl-xL Dual Inhibitors by Using a Hybridization Strategy Based on Structural Analysis of Target Proteins. *J. Med. Chem.* **2013**, *56* (23), 9635-9645.
422. Rega, M. F.; Wu, B.; Wei, J.; Zhang, Z.; Cellitti, J. F.; Pellecchia, M. SAR by Interligand Nuclear Overhauser Effects (ILOEs) Based Discovery of Acylsulfonamide Compounds Active against Bcl-xL and Mcl-1. *J. Med. Chem.* **2011**, *54* (17), 6000-6013.
423. Ge, Y.; Kazi, A.; Marsilio, F.; Luo, Y.; Jain, S.; Brooks, W.; Daniel, K. G.; Guida, W. C.; Sebti, S. M.; Lawrence, H. R. Discovery and Synthesis of Hydronaphthoquinones as Novel Proteasome Inhibitors. *J. Med. Chem.* **2012**, *55* (5), 1978-1998.
424. Castanet, A.-S.; Colobert, F.; Broutin, P.-E. Mild and regioselective iodination of electron-rich aromatics with N-iodosuccinimide and catalytic trifluoroacetic acid. *Tetrahedron Lett.* **2002**, *43* (29), 5047-5048.
425. Chaikovskii, V. K.; Filimonov, V. D.; Skorokhodov, V. I.; Ogorodnikov, V. D. Superactivity and dual reactivity of the system N-iodosuccinimide-H2SO4 in the iodination of deactivated arenes. *Russ. J. Org. Chem.* **2007**, *43* (9), 1278-1281.
426. Noda, Y.; Kashima, M. An Efficient and Regioselective Direct Aromatic Iodination Using Iodine and Nitrogen Dioxide. *Tetrahedron Lett.* **1997**, *38* (35), 6225-6228.
427. Blackmore, I. J.; Boa, A. N.; Murray, E. J.; Dennis, M.; Woodward, S. A simple preparation of iodoarenes, iodoalkenes and iodoalkynes by reaction of organolithiums with 2,2,2-trifluoro-1-iodoethane. *Tetrahedron Lett.* **1999**, *40* (36), 6671-6672.

428. Yusubov, M. S., Tveryakova, E. N., Krasnokutskaya, E. A., Perederyna, I. A., & Zhdankin, V. V. (2007). Solvent-Free Iodination of Arenes using Iodine–Silver Nitrate Combination. *Synth. Commun. 37*(8), 1259–1265.

429. Eichman, C. C.; Stambuli, J. P. Zinc-Mediated Palladium-Catalyzed Formation of Carbon−Sulfur Bonds. *J. Org. Chem.* **2009**, *74* (10), 4005-4008.

430. Itoh, T.; Mase, T. A General Palladium-Catalyzed Coupling of Aryl Bromides/Triflates and Thiols. *Org. Lett.* **2004**, *6* (24), 4587-4590.

431. Mispelaere-Canivet, C.; Spindler, J.-F.; Perrio, S.; Beslin, P. Pd2(dba)3/Xantphos-catalyzed cross-coupling of thiols and aryl bromides/triflates. *Tetrahedron* **2005**, *61* (22), 5253-5259.

432. Liu, L.; Stelmach, J. E.; Natarajan, S. R.; Chen, M.-H.; Singh, S. B.; Schwartz, C. D.; Fitzgerald, C. E.; O'Keefe, S. J.; Zaller, D. M.; Schmatz, D. M.; et al. SAR of 3,4-Dihydropyrido[3,2-d]pyrimidone p38 inhibitors. *Bioorg. Med. Chem. Lett.* **2003**, *13* (22), 3979-3982.

433. Kaldor, S. W.; Kalish, V. J.; Davies, J. F.; Shetty, B. V.; Fritz, J. E.; Appelt, K.; Burgess, J. A.; Campanale, K. M.; Chirgadze, N. Y.; Clawson, D. K.; et al. Viracept (Nelfinavir Mesylate, AG1343): A Potent, Orally Bioavailable Inhibitor of HIV-1 Protease. *J. Med. Chem.* **1997**, *40* (24), 3979-3985.

434. Kwart, H.; Evans, E. R. The Thio-Claisen Rearrangement. The Mechanism of Thermal Rearrangement of Allyl Aryl Sulfides. *J. Org. Chem.* **1966**, *31* (2), 413-419.

435. Louie, J.; Hartwig, J. F. Transmetalation, Involving Organotin Aryl, Thiolate, and Amide Compounds. An Unusual Type of Dissociative Ligand Substitution Reaction. *J. Am. Chem. Soc.* **1995**, *117* (46), 11598-11599.

436. Schopfer, U.; Schlapbach, A. A general palladium-catalysed synthesis of aromatic and heteroaromatic thioethers. *Tetrahedron* **2001**, *57* (15), 3069-3073.

437. Kwong, F. Y.; Buchwald, S. L. A General, Efficient, and Inexpensive Catalyst System for the Coupling of Aryl Iodides and Thiols. *Org. Lett.* **2002**, *4* (20), 3517-3520.

438. Bates, C. G.; Gujadhur, R. K.; Venkataraman, D. A General Method for the Formation of Aryl−Sulfur Bonds Using Copper(I) Catalysts. *Org. Lett.* **2002**, *4* (16), 2803-2806.

439. Foà, M.; Santi, R.; Garavalia, F. Phase-transfer catalysis in the nickel- and palladium-catalyzed formation of aryl and alkenyl sulfides. *J. Organomet. Chem.* **1981**, *206* (3), C29-C32.

440. Jang, M.; Lim, T.; Park, B. Y.; Han, M. S. Metal-Free, Rapid, and Highly Chemoselective Reduction of Aromatic Nitro Compounds at Room Temperature. *J. Org. Chem.* **2022**, *87* (2), 910-919.
441. Zhang, H.; Wang, X.; Mao, J.; Huang, Y.; Xu, W.; Duan, Y.; Zhang, J. Synthesis and biological evaluation of novel benzofuroxan-based pyrrolidine hydroxamates as matrix metalloproteinase inhibitors with nitric oxide releasing activity. *Bioorg. Med. Chem.* **2018**, *26* (15), 4363-4374.
442. Zhang, X.; Sheng, X.; Shen, J.; Zhang, S.; Sun, W.; Shen, C.; Li, Y.; Wang, J.; Lv, H.; Cui, M.; et al. Discovery and Evaluation of Pyrazolo[3,4-d]pyridazinone as a Potent and Orally Active Irreversible BTK Inhibitor. *ACS Med. Chem. Lett.* **2020**, *11* (10), 1863-1868.
443. Fujii, S.; Kikuchi, E.; Watanabe, Y.; Suzuyama, H.; Ishigami-Yuasa, M.; Mori, T.; Isobe, K.; Uchida, S.; Kagechika, H. Structural development of N-(4-phenoxyphenyl)benzamide derivatives as novel SPAK inhibitors blocking WNK kinase signaling. *Bioorg. Med. Chem. Lett.* **2020**, *30* (17), 127408.
444. Bartus, R. T. On Neurodegenerative Diseases, Models, and Treatment Strategies: Lessons Learned and Lessons Forgotten a Generation Following the Cholinergic Hypothesis. *Exp. Neurol.* **2000**, *163* (2), 495-529.
445. Topliss, J. G. Utilization of operational schemes for analog synthesis in drug design. *J. Med. Chem.* **1972**, *15* (10), 1006-1011.
446. Cernak, T.; Dykstra, K. D.; Tyagarajan, S.; Vachal, P.; Krska, S. W. The medicinal chemist's toolbox for late stage functionalization of drug-like molecules. *Chem. Soc. Rev.* **2016**, *45* (3), 546-576.
447. Moir, M.; Danon, J. J.; Reekie, T. A.; Kassiou, M. An overview of late-stage functionalization in today's drug discovery. *Expert Opin. Drug Discov.* **2019**, *14* (11), 1137-1149.
448. Montgomery, A. P.; Joyce, J. M.; Danon, J. J.; Kassiou, M. An update on late-stage functionalization in today's drug discovery. *Expert Opin. Drug Discov.* **2023**, *18* (6), 597-613.
449. Castellino, N. J.; Montgomery, A. P.; Danon, J. J.; Kassiou, M. Late-stage Functionalization for Improving Drug-like Molecular Properties. *Chem. Rev.* **2023**, *123* (13), 8127-8153.

450. Békés, M.; Langley, D. R.; Crews, C. M. PROTAC targeted protein degraders: the past is prologue. *Nat. Rev. Drug Discov.* **2022**, *21* (3), 181-200.
451. Lv, D.; Pal, P.; Liu, X.; Jia, Y.; Thummuri, D.; Zhang, P.; Hu, W.; Pei, J.; Zhang, Q.; Zhou, S.; et al. Development of a BCL-xL and BCL-2 dual degrader with improved anti-leukemic activity. *Nat. Commun.* **2021**, *12* (1), 6896.
452. Wimo, A.; Seeher, K.; Cataldi, R.; Cyhlarova, E.; Dielemann, J. L.; Frisell, O.; Guerchet, M.; Jönsson, L.; Malaha, A. K.; Nichols, E.; et al. The worldwide costs of dementia in 2019. *Alzheimers Dement.* **2023**, *19* (7), 2865-2873.
453. Govindan, K.; Chen, N.-Q.; Chuang, Y.-W.; Lin, W.-Y. Unlocking Amides through Selective C–N Bond Cleavage: Allyl Bromide-Mediated Divergent Synthesis of Nitrogen-Containing Functional Groups. *Org. Lett.* **2021**, *23* (24), 9419-9424.
454. Sureshbabu, B.; Ramkumar, V.; Sankararaman, S. A mild and efficient method for the synthesis of structurally diverse 1,2,3-triazolylidene palladium(II) diiodo complexes. Comparison of catalytic activities for Suzuki–Miyaura coupling. *J. Organomet. Chem.* **2015**, *799-800*, 232-238.
455. Peng, Z.; Hu, G.; Qiao, H.; Xu, P.; Gao, Y.; Zhao, Y. Palladium-Catalyzed Suzuki Cross-Coupling of Arylhydrazines via C–N Bond Cleavage. *J. Org. Chem.* **2014**, *79* (6), 2733-2738.
456. Wang, P.; Luchowska-Stańska, U.; van Basten, B.; Chen, H.; Liu, Z.; Wiejak, J.; Whelan, P.; Morgan, D.; Lochhead, E.; Barker, G.; et al. Synthesis and Biochemical Evaluation of Noncyclic Nucleotide Exchange Proteins Directly Activated by cAMP 1 (EPAC1) Regulators. *J. Med. Chem.* **2020**, *63* (10), 5159-5184.
457. Rajeswari, P. S.; Nagarajan, R.; P, S. K.; Emmanuvel, L. Synthesis of new Copper Catalyst with Pyrazole Based Tridentate Ligand and Study of Its Activity for Azide Alkyne Coupling. *J. Organomet. Chem.* **2021**, *931*, 121627.
458. Collier, P. N.; Twin, H. C.; Knegtel, R. M. A.; Boyall, D.; Brenchley, G.; Davis, C. J.; Keily, S.; Mak, C.; Miller, A.; Pierard, F.; et al. Discovery of Selective, Orally Bioavailable Pyrazolopyridine Inhibitors of Protein Kinase Cθ (PKCθ) That Ameliorate Symptoms of Experimental Autoimmune Encephalomyelitis. *ACS Med. Chem. Lett.* **2019**, *10* (8), 1134-1139.
459. He, W.; Zhou, B.; Liu, W.; Zhang, M.; Shen, Z.; Han, Z.; Jiang, Q.; Yang, Q.; Song, C.; Wang, R.; et al. Identification of A Novel Small-Molecule Binding Site of the Fat Mass and Obesity Associated Protein (FTO). *J. Med. Chem.* **2015**, *58* (18), 7341-7348.

460. Tagat, J. R.; McCombie, S. W.; Nazareno, D. V.; Boyle, C. D.; Kozlowski, J. A.; Chackalamannil, S.; Josien, H.; Wang, Y.; Zhou, G. Synthesis of Mono- and Difluoronaphthoic Acids. *J. Org. Chem.* **2002**, *67* (4), 1171-1177.
461. Behloul, C.; Bouchelouche, K.; Guijarro, D.; Nájera, C.; Yus, M. Detritylation of Protected Tetrazoles by Naphthalene-Catalyzed Lithiation. *Synthesis* **2014**, *46* (15), 2065-2070.
462. Miller, L. M.; Keune, W.-J.; Castagna, D.; Young, L. C.; Duffy, E. L.; Potjewyd, F.; Salgado-Polo, F.; Engel García, P.; Semaan, D.; Pritchard, J. M.; et al. Structure–Activity Relationships of Small Molecule Autotaxin Inhibitors with a Discrete Binding Mode. *J. Med. Chem.* **2017**, *60* (2), 722-748.
463. Amélia Santos, M.; Marques, S. M.; Tuccinardi, T.; Carelli, P.; Panelli, L.; Rossello, A. Design, synthesis and molecular modeling study of iminodiacetyl monohydroxamic acid derivatives as MMP inhibitors. *Bioorg. Med. Chem.* **2006**, *14* (22), 7539-7550.
464. Shigeno, M.; Tohara, I.; Sasaki, K.; Nozawa-Kumada, K.; Kondo, Y. Combined Brønsted Base-Promoted CO_2 Fixation into Benzylic C–H Bonds of Alkylarenes. *Org. Lett.* **2022**, *24* (26), 4825-4830.
465. Liao, L.-L.; Cao, G.-M.; Ye, J.-H.; Sun, G.-Q.; Zhou, W.-J.; Gui, Y.-Y.; Yan, S.-S.; Shen, G.; Yu, D.-G. Visible-Light-Driven External-Reductant-Free Cross-Electrophile Couplings of Tetraalkyl Ammonium Salts. *J. Am. Chem. Soc.* **2018**, *140* (50), 17338-17342.
466. Yamada, A.; Fujii, S.; Mori, S.; Kagechika, H. Design and Synthesis of 4-(4-Benzoylaminophenoxy)phenol Derivatives As Androgen Receptor Antagonists. *ACS Med. Chem. Lett.* **2013**, *4* (10), 937-941.
467. Lategahn, J.; Hardick, J.; Grabe, T.; Niggenaber, J.; Jeyakumar, K.; Keul, M.; Tumbrink, H. L.; Becker, C.; Hodson, L.; Kirschner, T.; et al. Targeting Her2-insYVMA with Covalent Inhibitors—A Focused Compound Screening and Structure-Based Design Approach. *J. Med. Chem.* **2020**, *63* (20), 11725-11755.
468. Madhavi Sastry, G.; Adzhigirey, M.; Day, T.; Annabhimoju, R.; Sherman, W. Protein and ligand preparation: parameters, protocols, and influence on virtual screening enrichments. *J. Comput. Aided Mol. Des.* **2013**, *27*, 221– 234.
469. Harder, E.; Damm, W.; Maple, J.; Wu, C.; Reboul, M.; Xiang, J. Y.; Wang, L.; Lupyan, D.; Dahlgren, M. K.; Knight, J. L.; Kaus, J. W.; Cerutti, D. S.; Krilov, G.; Jorgensen, W.

L.; Abel, R.; Friesner, R. A. OPLS3: A force field providing broad coverage of drug-like small molecules and proteins. *J. Chem. Theory Comput.* **2016**, *12*, 281– 296.

470. Watts, K. S.; Dalal, P.; Murphy, R. B.; Sherman, W.; Friesner, R. A.; Shelley, J. C. ConfGen: A conformational search method for efficient generation of bioactive conformers. *J. Chem. Inf. Model.* **2010**, *50*, 534– 546.
471. Friesner, R. A.; Banks, J. L.; Murphy, R. B.; Halgren, T. A.; Klicic, J. J.; Mainz, D. T.; Repasky, M. P.; Knoll, E. H.; Shelley, M.; Perry, J. K.; Shaw, D. E.; Francis, P.; Shenkin, P. S. Glide: A new approach for rapid, accurate docking and scoring. 1. Method and assessment of docking accuracy. *J. Med. Chem.* **2004**, *47*, 1739– 1749.
472. Friesner, R. A.; Murphy, R. B.; Repasky, M. P.; Frye, L. L.; Greenwood, J. R.; Halgren, T. A.; Sanschagrin, P. C.; Mainz, D. T. Extra precision glide: Docking and scoring incorporating a model of hydrophobic enclosure for protein–ligand complexes. *J. Med. Chem.* **2006**, *49*, 6177.

This Page Intentionally Left Blank

This Page Intentionally Left Blank

Appendix A

Selected Tables

Appendix A – Selected Tables

Table A: Factors secreted in the SASP.

SASP Factor	Class	Notes
Soluble factors		
IL-6	Interleukins	
IL-7		
IL-1a, -1b		
IL-13		
IL-15		
IL-8	Chemokines	
GRO-a, -b, -g		Growth-related oncogene
MCP-2		Membrane cofactor protein
MCP-4		
MIP-1a		Macrophage inflammatory protein
MIP-3a		
HCC-4		
Eotaxin-3		
GM-CSF	Other inflammatory factors	Granulocyte-macrophage colony-stimulating factor
MIF		Macrophage migration inhibitory factor
Amphiregulin	Growth factors and regulators	
Epiregulin		
Heregulin		
EGF		Endothelial growth factor
KGF		Keratinocyte growth factor
VEGF		Vascular endothelial growth factor
Angiogenin		
SCF		Stem cell factor
SDF-1		Stromal cell-derived factor

PIGF		Placental growth factor
IGFBP-2, -3, -4, -6, -7		Insulin-like growth factor binding protein
MMP-1, -3, -10, -12, -13, -14	Proteases and regulators	Matrix metalloproteinase
TIMP-1, -2		Tissue inhibitor of metalloproteinase
PAI-1, -2		Plasminogen activator inhibitor
t-PA		Tissue-type plasminogen activator
u-PA		Urokinase-type plasminogen activator
Cathepsin B		
Soluble or shed receptors or ligands		
ICAM-1, -3		Intercellular adhesion molecule
OPG		Osteoprotegerin
sTNFR-I		Soluble tumour necrosis factor receptor
sTNFR-II		
TRAIL-R3		Tumour necrosis factor-related apoptosis-inducing ligand
Fas		
u-PAR		u-PA receptor
SGP130		Soluble glycoprotein
EGF-R		Endothelial growth factor
Nonprotein soluble factors		
PGE2		Prostaglandin E2
NO		Nitric oxide
ROS		Reactive oxidative species
Insoluble factors		
Fibronectin		
Collagens		
Laminin		

Table B: Known senomorphics.

Name	Structure	Pathway affected
Natural Products		
Rapamycin	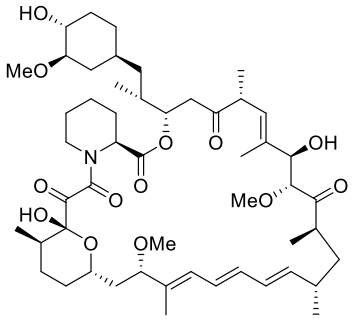	mTOR kinase inhibitor
Everolimus	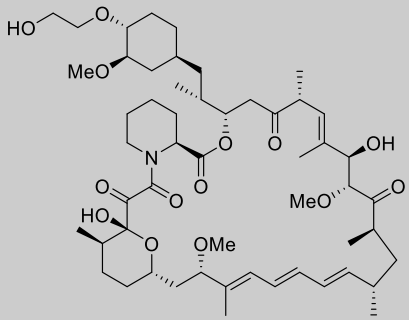	mTOR kinase inhibitor
Resveratrol	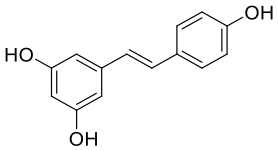	NF-κB pathway inhibitor NRF2 pathway activator
Apigenin	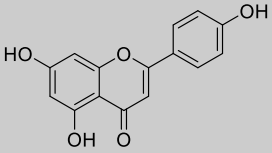	NF-κB pathway inhibitor
Kaempferol	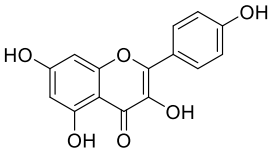	NF-κB pathway inhibitor SIRT1 inducer
Epigallocatechin gallate	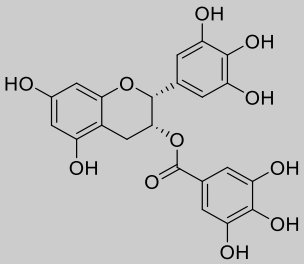	mTOR signaling inhibitor SIRT1, SIRT3 inducer NRF2 pathway activator

	FDA-Approved Drugs	
Metformin	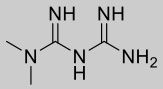	NF-κB pathway inhibitor Mitochondrial complex I inhibitor
Ruxotinilib	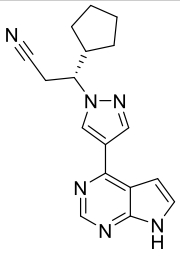	JAK1, JAK2 inhibitor
	Other Senomorphics	
Loperamide	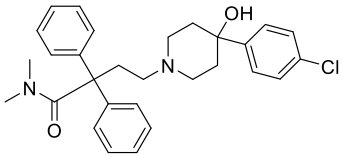	Ca^{2+} channel inhibitors
Niguldipine	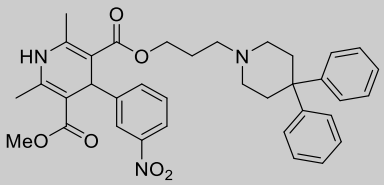	Ca^{2+} channel inhibitors
KU-60019	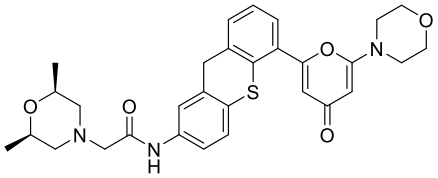	ATM kinase inhibitor

Table C: Known and potential senolytic small molecules

Name	Structure	Pathway affected
Kinase inhibitors		
Dasatinib	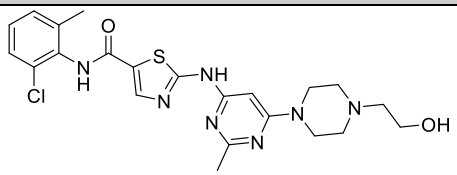	Abl, Tec and Src kinases
Nintedanib	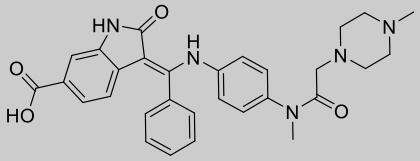	JAK2, STAT3 inhibitor
R406	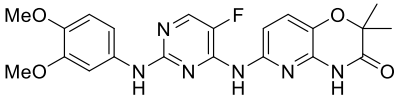	FAK, p38 MAPK inhibitor
Terreic acid	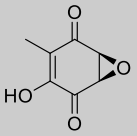	BTK inhibitor
Daidzein	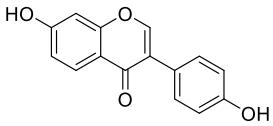	Unknown
PD-98059	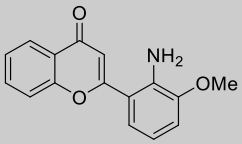	Unknown
Y-27632	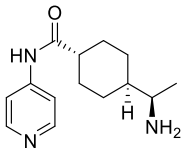	Unknown
KU-60019	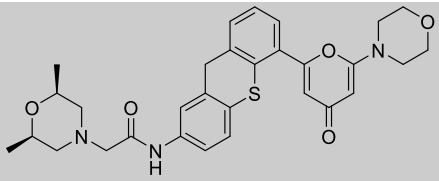	ATM kinase inhibitor
BCL-2 family inhibitors		
ABT-263	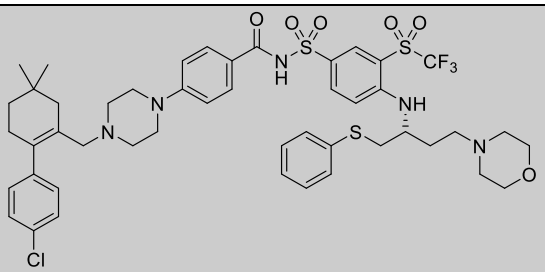	BCL-2, BCL-X_L inhibitor

ABT-737	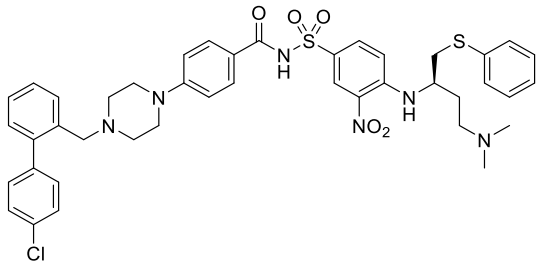	BCL-W, BCL-X_L inhibitor
A1331852	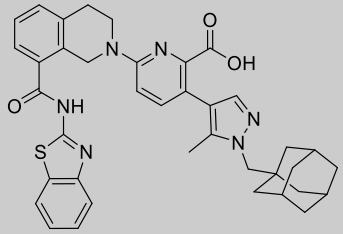	BCL-X_L inhibitor
A1155463	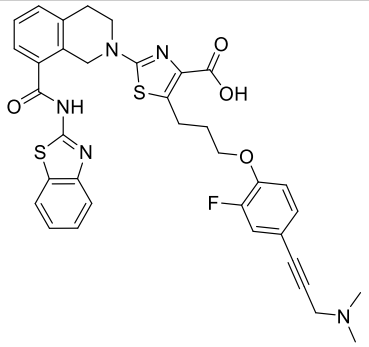	BCL-X_L inhibitor
S63835	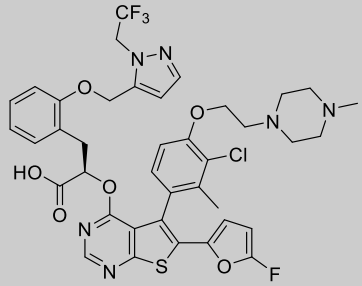	MCL-1 inhibitor
UMI-77	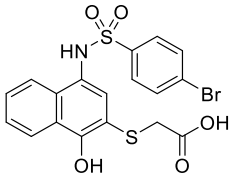	MCL-1 inhibitor
AZD5991	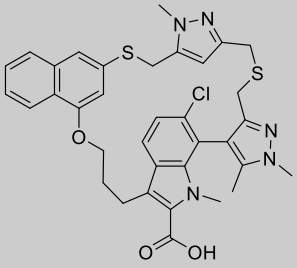	MCL-1 inhibitor

	Plant extracts	
Quercetin	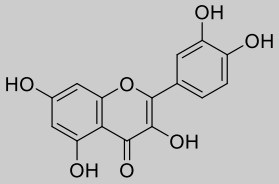	PI3K/AKT
Fisetin	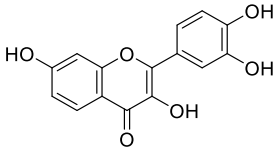	PI3K/AKT
EF24	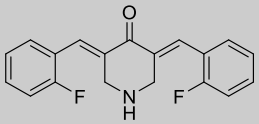	BCL-X_L, MCL-1
Procyanidin C1	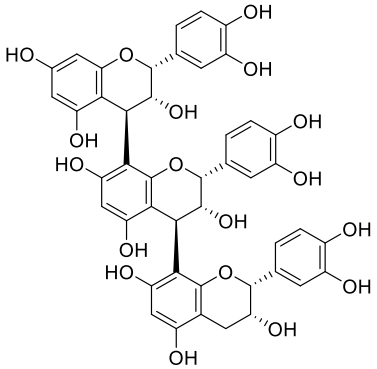	Unknown
Gingerenone A	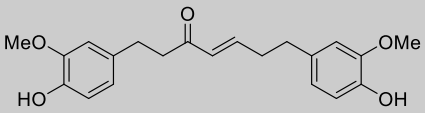	Unknown
Piperlongumine	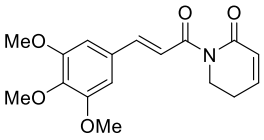	OXR1 inhibitor
	HSP inhibitors	
Geldanamycin	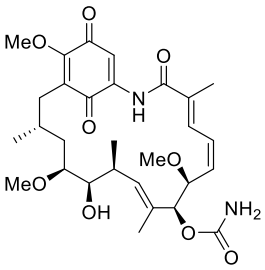	HSP90 inhibitor

Tanespimycin	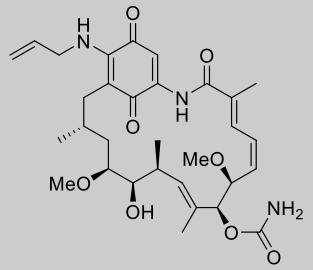	HSP90 inhibitor
Alvespimycin	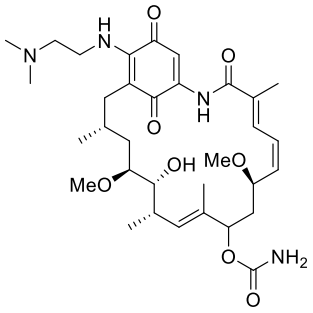	HSP90 inhibitor
25-hydroxycholesterol	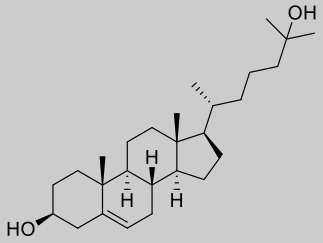	CRYAB inhibitor
	BET family inhibitors	
ARV825	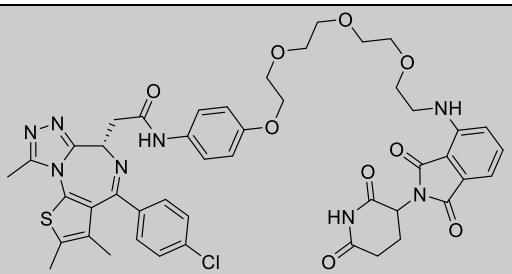	BET family degrader
JQ1	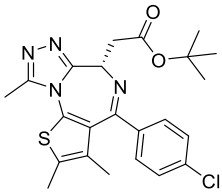	BET inhibitor
	p53 stabilisers	
RG-7112	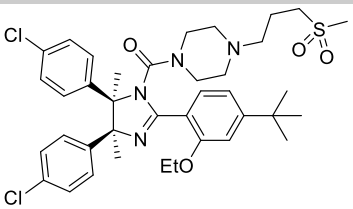	MDM2 inhibitor

P5091	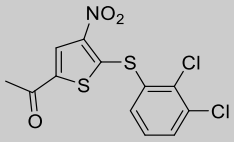	USP7 inhibitor
P22077	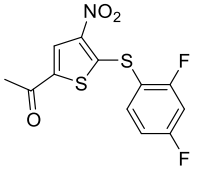	USP7 inhibitor
PPARα agonist		
Fenofibrate	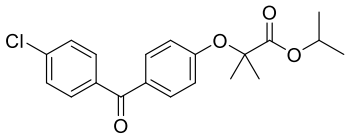	PPARα agonist
Repurposed cancer drugs		
GL-V9	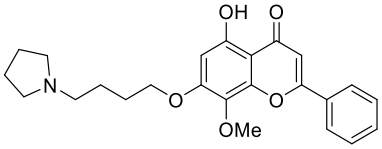	Alkalisation of lysosomes
Panobinostat	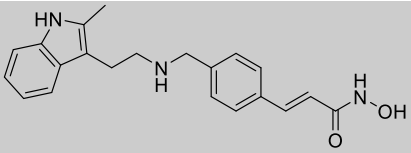	HDAC inhibitor
Antibiotics		
Azithromycin	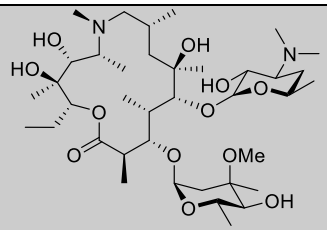	Antibiotic
Roxithromycin	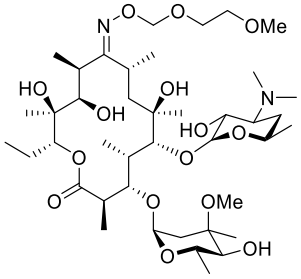	Antibiotic
Nigericin	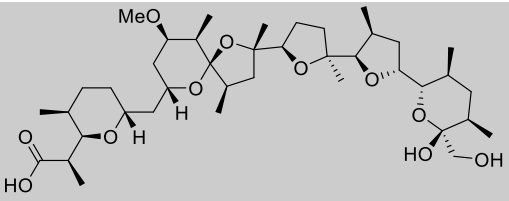	Antibiotic

This Page Intentionally Left Blank

This Page Intentionally Left Blank

Appendix B

UMI-77 Analogues for Docking

Appendix B – UMI-77 Analogues for Docking

The following compounds were designed as part of the SAR probing study of chapter 4. The energy-minimised structures of these compounds were docked to a structure of MCL-1 as described in **Chapter 4.4.** to design a library of UMI-77 derivatives.

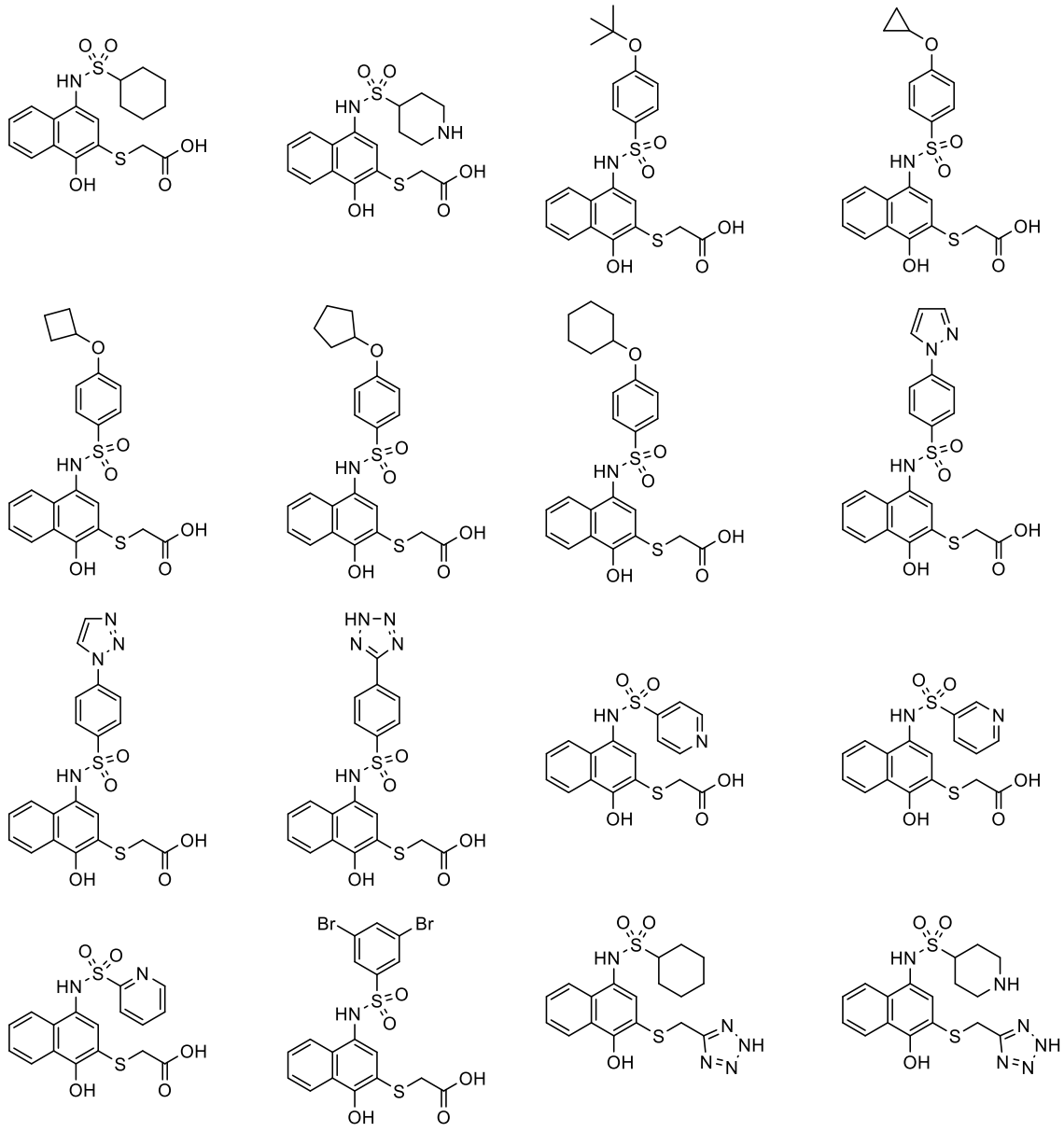

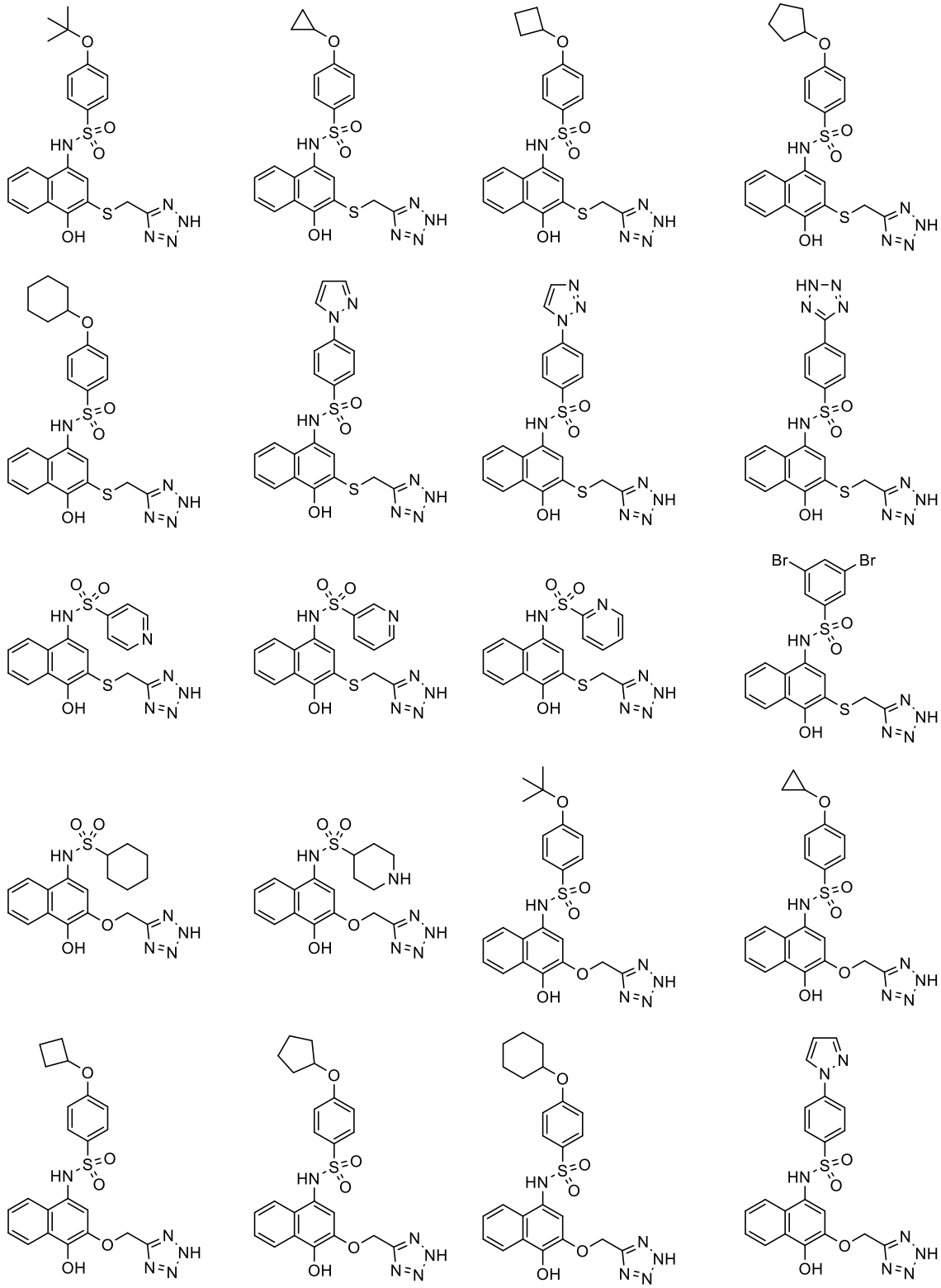

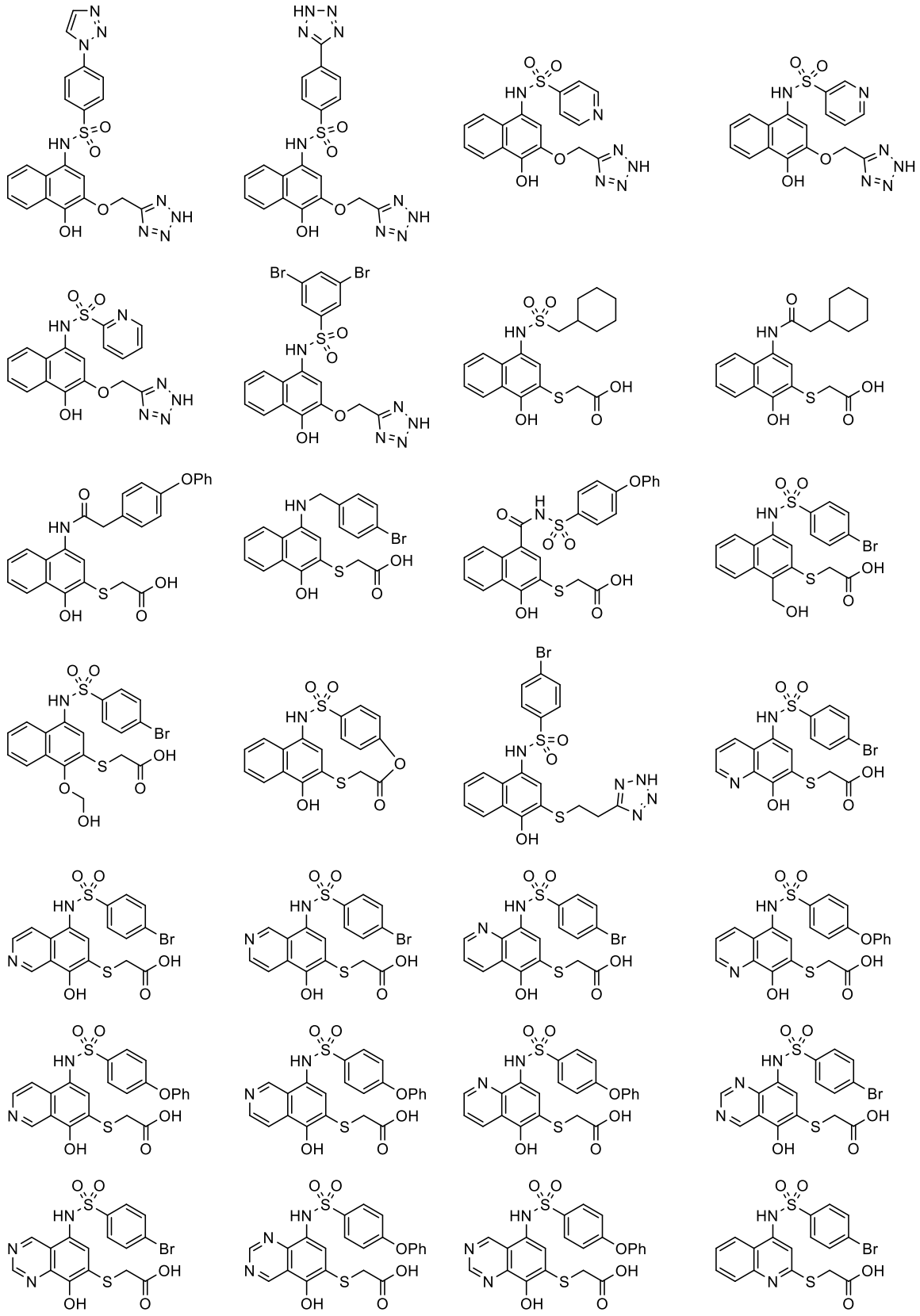

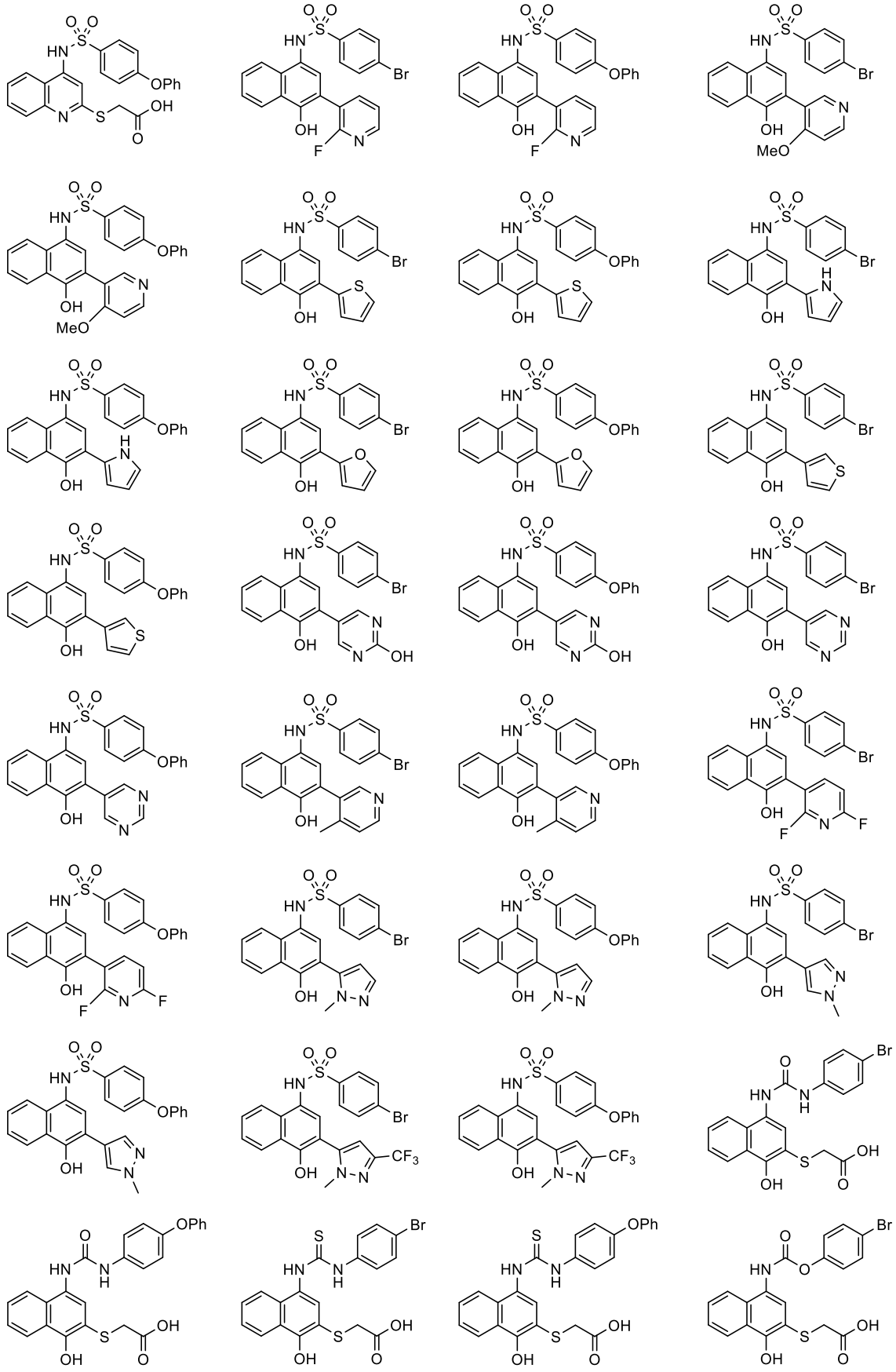

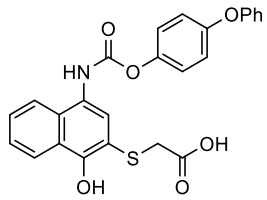
O
OPh
HN
O
S
OH
OH
O

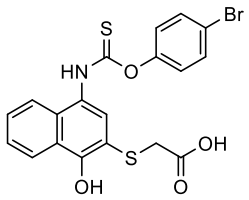
S
Br
HN
O
S
OH
OH
O

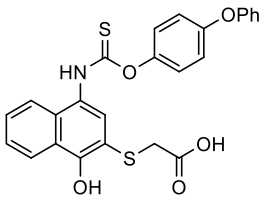
S
OPh
HN
O
S
OH
OH
O

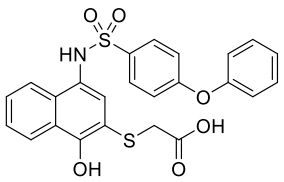
O
O
S
HN
O
S
OH
OH
O